Weak gravitational lensing: Detection of mass concentrations in wide field imaging data

Dissertation

zur
Erlangung des Doktorgrades (Dr. rer. nat.)
der
Mathematisch-Naturwissenschaftliche Fakultät
der
Rheinischen Friedrich-Wilhelms-Universität Bonn

vorgelegt von

Mischa Schirmer
aus
Dachau

Bonn, 2004

Angefertigt mit Genehmigung der Mathematisch-Naturwissenschaftlichen Fakultät der Rheinischen Friedrich-Wilhelms-Universität Bonn

1. Referent: Prof. Dr. Peter Schneider (Universität Bonn)

2. Referent: Prof. Dr. Matthias Bartelmann (Universität Heidelberg)

Tag der Promotion:

Contents

0.1 Inhalt und Zusammenfassung

Gravitationslinseneffekt Mit Hilfe der Allgemeinen Relativitätstheorie lässt sich zeigen, dass Massen die Raumzeit krümmen und dass frei fallende Körper diesen Krümmungen folgen. Dies gilt auch für Lichtstrahlen, die demnach in Gravitationsfeldern abgelenkt werden (Gravitationslinseneffekt, siehe auch Bartelmann & Schneider, 2001). Ist die entlang der Sichtlinie projizierte Massendichte eines Objekts groß genug, so kann das Licht einer Quelle auf verschiedenen Wegen um die Masse herumlaufen und zum Beobachter gelangen, der dann mehrere Abbilder der Quelle am Himmel sieht. Dies ist auch als *starker Linseneffekt* bekannt, der für Galaxienhaufen erstmals durch Soucail et al. (1987a,b) und Lynds & Petrosian (1986) nachgewiesen wurde, die stark verzerrte Mehrfachbilder ferner Galaxien durch den Haufen Abell 370 hindurch beobachteten. Seither wurden mehrere Dutzend solcher Haufen gefunden, die ähnliche Muster aufweisen.

Aufgrund der großen Masse eines Haufens sind die Verzerrungen (*Scherung*) in den Abbildern von Hintergrundgalaxien auch noch in größerer Winkelentfernung vom Haufen detektierbar. Dies gelingt jedoch nur noch statistisch, da die intrinsischen Elliptizitäten der Galaxien die zusätzlichen Verzerrungen durch den Linseneffekt stark zu dominieren beginnen. Dieser *schwache Linseneffekt* wurde erstmal zu Beginn der 90er Jahre nachgewiesen. Aufgrund der Beziehung zwischen der projizierten Flächenmassendichte der Linse und der Scherung in den Galaxienbildern lässt sich aus letzterer die Massenverteilung in der Linse rekonstruieren, sowie ein Schätzwert für ihre Gesamtmasse bestimmen. Der Vorteil dieser Methode liegt darin, dass sie unabhängig von der Leuchtkraft der Linse ist und keine Kenntnis über deren dynamischen Zustand benötigt. Eine Beschreibung der grundlegenden kosmologischen Physik sowie des Linseneffekts an sich findet sich in Kapitel 1.

Massenselektierte Galaxienhaufen Aufgrund der schnellen Entwicklung in der Teleskop- und Detektortechnologie und dem erstmaligen Einsatz von Weitwinkelkameras wurde es Ende der 90er Jahre erstmals möglich, die schwachen Scherfelder von Galaxienhaufen auch noch in größeren Abständen vom Haufenzentrum zu vermessen. Die Entwicklung mündete schließlich im Nachweis des sehr schwachen Linseneffekts der großräumigen Strukturen im Universum (Bacon et al., 2000; Kaiser et al., 2000; van Waerbeke et al., 2000; Wittman et al., 2000). Diese *Kosmische Scherung* ist direkt mit dem Fluktuationsspektrum des Dichtefelds im Universum verknüpft und daher von großem Interesse in der gegenwärtigen Forschung.

Mit den nunmehr vorhandenen Möglichkeiten, gleichzeitig tiefe und sehr weite Aufnahmen des Universums zu gewinnen, kann man den Linseneffekt nicht nur zur Bestimmung der Materieverteilung in Haufen benutzen, sondern auch zu deren Detektion, indem nach charakteristischen Verzerrungsmustern in den Galaxienabbildern gesucht wird. Diese Methode hat den Vorteil, dass die Galaxienhaufen direkt anhand ihrer fundamentalen physi-

kalischen Eigenschaft, der Masse, selektiert werden, und nicht anhand ihre Helligkeit. Eine derartig ausgewählte Stichprobe ist wünschenswert, da die Masse eines Haufens wesentlich von den kosmologischen Rahmenbedingungen abhängt und daher tiefergehende Rückschlüsse auf die zugrundeliegende Kosmologie und die Entwicklung dieser Haufen ermöglicht werden. Bereits die erste mit dieser Methode entdeckte Massenkonzentration ist außergewöhnlich, da sie mit keiner irgendwie gearteten räumlichen Konzentration von Galaxien assoziiert zu sein scheint (Erben et al., 2000). Seitdem wurden etwa 10 weitere Massenkonzentrationen auf diese Art selektiert, von denen etwa die Hälfte ebenfalls *dunkel* ist. Die physikalische Natur dieser dunklen Haufen - falls sie tatsächlich existieren und ihnen nicht irgend eine noch unbekannte Systematik zugrunde liegt - ist gegenwärtig ungeklärt. Entweder werden sie von Galaxien mit aussergewöhnlich niedriger Leuchtkraft gebildet, die in den Aufnahmen nicht nachweisbar sind, oder aber sie bestehen ausschliesslich aus Dunkler Materie. Beide Vorstellungen stellen eine Herausforderung sowohl an die gegenwärtigen Theorien der Bildung von Strukturen und Galaxien dar, als auch an die beobachtende Astrophysik.

Beobachtungsprogramm und Softwareentwicklung Um eine größere Stichprobe von masseselektierten Galaxienhaufen zu erhalten, und um die Existenz von dunklen Haufen zu überprüfen, führten wir eine große Beobachtungskampagne mit der Weitwinkelkamera am 2.2m- MPG/ESO-Teleskop durch. Bis zum gegenwärtigen Zeitpunkt konnten tiefe Aufnahmen von 20 Quadratgrad des Südsternhimmels unter sehr guten Beobachtungsbedingungen gewonnen werden. Für die Bearbeitung der sehr großen Datenmengen (mehrere TB) wurde eine automatische Reduktionspipeline entwickelt, da eine manuelle Handhabung in diesem Maßstab nicht mehr möglich ist.

Aufgrund der wachsenden Anzahl von zur Verfügung stehenden Weitwinkelkameras und ihrer technologisch bedingten eher kurzen Betriebsdauer (wenige Jahre) wurde die entwickelte Pipeline so flexibel wie möglich gehalten. Mit ihr lassen sich Daten, die weltweit an verschiedenen Teleskopen gewonnen wurden, problemlos reduzieren. Die Anforderungen an den Reduktionsprozess sind hierbei gerade für Messungen des schwachen Linseneffekts außerordentlich hoch, da die Formen kleiner, leuchtschwacher Galaxien zuverlässig bestimmt werden müssen. Dies kann nur gelingen, wenn das Rauschen in den koaddierten Bildern so niedrig wie möglich gehalten wird. Darüber hinaus muss die astrometrische Lösung, die die Abbildung der einzelnen Aufnahmen in das kombinierte Summenbild beschreibt, sehr exakt sein. Ansonsten werden die Galaxienbilder künstlich verzerrt, was die Scherungsmessung sehr viel schwieriger und unzuverlässiger macht. Aus diesem Grund mussten die verwendeten Algorithmen sehr sorgfältig getestet werden, bevor sie endgültigen Eingang in die Pipeline fanden. Die Softwareentwicklung und die Reduktion einiger sehr großer Testdatensätze wurde wiederholt parallel durchgeführt, bis ein optimales Ergebnis erreicht wurde. Hierauf, und auf die tatsächliche Reduktion der Daten wurden je zwei Jahre von Thomas Erbens und meiner Zeit verwendet. Dies berücksichtigt nicht die Entwicklungsarbeit, die von anderen Leuten geleistet wurde und deren Programme in unserer Pipeline Verwendung fanden. Etwa zwei Drittel der Zeit, die für die vorliegende Dissertation aufgewendet wurde, ist auf diese Entwicklungsarbeit und die Datenreduktion verwandt worden. Eine Beschreibung der Pipeline und die Besonderheiten in der Datenreduktion von Multichip-Kameras findet sich in Kapitel 2.

Selektionsmethode Der Schwerpunkt von Kapitel 3 liegt auf der Analyse der koaddierten Bilder und der Gewinnung des Linsensignals. Die maßgebliche Messgröße hierbei sind die

Formen der (eventuell) gelinsten Galaxien. Diese Aufgabe ist nicht einfach, da die Galaxien sehr weit entfernt sein müssen, um effektiv durch die gravitativen Gezeitenfelder eines näheren Haufens gelinst werden zu können. Daher erscheinen ihre Abbilder klein und leuchtschwach und sind sehr anfällig gegenüber atmosphärischen Turbulenzen und Ungenauigkeiten im Strahlengang eines Teleskops. Es wird ausführlich auf eine gängige Methode zur Korrektur dieser Effekte eingegangen und gezeigt, wie die Gravitationsfelder an sich die Formen der Galaxienbilder verändern. Sind die Scherungsmessungen erst einmal gewonnen und korrigiert worden, so kann anhand einer bestimmten Statistik ein durch einen Haufen verursachtes charakteristisches Verzerrungsmuster in den Galaxienbildern identifiziert werden. Darüber hinaus ermöglicht diese Statistik die gleichzeitige Bestimmung eines Signal-zu-Rausch Verhältnisses für eben diese Detektion. Die mathematische Beschreibung greift hierbei auf eine bestimmte Filterfunktion zurück, für die mehrere verschiedene Formen in der Literatur vorgeschlagen wurden. Diese wurden zusammen mit weiteren, in dieser Arbeit eingeführten, Filterfunktionen ausführlich getestet. In diesem Rahmen konnte ein sehr effizienter neuer Filter für die Detektion von Massenkonzentrationen identifiziert werden. Nachdem die nötigen Begriffsbildungen und Formalismen eingeführt worden sind, wird am Ende dieses Kapitels die Erstellung eines sauberen Objektkatalogs diskutiert.

Resultate In Kapitel 4 schließlich werden die benutzten Methoden anhand der Daten selbst noch einmal auf Konsistenz überprüft. Anschließend werden die Ergebnisse präsentiert, die aus den 20 Quadratgrad gewonnen werden konnten. Zunächst wird gezeigt, dass die Galaxien in den Feldern keine zufälligen Orientierungen haben, sondern kohärente Schermuster vorhanden sind, die mit der im vorigen Kapitel erwähnten Statistik klar nachgewiesen werden können. Diese lassen sich durch die Kosmische Scherung sowie durch das Linsensignal von Galaxienhaufen erklären, wie anhand von Simulationen gezeigt wird.

Daher wird im Anschluss eine masseselektierte Stichprobe von 100 hochsignifikanten Massenkonzentrationen präsentiert. Diese ist etwa 10 mal größer als die gesamte Anzahl masseselektierter, bisher in der Literatur publizierter Haufen. Etwa 60% dieser Haufen sind dunkel, während 30% mit Galaxienüberdichten assoziiert sind. Für die Hälfte dieser optischen Gegenstücke konnten Spektren in der Literatur gefunden werden, die dann auch deren Haufennatur bestätigten. Die verbleibenden 10% in der Stichprobe konnten nicht eindeutig nach hell und dunkel klassifiziert werden. Eine erste statistische Auswertung der hellen und dunklen Haufen zeigt, dass diese zufällig über die Detektorfläche der Kamera verteilt sind und daher keine instrumentellen Effekte die Daten beeinflussen. Darüber hinaus finden sich keine offensichtlichen Unterschiede in den Verteilungen der beiden Haufentypen hinsichtlich ihrer Größe und Signifikanz, ausgenommen einer überdurchschnittlichen Anzahl sehr kompakter und kleiner dunkler Haufen. Diese stellen möglicherweise Fehldetektionen dar. Diese Ergebnisse wurden durch eine Simulation überprüft, in der durch Randomisierung jegliche kohärente Schermuster in den Feldern beseitigt wurden. Hier zeigt sich, dass echte Massenkonzentrationen von Fehldetektionen dadurch unterschieden werden können, dass sie auf verschiedenen Filterskalen signifikant auftreten.

Anschließend werden anhand eines konkreten Beispiels verschiedene Methoden vorgestellt, die bei Vorhandensein weiterer Daten der gleichen Felder (z.B. Beobachtungen in anderen Wellenlängenbereichen) eine Identifikation der Massenkonzentrationen erlauben. Dies umfasst den Nachweis einer Überdichte von roten Galaxien an der Position der Massenkonzentration sowie den Nachweis von Röntgenemission, ausgehend von einem eventuell vorhandenen

heissen Gas, mit dem viele Galaxienhaufen angefüllt sind. Darüber hinaus wird vorgeschlagen, nach positiven Korrelationen zwischen den gefundenen Massenkonzentrationen und den bekannten helleren Quasaren in den jeweiligen Bildfeldern zu suchen. Von letzteren weiß man, dass sie oft durch massereiche Vordergrundobjekte gelinst werden und daher heller erscheinen.

Zweifelsohne muss in den kommenden Jahren noch wesentlich mehr Arbeit in die Klärung der Natur der dunklen Haufen investiert werden. Auch wenn diese Arbeit deutliche Hinweise auf die tatsächliche Existenz dieser Objekte liefert, bleiben sie rätselhaft. Ein tatsächlicher Beweis ihrer Existenz, entweder durch eine positive Korrelation mit Quasaren oder durch den Nachweis von sehr leuchtschwachen Galaxien an ihrer Position, wäre sehr nützlich. Mit der gefundenen Anzahl von 60 dunklen Haufen liegt eine sehr gute Stichprobe vor, aus der sich geeignete Kandidaten für eine detailliertere Analyse und Nachfolgebeobachtungen auswählen lassen.

0.2 Contents and Summary

Gravitational lensing The deflection and distortion of a light bundle by tidal gravitational fields is described in the framework of General Relativity (Bartelmann & Schneider, 2001). There, light bundles from a source follow exactly the curvature of spacetime, and thus can reach the observer from different directions if the projected density of an intervening mass is large enough (*strong lensing effect*). Such a lensing effect of a galaxy cluster was observed the first time by Soucail et al. (1987a,b) and Lynds & Petrosian (1986), who identified highly distorted multiple images of background galaxies close to the centre of the galaxy cluster Abell 370. Since then, several dozen additional clusters were found showing similar strong distortion effects.

Due to a galaxy clusters' large mass, the distortions (*shear*) of the shapes of lensed background galaxies are still measurable if the projected angular distance between the source and the lens is several arcminutes large. However, the distortion can then be detected statistically only, since the intrinsic ellipticity of a galaxy dominates the distortion induced by gravitational lensing. This *weak lensing effect* was measured the first time at the beginning of the nineties. Due to a well-known mathematical relationship between the projected surface mass density of the lens and the observed shear in the galaxy images, the latter can be used to reconstruct the (dark) matter distribution in the lens, and to obtain a mass estimate independent of the luminosity and the virialisation of the lens. A description of the basic (cosmological) physics behind gravitational lensing is given in Chapter 1, together with an introduction into the subject of gravitational lensing itself.

Mass-selected galaxy clusters With the rapid improvement of detector and telescope technology, and the advent of wide field imagers at the end of the nineties, it became possible to probe the shear fields of galaxy clusters to larger radii. The improved understanding of the shape measurement process of small and faint galaxies in such images led then to the discovery of the *Cosmic Shear*, i.e. the very weak gravitational lensing effect of the large scale structure in the universe (Bacon et al., 2000; Kaiser et al., 2000; van Waerbeke et al., 2000; Wittman et al., 2000). The Cosmic Shear is directly related to the power spectrum of the underlying density field, and is therefore of great interest in cosmology.

Having deep wide field images at hand, the lensing argument can be turned around and one can use the weak lensing effect to search for mass concentrations in the universe. This method has the advantage that the galaxy clusters are detected directly by their most fundamental property, the mass, and not by their luminosity. The mass of a cluster, in turn, is a sensitive measure of cosmology and thus a mass-selected (more accurately: shear-selected) sample of galaxy clusters is highly desireable in this respect. The first mass concentration that has been detected serendipitously by this method is still a mystery, since it is entirely dark (Erben et al., 2000). No overdensity of galaxies is seen at its position. Since then, about 10 mass concentrations were found in this way, about half of them being dark. The physical nature of the latter objects, if they are indeed real and not due to some yet unknown systematics, is still unclear. Either these objects consist of very underluminous galaxies that are not seen in the exposures, or they are constituted of dark matter only. Both scenarios are a challenge for current theories of structure and galaxy formation as well as for observations.

Observations and software development In order to establish a larger sample of shear-selected galaxy clusters, our group conducted a weak lensing survey with the Wide Field

Imager at the 2.2m MPG/ESO telescope. So far, 20 square degrees of the southern sky were mapped to great depth in excellent observational conditions. For the reduction of the very large amount of data (several TB), a fully automatic pipeline had to be developed, since a manual processing of such data is no longer feasible. Due to the growing number of Wide Field Imagers and the comparatively short duty time of astronomical instruments, this pipeline was designed to be as flexible as possible in order to be easily adapted to any imager and telescope in the world. The demands on the data reduction process are very high, since the shapes of faint and small galaxies have to be measured reliably. This can only be achieved if the signal-to-noise in the reduced images is as best as possible. Furthermore, the astrometric solution that describes the mapping of the individual exposures onto the coadded image has to be very exact. Otherwise, galaxy shapes are artificially distorted, making a shear measurement even more difficult. For these reasons, a lot of careful testing of the algorithms used had to be done. The software development and the data reduction of some very large test data sets took place in parallel, and were iterated until satisfactory results were achieved. This, and the actual reduction of the survey data consumed more two four years each of Thomas Erben's and my time, not mentioning the much larger effort that has been put by other people into the software modules we make use of in the pipeline. About two thirds of the time dedicated to the present thesis were occupied by this developmental work and the reduction of the survey data. A description of the reduction pipeline and the techniques required especially for multi-chip cameras is given in Chapter 2.

Selection method In Chapter 3 the focus of interest is on the analysis of the reduced images, and the extraction of the desireable weak lensing signal. The basic quantity which is to be obtained from the images are the shapes of the potentially lensed galaxies. This task is not trivial, since those galaxies must be very distant in order to be lensed and distorted efficiently by an intervening galaxy cluster. Thus their images are faint and small, and their shapes are prone to atmospheric turbulence and many technical aspects of a telescope. After evaluating how these image shapes are changed by the tidal gravitational fields of a galaxy cluster, a widely used technique to correct for various atmospheric and telescopical distortion and smearing effects is described. Having the corrected image shapes at hand, a statistics is introduced that allows the identification of a distortion pattern characteristic for galaxy clusters, and an estimate of the signal-to-noise of its detection. This statistics involves a filter function, for which several suggestions are given in the literature. Further possibilities are introduced in this work, and the various filters are tested extensively against each other. A very effective new filter was found in this process for the detection of mass concentrations. After having introduced all the necessary techniques and terminologies, the actual object catalogue extraction is described, and it is explained what kind of filtering steps have to be applied for the cleaning of this catalogue.

Results Chapter 4, finally, verifies the used evaluation methods and presents the results obtained from the 20 square degrees of the survey. It is shown that the galaxies in the survey fields are not randomly oriented, but show significant coherent shear patterns. Simulations show that these can be explained by the presence of Cosmic Shear and cluster lensing.

In order to prove the existence of clusters in the data, a shear-selected sample of 100 mass concentrations with a signal-to-noise of at least 4 is presented and analysed. This sample is about ten times larger than the total number of shear-selected clusters that have been

presented in the literature so far. About 60% of the mass concentrations found are dark, whereas 30% are bright, having obvious optical counterparts. Half of the latter are already spectroscopically confirmed in the literature, the other half have been previously unknown. The remaining 10% of the sample could not be classified unambiguously as being bright or dark. First statistics of the bright and the dark sample show that they are randomly selected from the Wide Field Imager's field of view, thus no systematic instrumental effects are found in the data. Furthermore, the populations of the bright and dark mass peaks show very similar distributions in their size as well as in their significance, apart from the very smallest angular scale probed where disproportionate many dark peaks are found. It is argued that these could probably be spurios detections. These findings are cross-checked by simulations, in which any lensing signal has been destroyed by randomisation of the galaxy orientations. It is shown that true mass peaks can be discerned from spurious peaks in the sense that they appear on a significant level for a broader range of filter scales.

Thereafter, various verification methods for the mass detections found are presented by means of an example. These encompass the identification of red cluster member galaxies at the position of a peak as well as X-ray radiation of the hot intracluster gas. Besides, it is suggested to correlate the mass concentrations found with the known bright quasars in the field, since the latter are known to be often gravitationally lensed and therefore brightened by the intervening matter.

Clearly, much more work has to be put onto the subject of dark matter concentrations in the coming years. Even though further evidence for their existence and some basic descriptive statistics was obtained in this work, their nature remains entirely unresolved. An actual proof of their existence, either by a positive correlation with quasars in the field, or by the identification of very underluminous galaxies at their positions, would be highly desireable. With 60 of those enigmatic objects a very good sample is at hand from which candidates for a more detailed analysis and follow-up observations can be selected.

Chapter 1

Hazards in a Photon's life

In this chapter the principles of the propagation of a photon through the universe are described, starting with General Relativity, and arriving at the Friedmann-Lemaître description of a homogeneous and isotropic cosmos. Basic concepts such as cosmological redshift and various distance measures are introduced. A summary of the mechanism of structure formation in a Friedmann cosmology follows.
With these tools at hand the underlying physics of this thesis is presented, the deflection of light in the tidal gravitational fields of the intervening matter. The chapter ends with the end of the photon's life... its wild passage through the Earth's atmosphere, multiple deflections in a telescope's imperfect optics, and the final absorption in the observer's CCD.

1.1 From General Relativity to cosmology

The field equations Gravitation, though being the weakest of the four known intercations, is the dominating force in the universe on larger scales. It governs the formation of all major structures, from planets to superclusters of galaxies. On an even larger scale gravitation determines the dynamics of the entire universe. Currently, our best approach for the description of gravitation is General Relativity, which tightly connects the pull of matter to the curvature and dynamics of spacetime. In their most general form, and in units of $c = 1 = G$ which will be used throughout this section, the field equations read

$$G_{\mu\nu} = 8\pi T_{\mu\nu} - g_{\mu\nu}\Lambda \,, \tag{1.1}$$

where the *Einstein tensor* $\mathbf{G}$ describes the geometry of spacetime and the *stress-energy tensor* $\mathbf{T}$ contains all sources of mass and energy. $\mathbf{g}$ is the generalisation of the metric tensor $\boldsymbol{\eta} = \mathrm{diag}(-1, 1, 1, 1)$ for the flat and static Minkowskian spacetime[1] to curved spacetime, and Λ stands for the cosmological constant. The latter is often interpreted as *vacuum energy* emerging from the virtual particle zoo, but its true nature is still entirely unclear. Predictions from quantum field theory for Λ are about 120 orders of magnitude larger than the observationally favoured value, a discrepancy which is still unsolved. For this work the presence of Λ is of some relevance, but its nature is not.

So far, exact solutions for the field equations were only found for highly symmetric cases. In general, the problem is to find a metric $\boldsymbol{g}$ for a given matter- and energy distribution $\boldsymbol{T}$,

[1] Note that in this work the $(- + ++)$ convention is used for the metric. When using the $(+ - --)$ convention the field equations read $\boldsymbol{G} = 8\pi\boldsymbol{T} + \boldsymbol{g}\Lambda$.

with $\boldsymbol{g}$ deeply buried inside the Einstein tensor $\boldsymbol{G}$. The metric is often represented by the line element

$$\mathrm{d}s^2 = g_{\mu\nu}\,\mathrm{d}x^\mu\,\mathrm{d}x^\nu \quad \text{with} \quad \mu,\nu \in \{0,1,2,3\}\,, \tag{1.2}$$

where implicit summation over identical indices on different levels is assumed.

Solution for a symmetric universe The matter distribution in the local universe appears largely irregular, but on scales of several hundred Mpc the distribution becomes isotropic. Assuming that an observer in the universe is in no way privileged (*Copernican principle*), one deduces that the universe as a whole appears isotropic from any point of view, and must be, therefore, homogeneous. The assumption of isotropy and homogeneity is called the *cosmological principle*. Robertson (1935) and Walker (1936) found independently of each other a solution of equation (1.1) for such an idealised cosmology with constant curvature. The line element of this metric, which was already used by Friedmann (1922), reads

$$\mathrm{d}s^2 = -\mathrm{d}t^2 + a^2(t)\left[\mathrm{d}w^2 + f_K^2(w)\left(\mathrm{d}\theta^2 + \sin^2\theta\,\mathrm{d}\phi^2\right)\right]\,, \tag{1.3}$$

where w is the (*comoving*) radial coordinate, t the proper time of a comoving observer, $a(t)$ the expansion factor, and θ and ϕ are the angular coordinates. The function $f_K(w)$ discriminates between three-dimensional spacelike hypersurfaces of constant time t with positive, zero, or negative curvature K. It is given by

$$f_K(w) = \begin{cases} \frac{1}{\sqrt{K}}\sin(\sqrt{K}w) & K > 0 \\ w & K = 0\,. \\ \frac{1}{\sqrt{-K}}\sinh(\sqrt{-K}w) & K < 0 \end{cases} \tag{1.4}$$

With this metric and the field equations at hand, the Friedmann equations can be derived, describing the dynamics of spacetime. Here the general procedure is quickly outlined, the details can be found in the literature, amongst many others e.g. in Misner et al. (1973).
In a first step the connection coefficients $\Gamma^\alpha{}_{\mu\nu}$, which allow the comparison of a tensor field between two neighbouring events in a curved spacetime, are calculated from the metric as

$$\Gamma^\alpha{}_{\mu\nu} = \frac{1}{2}\,g^{\alpha\beta}\left(g_{\beta\nu,\mu} + g_{\beta\mu,\nu} - g_{\mu\nu,\beta}\right) \qquad \text{with} \qquad \mathrm{g}_{\alpha\beta,\gamma} := \frac{\partial \mathrm{g}_{\alpha\beta}}{\partial \mathrm{x}^\gamma}\,. \tag{1.5}$$

Based on these coefficients the Riemann tensor $\boldsymbol{R}$, describing the curvature of spacetime, is derived,

$$R^\alpha{}_{\beta\gamma\delta} = \Gamma^\alpha{}_{\beta\delta,\gamma} - \Gamma^\alpha{}_{\beta\gamma,\delta} + \Gamma^\alpha{}_{\mu\gamma}\,\Gamma^\mu{}_{\beta\delta} - \Gamma^\alpha{}_{\mu\delta}\,\Gamma^\mu{}_{\beta\gamma}\,. \tag{1.6}$$

Finally, the Einstein tensor $\boldsymbol{G}$ is built from $\boldsymbol{R}$ and $\boldsymbol{g}$,

$$G_{\mu\nu} = R^\alpha{}_{\mu\alpha\nu} - \frac{1}{2}\,g_{\mu\nu}\,g^{\beta\gamma}\,R^\alpha{}_{\beta\alpha\gamma}\,. \tag{1.7}$$

When performing these three steps with the metric given in the line element (1.3), and making use of the two relations

$$[f_K'(w)]^2 = 1 - K f_K^2(w)\,, \qquad f_K''(w) = -K f_K^2(w) \qquad (\text{for all } K)\,, \tag{1.8}$$

as can be seen from (1.4), one finds a diagonal[2] Einstein tensor with the components

$$G_{tt} = 3\,\frac{K+\dot{a}^2}{a^2} \tag{1.9}$$

$$G_{ww} = a^2\left(-\frac{K+\dot{a}^2}{a^2} - 2\frac{\ddot{a}}{a}\right) \tag{1.10}$$

$$G_{\theta\theta} = a^2\, f_K^2(w)\left(-\frac{K+\dot{a}^2}{a^2} - 2\frac{\ddot{a}}{a}\right) \tag{1.11}$$

$$G_{\phi\phi} = a^2\, f_K^2(w)\sin^2\theta\left(-\frac{K+\dot{a}^2}{a^2} - 2\frac{\ddot{a}}{a}\right)\,. \tag{1.12}$$

Here (t, w, θ, ϕ) are the $(0, 1, 2, 3)$-components, respectively. In these $G_{\mu\mu}$ the coefficients of the total derivatives in the line element (1.3) are rediscovered. Thus the same Einstein tensor, transformed to an orthonormal coordinate system, reads

$$G_{\hat{t}\hat{t}} = 3\,\frac{K+\dot{a}^2}{a^2}\,, \quad G_{\hat{i}\hat{i}} = \left(-\frac{K+\dot{a}^2}{a^2} - 2\frac{\ddot{a}}{a}\right)\,, \qquad \hat{i} \in \{w, \theta, \phi\}\,. \tag{1.13}$$

The Friedmann equations In an isotropic and homogeneous universe the matter and energy is described by $\boldsymbol{T} = \mathrm{diag}(\rho, p, p, p)$, where $\rho = \rho(t)$ and $p = p(t)$ are functions of time only, representing the homogeneous density and the pressure. The combination of equations (1.1) and the $G_{\hat{\mu}\hat{\mu}}$ in (1.13) then yields the two Friedmann equations

$$\left(\frac{\dot{a}}{a}\right)^2 = \frac{8\pi\rho}{3} - \frac{K}{a^2} + \frac{\Lambda}{3}\,, \tag{1.14}$$

$$2\,\frac{\ddot{a}}{a} = -8\pi p - \frac{K}{a^2} + \Lambda - \left(\frac{\dot{a}}{a}\right)^2\,. \tag{1.15}$$

Differentiating (1.14) with respect to t and inserting it into (1.15) yields the conservation law of energy in the form

$$\frac{\mathrm{d}}{\mathrm{d}t}\,(\rho\, a^3) = -p\,\frac{\mathrm{d}}{\mathrm{d}t}\,(a^3). \tag{1.16}$$

Thus the initial value equation (1.14) and the conservation of energy are sufficient to describe the global evolution of the universe. Matter, radiation, and the cosmological constant are the dominant sources of gravitation on the right hand side of (1.1), where the matter can be regarded as pressureless *dust*, i.e. collisionless particles moving at non-relativistic speeds. The equations of state for these three constituents are then $p_{\mathrm{d}} = 0$, $p_{\mathrm{r}} = \rho_{\mathrm{r}}/3$ and $p_\Lambda = -\rho_\Lambda$. Their evolution with cosmological time t is determined by (1.16) as

$$\rho_{\mathrm{d}} \propto a^{-3} \tag{1.17}$$

$$\rho_{\mathrm{r}} \propto a^{-4} \tag{1.18}$$

$$\rho_\Lambda = \mathrm{const}\,. \tag{1.19}$$

[2]The diagonality arises from the assumed symmetry, i.e. isotropy and homogeneity.

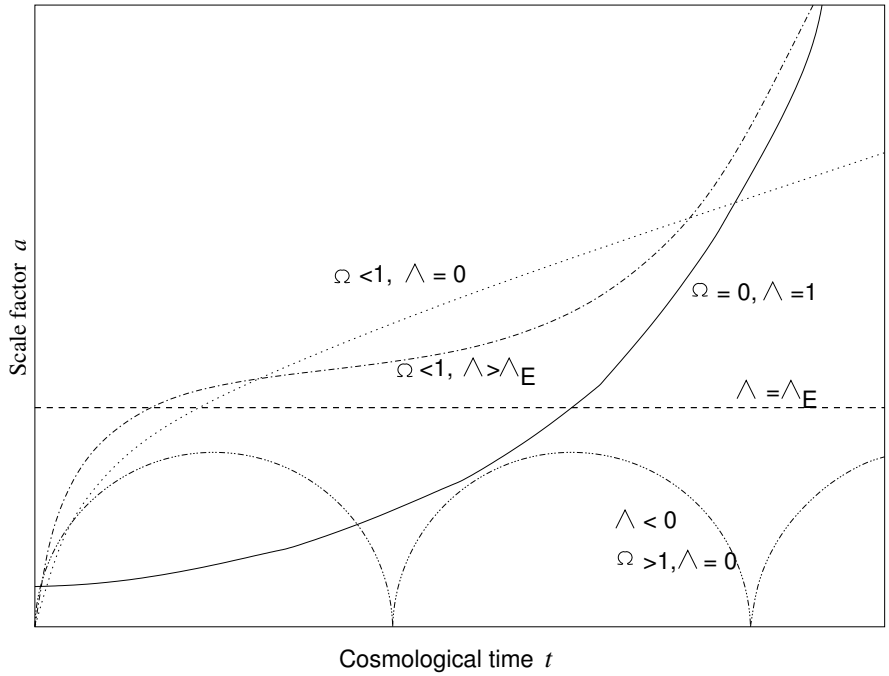

Figure 1.1: Some solutions of the Friedmann-Lemaître equation, depicting typical expansion histories of various cosmologies obeying the cosmological principle. A universe with $\Lambda = \Lambda_{\rm E} = 8\pi\rho - 3K/a^2$ is called *Einstein cosmos*, in which Λ prevents a static universe from collapsing under its own gravitational pull. Our universe has $\Omega_0 \sim 0.3$ and $\Omega_\Lambda \sim 0.7$. Note that the individual curves are not to scale, they just show the general appearance of the solutions.

As an initial condition for (1.14) $a(t_0) = 1$ is used, with t_0 being the cosmological time today. Relation (1.14), known as the Friedmann-Lemaître equation, can be rewritten in the form

$$H^2(t) = H_0^2 \left(\frac{\Omega_0}{a^3} - \frac{K}{a^2 H_0^2} + \Omega_\Lambda \right) , \tag{1.20}$$

where the *Hubble function* was defined as $H(t) := \dot{a}(t)/a(t)$, describing the expansion rate of the universe, with $H_0 = H(t_0)$.

$$\Omega_0 := \frac{8\pi}{3H_0^2}\,\rho_0 \qquad \text{and} \qquad \Omega_\Lambda := \frac{\Lambda}{3H_0^2} \tag{1.21}$$

are the *matter density* and *vacuum density parameters* at present times. The radiation density is neglected in this expression, since it decays much faster than the matter density due to its dependence on a^{-4}. Solving (1.20) for K at $t = t_0$ and substituting the result back into (1.20) yields the Friedmann-Lemaître equation in its commonly used form,

$$H^2(t) = H_0^2 \left(\frac{\Omega_0}{a^3} + \frac{1 - \Omega_0 - \Omega_\Lambda}{a^2} + \Omega_\Lambda \right) . \tag{1.22}$$

Among others, an explicit solution of (1.22) for the scale factor $a(t)$ can be given for a flat universe with $1 - \Omega_0 - \Omega_\Lambda = 0$. By means of variable separation the differential equation

(1.22) can be transformed into an integral, yielding $t(a)$ as

$$t - t_0 = \frac{2}{3H_0\sqrt{\Omega_\Lambda}} \ln\left(\frac{a^{3/2}\Omega_\Lambda + \sqrt{\Omega_0\Omega_\Lambda + a^3\Omega_\Lambda^2}}{\Omega_\Lambda + \sqrt{\Omega_0\Omega_\Lambda + \Omega_\Lambda^2}}\right) . \tag{1.23}$$

This expression can be inverted. Determining t_0 such that $a(0) = 0$ and using $\Omega_0 = 1 - \Omega_\Lambda$ then yields after a series of simplifications

$$a(t) = \left(\sqrt{\frac{\Omega_0}{\Omega_\Lambda}}\ \sinh(\omega t)\right)^{2/3}, \quad \text{with} \quad \omega = \frac{3\,H_0\sqrt{\Omega_\Lambda}}{2}. \tag{1.24}$$

Peacock (2001) and Carroll (1992) derived (1.23) in a different form. Figure 1.1 shows some typical solutions for the Friedmann-Lemaître equation. Several of the former emerge from a hot and compact beginning and are commonly called *big bang* models.

1.2 Redshift and distances

Cosmological redshift Consider a photon emitted by a galaxy at a comoving radial distance w, and absorbed at the observer's position $w = 0$. Both emitter and absorber are comoving with the cosmological expansion. Orienting the coordinate system such that the photon travels along the polar axis, its line element reads $ds^2 = 0 = -c^2\,\mathrm{d}t^2 + a^2(t)\,\mathrm{d}w^2$, where c is the speed of light. Two consecutive maxima of the light wave are emitted at cosmological times $t_{\mathrm{e}1}$ and $t_{\mathrm{e}2}$, and absorbed at $t_{\mathrm{a}1}$ and $t_{\mathrm{a}2}$. The wavelengths of the photon at times of emission and absorbtion are

$$\lambda_e = c\,(t_{\mathrm{e}2} - t_{\mathrm{e}1}) \qquad \text{and} \qquad \lambda_a = c\,(t_{\mathrm{a}2} - t_{\mathrm{a}1})\,, \tag{1.25}$$

respectively. The comoving distance travelled by both maxima is by definition the same. By integrating the photon's line element one gets

$$0 = \int_{t_{\mathrm{e}2}}^{t_{\mathrm{a}2}} a^{-1}(t)\,\mathrm{d}t \ - \int_{t_{\mathrm{e}1}}^{t_{\mathrm{a}1}} a^{-1}(t)\,\mathrm{d}t\,. \tag{1.26}$$

Exchanging the integration limits then gives for infinitely small time intervals between the emission (absorption) of the two maxima

$$0 = \int_{t_{\mathrm{a}1}}^{t_{\mathrm{a}2}} a^{-1}(t)\,\mathrm{d}t \ - \int_{t_{\mathrm{e}1}}^{t_{\mathrm{e}2}} a^{-1}(t)\,\mathrm{d}t = \frac{t_{\mathrm{a}2} - t_{\mathrm{a}1}}{a(t_{\mathrm{a}1})} - \frac{t_{\mathrm{e}2} - t_{\mathrm{e}1}}{a(t_{\mathrm{e}1})}\,. \tag{1.27}$$

Using (1.25) the ratio of the emitted and absorbed wavelengths then becomes

$$\frac{\lambda_{\mathrm{a}}}{\lambda_{\mathrm{e}}} = \frac{t_{\mathrm{a}2} - t_{\mathrm{a}1}}{t_{\mathrm{e}2} - t_{\mathrm{e}1}} = \frac{a(t_{\mathrm{a}1})}{a(t_{\mathrm{e}1})}\,. \tag{1.28}$$

Finally, the *cosmological redshift* is defined as

$$z := \frac{\lambda_{\mathrm{a}} - \lambda_{\mathrm{e}}}{\lambda_{\mathrm{e}}} = \frac{a(t_{\mathrm{a}})}{a(t_{\mathrm{e}})} - 1\,. \tag{1.29}$$

Distances in the universe Contrary to Euclidean spacetime, in a dynamic and curved spacetime such as a Friedmann universe distances can no longer be measured in an unique way. The most commonly used distance measures are the *proper distance*, the *comoving distance*, the *angular diameter distance* and the *luminosity distance*.

The definition of the proper distance is based on the light travel time between two events at redshifts $z_2 > z_1$, given by $\mathrm{d}D_{\mathrm{prop}}(z_1, z_2) = -c\,\mathrm{d}t$. Changing the integration variable from cosmological time to the observable redshift, $\mathrm{d}D_{\mathrm{prop}}(z_1, z_2) = -c\,a/(a\,\dot{a})\,\mathrm{d}a = -c/(aH)\,\mathrm{d}a$, and expanding the Hubble function H then yields

$$D_{\mathrm{prop}}(z_1, z_2) = \frac{c}{H_0} \int_{a(z_2)}^{a(z_1)} \left[\frac{\Omega_0}{a} + (1 - \Omega_0 - \Omega_\Lambda) + a^2\,\Omega_\Lambda \right]^{-1/2} \mathrm{d}a\ . \tag{1.30}$$

For a flat universe ($1 - \Omega_0 - \Omega_\Lambda = 0$), this expression can be evaluated analytically,

$$D_{\mathrm{prop}}(z_1, z_2) = \frac{2\,c}{3H_0\sqrt{\Omega_\Lambda}} \left[\ln\left(a^{3/2}\Omega_\Lambda + \sqrt{\Omega_0\Omega_\Lambda + a^3\Omega_\Lambda^2} \right) \right]_{a(z_2)}^{a(z_1)}\ . \tag{1.31}$$

In analogy to the proper distance one derives the *comoving distance*. This is the distance between the source and the observer on a spacelike hypersurface, defined by points with identical cosmological time $t = t_0$. Starting again with the line element one has $\mathrm{d}D_{\mathrm{com}}(z_1, z_2) = \mathrm{d}w = -c/a\,\mathrm{d}t = -c/(a^2 H)\,\mathrm{d}a$, resulting in

$$\begin{aligned} D_{\mathrm{com}}(z_1, z_2) &= \frac{c}{H_0} \int_{a(z_2)}^{a(z_1)} \left[a\,\Omega_0 + a^2\,(1 - \Omega_0 - \Omega_\Lambda) + a^4\,\Omega_\Lambda \right]^{-1/2} \mathrm{d}a \\ &= w(z_1, z_2)\,. \end{aligned} \tag{1.32}$$

For gravitational lensing the *angular diameter distance* is of great importance. It is defined in analogy to Euclidean space as the ratio of the source area δA and the solid angle $\delta\Omega$, under which the source is seen by the observer: $D_{\mathrm{ang}}(z_1, z_2) = (\delta A/\delta\Omega)^{1/2} = a(z_2) f_K\,(w(z_1, z_2))$. Using (1.32), the angular diameter distance reads

$$D_{\mathrm{ang}}(z_1, z_2) = a(z_2) f_K\,[D_{\mathrm{com}}(z_1, z_2)]\ . \tag{1.33}$$

The *luminosity distance* is as well derived in analogy to Euclidean space. Taking into account the delay in the arrival time of the photons due to the expansion of the universe, their redshift and the photon number conservation, one obtains

$$D_{\mathrm{lum}}(z_1, z_2) = \frac{a(z_1)^2}{a(z_2)}\, f_K\,[D_{\mathrm{com}}(z_1, z_2)]\ . \tag{1.34}$$

Note that due to the prefactors of a and the non-linearity of f_{K} the angular diameter distances and the luminosity distances are not additive, i.e. $D(z_1, z_3) \neq D(z_1, z_2) + D(z_2, z_3)$.

1.3 Structure formation

Since the detection of structures such as galaxy clusters is at the focus of interest in this work, the basic principle of the gravitational collapse of structures is outlined in this section. Based on a linearised Newtonian description, it is shown that the density field in the universe is gravitationally unstable with respect to small perturbations, i.e. inhomogeneities are not damped by the expansion of the universe, but grow in amplitude. At the end of this section the power spectrum is introduced, which is used for a statistical description of the density field.

1.3.1 Evolution of the density field

The Euler-Newtonian system For some basic considerations of structure formation it is sufficient to look at a local volume of the universe, which is small enough not to feel the curvature of spacetime, but large enough to be called representative. A typical scale that satisfies this condition is ≈ 200 Mpc. Fill this volume with massive particles moving with non-relativistic speeds. The latter assumption is necessary since otherwise small-scale fluctuations in the density field of this system would have been washed out in the early phase of the universe, and nowadays galaxies wouldn't exist. Furthermore, it is assumed that these initial fluctuations are small, so that their gravitational fields are small ($\Phi/c^2 \ll 1$) and can be described using Newtonian gravity. This condition is perfectly satisfied, since the largest bound objects to date (superclusters of galaxies) have gravitational potentials on the order of $\Phi/c^2 = 0.001$. As long as neighbouring world lines do not intersect (*shell crossing*), the description of such a system is given by the *Euler-Newtonian-System* (ENS),

$$\begin{aligned} \partial_t \rho + \boldsymbol{\nabla} \cdot (\rho \boldsymbol{v}) &= 0\,, && (1.35)\\ \partial_t \boldsymbol{v} + (\boldsymbol{v} \cdot \boldsymbol{\nabla})\, \boldsymbol{v} &= \boldsymbol{g} - \frac{\boldsymbol{\nabla} p}{\rho}\,, && (1.36)\\ \boldsymbol{\nabla} \times \boldsymbol{g} &= 0\,, && (1.37)\\ \boldsymbol{\nabla} \cdot \boldsymbol{g} &= -4\pi G\rho + \Lambda\,. && (1.38) \end{aligned}$$

The first equation is the continuity equation, stating that no energy (matter) can be lost. The second expression is known as the the Euler equation and guarantees momentum conservation. The third equation states the conservative character of the gravitational force field, and from the last equation one can see that a (positive) cosmological constant is a source of negative gravity, acting against the pull of the matter field ρ. Hereafter, bold faced quantities denote vector fields.

In order to look at the formation of structures, one adds deviations (*peculiar motions*) to the homogeneous and isotropic Hubble flow,

$$\begin{aligned} \rho &= \rho_H + \tilde{\rho}\,, && (1.39)\\ \boldsymbol{v} &= \boldsymbol{v}_H + \tilde{\boldsymbol{u}}\,, && (1.40)\\ \boldsymbol{g} &= \boldsymbol{g}_H + \tilde{\boldsymbol{w}}\,, && (1.41)\\ p &= p_H + \tilde{p}\,, && (1.42) \end{aligned}$$

and defines the *density contrast* δ as

$$\delta := \frac{\rho - \rho_H}{\rho_H}\,, \qquad \text{respectively} \quad \tilde{\rho} = \rho_H\, \delta\,. \tag{1.43}$$

Then one takes out the homogeneous Hubble expansion $v_H = H\, r$ from the system, i.e. one transforms to comoving coordinates $\boldsymbol{q} := \boldsymbol{x}/a(t)$. Renaming $\tilde{\boldsymbol{u}} \to \boldsymbol{u}$, $\tilde{\boldsymbol{w}} \to \boldsymbol{w}$, and $\tilde{p} \to p$

yields the ENS for the peculiar motions,

$$\dot{\delta} + \frac{1}{a}(1+\delta)\,\boldsymbol{\nabla}\cdot\boldsymbol{u} = 0 \tag{1.44}$$

$$\dot{\boldsymbol{u}} + H\boldsymbol{u} = \boldsymbol{w} - \frac{\boldsymbol{\nabla} p}{a\,\rho_H(1+\delta)} \tag{1.45}$$

$$\frac{1}{a}\,\boldsymbol{\nabla}\times\boldsymbol{w} = 0 \tag{1.46}$$

$$\frac{1}{a}\,\boldsymbol{\nabla}\cdot\boldsymbol{w} = -4\pi G\rho_H\,\delta\;. \tag{1.47}$$

Here it is defined that $\dot{(\ )} := \partial_t + 1/a\,(\boldsymbol{u}\cdot\boldsymbol{\nabla})$. Note that the cosmological constant Λ does not appear as a source of gravity in the last equation any more.

Gravitational instability in the linear regime An approximate solution of the ENS for the peculiar system comes with its linearisation for $\delta \ll 1$,

$$\partial_t\,\delta + \frac{1}{a}\,\boldsymbol{\nabla}\cdot\boldsymbol{u} = 0 \tag{1.48}$$

$$\partial_t\,\boldsymbol{u} + H\boldsymbol{u} = \boldsymbol{w} - \frac{\boldsymbol{\nabla} p}{a\,\rho_H} \tag{1.49}$$

$$\frac{1}{a}\,\boldsymbol{\nabla}\times\boldsymbol{w} = 0 \tag{1.50}$$

$$\frac{1}{a}\,\boldsymbol{\nabla}\cdot\boldsymbol{w} = -4\pi G\rho_H\,\delta\;. \tag{1.51}$$

Using the equation of state $\boldsymbol{\nabla}p = c_s^2\boldsymbol{\nabla}\rho$, where c_s is the speed of sound, taking the gradient of the second equation in the linearised ENS and combining with the first one then yields

$$\partial_t^2\,\delta + 2H\,\partial_t\,\delta - 4\pi G\rho_H\,\delta = \begin{cases} c_s^2/a^2\;\boldsymbol{\nabla}^2\delta & (p\neq 0) \\ 0 & (p=0) \end{cases}\;. \tag{1.52}$$

To get an idea of the dynamics of this equation, look at the $p = 0$ case. One solution $\delta_-(t)$ for this differential equation is then the Hubble function $H(t)$, as can be verified by insertion. A second solution $\delta_+(t)$ can be determined by means of the Wronski determinant. The general solution is given by a linear combination of both. As an example, consider the $(1-\Omega_0-\Omega_\Lambda = 0)$ cosmology. From (1.24) one has

$$\delta_-(t) = H(t) = \frac{\dot{a}}{a} = \frac{2}{3}\,\omega\,\coth(\omega t)\;. \tag{1.53}$$

This is a monotonically falling function, and thus corresponds to the decaying mode. The growing mode $\delta_+(t)$ (the *growth factor*) can not be expressed with elementary functions. Instead, a numerical solution of (1.52) is shown in Fig. 1.2. One can see that the matter field in the test volume is gravitationally unstable concerning small perturbations, i.e. structures can grow.

A major disadvantage of the linear regime is that present structures grow in a self-similar fashion only, i.e. no new and more complicated structures can form. Numerical N-body simulations are used to understand the formation of structures such as clusters of galaxies as they are observed today.

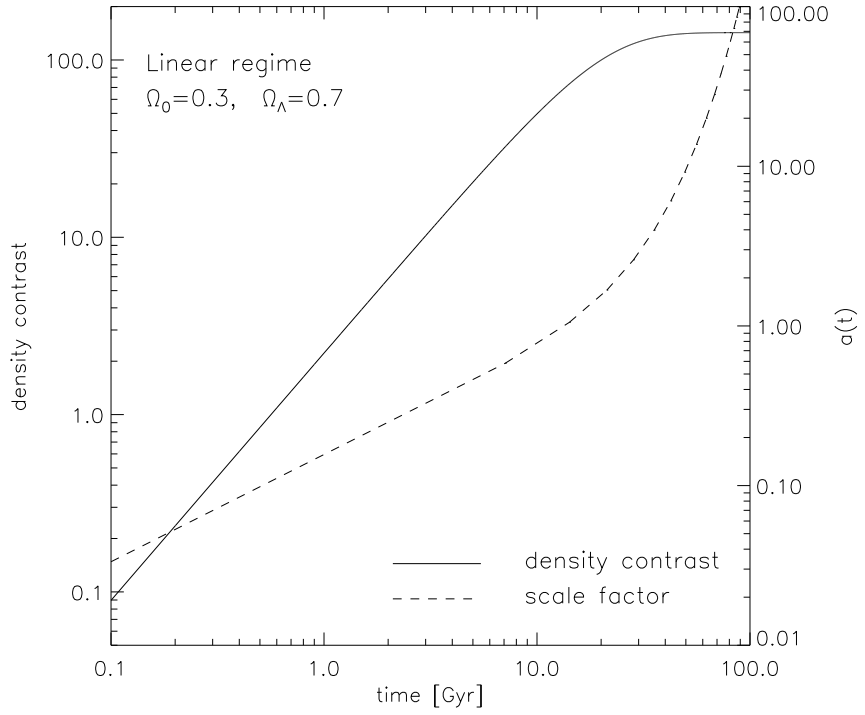

Figure 1.2: Extrapolated evolution of the density contrast in a flat ($\Omega_0 = 0.3$, $\Omega_\Lambda = 0.7$) universe, given the linear regime in (1.52) with $p = 0$ and $\rho_0 = 10^{-29}\,\mathrm{g\,cm^{-3}}$. The density contrast follows a power law, $\delta \propto t^n$, and then saturates once the exponential expansion in equation (1.24) of the universe starts dominating the scale factor. The power law index n increases with ρ_0, and $n = 1$ for $\rho_0 \approx 5.5 \cdot 10^{-29}\,\mathrm{g\,cm^{-3}}$. The linear regime (1.52) is only applicable for $\delta \ll 1$.

1.3.2 Power spectrum

The actual matter distribution in the universe at a given time t, respectively its density contrast δ, is a random field and can not be predicted by theory. However, it is possible to describe the evolution of its statistical properties with time. Two such descriptors are the *two-point correlation function*

$$\zeta(\boldsymbol{r}) = \langle \delta(\boldsymbol{x})\, \delta^*(\boldsymbol{x} + \boldsymbol{r}) \rangle \tag{1.54}$$

and its Fourier transform, the *power spectrum*

$$P_\delta(\boldsymbol{k}) = \int \mathrm{d}^3 r\; \zeta(\boldsymbol{r}) \exp(\mathrm{i}\boldsymbol{k}\boldsymbol{r})\,, \tag{1.55}$$

where k is the comoving wave vector. For a full description of a random field also higher-order correlation functions are needed. A special case are *Gaussian* random fields, which are characterised by mutually independent Fourier components δ_k. If their phases are random, then the central limit theorem states that the δ_k are Gaussian distributed. Such a random field is then entirely described by its power spectrum. It is commonly assumed that the

quantum fluctuations in the early universe lead to such a Gaussian character of the initial density field.

The functional behaviour of P_δ is not a priori clear. If one assumes that there is no preferred length scale in the initial power spectrum, the only allowed functional form for P is a power law, $P_\delta(k) \propto k^n$, where n is the *spectral index* determining whether structures form first on large or on small scales. If fluctuations occur on all scales at the same level, then $n = 1$.

The translation of δ at some redshift z into present times, i.e. the evolution of the density contrast, is governed by the *transfer function*

$$T_k = \frac{\delta(k,0)}{\delta(k,z)\,\delta_+(z)}\,, \tag{1.56}$$

where δ_+ is the linear growth factor between some redshift z and the present, as was introduced in the previous example. This linear extrapolation, however, can only explain the density contrast on very large scales. Smaller and more compact structures such as clusters of galaxies and galaxies themselves are non-linear features, arising from interactions of fluctuations with different scale k. The effect of this non-linear evolution on the power spectrum was fitted by Peacock & Dodds (1996), resulting in more power on smaller scales driving the cluster formation.

A normalisation of the power spectrum has to be obtained from observations, determining the amplitude of the spectrum for different scales. The power spectrum can be scaled such that it reproduces the local abundance of galaxy clusters, which fixes the amplitude on scales of the order of 10 Mpc. Second, the variance of the density field can be observed in the distribution of galaxies on the sky, assuming that the luminous matter follows the dark matter. For this purpose, galaxy counts in spheres with a radius of 8 Mpc are compared, which results in $\sigma_8 \approx 0.9$. The main uncertainty here is the unkown exact relation between the luminous and the dark matter. Third, the power spectrum can be normalised by means of the fluctuations in the cosmic microwave background (see next section), fixing the amplitude for the largest scales.

1.3.3 The microwave background

Anisotropies Those Friedmann-Lemaître models which are in agreement with current observations predict that the universe started from a hot and very dense beginning. A relic, and the most important observational proof of this hot beginning, is the cosmic microwave background (CMB), which has a thermal Planck spectrum with a temperature of 2.73 K. In the CMB one sees the universe at an age of about 300000 years, when its temperature fell below about 3000 K so that electrons and protons could combine and form neutral atoms. This is the time of decoupling between the matter and the radiation field, allowing photons to travel freely. In the CMB one sees these photons, the *last scattering surface*, redshifted to $z \approx 1100$.

The observed isotropy of the CMB is one of the strongest arguments for the validity of the cosmological principle. At the same time, this isotropy imposes a severe problem for cosmological theories. Defining the comoving *particle horizon* as

$$r_H = \int_0^t \frac{c}{a(t')}\,\mathrm{d}t'\,, \tag{1.57}$$

which is the size of the region that could become causally connected since the beginning of the universe, one finds that $r_H(z = 1100) \approx 100$ Mpc. This corresponds to an angle of about 1 degree in the CMB, meaning that the CMB is causally disconnected on larger scales. Thus the isotropy of the CMB can only be explained by a short period of *inflation* in the very early, causally connected universe, which increased its size by at least 60 e-foldings.

The CMB shows very small anisotropies $\delta T/T = 10^{-5}$ on angular scales of up to 90 degrees. These do not come unexpected since the structures seen today must have been already present at a redshift of $z = 1100$, eventually stemming from quantum fluctuations in the very early universe. These density variations cause the observed temperature fluctuations in the CMB through various processes. First, photons have to escape from the overdensities' gravitational potentials and are redshifted (Sachs-Wolfe effect). Second, photons are scattered from electrons in a moving plasma, causing some Doppler shift. Third, overdense regions are hotter and recombine later, appearing thus less redshifted (adiabatic effect). The SW-effect dominates on large scales, whereas on scales smaller than about 1.8 degrees the other two effects take over, with the adiabatic effect dominating.

Dark matter Various observations indicate that the structures in the universe are largely made of *dark matter*, i.e. matter that does not radiate but only interact by means of gravitation. Strong evidence comes from clusters of galaxies, whose apparent gravitational potential must be $10 - 50$ times deeper than what their luminous matter indicates: member galaxies show a velocity distribution ~ 10 times broader than expected, and the clusters themselves are often filled with a $10^7 - 10^8$ K hot plasma which should have easily escaped from the potential if there was only the luminous matter.

Further evidence for the existence of dark matter comes from the anisotropies in the CMB itself. With normal (baryonic) matter only, one expects hardly any anisotropies in the CMB, since before recombination the strong radiation pressure dilutes any baryonic overdensities. Structures could only form afterwards, resulting in density contrasts lower than the one observed in galaxies and clusters of galaxies. Dark matter, however, decoupled much earlier from the radiation field and could clump together, attracting baryonic matter, too. This infall was counterbalanced by radiation, driving the baryons out of the dark potentials again. Thus the amplitudes of the adiabatic anisotropies in the CMB underestimate the actual density contrast by a factor of about 10. Without non-baryonic dark matter none of today's galaxies would ever have formed.

1.4 Light deflection in gravitational fields

The metric $\boldsymbol{g}$ of spacetime, and thus the matter inside, governs the propagation of all freely falling particles. This section introduces the basic concepts of light deflection in such gravitational fields. An illustration of the lens geometry is shown in Fig. 1.3, which also defines some of the basic lensing terms.

The following approximations and assumptions can safely be made:

1. The gravitational potential of the most massive known objects in space, clusters and superclusters of galaxies, are on the order of $\Phi/c^2 \approx 0.001 \ll 1$. In addition, the peculiar velocities in such clusters are $v_{\rm pec}/c \approx 0.003 \ll 1$, thus frame dragging (Lense-Thirring effect) is absent from the problem. Hence, the gravitational fields can be described with non-relativistic Newtonian physics.

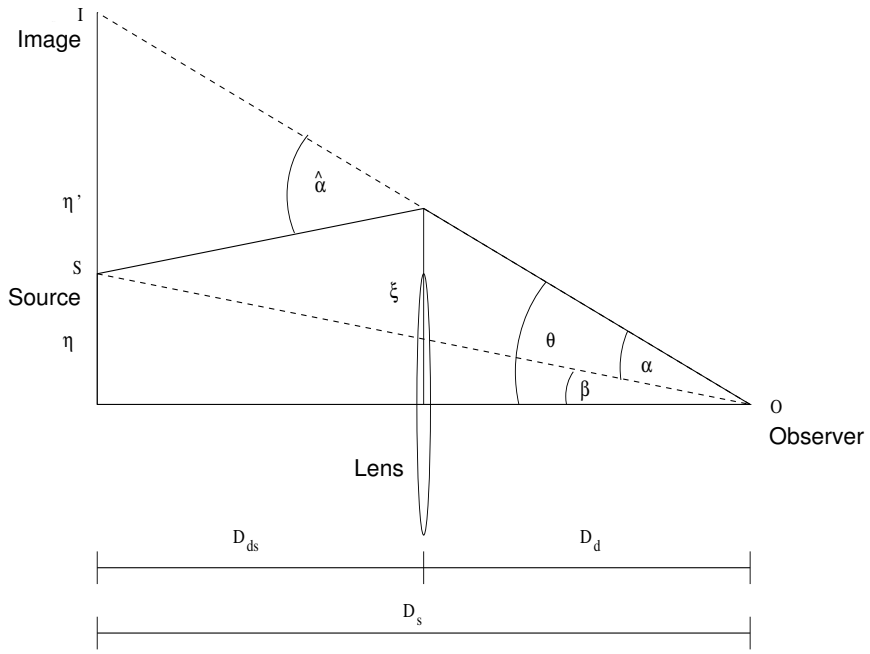

Figure 1.3: Geometry of a single gravitational lens. The path of light from a source S is deflected by $\hat{\boldsymbol{\alpha}}$, so that the observer sees the source at the image position I. $\boldsymbol{\alpha}$ is called the *reduced deflection angle*. $\boldsymbol{\eta}$ and $\boldsymbol{\eta}'$ are the distances of the source and its image from the *optical axis* in the source plane. The optical axis is defined as the connecting line between the observer and the barycenter of the lensing mass distribution. $\boldsymbol{\xi}$ is the impact parameter, the distance at which the light path passes the gravitational lens. $\boldsymbol{\theta}$ and $\boldsymbol{\beta}$ are the angles under which the observer sees the source with and without the lens. D_d, D_ds and D_s are the angular diameter distances from the observer to the lens (the *deflector*), from the lens to the source, and from the observer to the source, respectively. Remember that angular diameter distances are not additive. Source, lens and observer form the *lens system*. This figure was adapted from Bartelmann & Narayan (1996).

2. The extent of the lens is very small compared to the total extent of the lens system. In the case of cluster lensing the extent of the lens is typically some Mpc, whereas the distances between source, lens and observer are usually several Gpc. One can thus project the mass distribution of the lens along the line of sight into a two-dimensional mass sheet, and assume that all the light deflection takes place in this *lens plane*. This assumption is known as *thin lens approximation*. It does not hold for lensing by large-scale structure.

General relativity enters the description only in a few places. Most notably, the angular diameter distances from equation (1.33) are used for the description of the lens geometry, and second, the deflection angle is derived from the line element as is shown below. Details of the formalism presented below can be found e.g. in Bartelmann & Narayan (1996) and Bartelmann & Schneider (2001).

1.4.1 The lens equation

Using the notation in Fig. 1.3, the small angle approximation and the theorem of intersecting lines,

$$\frac{\boldsymbol{\xi}}{D_\mathrm{d}} = \frac{\boldsymbol{\eta}'}{D_\mathrm{s}} \tag{1.58}$$

one finds

$$\boldsymbol{\eta} = \boldsymbol{\eta}' - \hat{\boldsymbol{\alpha}}\, D_\mathrm{ds} = \boldsymbol{\xi}\frac{D_\mathrm{s}}{D_\mathrm{d}} - \boldsymbol{\alpha} D_\mathrm{s}\,. \tag{1.59}$$

Note that the angular diameter distances were defined in such a way that the relation (1.58) holds. Dividing the last equation by D_s yields the *lens equation*

$$\boldsymbol{\beta} = \boldsymbol{\theta} - \boldsymbol{\alpha}(\boldsymbol{\theta})\,, \tag{1.60}$$

which could have been also obtained directly from Fig. 1.3. The lens equation (1.60) is non-linear in general, and allows for multiple images of the same source, i.e. the light can reach the observer along different paths. It is shown in the literature (see Schneider et al., 1992, for example), that this equation can be derived entirely from General Relativity. There it is contained as a special case for weak fields, where the line element of the Minkowski spacetime is perturbed by a gravitational potential $\Phi \ll c^2$. Since the deflection of the light ray is a very local event, the expansion of the universe and its curvature can be neglected in the deflection process. In this case, an approximation of the static Minkowskian line element for a photon traveling along the polar axis is

$$\mathrm{d}s^2 = 0 = -\left(1 + \frac{2\phi}{c^2}\right) c^2\,\mathrm{d}t^2 + \left(1 + \frac{2\phi}{c^2}\right)^{-1} \mathrm{d}r^2\,. \tag{1.61}$$

Thus,

$$\left|\frac{\mathrm{d}r}{\mathrm{d}t}\right| = c_\mathrm{eff} = c\left(1 + \frac{2\Phi}{c^2}\right) = \frac{c}{n} \quad \text{with} \;\; n \approx \left(1 - \frac{2\Phi}{c^2}\right)\,. \tag{1.62}$$

Here n is the refractive index, introduced in analogy to conventional optics. The deflection angle is then defined as the line integral of the gradient of n perpendicular to the light path γ, integrated along γ,

$$\hat{\boldsymbol{\alpha}} = -\int_\gamma \nabla_\perp n\,\mathrm{d}l = \frac{2}{c^2}\int_\gamma \nabla_\perp \Phi\,\mathrm{d}l\,. \tag{1.63}$$

Since deflection angles in gravitational lensing are typically just a few arcseconds, the line integral can be replaced by an integral along an unperturbed path of light with the same impact parameter $\boldsymbol{\xi}$.

1.4.2 Convergence and shear

Since the deflection of light in a gravitational potential is a very local effect when compared to the total extent of the lens system, one introduces the *lensing potential* $\psi(\boldsymbol{\theta})$ as the projection of $\Phi = \Phi(\boldsymbol{\xi}, z)$ along the optical axis onto the lens plane. Φ is written as a function of the impact parameter $\boldsymbol{\xi} = D_\mathrm{d}\boldsymbol{\theta}$ and of the distance z along the unperturbed light ray starting from the point of closest approach. The lensing potential is scaled such that its gradient yields the reduced deflection angle $\boldsymbol{\alpha}$ (see eq. (1.63) for comparison),

$$\psi(\boldsymbol{\theta}) = \frac{2}{c^2}\frac{D_\mathrm{ds}}{D_\mathrm{d} D_\mathrm{s}}\int \Phi(D_\mathrm{d}\boldsymbol{\theta}, z)\,\mathrm{d}z \tag{1.64}$$

$$\begin{aligned} \nabla_\theta \psi &= D_\mathrm{d} \nabla_\xi \psi = \frac{2}{c^2} \frac{D_\mathrm{ds}}{D_\mathrm{s}} \int \nabla_\xi \Phi(\boldsymbol{\xi}, z)\, \mathrm{d}z \qquad (1.65) \\ &= \frac{2}{c^2} \frac{D_\mathrm{ds}}{D_\mathrm{s}} \int \nabla_\perp \Phi \, \mathrm{d}z = \boldsymbol{\alpha} \,. \end{aligned}$$

The projected mass distribution has a surface mass density

$$\Sigma(\boldsymbol{\xi}) = \int \rho(\boldsymbol{\xi}, z)\, \mathrm{d}z \,. \qquad (1.66)$$

Using this and Poisson's equation $\Delta\Phi = 4\pi G \rho(\boldsymbol{\xi}, z)$, one finds that the Laplacian of ψ is proportional to Σ,

$$\begin{aligned} \Delta_\theta \psi &= D_\mathrm{d}^2\, \Delta_\xi \psi = \frac{2}{c^2} \frac{D_\mathrm{d} D_\mathrm{ds}}{D_\mathrm{s}} \int \Delta_\xi \Phi \, \mathrm{d}z \qquad (1.67) \\ &= 2 \frac{4\pi G}{c^2} \, \frac{D_\mathrm{d} D_\mathrm{ds}}{D_\mathrm{s}} \int_{-\infty}^{\infty} \rho(\boldsymbol{\xi}, z)\, \mathrm{d}z \\ &= 2 \frac{4\pi G}{c^2} \, \frac{D_\mathrm{d} D_\mathrm{ds}}{D_\mathrm{s}} \, \Sigma(\boldsymbol{\theta}) \qquad (1.68) \end{aligned}$$

Introducing the *critical surface mass density*

$$\Sigma_\mathrm{cr} = \frac{c^2}{4\pi G} \frac{D_\mathrm{s}}{D_\mathrm{d} D_\mathrm{ds}} \qquad (1.69)$$

the Laplacian of ψ reads

$$\Delta_\theta \psi = 2 \, \frac{\Sigma(\boldsymbol{\theta})}{\Sigma_\mathrm{cr}} =: 2\kappa(\boldsymbol{\theta}) \,. \qquad (1.70)$$

The surface mass density Σ, scaled with its critical value, is called *convergence* κ. For $\kappa \ll 1$ one has the *weak lensing regime*, whereas a lens with $\Sigma > \Sigma_\mathrm{cr}$ is called *supercritical*, meaning that multiple images and other strong lensing effects can occur.

Relation (1.70) can be inverted and yields, up to harmonic functions,

$$\psi(\boldsymbol{\theta}) = \frac{1}{\pi} \int \mathrm{d}\boldsymbol{\theta}' \, \kappa(\boldsymbol{\theta}') \ln|\boldsymbol{\theta} - \boldsymbol{\theta}'| \,. \qquad (1.71)$$

Taking the gradient gives by definition the deflection angle,

$$\boldsymbol{\alpha}(\boldsymbol{\theta}) = \frac{1}{\pi} \int \mathrm{d}\boldsymbol{\theta}' \, \kappa(\boldsymbol{\theta}') \, \frac{\boldsymbol{\theta} - \boldsymbol{\theta}'}{|\boldsymbol{\theta} - \boldsymbol{\theta}'|^2} \,. \qquad (1.72)$$

Linearised lens mapping As far as the lensing formalism was presented up to here, the deflection of a single light ray was the subject of interest, and no assumptions were made about the source. In general, sources such as distant background galaxies are extended objects, and a bundle of light rays is received by the observer, stemming from many different points in the source. Due to its finite width a light bundle passes by the lens at various distances, probing the lensing potential at different positions. This means that the image of an extended source appears distorted as compared to the unlensed case.

If the cross section of the light bundle in the lens plane is small compared to the extent of the projected mass distribution, then the lens mapping can be locally linearised since

the lensing potential and thus the deflection angle do not vary considerably for the various light rays in the bundle. This clearly holds for cluster lensing, where the angular extent of the cluster is on the order of a few arcminutes, whereas the apparent diameter of the lensed background galaxies is typically a hundred to a thousand times smaller. Under this assumption the aforementioned differential effects are described by the Jacobian matrix of the lens mapping (1.60),

$$\boldsymbol{A} \equiv \frac{\partial \boldsymbol{\beta}}{\partial \boldsymbol{\theta}} = \left(\delta_{ij} - \frac{\partial \alpha_i(\boldsymbol{\theta})}{\partial \theta_j} \right) = \left(\delta_{ij} - \frac{\partial^2 \psi(\boldsymbol{\theta})}{\partial \theta_i \partial \theta_j} \right) = \mathbf{1} - (\psi_{,ij}) \ . \tag{1.73}$$

Hence the deviation from the identical (unlensed) mapping is described by the Hessian matrix $(\psi_{,ij})$ of the lensing potential. The Jacobian $\boldsymbol{A}$ can be rewritten by introducing in addition to κ another linear combination of $\psi_{,ij}$, the two-component complex *shear* γ,

$$\gamma = \gamma_1 + \mathrm{i}\,\gamma_2 = |\gamma|\, e^{2\mathrm{i}\varphi} \tag{1.74}$$

where

$$\begin{aligned} \gamma_1 &:= \frac{1}{2}\,(\psi_{,11} - \psi_{,22}) \\ \gamma_2 &:= \psi_{,12}\,. \end{aligned}$$

With this definition and the convergence in (1.70), $\boldsymbol{A}$ becomes

$$\begin{aligned} \boldsymbol{A} &= \begin{pmatrix} 1-\kappa-\gamma_1 & -\gamma_2 \\ -\gamma_2 & 1-\kappa+\gamma_1 \end{pmatrix} \\ &= (1-\kappa) \begin{pmatrix} 1 & 0 \\ 0 & 1 \end{pmatrix} - |\gamma| \begin{pmatrix} \cos 2\varphi & \sin 2\varphi \\ \sin 2\varphi & -\cos 2\varphi \end{pmatrix} . \end{aligned} \tag{1.75}$$

Defining the observable *reduced shear* g as

$$g := \frac{\gamma}{1-\kappa}\,, \tag{1.76}$$

the lens mapping can also be written as

$$\boldsymbol{A} = (1-\kappa) \begin{pmatrix} 1-g_1 & -g_2 \\ -g_2 & 1+g_1 \end{pmatrix} . \tag{1.77}$$

In these representations of $\boldsymbol{A}$ the meaning of κ and γ, respectively g, becomes clear. Without the shear γ the convergence alone causes an isotropic magnification of the source, leaving its shape unchanged. The (reduced) shear, however, introduces a distortion in the image shape, where $|\gamma|$ describes the strength of the distortion and φ its orientation. With $\kappa \neq 1$ and $\gamma \neq 1$, an intrinsically circular source is mapped onto an ellipse with major and minor axes $(1-\kappa-|\gamma|)^{-1}$ and $(1-\kappa+|\gamma|)^{-1}$, respectively. The factor 2 in the trigonometric functions of (1.75) accounts for the invariance of the shape of an ellipse under a rotation of 180 degrees.

In analogy to conventional optics a *magnification* μ can be defined in the lens mapping. It is given by the ratio of the image size $\delta\theta^2$ and the size of the source, $\delta\beta^2$. The distortion that is introduced in the light bundle and thus its cross section is described by the determinant of $\boldsymbol{A}$. The magnification is

$$\mu = \frac{\delta\theta^2}{\delta\beta^2} = \frac{1}{\det \boldsymbol{A}} = \frac{1}{(1-\kappa)^2 - |\gamma|^2} \tag{1.78}$$

Based on Liouville's theorem (photon number conservation), the surface brightness of the source is conserved in the lensing process. Thus the flux ratio between the source and the image is given by the geometric magnification.

A gravitational lens suffers from all aberrations known from conventional optics, apart from one. The equivalence principle guarantees that there are no chromatic errors, i.e. light deflection in gravitational fields is independent of wavelength.

The principle of mass reconstruction Inserting equation (1.71) into the definition (1.74) of the shear yields a relation between the shear and the convergence,

$$\gamma(\boldsymbol{\theta}) = \frac{1}{\pi}\int \mathrm{d}^2\theta'\,\kappa(\boldsymbol{\theta}')\,D(\boldsymbol{\theta}-\boldsymbol{\theta}') \qquad \text{with} \tag{1.79}$$

$$D(\boldsymbol{\theta}) = \frac{-\theta_1^2+\theta_2^2-2\mathrm{i}\theta_1\theta_2}{\theta^4}\,. \tag{1.80}$$

Kaiser & Squires (1993) derived the inversion of this relation, obtaining the convergence κ from the shear γ,

$$\kappa(\boldsymbol{\theta}) = \frac{1}{\pi}\,\mathrm{Re}\left(\int \mathrm{d}^2\theta'\,\gamma(\boldsymbol{\theta}')\,D^*(\boldsymbol{\theta}-\boldsymbol{\theta}')\right) + \kappa_0\,, \tag{1.81}$$

where the asterisk * denotes complex conjugation. Thus the convergence can be obtained from the shear only up to an additive constant κ_0. This is known as the *mass sheet degeneracy*. A more general variant of this degeneracy is given by the invariance transformation

$$T:\ \boldsymbol{A} \to \lambda\boldsymbol{A} \tag{1.82}$$

of the lens mapping,

$$\begin{aligned}
\lambda\boldsymbol{A} &= \lambda\,(1-\kappa)\begin{pmatrix}1&0\\0&1\end{pmatrix} - \lambda|\gamma|\begin{pmatrix}\cos 2\varphi & \sin 2\varphi\\ \sin 2\varphi & -\cos 2\varphi\end{pmatrix} \\
&= \big(1-\kappa'\big)\begin{pmatrix}1&0\\0&1\end{pmatrix} - |\gamma'|\begin{pmatrix}\cos 2\varphi & \sin 2\varphi\\ \sin 2\varphi & -\cos 2\varphi\end{pmatrix} \\
&= \big(1-\kappa'\big)\begin{pmatrix}1-g_1 & -g_2\\ -g_2 & 1+g_1\end{pmatrix}\,.
\end{aligned} \tag{1.83}$$

Here it was implicitly defined that

$$\kappa' := 1-\lambda(1-\kappa)\,, \qquad \gamma' := \lambda\gamma \qquad (\text{ and thus } \ \mu' := \lambda^{-2}\mu\ )\,. \tag{1.84}$$

From the definition (1.76) of g and from (1.77) one can see that the reduced shear, and thus the shape of an image, remains unchanged under this transformation, $g' = g$. Hence, from the image shapes alone, the surface mass density of the lens can not be reconstructed unambiguously. One needs to take into account magnification effects, or assume $\kappa = 0$ on average at a large distance from the lens to break this degeneracy. This invariance transformation will be accounted for in section 3.2.1, where the shear selection method for galaxy clusters is introduced.

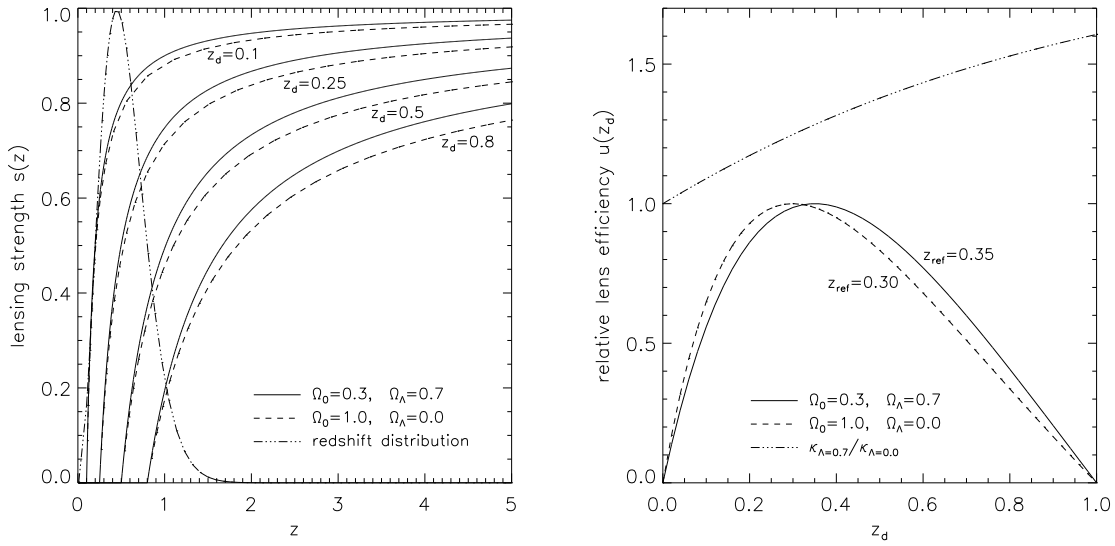

Figure 1.4: Left: Relative lensing strength from equation (1.86), for lens redshifts $z_\mathrm{d} \in [0.1, 0.25, 0.5, 0.8]$ and two different cosmologies as a function of source redshift. Overlaid is a redshift distribution taken from Brainerd et al. (1996), characteristic for the galaxies in the data used for this work (see also section 3.4). Lenses at various redshifts have different sensitivities with respect to the redshift distribution.
Right: Relative lensing efficiency calculated for a singular isothermal sphere (*SIS*) with $\rho \propto 1/r^2$ and a fixed source redshift of $z_s = 1.0$. For an SIS $\kappa \propto D_\mathrm{ds} D_\mathrm{d}/(D_\mathrm{s}\, r) =: D/r$. Shown is the ratio $\kappa(z_\mathrm{d})/\kappa(z_\mathrm{ref}) = D(z_\mathrm{d})/D(z_\mathrm{ref})$, i.e. the strength of a lens at redshift z_d is compared to the strength of a lens at reference redshift z_ref. In a ($\Omega_0 = 0.3$, $\Omega_\Lambda = 0.7$)-cosmology lensing is most efficient when the lens is at a redshift of $z_\mathrm{d} \approx 0.35$, compared to $z_\mathrm{d} \approx 0.30$ when $\Omega_0 = 1.0$. Furthermore, lensing becomes inefficient when the lens is at an exceedingly low or high redshift with respect to the sources. The dash-dotted line compares the strength of the same lens at redshift z_d in the two model universes. Mass profiles other than the SIS yield comparable results.

Relative lensing strength It is useful to illustrate the strength of a gravitational lens at redshift z_d as a function of source redshift z. For this purpose one compares the convergence and the shear for a redshift z to their counterparts at redshift infinity,

$$\kappa(z) = \frac{\Sigma(z; z_\mathrm{d})}{\Sigma_\mathrm{cr}(z; z_\mathrm{d})} = \frac{\Sigma(z; z_\mathrm{d})}{\Sigma_\mathrm{cr}(\infty; z_\mathrm{d})} \frac{\Sigma_\mathrm{cr}(\infty; z_\mathrm{d})}{\Sigma_\mathrm{cr}(z; z_\mathrm{d})} H(z - z_\mathrm{d}) = \kappa_\infty\, s(z; z_\mathrm{d}) \tag{1.85}$$

where

$$s(z; z_\mathrm{d}) = \frac{\Sigma_\mathrm{cr}(\infty; z_\mathrm{d})}{\Sigma_\mathrm{cr}(z; z_\mathrm{d})} H(z - z_\mathrm{d}) \tag{1.86}$$

is the *relative lensing strength* (see left panel in Fig. 1.4) and κ_∞ the convergence for a source at redshift infinity. The Heaviside function guarantees that galaxies closer than the lens remain unlensed. A similar relation holds for the shear,

$$\gamma(z) = \gamma_\infty\, s(z; z_\mathrm{d})\,. \tag{1.87}$$

This rescaling preserves the relation (1.79) between γ and κ.

1.5 Light deflection in the atmosphere

Seeing Before a light beam with an imprinted lensing signal arrives at a telescope's detector, it has to pass through the turbulent atmosphere of Earth. Pressure and temperature gradients change the effective refractive index n of the atmosphere along the path of light, causing a smearing of the cross section of the light bundle and an erratic motion in the detector plane over time. This effect is called *atmospheric seeing*[3]. In the detector plane the light profile of a point source such as a star gets broadened by the seeing and by diffraction effects in the telescope. Such a light profile is called PSF (*point spread function*).

Partially, the PSF is caused by *dome* and *telescope seeing*, caused by turbulences and convective motions mostly due to temperature gradients inside the dome and the optics. The closer the disturbing atmospheric layer is to the focal plane, the more it can become a dominant source of seeing. The reason for this is of purely geometrical nature: A larger change in n at high altitudes leads to a very large displacement of the light beam at the telescope, making it likely that the according photons will be absorbed by the telescope's baffle system. Light deflections due to changes in n in the local environment and inside the dome, however, can fully propagate to the detector. Even very thin layers of warmer air, e.g. just above the surface of the main mirror, can easily become as disturbing as the whole atmosphere above (*mirror seeing*). Warm laminar streamings perpendicular to the optical path can even cause significant anisotropies in the PSF. Proper ventilation systems inside the telescope and the dome destroy such optically disturbing layers and flows of warm air.

Thus, for an analysis of weak gravitational lensing effects very stable atmospheric conditions are required, since the shapes of small galaxies have to be measured reliably. Besides, the dome and the telescope must have cooled down to ambient temperatures. Since the typical angular size of a lensed background galaxy is on the order of $0\farcs2$, the size of the PSF should be equal or smaller than about 1.0 arcseconds for a weak lensing analysis. Otherwise the lensing signal is too much diluted by the seeing. In section 3.1.2 it is shown how one can correct to first order for the anisotropic and smearing effects of the PSF.

[3]The mathematical description is in its principles very similar to the one for gravitational lensing, which was derived from an effective refractive index due to gravitational fields. The main difference is that many such deflections take place in the Earth's atmosphere, whereas for example in the case of cluster lensing a single lens event accounts for most of the shear signal.

Chapter 2

From Photons to Images

This chapter describes the data reduction process, emphasising the reduction of multi-chip cameras. In the first section an overview of the Garching-Bonn Deep Survey (hereafter: GaBoDS) is given, the database upon which this weak lensing survey relies. It is followed by a description of the pre-processing steps, the astrometric and photometric calibration of the data and the image coaddition.

2.1 The Garching-Bonn Deep Survey

2.1.1 The instrument

Observations for GaBoDS were conducted with the Wide Field Imager at the 2.2m MPG/ESO telescope at La Silla, Chile. Hereafter, this specific instrument will be refered to as *WFI@2.2*, whereas the term *WFI* will be used for wide field imaging instruments in general. WFI@2.2 is a multi-chip camera consisting of eight back-illuminated 2k×4k Marconi/EEV CCDs with a pixel size of 15 microns. The area covered on the sky is $34' \times 33'$, corresponding to a pixel scale of $0\farcs238$. WFI@2.2 is attached at the Cassegrain focus of the MPG/ESO telescope, which has a 2.2m hyperbolic primary and a 1.0m hyperbolic secondary mirror. This Ritchey-Chretién layout allows for a very flat focal plane with very good PSF properties throughout the fully illuminated field of view, which is essential for large detector arrays. The native focal ratio of the telescope is f/8.0, which is shortened to f/5.9 by means of a focal reducer, having six lenses in two groups. This reducer also corrects efficiently for remaining optical abberations and field curvature. A cut through the instrument along the optical axis and the layout of the detector array are shown in Fig. 2.1.

Terminology The following list gives an explanation for the most frequently used terms in the next sections.

- *CCD, chip* – one of the detectors in a multi-chip camera
- *exposure* – a single WFI shot through the telescope
- *image* – the part of the exposure that belongs to a particular CCD
- *science image* – an image of the actual target, not a calibration image
- *mosaic* – all images are coadded, i.e. the final product

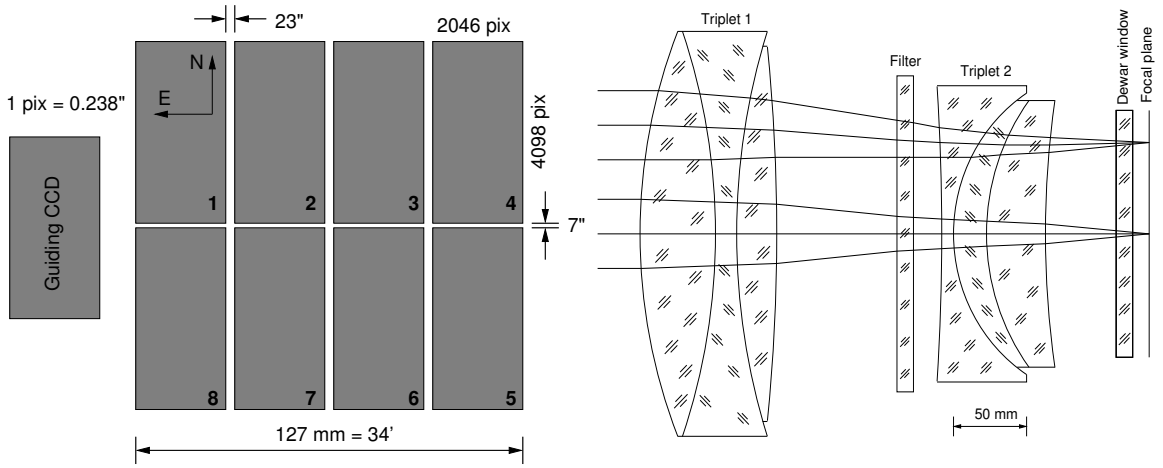

Figure 2.1: Left: The layout of the WFI@2.2 detector array. The size of the gaps between the CCDs is not to scale. Right: A cut through the WFI@2.2 focal reducer/corrector. Both figures were taken and modified from the WFI@2.2 user manual (Baade, 2000).

- *dithering* – offsetting the telecope between the exposures
- *overlap* – images from different CCDs and exposures overlap if the dithering between the exposures was large enough
- *bias* – exposure with zero seconds exposure time, thus containing pure read-out noise of the camera electronics, only.
- *dark* – exposure with a certain exposure time, keeping the shutter closed. It contains the read-out noise and the accumulated thermic dark current of the CCD. Chip defects are easily recognised in these exposures.
- *flatfield* – exposure of an evenly illuminated area. This can either be a screen in the telescope dome (*domeflat*), or the sky close to zenith shortly after sunset or before sunrise (*skyflat*). The flatfield contains the total throughput of the telescope, including filters and the detector.
- *gain* – a factor relating the number of photons absorbed in the detector to the number of released electrons
- *superflat* – a flatfield calculated from the data itself after it has been calibrated by the bias and the normal flatfield. Useful for correcting remaining residuals in the sky background of the images.

2.1.2 Survey characteristics

Data mining the ESO archive The present weak lensing analysis initially aimed at a sky coverage of at least 10 square degrees for the GaBoDS. Only about 3.7 square degrees were finally observed, however, in 20 allocated nights of our own GO programme (PI: P. Schneider) due to unfavourable weather conditions. Including available data from the EIS[1] Deep Public

[1]ESO Imaging Survey

Survey and COMBO-17[2] left us with about 3 missing square degrees. A manual search in the large ESO archive turned out to be unfeasible, since the search engine available at that time did not allow for filtering with respect to our requirements. The only usable fields known beforehand in the archive were the ones from the Deep Public Survey and one observation of the Capodimonte Deep Field. Other WFI@2.2 data such as the five COMBO-17 fields were taken during MPG time before the 2.2m telescope started into service mode operation, and were thus not publicly available through the archive. Besides, the very low number[3] of publications based on data taken with WFI@2.2 did not allow a direct identification of further usable data. Therefore an ASTROVIRTEL program[4,5] was proposed, aiming at an enhancement of the *querator*[6] search engine's capabilities (Pierfederici, 2001). In order for a field to be included in the GaBoDS, the following requirements addressed by *querator* had to be met:

- minimum exposure time in R-band: ~ 5 ksec,
- image seeing $\leq 1\farcs0$,
- random field, at high galactic latitude,
- empty field, i.e. avoidance of known very massive structures in or next to the field, no bright stars or large foreground objects inside the field.

The first item in this list guaranteed a high enough number density (≥ 10 arcmin^{-2}) of galaxies with securely measurable shapes for the lensing analysis. Furthermore, as was mentioned previously in section 1.5, exposures had to be taken in excellent seeing conditions, since the S/N for shape measurements decreases with the squared size of the PSF. The random character of the fields was needed to avoid a biasing towards certain types of objects, such as quasars or clusters of galaxies. In addition, in this way it was ensured that the fields sparsely sample the universe along independent lines of sight, keeping thus the effect of cosmic variance small. The last point in the above list was to further guarantee that a given pointing would be usable for the purposes of this work: massive structures such as large clusters of galaxies bias the search for unknown dark matter haloes. One has to keep in mind that this introduces a bias towards lower density lines of sight. By avoiding bright and large foreground objects the usable area of a field is kept as large as possible.

About data quality It is clear that 'data quality' is a very ambiguous term, highly dependent on the science which is to be drawn from the data. Given the involved, time consuming reduction of WFI data, the quality of archival data had to be assessed as well as possible before any request or data reduction. This is straightforward for the total exposure time, available filters, presence of bright objects, availability of calibration exposures, and the ambient conditions during which the observation was performed (moon; clouds; seeing, according to the seeing monitor). However, not all of those can be expressed in terms of numbers, and some judgement had to be done upon visual inspection of the data. Other data quality

[2] MPIA Heidelberg

[3] Only about a dozen papers based on WFI@2.2 data had been published up to April 2002.

[4] ASTROVIRTEL cycle 2: Erben et al., *Gravitational lensing studies in randomly distributed, high galactic latitude fields*

[5] http://www.stecf.org/astrovirtel

[6] http://archive.eso.org/querator

issues, such as image seeing or PSF properties could not be evaluated without more complex operations on the data itself. To address most of these points, the following demands were defined to ASTROVIRTEL and *querator*:

- measure the image seeing for all archived WFI@2.2 data,
- provide a preview facility, allowing quick visual inspection of the data ahead of a request,
- make available the submitted proposal abstract ('why was this particular observation done?')

All items but the last one were implemented. The image seeing, crucial for a weak lensing analysis, was determined by automatically extracting all non-saturated stars from one of the eight WFI@2.2 chips, and averaging their FWHM. It was superior to the DIMM[7] seeing, since the DIMM on La Silla could not pick up local effects such as dome seeing, zenith distance, flexure and temperature of the telescope's Serrurier[8] structure, focus and tracking. On average the DIMM seeing has been found to be $0\farcs1 - 0\farcs2$ better than the image seeing for WFI@2.2. It was only in rare cases that the difference between the two dropped below $0\farcs1$.

In this way a list of useful candidate fields was extracted from the archive, minimising the amount of unusable data slipping into the reduction process. Fields that were rejected at this late step suffered from scattered light or had very bad PSF properties. Checking the PSF anisotropies on an image is a very time consuming task and was thus not blindly performed on all data in the archive. Instead, each selected data set was investigated manually, and an individual threshold for the PSF depending on the overall quality of the set was chosen. Exposures with anisotropies above this threshold were excluded from the coaddition. For example, if there was a large data set with good quality, the threshold was chosen to be more conservative and one still got a decent deep image. On the other hand, if the PSF quality was comparatively low for another data set, then more exposures with a degraded PSF were stacked in order to reach a useful depth. Yet one should keep in mind that exposures of the WFI@2.2 with a rather bad PSF are still rated very good when compared to other wide field imaging instruments. As a rule of thumb, exposures with PSF anisotropies of $\approx 6\%$ or larger were rejected from the coadditions. The left hand panel of Figure 2.2 illustrates the PSF anisotropies for WFI@2.2 chips 1 and 8 for 700 randomly selected exposures in the GaBoDS. This gives a rough impression of the spread in image quality one can expect when the data is taken by about a dozen different observers (including some service mode observations) in sub-arcsecond seeing conditions. If the observer regularily takes care of the focus of the instrument, then the PSF anisotropies of WFI@2.2 are reproducably better than $\approx 3\%$. At the time of GaBoDS, however, this could easily consume 30-60 minutes per night.

Using the enhanced *querator* about 5 square degrees (20 pointings) of data were found in the ESO archive which passed the criteria, not counting the already known fields such as the ones from the EIS Deep Public Survey. This was about twice the expected area, but it must be noted that 15 of the pointings were done by a single observer, searching for trans-neptunian objects. The efficiency of the archive search with querator was about 75%, i.e. three out of four candidate fields were usable. Thus the missing sky coverage for GaBoDS

[7] Difference Image Motion Monitor

[8] A frequently used design for the telescope structure connecting the upper part with the secondary mirror to the lower part with the main mirror cell.

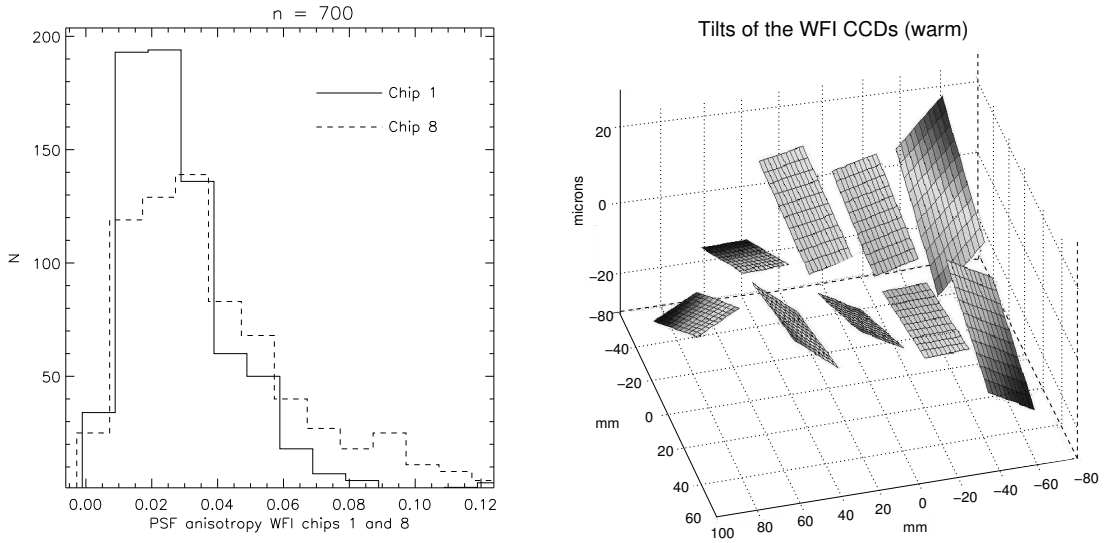

Figure 2.2: Characteristic PSF anisotropies (modulus of the ellipticity) of 700 randomly chosen exposures for two selected CCDs of the WFI@2.2 mosaic. The exposure times were typically in the range of 300-500 seconds, and the zenithal distances were usually smaller than 40 degrees. The anisotropy is defined as the modulus of the stellar ellipticity. Clearly, the characteristics for the two CCDs are different, which is due to the fact that they are not exactly in the same focal plane (right panel, copied from the WFI@2.2 homepage). The WFI@2.2 CCDs are confined within ± 20 microns and react thus differently to the chosen focus of the telescope. Anisotropies larger than $4 - 5\%$ are usually due to a defocused camera. Very large zenithal distances and a rarely failing mirror support system can cause anisotropies, too. The exposures that went into the above statistic were taken by about a dozen different observers, and give an idea of the quality of archival data (very bad images were excluded beforehand of the statistic). See Fig. 2.4 for more information.

was complemented with advanced data mining of the ESO archive. Tables 2.1 and 2.2 lists all fields in the GaBoDS that were used for this work together with their sources.

2.1.3 Main characteristics of the GaBoDS fields

Making heavy use of archival data, more than 19 square degrees of high quality R-band exposures with only 10 clear nights of own observations were collected. For nearly half of the fields multicolour information was also available. As can be seen from Fig. 2.3, the GaBoDS fields can be split into a shallow part (9.6 square degrees, 4-7 ksec total exposure time), a medium deep part (7.4 square degrees, 8-11 ksec) and a deep part (2.6 square degrees, 13-56 ksec). The survey fields are randomly distributed at high galactic latitude in the southern sky. The image seeing in the mosaics is equal to or better than $1\farcs0$, and our astrometric solution is accurate enough not to introduce artificial PSF anisotropies (see section 2.2.3 for details). The typical PSF quality of a field in the survey can be seen in the lower right panel of Fig. 2.4. There the PSF anisotropies of a mosaic consisting of 57 exposures are shown, giving a total integration time of 27.1 ksec. The image seeing of this particular field is $0\farcs8$, thus possible shortcomings in the astrometric algorithm could easily be seen. The rms PSF anisotropy merely amounts to 0.8%, making WFI@2.2 very well suitable for weak

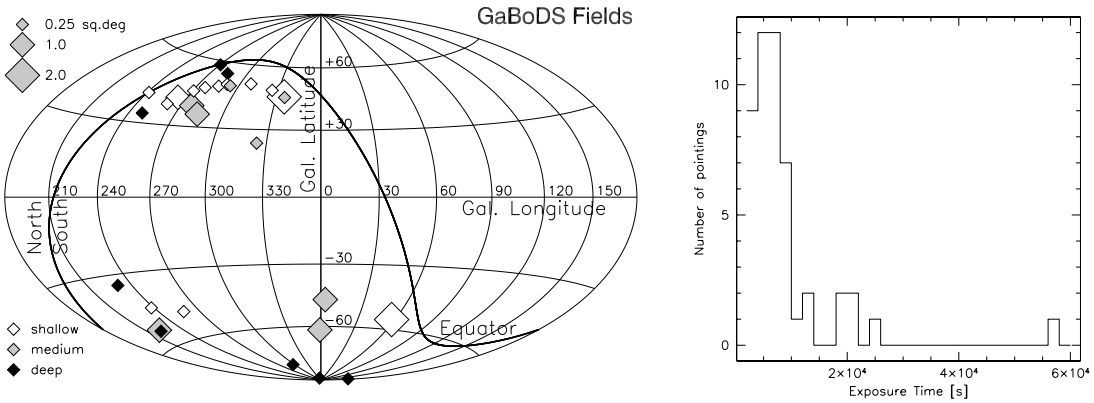

Figure 2.3: Left. Sky distribution of the GaBoDS fields. The size of the symbols depicts the covered sky area. All fields are at high galactic latitude. Note that a single exposure with WFI covers a bit more than the stated 0.25 square degrees, the exact figure is 0.32 square degrees. Right: Exposure times in GaBoDS. The peak at 56 ksec represents the Chandra Deep Field South (CDF-S).

gravitational lensing studies. The larger anisotropies in the field corners, especially in the lower left, are due to a combination of slightly tilted CCDs with respect to the focal plane, and residual optical abberations off axis.

Such quality of the data can only be achieved with a very carefully and frequently refocused telescope. The effect of a slightly defocused telescope on the PSF is shown in the remaining three panels of Fig. 2.4. One can see that anisotropies become significant once the detector is out of focus. Furthermore, the PSF rotates by 90 degrees when the focal plane passes through the detector plane. This is characteristic for tangential and sagittal astigmatism. Still the PSF of WFI@2.2 is very homogeneous over the field of view, even when crossing chip borders. Thus larger dither patterns can be used for the observations, and a single smooth model can be fitted to the PSF in the mosaic. A detailed description of the applied PSF correction method is given in section 3.1.2.

2.2 Data reduction with the GaBoDS pipeline

The advent of multi-chip CCD cameras imposes new, high demands on data reduction. Preprocessing steps such as debiasing or flatfielding can be done independently on a chip-by-chip basis, allowing for efficient parallel processing on a multi-processor machine with sufficient disk space. Whereas these steps can be tackled using the same well-known algorithms as for single-chip cameras, an accurate astrometric and photometric calibration of WFI data requires techniques going well beyond those routines. Different sensitivities of the CCDs and gaps between them lead to a very inhomogeneous exposure time and accordingly noise in the coaddition. An accurate weighting scheme is essential in order to retain control over these effects in the mosaic. In the following our approach to WFI data reduction is described.

An almost fully automatic pipeline (apart from absolute photometry) for WFI reduction was developed, based on existing software modules wherever possible, such as *EIS drizzle*[9],

[9]http://www.eso.org/science/eis

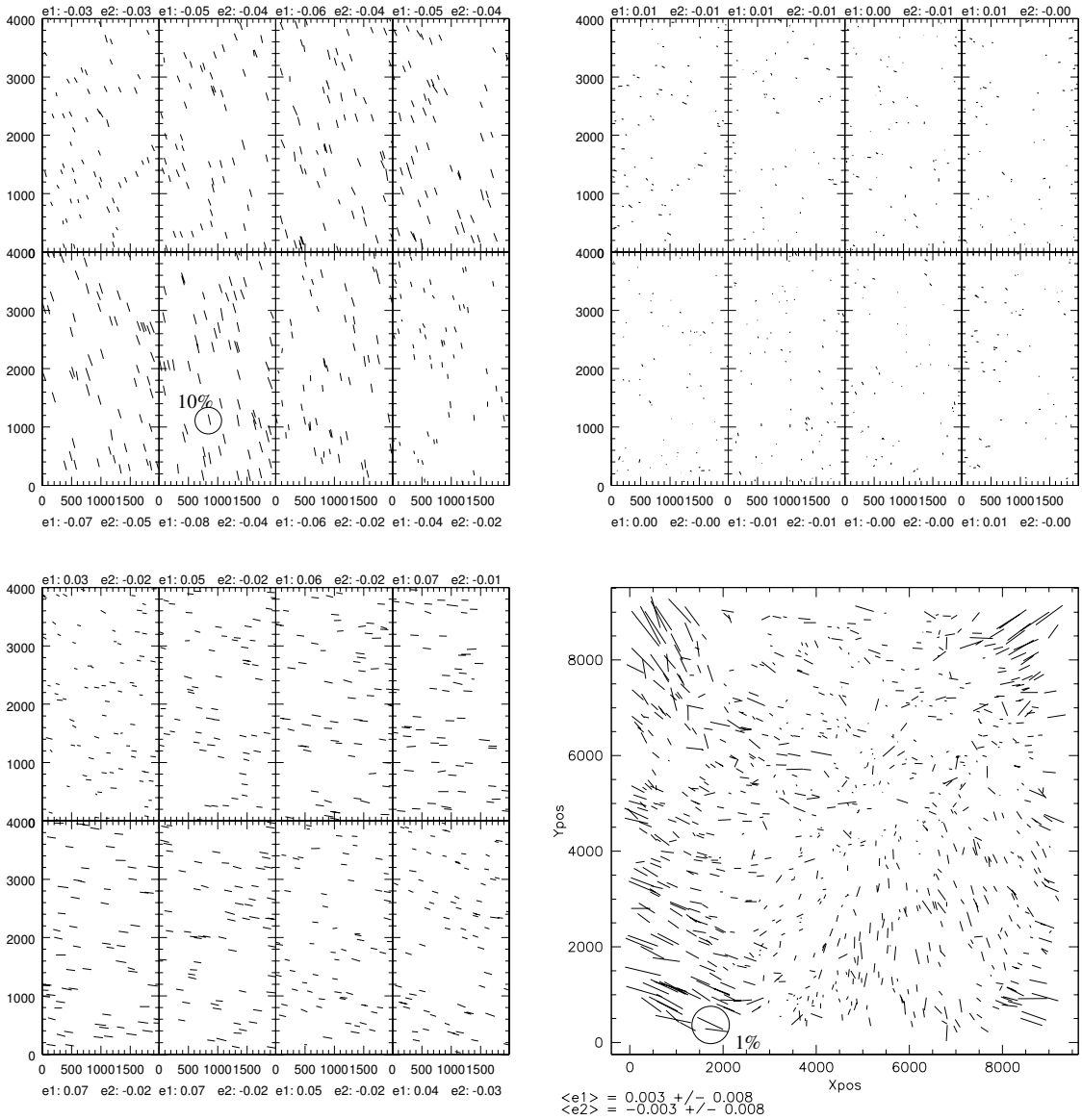

Figure 2.4: PSF anisotropies for an intrafocal (upper left), focal (upper right) and extrafocal (lower left) exposure. The chosen scale for the stick length is the same for those three plots in order to show the increase in the anisotropies with respect to the focused exposure. The mean stellar ellipticities are 6.6%, 0.9% and 5.9%, respectively. The lower right panel depicts typical PSF anisotropies of a WFI@2.2 R-band mosaic (~ 57 exposures with ~ 500 sec exposure time each). Note that the largest PSF anisotropies in the mosaic are as small as $\approx 1.0\%$. Compared to the other three PSF plots a different scale for the stick length was used in order to clearly show the anisotropies.

the Terapix[10] software suite, *FLIPS*[11] (J.-C. Cuillandre, not yet publicly available), *Eclipse*[12], *Imcat*[13] (N. Kaiser) and *LDAC*[14] (E. Deul, Leiden Data Analysis Center, used for catalogue format and handling). Most of these packages are stand-alone C-programs. *IRAF* was not used in the pipeline, apart from the drizzle coaddition, since it did not allow for efficient scripting and reduction of this specific kind of data. A number of bash shell scripts were wrapped around those tools, which allows for an efficient, flexible and automatised end-to-end reduction of WFI data in parallel mode. The usage of the pipeline is not restricted to the WFI@2.2. Data from other instruments such as FORS1/2@VLT, ISAAC@VLT, SUPRIME-CAM@SUBARU, MOSAIC-I@CTIO, MOSAIC-II@KPNO, WFI@AAO and WFI@INT has already been successfully reduced. Supported architectures are Solaris, AIX, Linux and Dec-Alpha.

The pipeline was designed with the GaBoDS data in mind, i.e. empty fields at high galactic latitude, with a fairly large dither pattern of up to $3'.0$, and a very large number of single exposures per pointing. The reduction of various test data sets with very different characteristics in terms of crowding and extent of objects has shown that the GaBoDS pipeline can handle such fields easily, too. Figure 2.9 at the end of this chapter shows the effects of some of the data reduction steps on a set of images.

2.2.1 The pre-processing

Overscan correction, debiasing, flat fielding Apart from the astrometric, photometric and coaddition processes, all chips are processed individually, allowing for an easy parallelisation of the code. During pre-reduction, any instrumental signatures present in the data are removed. This includes overscan correction, bias subtraction and flat fielding with skyflats[15]. For the master biases all bias exposures are median combined with outlier rejection. Flat fields are combined in the same way, but each flat exposure is normalised to 1 before the combination. Thus the different gains in the science images are still present after the flat fielding step. This is due to the fact that the chip-to-chip gain variations can be better determined from a superflat, which is drawn from already flatfielded exposures.

Creation of a superflat Residuals of around 3-4% after normal flat fielding are common for WFI@2.2, depending on sky brightness and the filter in use. A superflat is computed for correction of this effect, by median combining all exposures from a given observing run, using outlier rejection. Pixels that are affected by stars or galaxies are detected with *SExtractor* (Bertin & Arnouts, 1996) and masked beforehand. By doing so the contribution to the superflat of bright extended haloes around stars is prevented. This superflat is then heavily smoothed, yielding an *illumination correction* for each chip. All images are divided by their individual illumination correction. They are also normalised to the same (the highest) gain, which is accurately determined by comparing the modes of the individual superflats. Remaining residuals in the sky background are typically below 2%, and with absence of bright stars, even below 1%.

[10] http://terapix.iap.fr
[11] http://www.cfht.hawaii.edu/~jcc/Flips/flips.html
[12] http://www.eso.org/projects/aot/eclipse
[13] http://www.ifa.hawaii.edu/~kaiser/imcat
[14] ftp://ftp.strw.leidenuniv.nl/pub/ldac/software
[15] For WFI@2.2m telescope dome flats are inferior compared to skyflats.

In case one has taken a sufficiently large number of exposures (more than, say, 15), but not enough skyflats (for example only 3 or 4), dividing the flatfielded images with the unsmoothed superflat instead of the illumination correction can help. This is because there can be remaining systematics (mostly high-frequency pixel-to-pixel noise) in the master skyflat due to the small number of individual skyflats. These systematics are then inherited by the images and the superflat. Dividing by the superflat instead of its smoothed version, the illumination correction can thus correct for the poor skyflat sampling. The gain can be up to 10 % in the background noise. In case of fringing (see next paragraph), however, one has to use the illumination correction instead of the superflat.

Defringing Besides the illumination correction, a fringing model is calculated by subtracting the illumination correction from the superflat. This fringing model is then individually scaled for each image and subtracted. Hereby it is assumed[16] that the amplitudes of the observed fringes scale directly with the sky background. For WFI@2.2 the fringing in the R-band is of the order of a few percent as compared to the sky background. Its correction makes sense only if more than $\sim$ 10 exposures were used in the calculation of the model. Otherwise the pixel-to-pixel noise in the fringing model is larger than the fringing amplitude itself. This would introduce more noise into the individual defringed images than what is taken out by the correction of the lower frequency fringes. Since for weak lensing studies one is interested in measuring shapes of faint and small galaxies, one wants to avoid additional pixel-to-pixel noise such as from this source. However, all mosaics in the GaBoDS survey were constructed from many more than just 10 exposures, thus the contribution of additional high frequency noise is small, and one profits from taking out the gentle fringing pattern. In the case of the redder I-band the fringing can be much more prominent, and is in general much more difficult to remove.

2.2.2 The importance of dithering

Offsetting the telescope between the exposures is fundamential for high-quality, high-S/N mosaics. Hereby the *dither box*, i.e. the box that encompasses all dither offsets, should be clearly larger than the gaps between the CCDs of the camera. Using such a wide dither pattern has several advantages as compared to the *staring* mode (no offsets at all) or to the application of only small offsets.

First, the CCDs in a multi-chip camera are fully independent from each other. They see the sky through different sections of the filter, and they have their individual flatfields, gains and read-out noise. Choosing a wide dither pattern is the only way to establish a global photometric solution for the mosaic, based on enough overlap objects. Even though the science presented in this work can be done without a global photometric system (and for a few of the ASTROVIRTEL fields this was the case since they were obtained in staring mode), other projects that are based on this data rely on a global photometry. The latter also holds for projects that require excellent astrometry over the entire field. For example, the CDF-S field that was reduced with the GaBoDS pipeline serves as the astrometric reference for GOODS (Great Observatories Origin Deep Survey), based on which all space- and ground-

[16]This assumption only holds for photometric nights. In non-photometric nights it can be impossible to remove fringing in the I-band, since the model is changing within minutes on scales smaller than the field of view of a single CCD.

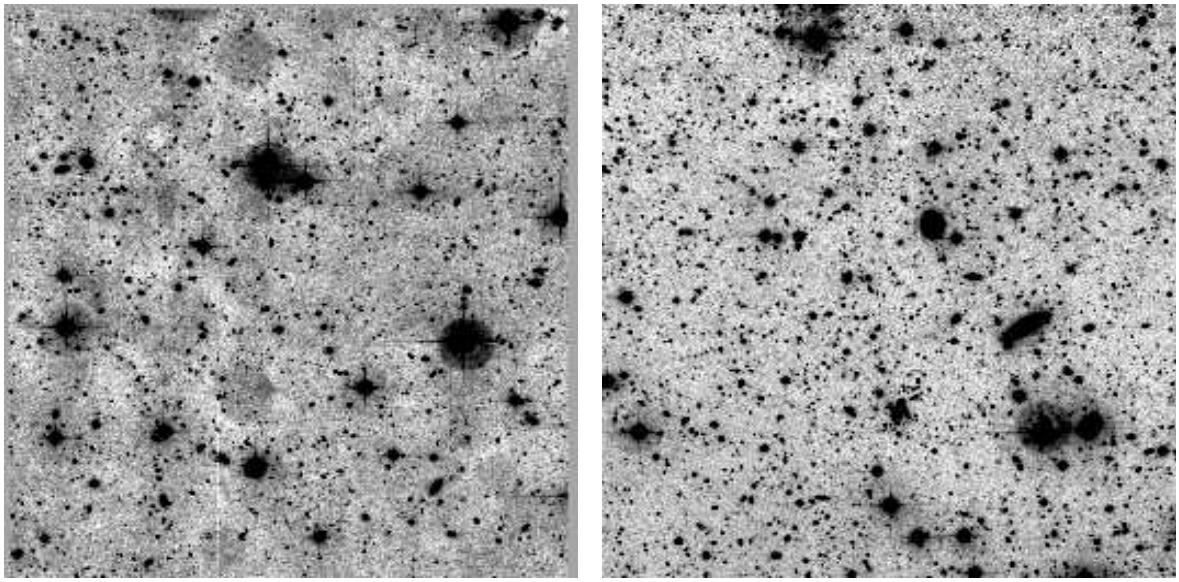

Figure 2.5: Sky background variations in a mosaic obtained in staring mode (left), and for one obtained with a wide dither pattern (right). The contrast scaling for both mosaics is the same.

based observations in the different wavelengths will be registered with respect to each other.

Second, the wide dither pattern allows for a significantly better superflatfielding of the data, since the objects do not fall on top of themselves and thus for every pixel an good estimate of the background can be obtained. Besides, remaining very low-amplitude patterns in the sky background caused by improper flatfields etc. do not add in the mosaic, but are averaged out. Thus, a wide dither pattern will lead to an improved sky background from which both, photometry and shape measurements of faint objects, profit. Besides, two of the spin-off projects of GaBoDS, the search for low surface brightness galaxies and for tidal streams, could not be done on mosaics with a highly variable sky background (see Fig. 2.5 for an illustration).

Third, the object S/N in a mosaic with a wide dither pattern is clearly superiour to one obtained in staring mode. The reason for this is that the master bias and the master skyflat are not noise-free, since they are created from a finite number of images. An identical copy of this calibration noise in the master bias and skyflat is then created in each science image during the preprocessing. If no dither offsets are applied, then the calibration noise in the n science images is stacked on top of itself during the coaddition, and thus increases in the same way as the flux of the objects ($\propto n$) instead of averaging out ($\propto \sqrt{n}$). Depending on the ratio of the calibration noise and the noise in the uncalibrated images themselves, the effective exposure time of the mosaic can be very significantly reduced. This is especially true for observations gained under excellent (dark) conditions, since the sky noise in the science images is then reduced, and the calibration noise becomes more important. One should therefore always aim at a sufficient number of calibration exposures, *and* go for larger dither offsets. This holds for single-chip cameras, too.

2.2.3 Astrometric calibration

After the pre-processing a global astrometric solution and a global relative photometric solution is calculated for all images. This is where the reduction of WFI data becomes much more complicated than the one for single-chip cameras.

In the first step, high S/N objects in each image are detected by *SExtractor*, and a catalogue of non-saturated stars is generated. Based on a comparison with the USNO-A2 astrometric reference catalogue, a zero-order, single shift astrometric solution is calculated for each image. For a single-chip camera with a small field of view such an approach is often sufficient, but it no longer holds for multi-chip cameras with a large field of view. There the CCDs can be rotated with respect to each other, tilted against the focal plane (see Fig. 2.2), and in general cover areas at a distance from the optical axis where field distortions become prominent[17]. Figure 2.6 shows the difference between a zero order (single shift with respect to a reference catalogue) and a full astrometric second order solution per image. From this figure it is obvious that the simple shift-and-add approach will not work for the whole mosaic. The issue is further complicated by the gaps between the CCDs and large dither patterns that are used to cover them. Thus, images with very different distortions overlap. In addition, due to the large field of view, the observed patch of the sky must no longer be treated as a flat plane, but as a spherical curved surface.

In the second step Mario Radovich's *Astrometrix*[18] (Terapix) package is used to determine third order polynomials for the astrometric solution of each image. This corrects for the above mentioned effects, and thus allows for the proper mosaicing in the later coaddition process. For this purpose all high S/N objects (stars and galaxies) detected in the first step are identified with each other, including those from the overlap regions. The latter ones are most important in establishing a global astrometric (and photometric) solution, since the accuracy of available reference catalogues such as the USNO-A2 with an rms of $0\farcs2$ is insufficient for sub-pixel registration. Thus the astrometric solution is determined from the data itself. The USNO-A2 is used only to fix the solution with respect to absolute sky coordinates within the stated $0\farcs2$ rms. With *Astrometrix* an internal astrometric accuracy of $1/20 - 1/10$th of a pixel ($0\farcs02$–$0\farcs01$) is consistently achieved, thus the final PSF is mostly determined by the intrinsic PSFs of the individual exposures (see Fig. 2.4). Additional artificial seeing and PSF anisotropies are introduced into the mosaic on a very low level only, even for very large data sets such as the CDF-S, consisting of 150 WFI@2.2 R-band exposures. This is a crucial requirement for this work.

2.2.4 Photometric calibration

Once an astrometric solution is found, a relative photometric solution is straightforward. Relative fluxes of objects in different exposures and overlap regions are compared, allowing the calculation of relative photometric zeropoints for all images in the data set. Given two overlapping images k and j, consider all $i = 1...N$ objects and calculate the mean deviation of magnitudes K and J

$$M_{k,j} := \frac{\Sigma_i W_i (K_i - J_i)}{\Sigma_i W_i} \,, \tag{2.1}$$

[17] A ZEMAX analysis (Philipp Keller, private communication) for the full optical system of WFI@2.2 shows that the radial field distortion increases with $\delta = a_1 r^2 + a_2 r^6$. However, the total amplitude of this distortion is very small (~ 30 pixels), which is in agreement with the WFI user manual (Baade, 2000).

[18] http://www.na.astro.it/~radovich/WIFIX/astrom.ps

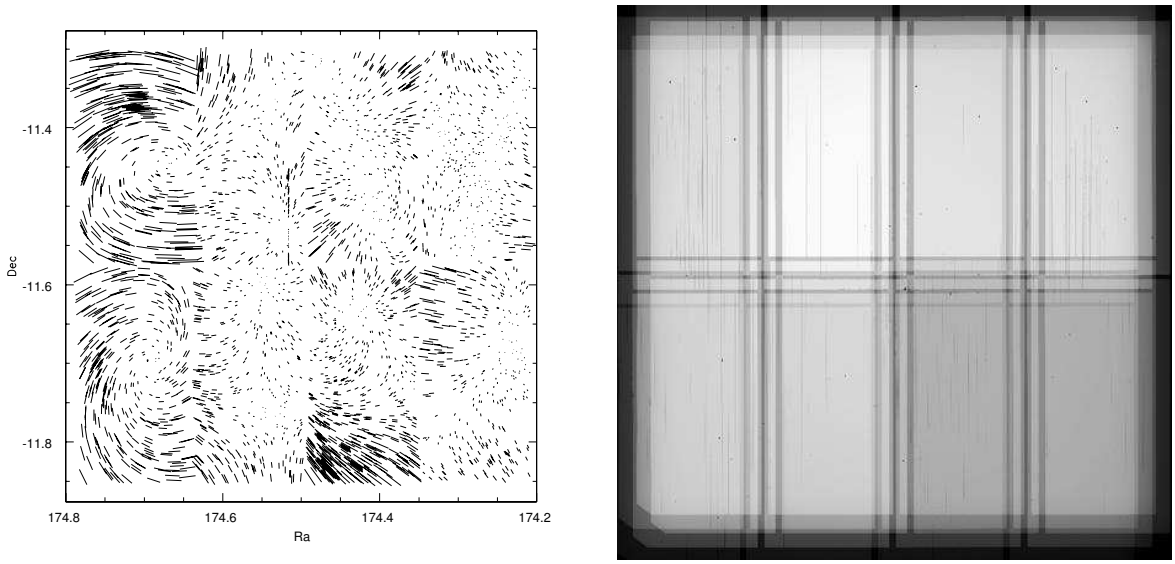

Figure 2.6: Left: Difference in object position between a single-shift approach and a full two-dimensional second order astrometric solution for the WFI@2.2. In other words, shown are the higher order terms needed for matching the images to the sky. The patterns belonging to the left two CCDs are due to a rotation with respect to the mosaic. The maximum position difference in the plot is about six pixels, still a fairly small value compared to other telescope designs. It becomes clear that a single, global distortion polynomial for all 8 CCDs does not work. Instead, every image has to be treated individually.
Right: Coadded weight of a small WFI@2.2 data set consisting of five exposures. One clearly identifies regions with less effective exposure time due to gaps between CCDs and different pixel sensitivities. The size of the dither pattern also becomes obvious. Brighter regions correspond to pixels with higher weight. The variations from chip to chip are due to differences in the gain and the flatfield.

with $W_i = (\sigma_K^2 + \sigma_J^2)^{-1}$, where the σ are the measurement errors of the corresponding magnitudes. Objects deviating in $K_i - J_i$ more than a user defined threshold are excluded from the statistics that follows. The relative zeropoints ZP_l for all N overlapping images are determined by a χ^2 minimisation with respect to ZP_k,

$$\chi^2 = \sum_{k,j}^{N} \left[M_{k,j} - (ZP_k - ZP_j)\right]^2 \ . \tag{2.2}$$

Finally, the relative photometric zeropoints are normalised so that their mean is zero. This approach assumes that the relative zeropoints are constant for each image[19]. An automatic absolute photometric solution is not yet implemented in the pipeline.

2.2.5 A statistically optimised weighting scheme

The effective exposure time for a mosaic is highly non-uniform. Read noise and the flatfields are chip-dependent, and gaps between the CCDs contribute further to the inhomogeneous depth of a mosaic. Applying a statistically optimised weighting scheme to the images during coaddition allows for a significantly improved object S/N ratio (up to a factor of ~ 1.5).

[19]Zeropoint variations for images taken with WFI@2.2 that were not superflat corrected are described in: http://www.ls.eso.org/lasilla/sciops/wfi/zeropoints .

In a first step, a pixel is assigned its normalised skyflat value as a weight, which contains the information about relative gains between the CCDs and pixel-to-pixel sensitivities. For the detection of permanent image defects, such as hot or dead pixels and bad columns, dark exposures and superflats are used. Affected pixels are set to zero in the corresponding weight map. Thus each CCD in the WFI mosaic has its own basic (*'global'*) weight image after the first step. The global weight for a particular CCD does not change in a data set unless the images from this CCD were flatfielded with different skyflats or were taken more than about a week apart.

In a second step these global weights are adjusted individually for each image. Contrary to other methods, 'bad' pixels (hot or cold pixels, pixels affected by cosmics, reflections or satellite tracks) are not detected by comparing all images in the stack, but on the individual images themselves. Hot pixels and cosmics are easily identified with *SExtractor* in conjunction with *Eye* (Terapix), since they appear much sharper than the stellar PSF even under good seeing conditions. There is some redundancy in this step, since quite a few of the permanent pixel defects that are already recognised in the first step are detected a second time. Bright reflections and satellite tracks, however, need to be masked by hand, the only step in the pipeline which is not yet automatised. Moving objects like asteroids go unmasked and show up as dashed lines in the mosaic. During coaddition, the individual weight images are scaled with correction factors for airmass and varying photometric conditions. Changing seeing conditions from image to image can be included on an optional basis, too. All individual weights are resampled and coadded in exactly the same way as the respective science images, yielding the noise properties for all pixels in the final mosaic (see Fig. 2.6 for an example).

2.2.6 The coaddition process

Before the coaddition, all images are sky subtracted. In order to model the sky background, all objects in an image with a $S/N \geq 1.0$ in the field are detected with *SExtractor* and replaced with the mean sky background as determined from the remaining pixels. The S/N threshold can vary, depending on the individual data set and the objects therein. This *object-subtracted* image is then convolved with a very broad smoothing kernel (width between 200 and 500 pixels) and subtracted from the science image itself.

For the coaddition, the *EIS drizzle* in *IRAF* is used. It allows for a weighted mean coaddition, guaranteeing the best S/N in the mosaic. For the coadding, the *input* pixels from the images are mapped onto the initially empty *output* grid, using the full astrometric solution. This process is known as *resampling*, and guarantees that a varying pixel scale is correctly taken into account also from a photometric point of view. In general, an individual input pixel lands somewhere on top of several neighbouring output pixels, and is distorted and rotated. Its flux is then accordingly distributed amongst these output pixels, which leads to correlated noise in the mosaic. Such a procedure is called *forward mapping*. The *EIS drizzle* approach strongly simplifies the calculation (the *kernel*) of the flux distribution, in the sense that only non-integer shifts are taken into account, whereas rotations and distortions of the mapped pixels are neglected. A general description of the drizzling approach is given in Gonzaga et al. (1998).

Alternatively, one can use *SWarp* (E. Bertin, Terapix), which makes use of a more advanced kernel for the resampling, and uses a technique called *reverse mapping* for the coaddition. In this approach all input images get individually undistorted and resampled. An individual pixel in the output image is then mapped onto all n resampled input images, using

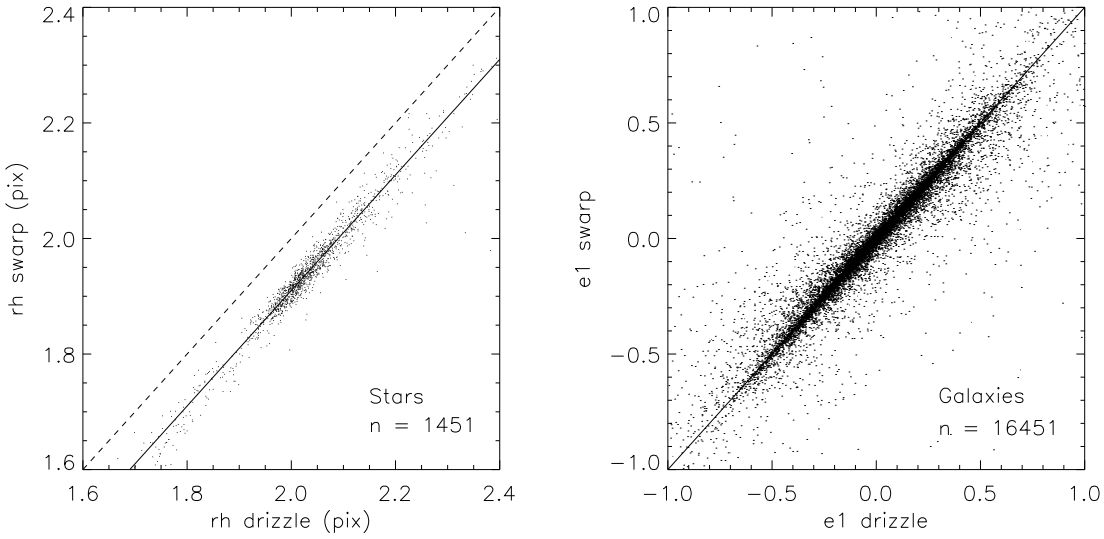

Figure 2.7: Comparison of image seeing and ellipticities between two mosaics created with *SWarp* respectively *EIS drizzle*. The left panel shows that the swarped image has an image seeing that is 0.09 pixels smaller than the one for the drizzled image (plotted are the half light radii for unsaturated stars). The absolute mean values for the image seeing are 0.″95 for the drizzled image and 0.″91 for the swarped one. The latter value is consistent with the expected image seeing (the geometrical mean of the seeing in the individual images), given a perfect coaddition procedure. The same astrometric solution was used for both coadditions. Thus *EIS drizzle* slightly increases the size of the PSF, an effect of its simplified kernel. In Fig. 2.8 it is shown that the PSF anisotropies are identical for both coaddition strategies.
The right panel shows the PSF corrected image ellipticities for galaxies (see Sect. 3.1.2). It becomes clear that the coaddition method does not bias the shape measurement.

the inverse astrometric solution. Thus n flux estimates for the output pixel are at hand, from which an optimal value is calculated (see Bertin, 2002, for details).

The advantages of *SWarp* over drizzle are that the mosaic does not have correlated noise, and has a slightly better image seeing (see left panel of Fig. 2.7). Apart from these the differences become negligible when a larger number of exposures is stacked ($n \approx 10 - 20$). In particular, the measured ellipticities of faint background galaxies remain unbiased when switching from *SWarp* to *drizzle* (see right panel of Fig. 2.7). Besides, the PSF patterns for *SWarp* and *drizzle* are remarkably similar as can be seen from Fig. 2.8.

In the drizzling approach used, four factors determine the value of an output pixel in the mosaic. Given is a value I_i from an input pixel in the science image, and an associated value W_i in the weight map. I_i represents the part of the input pixel that is mapped onto the corresponding output pixel. Besides, I_i is scaled with factors f_i to the consistent photometric zeropoint and normalised to a fixed exposure time of 1 second. This scaling reads

$$f_i = 10^{-0.4\,ZP_i}/t_i, \tag{2.3}$$

where t_i is the exposure time and ZP_i the relative photometric zeropoint. All images are also

weighted according to their sky noise. This weight scale is given by

$$w_i = \frac{1}{\sigma^2_{\mathrm{sky,i}} f_i^2}. \tag{2.4}$$

Here it is taken into account that the noise also scales with the flux scale f_i. The values I_{out} and W_{out} in a stack of N exposures then read

$$I_{\mathrm{out}} = \frac{\sum_{i=1}^{N} I_i f_i W_i w_i}{\sum_{i=1}^{N} W_i w_i} \quad , \qquad W_{\mathrm{out}} = \sum_{i=1}^{N} W_i w_i \ . \tag{2.5}$$

EIS drizzle creates its output with the TAN projection. Alternatively, the COE projection can be used (see Greisen & Calabretta, 2002, for further information on sky projections). In the mosaics North is up and East to the left. A reference coordinate can be specified for the coaddition. Thus, if multicolour information is available for a particular pointing, the mosaics in the different bands are automatically registered with sub-pixel accuracy.

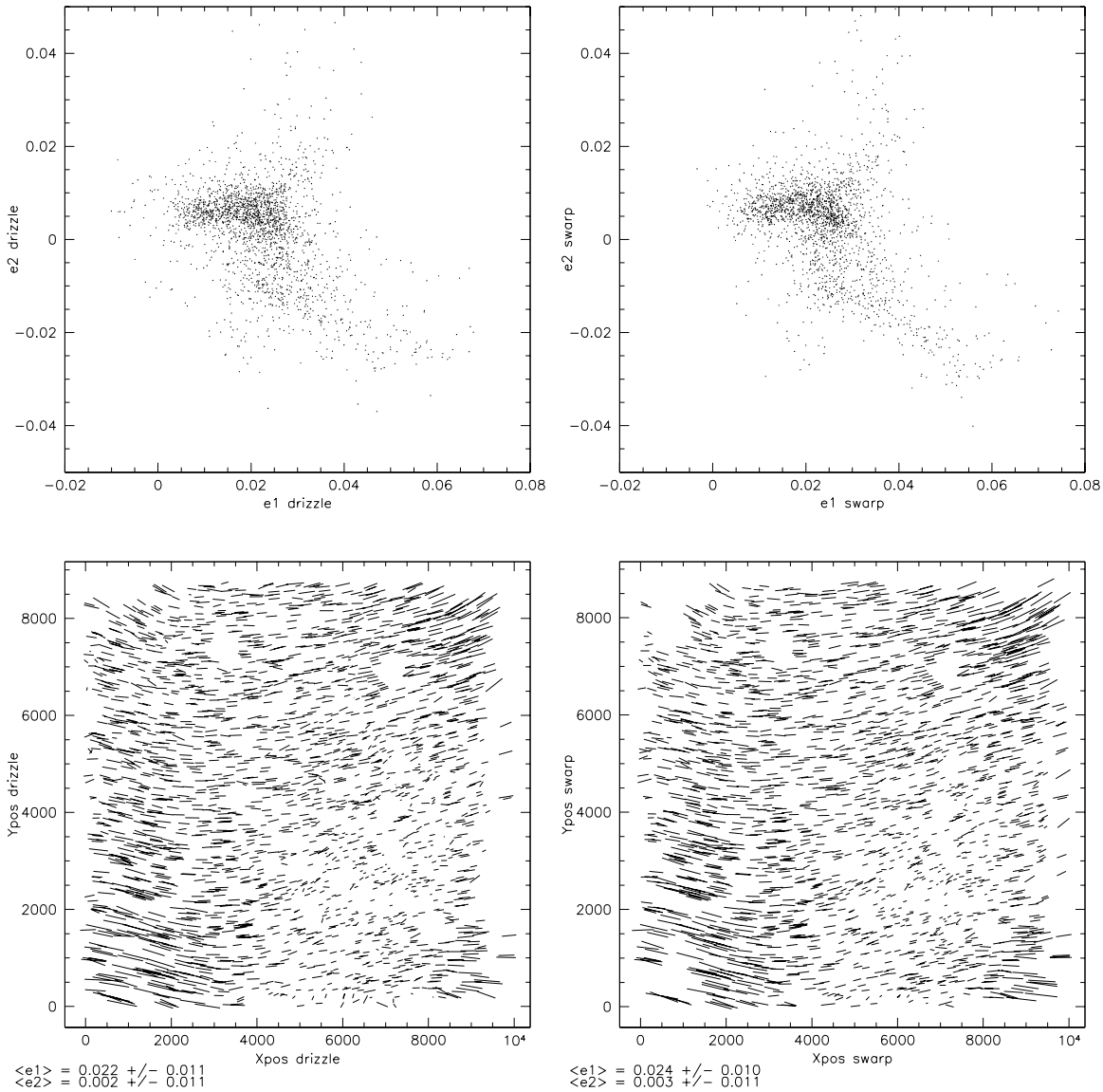

Figure 2.8: PSF anisotropies in a drizzled (left column) and a swarped (right column) mosaic of the same data set. The patterns are virtually identical. Yet *EIS drizzle* marginally increases the size of the PSF, as was shown in the left panel of Fig. 2.7.

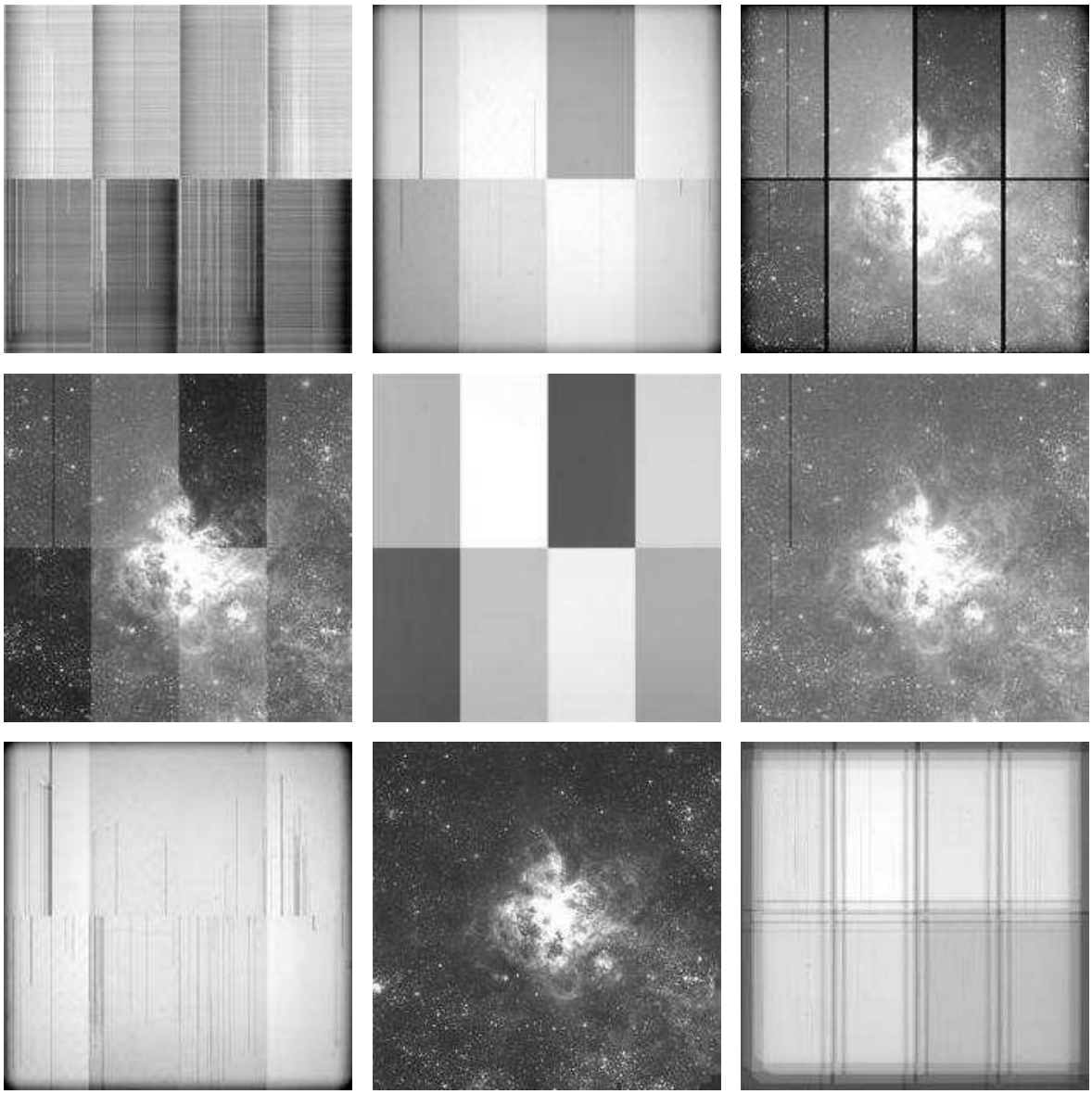

Figure 2.9: Individual calibration exposures and their effect on the exposures as they run through the pipeline. From left (l) to right (r), and from top (t) to bottom (b) this is: (tl) the master bias, (tm) the master skyflat, (tr) the raw exposure, (ml) the debiased and flatfielded images, (mm) the illumination correction including the gain differences, (mr) the superflatted and gain corrected images, (bl) weight for an individual exposure, (bm) the mosaic, (br) the coadded weight.

Table 2.1: GaBoDS fields

Field	α(2000.0)	δ(2000.0)	Exp time	Source
Field	α(2000.0)	δ(2000.0)	Exp time	Source
C04p3	215.098018	−10.75340	4000	ASTROVIRTEL
CAPO-DF	186.037876	−13.10764	13000	ESO archive
CDF-S	53.133442	−27.82255	57200	EIS COMBO-17 GOODS
CL1037−1243	159.444072	−12.75499	3600	EDisCS
CL1040−1155	160.139300	−11.96379	3600	EDisCS
Cl1054−1146	163.581888	−11.81304	3600	EDisCS
Cl1054−1245	163.647353	−12.79700	3600	EDisCS
CL1059−1253	164.755650	−12.92051	3000	EDisCS
CL1119−1129	169.784677	−11.52558	3600	EDisCS
CL1138−1133	174.508878	−11.59953	3600	EDisCS
A1347_P1	175.257022	−25.51474	13500	own observation
A1347_P2	175.792544	−25.50918	7500	own observation
A1347_P3	175.239760	−25.00933	7000	own observation
A1347_P4	175.794592	−24.99836	8000	own observation
A901	149.077714	−10.02734	18100	COMBO-17
AM1	58.811816	−49.66762	7500	ASTROVIRTEL
B8m1	340.34884	−10.08953	4500	ASTROVIRTEL
B8m2	340.348548	−10.58954	5400	ASTROVIRTEL
B8m3	340.346888	−11.08857	5400	ASTROVIRTEL
B8p0	340.348861	−9.59009	7200	ASTROVIRTEL
B8p1	340.346051	−9.08957	4500	ASTROVIRTEL
B8p2	340.345309	−8.58963	5400	ASTROVIRTEL
B8p3	340.345149	−8.08951	5400	ASTROVIRTEL
C0400	214.360609	−12.25356	4800	ASTROVIRTEL
C04m1	214.727417	−12.75342	4000	ASTROVIRTEL
C04m2	214.478576	−13.25319	4000	ASTROVIRTEL
C04m3	215.318002	−13.75352	4000	ASTROVIRTEL
C04m4	215.111423	−14.25337	4000	ASTROVIRTEL
C04p1	214.726983	−11.75319	4000	ASTROVIRTEL
C04p2	214.727266	−11.25366	4000	ASTROVIRTEL

Table 2.2: GaBoDS fields (continued)

CL1202−1224	180.645603	−12.44172	3600	EDisCS
CL1216−1201	184.170966	−12.06268	3600	EDisCS
CL1301−1139	195.467853	−11.63099	3600	EDisCS
CL1353−1137	208.306268	−11.59813	3600	EDisCS
CL1420−1236	215.066773	−12.64986	3600	EDisCS
Comparison	65.307669	−36.28380	5300	ASTROVIRTEL
DEEP1a	343.795067	−40.19886	7200	EIS
DEEP1b	343.058572	−40.22481	3900	EIS
DEEP1c	342.328125	−40.20702	3900	EIS
DEEP1e	341.966792	−39.52874	9000	EIS
DEEP2a	54.372223	−27.81551	6000	EIS
DEEP2b	53.746626	−27.80862	5100	EIS
DEEP2d	52.506344	−27.81774	3000	EIS
DEEP2e	53.122917	−27.30467	7500	own observation
DEEP2f	53.669953	−27.32400	7000	own observation
DEEP3a	171.245593	−21.68289	7200	EIS
DEEP3b	170.661597	−21.70969	9300	EIS
DEEP3c	170.019096	−21.69960	9000	EIS
DEEP3d	169.428759	−21.70164	9300	own observation
FDF	16.445419	−25.85742	11840	COMBO-17
F17_P1	216.419162	−34.69460	10000	own observation
F17_P3	217.026113	−34.69463	10000	own observation
F4_P1	321.656115	−40.25193	9500	own observation
F4_P2	321.719420	−39.76761	7000	own observation
F4_P3	322.320122	−40.23769	10000	own observation
F4_P4	322.323894	−39.72689	7500	own observation
NDF	181.362371	−7.65226	21800	MPE IR group
NGC300	13.721845	−37.67132	15000	ASTROVIRTEL
Pal3	151.432117	−0.00344	4200	ASTROVIRTEL
S11	175.748601	−1.73458	21500	COMBO-17
SGP	11.498527	−29.61047	20000	COMBO-17
SHARC-2	76.333333	−28.81805	11400	own observation

Chapter 3

Finding galaxy clusters by weak lensing

In this chapter it is demonstrated how a dark matter halo can be detected by means of its lensing signal (*shear selection*). For this purpose, an object catalogue must be created from the coadded image that was produced in the previously described manner, containing information about the lensed galaxies in this image. This catalogue must be filtered with respect to several criteria in order to be useful for the subsequent analysis. The catalogue production and filtering are explained in section 3.3, after the basic concepts of the techniques used have been introduced and the motivation for several filtering steps became clear.

In section 3.1, a measure for the ellipticities of galaxy images is defined. It is shown how the lensing signal can be recovered from these ellipticities, and how one can correct to first order for various PSF effects. Thereafter, it is demonstrated in section 3.2 in what way the extracted lensing signal can be used for the detection of clusters of galaxies. At the end of this chapter an estimate of this method's detection limits in terms of redshift and galaxy cluster mass is given for the underlying GaBoDS data.

3.1 Recovering gravitational shear

As was shown in equation (1.75), a circular source is mapped into an ellipse under the action of the gravitational shear γ. Since galaxies have an intrinsic ellipticity, the shear signal can not be obtained from a single galaxy alone, but must be measured from a larger number of lensed background sources. Figure 3.1 shows the effect a galaxy cluster has on the images of unlensed background galaxies. It induces a tangentially oriented distortion pattern in them. The extraction of this signal requires a measurement of the shape of the individual galaxies, whose angular sizes are very small, typically comparable to the PSF. Thus, PSF effects have to be taken into account, which makes the measurement of a weak lensing signal one of the more difficult tasks in observational astronomy.

3.1.1 Image ellipticities

Basic definitions Let $I(\boldsymbol{\theta})$ be the surface brightness of a galaxy on the sky. Choose the coordinate system such that the first moment of the surface brightness vanishes, i.e. the

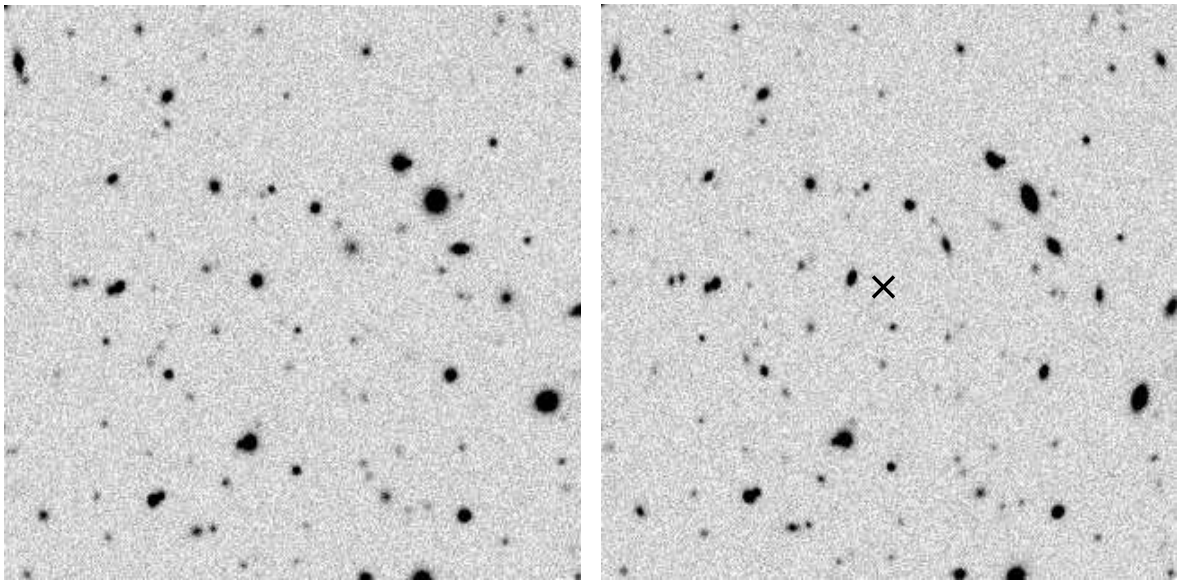

Figure 3.1: Tangential distortion pattern caused by cluster lensing. The left panel shows a simulated image of background galaxies created with *SkyMaker* (E. Bertin). The assumed exposure time was 50 ksec, the image seeing is $0\farcs6$ and the field is $75''$ wide. In the right panel the shear field of a model cluster with a critical central surface mass density of $\kappa = 1.47$ was imprinted into the galaxy catalogue before the image creation. The cluster was taken from a dark matter simulation by Jain & van Waerbeke (2000), its position is marked by the small cross. As can be seen, the tidal gravitational field of a galaxy cluster imprints a tangentially aligned, coherent distortion pattern onto the images of the background galaxies. Note that the real exposures in GaBoDS are typically a factor of five less in exposure time, and have 50% larger seeing. Besides, the fields were selected in a way to avoid such massive clusters, i.e. the alignment patterns sought in this work are significantly weaker than the one shown here.

origin of the coordinate system is put at the image "centre",

$$Q_i = \int \theta_i I(\boldsymbol{\theta}) \, \mathrm{d}^2\theta = 0 \,. \tag{3.1}$$

Based on the second brightness moments

$$Q_{ij} = \int \theta_i \theta_j I(\boldsymbol{\theta}) \, \mathrm{d}^2\theta \,, \tag{3.2}$$

two complex image ellipticities χ, alternatively ε, are defined,

$$\chi = \frac{Q_{11} - Q_{22} + 2\mathrm{i}Q_{12}}{Q_{11} + Q_{22}} \,, \tag{3.3}$$

$$\varepsilon = \frac{Q_{11} - Q_{22} + 2\mathrm{i}Q_{12}}{Q_{11} + Q_{22} + 2\sqrt{Q_{11}Q_{22} - Q_{12}^2}} \,. \tag{3.4}$$

χ and ε are entirely equivalent to each other, both concepts are used in the literature. The two are related through

$$\varepsilon = \frac{\chi}{1 + \sqrt{1 - |\chi|^2}} \,. \tag{3.5}$$

To understand these two definitions, consider a galaxy with elliptical isophotes, position angle φ and a ratio $r \in]0,1]$ of the minor and major axes. The two ellipticities for this galaxy then read

$$\chi = \frac{1-r^2}{1+r^2}\,\mathrm{e}^{2\mathrm{i}\varphi} \tag{3.6}$$

$$\varepsilon = \frac{1-r}{1+r}\,\mathrm{e}^{2\mathrm{i}\varphi}\,. \tag{3.7}$$

Transformation under a gravitational shear field Now that a measure for the ellipticity of an image with arbitrary surface brightness profile is at hand, how does a tidal gravitational field change this quantity? It was shown by e.g. Schneider & Seitz (1995) that a gravitational lens relates the unlensed intrinsic source ellipticity χ_s to the lensed image ellipticity χ by

$$\chi = \frac{\chi_\mathrm{s} + 2g + g^2\chi_\mathrm{s}^*}{1 + |g|^2 + 2\,\mathrm{Re}(g\chi_\mathrm{s}^*)}\,. \tag{3.8}$$

The operator * denotes complex conjugation, and g is the reduced shear defined in equation (1.76). The corresponding transformation for ε was given by Seitz & Schneider (1997),

$$\varepsilon = \begin{cases} \frac{\varepsilon_\mathrm{s}+g}{1+g^*\varepsilon_\mathrm{s}} & \text{for} \quad |g| \le 1 \\ \frac{1+g\varepsilon_\mathrm{s}^*}{\varepsilon_\mathrm{s}^*+g^*} & \text{for} \quad |g| > 1 \end{cases}\,. \tag{3.9}$$

Note the case distinction for $|g|$. In the weak lensing regime $|\gamma| \ll 1$ and $\kappa \ll 1$, thus $|g| \ll 1$. This also holds for the GaBoDS fields which are biased towards lower density lines of sight, hence for this work

$$\varepsilon \approx \varepsilon_\mathrm{s} + g \approx \varepsilon_\mathrm{s} + \gamma\,. \tag{3.10}$$

From ellipticities to shear Since the intrinsic shape of a galaxy is not known in the presence of lensing, the reduced shear can not be extracted from equation (3.10). The assumption is made, instead, that the ellipticities of background galaxies are random and uncorrelated in the absence of lensing[1]. Then the (reduced) shear at the position $\boldsymbol{\theta}$ can be recovered from the image ellipticities by averaging over a sufficient number of galaxies that are close enough to $\boldsymbol{\theta}$, so that the local lens properties κ and γ do not vary significantly between them. It is first assumed that all sources are at the same redshift, since κ and γ are calculated from the lensing potential ψ in equation (1.64), and thus depend of the redshifts in the lens system. One obtains

$$\langle\varepsilon\rangle \approx \langle\varepsilon_\mathrm{s}\rangle + g = 0 + g \approx \gamma \tag{3.11}$$

as an unbiased estimator for the local shear. Sufficiently deep exposures with a high enough number density of background galaxies ($n \gtrsim 10$ arcmin^{-2}) should be obtained for a sufficient

[1]This certainly holds for spatially uncorrelated galaxies, but it was shown that alignments in the intrinsic ellipticities may exist once galaxies are physically connected (see Heymans & Heavens, 2003; Jing, 2002, for details). The contribution of such alignments to the weak lensing signal is believed to be on the 10% level for deeper surveys such as GaBoDS, and is thus neglected in this work.

weak lensing analysis with this estimator. Its rms was determined by Schneider et al. (2000) to be

$$\sigma_{\rm g} \approx \sigma_\varepsilon \, \frac{1-|g|^2}{\sqrt{n}} \,, \tag{3.12}$$

where σ_ε is the dispersion of the intrinsic source ellipticities ε_s, and n is the number of galaxies in the aperture.

However, the effect of a source redshift distribution on the lensing strength can be significant (see Fig. 1.4) and should not be neglected. Relations for the shear estimator including a known source redshift distribution are given in Seitz & Schneider (1997) and Bartelmann & Schneider (2001). There it is shown that in the weak lensing regime a slight modification of equation (3.10) can account for the redshift distribution,

$$\langle\varepsilon\rangle \approx \langle s\rangle \, \gamma_\infty \,, \qquad \text{with} \quad \langle s\rangle = \int p(z)\, s(z)\, {\rm d}z \; = s(z_0) \tag{3.13}$$

where $p(z)$ is the source redshift distribution and $s(z)$ the relative lensing strength as defined in equation (1.86). Thus one can replace the redshift distribution with a single redshift z_0 defined such that the relative lensing strength $s(z_0) = \langle s\rangle$.

Individual galaxy weighting Erben et al. (2001) introduced a weighting scheme that estimates the reliability of the shear information gained from an individual galaxy. For this purpose, the variance $\sigma_{\rm g}^2$ of the reduced shear is calculated from a sample of galaxies with similar properties in the two-dimensional parameter space consisting of the half-light radius $r_{\rm h}$ and the detection S/N. The 20 nearest neighbours in the $(r_{\rm h}, S/N)$-space are used for the calculation of this variance. The individual weighting factors are determined as $w_i = 1/\sigma_{\rm g}^2$.

3.1.2 PSF correction

In this section the *KSB* method (Kaiser et al., 1995) for the PSF corrections is summarised, together with an extension of Luppino & Kaiser (1997) and a modification proposed by Hoekstra et al. (1998). Contrary to other methods such as those proposed by Bonnet & Mellier (1995) and Wilson et al. (1996), *KSB* does not rely on calibrations gained from simulations, but derives all PSF corrections from the individual data directly. It has been widely used and tested and was found to yield good results (see Erben et al., 2001; Hoekstra et al., 1998, for example).

For practical purposes the quadrupole moments (3.2) of the brightness distribution need to be replaced by weighted moments,

$$Q_{ij} = \int \theta_i \theta_j I(\boldsymbol{\theta})\, W\left(\theta^2/\sigma^2\right)\, {\rm d}^2\theta \,. \tag{3.14}$$

Here W is an isotropic Gaussian, suppressing the background noise and the influence of neighbouring objects. Its width σ depends on the individual object size.
The following very technical description is mostly taken from Bartelmann & Schneider (2001). These quantities and relations are needed for the first half of *KSB*:

- $P(\boldsymbol{\theta})$, the normalised PSF
- $P^{\rm iso}(\boldsymbol{\theta})$, the azimuthally averaged, isotropic part of the PSF

- $q(\boldsymbol{\theta})$, the anisotropic part of the PSF – see equation (3.15)
- $I^{\mathrm{s}}(\boldsymbol{\theta})$, the unlensed image of the source without any PSF
- $I(\boldsymbol{\theta})$, the lensed image without any PSF
- $I^0(\boldsymbol{\theta})$, the unlensed image blurred with P^{iso}
- $I^{\mathrm{iso}}(\boldsymbol{\theta})$, the lensed image blurred with P^{iso}
- $I^{\mathrm{obs}}(\boldsymbol{\theta})$, the actually observed surface brightness.

$$P(\boldsymbol{\theta}) = \int \mathrm{d}^2\vartheta\, q(\boldsymbol{\vartheta})\, P^{\mathrm{iso}}(\boldsymbol{\theta} - \boldsymbol{\vartheta}) \tag{3.15}$$

defines the PSF as a convolution of the isotropic part with the anisotropic kernel q. Both q and P^{iso} are chosen to have vanishing first moments and are normalised to unity. For the surface brightnesses introduced the corresponding convolutions with the PSF or its isotropic part are

$$I^{\mathrm{obs}}(\boldsymbol{\theta}) = \int \mathrm{d}^2\vartheta\, I(\boldsymbol{\vartheta})\, P(\boldsymbol{\theta} - \boldsymbol{\vartheta})\,, \tag{3.16}$$

$$I^{\mathrm{iso}}(\boldsymbol{\theta}) = \int \mathrm{d}^2\vartheta\, I(\boldsymbol{\vartheta})\, P^{\mathrm{iso}}(\boldsymbol{\theta} - \boldsymbol{\vartheta})\,, \tag{3.17}$$

$$I^0(\boldsymbol{\theta}) = \int \mathrm{d}^2\vartheta\, I^{\mathrm{s}}(\boldsymbol{\vartheta})\, P^{\mathrm{iso}}(\boldsymbol{\theta} - \boldsymbol{\vartheta})\,. \tag{3.18}$$

The second moments of the PSF anisotropy q are assumed to be small. This holds very well for the GaBoDS data where the mean PSF anisotropies are of the order of 1% (see Fig. 2.4).

Correcting for PSF anisotropies Relating the observed image I^{obs} to the isotropically smeared image I^{iso}, the impact of the PSF anisotropy can be quantified. According to the splitting of the PSF into an isotropic and an anisotropic part, the observed image can be described as

$$I^{\mathrm{obs}}(\boldsymbol{\theta}) = \int \mathrm{d}^2\varphi\, q(\boldsymbol{\theta} - \boldsymbol{\varphi})\, I^{\mathrm{iso}}(\boldsymbol{\varphi})\,. \tag{3.19}$$

Setting $\boldsymbol{\vartheta} = \boldsymbol{\theta} - \boldsymbol{\varphi}$, and assuming for the moment that $f(\boldsymbol{\theta})$ is an arbitrary function, one has

$$\int \mathrm{d}^2\theta\, f(\boldsymbol{\theta}) I^{\mathrm{obs}}(\boldsymbol{\theta}) = \int \mathrm{d}^2\varphi\, I^{\mathrm{iso}}(\boldsymbol{\varphi}) \int \mathrm{d}^2\vartheta\, f(\boldsymbol{\varphi} + \boldsymbol{\vartheta})\, q(\boldsymbol{\vartheta})\,. \tag{3.20}$$

Expanding $f(\boldsymbol{\varphi} + \boldsymbol{\vartheta})$ into a Taylor series, the last integral in (3.20) is to second order

$$f(\boldsymbol{\varphi}) \int \mathrm{d}^2\vartheta\, q(\boldsymbol{\vartheta}) + \int \mathrm{d}^2\vartheta\, \vartheta_k\, q(\boldsymbol{\vartheta})\, \partial_k f(\boldsymbol{\varphi}) + \frac{1}{2} \int \mathrm{d}^2\vartheta\, \vartheta_k\, \vartheta_l\, q(\boldsymbol{\vartheta})\, \partial^2_{kl} f(\boldsymbol{\varphi})\,.$$

Here implicit summation over the indices k, l is assumed. The second term in this sum disappears since the first moments of q are zero. Defining q_{ij} as the second moments of q, and making use of the fact that q is normalised, one has

$$\int \mathrm{d}^2\theta\, f(\boldsymbol{\theta}) I^{\mathrm{obs}}(\boldsymbol{\theta}) \approx \int \mathrm{d}^2\varphi\, I^{\mathrm{iso}}(\boldsymbol{\varphi}) f(\boldsymbol{\varphi}) + \frac{1}{2}\, q_{kl} \int \mathrm{d}^2\varphi\, I^{\mathrm{iso}}(\boldsymbol{\varphi})\, \partial^2_{kl} f(\boldsymbol{\varphi})\,. \tag{3.21}$$

In the following only terms linear in q are kept. With this approximation the $I^{\rm iso}$ in the integral involving the derivative can be replaced by $I^{\rm obs}$. Substituting $f(\boldsymbol{\theta}) = \theta_i\theta_j W(\theta^2/\sigma^2)$, and solving for the integral with $I^{\rm iso}$ yields the second brightness moments,

$$Q_{ij}^{\rm iso} = Q_{ij}^{\rm obs} - 1/2\, Z_{ijkl}\, q_{kl} \qquad \text{with} \tag{3.22}$$

$$Z_{ijkl} = \int \mathrm{d}^2\varphi\, I^{\rm obs}(\boldsymbol{\varphi})\, \partial_{kl}^2 \left[\varphi_i\varphi_j\, W\left(\frac{\varphi^2}{\sigma^2}\right)\right] . \tag{3.23}$$

Having this expression for the Q_{ij} at hand, one can calculate the complex ellipticity χ defined in equation (3.4). Defining $q_1 = q_{11} - q_{22}$ and $q_2 = 2q_{12}$, and keeping again only terms up to first order in q_α, one obtains a relation between the ellipticities of the observed image and a hypothetical image smeared by an isotropic PSF only,

$$\chi_\alpha^{\rm iso} = \chi_\alpha^{\rm obs} - P_{\alpha\beta}^{\rm sm}\, q_\beta \, . \tag{3.24}$$

The following terms are used in this relation,

$$P_{\alpha\beta}^{\rm sm} = \frac{1}{\mathrm{Tr}\, Q^{\rm obs}} \left(X_{\alpha\beta} - \chi_\alpha^{\rm obs}\, x_\beta\right), \tag{3.25}$$

$$X_{\alpha\beta} = \int \mathrm{d}^2\varphi\, I^{\rm obs}(\boldsymbol{\varphi}) \left[\left(W + \frac{2\varphi^2}{\sigma^2}\, W'\right)\delta_{\alpha\beta} + \frac{\eta_\alpha(\boldsymbol{\varphi})\eta_\beta(\boldsymbol{\varphi})}{\sigma^4}\, W''\right], \tag{3.26}$$

$$x_\alpha = \int \mathrm{d}^2\varphi\, I^{\rm obs}(\boldsymbol{\varphi}) \left(2W' + \frac{\varphi^2}{\sigma^2}\, W''\right) \frac{\eta_\alpha(\boldsymbol{\varphi})}{\sigma^2} \, . \tag{3.27}$$

Here $\delta_{\alpha\beta}$ is the Kronecker symbol, and $\eta_1(\boldsymbol{\varphi}) = \varphi_1^2 - \varphi_2^2$ and $\eta_2(\boldsymbol{\varphi}) = 2\varphi_1\varphi_2$. The linear response of the ellipticity to an anisotropy in the PSF is described by the *smear polarisability*, $P_{\alpha\beta}^{\rm sm}$. Note that the ellipticities of larger images are less affected by the anisotropy than the ones of smaller images, since the previously defined correction factor $P_{\alpha\beta}^{\rm sm}$ is divided by $\mathrm{Tr}\, Q^{\rm obs}$, which becomes the larger the larger the image gets.

In order to make use of equation (3.24), one has to determine the q_α. These can be measured directly from the stars in the images, since stars are intrinsically round and not affected by lensing. Thus their $\chi_\alpha^{*,\rm iso} = 0$, and from (3.24) one obtains

$$q_\alpha = (P^{*,\rm sm})_{\alpha\beta}^{-1}\, \chi_\beta^{*,\rm obs} \, . \tag{3.28}$$

Since the PSF in the coadded WFI@2.2 images varies smoothly over the field of view and over the chip boundaries (see Fig. 2.4), a two-dimensional polynomial can be fitted to q. Thus the anisotropy at any given position in the field is known, and the ellipticities can be individually corrected for it.

Correcting for isotropic PSF smearing The isotropic smearing of a PSF has a circularising effect on the ellipticity of galaxy images, diluting the imprinted shear signal. In the following a correction for this effect is derived. In addition, an effective PSF $\hat{P}$ is introduced which contains the gravitational shear as an anisotropic component, thus the previously found relations can be applied. Combining this result with the one obtained above yields a first order correction for PSF anisotropies and isotropic PSF smearing, and allows for the evaluation of the reduced shear g.

Using the locally linearised lens mapping (1.73), the lensed image without any PSF reads $I(\boldsymbol{\theta}) = I^{\rm s}(\boldsymbol{A\theta})$. One can then relate the lensed and isotropically blurred image $I^{\rm iso}$ to the source $I^{\rm s}$ as

$$\begin{aligned} I^{\rm iso}(\boldsymbol{\theta}) &= \int {\rm d}^2\varphi\, I^{\rm s}(\boldsymbol{A\theta})\, P^{\rm iso}(\boldsymbol{\theta}-\boldsymbol{\varphi}) && (3.29)\\ &= (\det\boldsymbol{A})^{-1} \int {\rm d}^2\zeta\, I^{\rm s}(\boldsymbol{\zeta})\, P^{\rm iso}(\boldsymbol{\theta}-\boldsymbol{A}^{-1}\boldsymbol{\zeta}) && (3.30)\\ &=: \hat{I}(\boldsymbol{A\theta})\,, && (3.31) \end{aligned}$$

where

$$\begin{aligned} \hat{I}(\boldsymbol{\theta}) &= \int {\rm d}^2\varphi\, I^{\rm s}(\boldsymbol{\varphi})\hat{P}(\boldsymbol{\theta}-\boldsymbol{\varphi})\,, && (3.32)\\ \hat{P}(\boldsymbol{\theta}) &:= (\det\boldsymbol{A})^{-1} P^{\rm iso}(\boldsymbol{A}^{-1}\boldsymbol{\theta})\,. && (3.33) \end{aligned}$$

Calculating the $\hat{Q}_{ij}$ from $\hat{I}$ gives

$$\begin{aligned} \hat{Q}_{ij} &= \int {\rm d}^2\beta\, \beta_i\beta_j\, \hat{I}(\boldsymbol{\beta})\, W\left(\frac{\beta^2}{\hat{\sigma}^2}\right) && (3.34)\\ &= \det\boldsymbol{A}\, A_{ik}A_{jl} \int {\rm d}^2\theta\, \theta_k\theta_l\, I^{\rm iso}(\boldsymbol{\theta})\, W\left(\frac{\theta^2-\delta_\alpha\,\eta_\alpha(\boldsymbol{\theta})}{\sigma^2}\right), \end{aligned}$$

where $\hat{\sigma}^2 = (1-\kappa)^2(1+|g|^2)\,\sigma^2$, and $\delta := 2g/(1+|g|^2)$. For small δ the weighting function can be replaced by a Taylor series up to first order, which then yields an expression between $\hat{\chi}$ and $\chi^{\rm iso}$,

$$\hat{\chi}_\alpha = \chi^{\rm iso}_\alpha - C_{\alpha\beta}\, g_\beta\,. \qquad (3.35)$$

In this relation the following definitions were used,

$$\begin{aligned} C_{\alpha\beta} &= 2\delta_{\alpha\beta} - 2\chi^{\rm obs}_\alpha\chi^{\rm obs}_\beta + \frac{2}{{\rm Tr}\,Q^{\rm obs}}\left(B_{\alpha\beta} - \chi^{\rm obs}_\alpha L_\beta\right)\\ B_{\alpha\beta} &= \int {\rm d}^2\theta\, I^{\rm obs}(\boldsymbol{\theta})\, W'\left(\frac{\theta^2}{\sigma^2}\right)\frac{\eta_\alpha(\boldsymbol{\theta})\,\eta_\beta(\boldsymbol{\theta})}{\sigma^2}\\ L_\alpha &= \int {\rm d}^2\theta\, I^{\rm obs}(\boldsymbol{\theta})\, W'\left(\frac{\theta^2}{\sigma^2}\right)\frac{\theta^2\,\eta_\alpha(\boldsymbol{\theta})}{\sigma^2}\,. \qquad (3.36) \end{aligned}$$

$C_{\alpha\beta}$ is called the *shear polarisability*. In principle it should be calculated from $I^{\rm iso}$ instead of $I^{\rm obs}$, but due to the smallness of q the difference between $C^{\rm iso}_{\alpha\beta}\,g_\beta$ and $C^{\rm obs}_{\alpha\beta}\,g_\beta$ in (3.35) is neglected, since g is also small. Thus the shear polarisability can be calculated from the observed light profile, as was the case for the smear polarisability.

In full analogy to the correction of PSF anisotropies, $\hat{P}$ is split into an isotropic and an anisotropic part (the shear). One finds

$$\begin{aligned} \hat{P}(\boldsymbol{\theta}) &= \int {\rm d}^2\varphi\, \hat{P}^{\rm iso}(\boldsymbol{\varphi})\, \hat{q}(\boldsymbol{\theta}-\boldsymbol{\varphi}) && (3.37)\\ \hat{I}^0(\boldsymbol{\theta}) &= \int {\rm d}^2\varphi\, I^{\rm s}(\boldsymbol{\varphi})\, \hat{P}^{\rm iso}(\boldsymbol{\theta}-\boldsymbol{\varphi}) && (3.38)\\ \hat{I}(\boldsymbol{\theta}) &= \int {\rm d}^2\varphi\, \hat{I}^0(\boldsymbol{\varphi})\, \hat{q}(\boldsymbol{\theta}-\boldsymbol{\varphi})\,, && (3.39) \end{aligned}$$

thus the relation between $\hat{I}$ and $\hat{I}^0$ is the same as between $I^{\rm obs}$ and $I^{\rm iso}$, and the ellipticities become

$$\hat{\chi}^0_\alpha = \hat{\chi}_\alpha - \hat{P}^{\rm sm}_{\alpha\beta}\,\hat{q}_\beta\,. \tag{3.40}$$

Again one makes use of the fact that $\hat{q}$ is small, so are the differences between $I^{\rm obs}$, $I^{\rm iso}$ and $\hat{I}$. Continuing the first-order approximation, the $\hat{P}^{\rm sm}$ can be calculated from $I^{\rm obs}$ instead of $\hat{I}$, and thus $\hat{P}^{\rm sm} = P^{\rm sm}$ is expressed in terms of observables, too.

The $\hat{\chi}_\alpha$ can be eliminated by combining equations (3.35) and (3.40),

$$\chi^{\rm iso}_\alpha = \hat{\chi}^0_\alpha + C_{\alpha\beta}\,g_\beta + P^{\rm sm}_{\alpha\beta}\,\hat{q}_\beta\,. \tag{3.41}$$

As for the true PSF anisotropies q, a relation for the shear-induced $\hat{q}$ and the reduced shear g can be inferred from this equation from stellar sources, since their $\hat{\chi}^0$ and $\chi^{\rm iso}$ vanish,

$$\hat{q}_\alpha = -(P^{*,{\rm sm}})^{-1}_{\alpha\beta}\,C^*_{\beta\gamma}\,g_\gamma\,. \tag{3.42}$$

With this result at hand, and combining it with equations (3.24) and (3.28) from the anisotropy correction, one finally obtains the full correction as

$$\hat{\chi}^0_\alpha = \chi^{\rm obs}_\alpha - P^{\rm sm}_{\alpha\beta}\,q_\beta - P^{\rm g}_{\alpha\beta}\,g_\beta \tag{3.43}$$

with

$$q_\beta \;=\; (P^{*,{\rm sm}})^{-1}_{\beta\gamma}\,\chi^{*,{\rm obs}}_\gamma\,, \tag{3.44}$$

$$P^{\rm g}_{\alpha\beta} \;=\; C_{\alpha\beta} - P^{\rm sm}_{\alpha\gamma}(P^{*,{\rm sm}})^{-1}_{\gamma\delta}\,C^*_{\delta\beta}\,. \tag{3.45}$$

Quantities with an asterisk * are calculated from stellar sources. It was shown by Hoekstra et al. (1998) that the correction factors obtained from stars should better be calculated with the same scale σ in the weight function as is used for an individual galaxy, although the formalism here does not imply such a necessity. Thus, for practical purposes, a set of correction factors is calculated for a sample of ≈ 10 different weighting scales. The closest match for a particular galaxy is then selected for the correction.

Practical shear estimate An estimate of the reduced shear g is obtained by inverting (3.43). In matrix notation,

$$g = (P^{\rm g})^{-1}(\chi^{\rm obs} - P^{\rm sm}q) - (P^{\rm g})^{-1}\hat{\chi}^0. \tag{3.46}$$

Since $\hat{\chi}^0$ is dominated by the intrinsic ellipticity of the galaxy, this measure for g is very noisy. Since $\left\langle (P^{\rm g})^{-1}\hat{\chi}^0 \right\rangle \approx 0$ (Erben et al., 2001),

$$\langle g \rangle = \left\langle (P^{\rm g})^{-1}(\chi^{\rm obs} - P^{\rm sm}q) \right\rangle \tag{3.47}$$

is an unbiased estimator of the reduced shear.

A further simplification of this formalism is the approximation of the matrix approach with a scalar description, i.e. $P^{\rm sm}_{\alpha\beta} \approx \frac{1}{2}\,\delta_{\alpha\beta}\,{\rm Tr}\,(P^{\rm sm})$ and $P^{\rm g}_{\alpha\beta} \approx \frac{1}{2}\,\delta_{\alpha\beta}\,{\rm Tr}\,(P^{\rm g})$ (see Erben et al., 2001). The scalar correction is found to yield slightly less noisy results than the full matrix approach.

3.2 Using weak shear for cluster detection

As was illustrated in Fig. 3.1, the tidal gravitational field of a cluster-sized mass concentration induces a coherent distortion pattern into the images of distant background galaxies. By scanning the field for such characteristic distortion patterns one can detect mass concentrations directly, irrespective of their luminosity (see Erben et al., 2000; Umetsu & Futamase, 2000; Wittman et al., 2001; Schirmer et al., 2003, for examples). However, the total mass of such clusters inside a given aperture can not be determined from shear information alone due to the invariance $g' = g$ under the transformation (1.82) in the lens mapping. A quantity related to the total mass, however, is the difference in the mean mass inside a circle with radius θ_1 and inside an outer ring with $\theta_1 \leq r \leq \theta_2$. Thus an additive constant to κ (see equation (1.81)) is eliminated. This measure is known as the ζ-statistics,

$$\zeta(\boldsymbol{\theta}; \theta_1, \theta_2) := \bar{\kappa}(\boldsymbol{\theta}; 0, \theta_1) - \bar{\kappa}(\boldsymbol{\theta}; \theta_1, \theta_2)\,, \tag{3.48}$$

suggested by Kaiser (1995). Calculating such a quantity on a grid that has been laid over a data field immediately picks out overdense and underdense regions of various sizes, depending on the filter scale. A great advantage of such a statistics is that the same measure, applied to mock catalogs with randomised ellipticities, yields a direct handle on the S/N ratio and thus the reliability of a particular cluster detection. If, in addition to the detection S/N, the cluster redshift is available, an estimate for the cluster's total mass can be obtained.

3.2.1 $M_{\rm ap}$-statistics

For the purpose of this work a generalised version of the ζ-statistics is used, i.e. the *aperture mass statistics* $M_{\rm ap}$, introduced by Schneider (1996). $M_{\rm ap}$ is a filtered integral of κ inside an aperture at a given position $\boldsymbol{\theta}_0$,

$$M_{\rm ap}(\boldsymbol{\theta}_0) = \int \mathrm{d}^2\theta\, \kappa(\boldsymbol{\theta} + \boldsymbol{\theta}_0)\, U(\theta)\,, \tag{3.49}$$

where $U(\theta) \equiv U(|\boldsymbol{\theta}|)$ is a radially symmetric filter function. For

$$U(\theta) = \begin{cases} (\pi\theta_1^2)^{-1} & 0 \leq \theta \leq \theta_1 \\ \left[\pi(\theta_1^2 - \theta_2^2)\right]^{-1} & \theta_1 < \theta \leq \theta_2 \\ 0 & \theta_2 < \theta \end{cases} \tag{3.50}$$

the $M_{\rm ap}$-statistics is identical with the ζ-statistics.

Expressing $M_{\rm ap}$ in terms of shear In the above form $M_{\rm ap}$ is not particularly useful for practical purposes since κ is not directly observable. However, Schneider (1996) showed that $M_{\rm ap}$ can be expressed in terms of γ when substituting κ with the inversion given in equation (1.81),

$$\begin{aligned} M_{\rm ap}(\boldsymbol{\theta}_0) &= \frac{1}{\pi} \int \mathrm{d}^2\theta\; U(\theta)\, \mathrm{Re}\left(\int \mathrm{d}^2\theta'\, \gamma(\boldsymbol{\theta}')\, D^*(\boldsymbol{\theta} + \boldsymbol{\theta}_0 - \boldsymbol{\theta}') \right) + \\ &+ \frac{1}{\pi}\, \kappa_0 \int \mathrm{d}^2\theta\, U(\theta)\,. \end{aligned} \tag{3.51}$$

This relation allows for the elimination of the additive constant κ_0 if the filter function U is chosen to be *compensated*, i.e.

$$\int \mathrm{d}^2\theta\, U(\theta) = \int_0^{2\pi} \mathrm{d}\varphi \underbrace{\int_0^\infty \mathrm{d}\theta\, \theta\, U(\theta)}_{=0} = 0\,. \tag{3.52}$$

Substituting

$$\boldsymbol{\varphi} := \boldsymbol{\theta}' - \boldsymbol{\theta}_0 \;\;,\quad \Theta := \theta_1 + \mathrm{i}\theta_2 = \theta\,\mathrm{e}^{\mathrm{i}\,\eta} \;\;,\quad \Phi := \varphi_1 + \mathrm{i}\varphi_2 = \varphi\,\mathrm{e}^{\mathrm{i}\,\alpha}\,, \tag{3.53}$$

and using $D(\boldsymbol{\theta}) = -1/(\Theta^*)^2$, equation (3.51) becomes

$$\begin{aligned} M_{\mathrm{ap}}(\boldsymbol{\theta}_0) &= \frac{-1}{\pi}\,\mathrm{Re}\left(\int \mathrm{d}^2\varphi\,\gamma(\boldsymbol{\varphi}+\boldsymbol{\theta}_0)\int \mathrm{d}^2\theta\, U(\theta)\,\frac{1}{(\Theta-\Phi)^2}\right) \\ &= \frac{-1}{\pi}\,\mathrm{Re}\left(\int \mathrm{d}^2\varphi\,\gamma(\boldsymbol{\varphi}+\boldsymbol{\theta}_0)\int_0^\infty \mathrm{d}\theta\,\theta\, U(\theta)\int_0^{2\pi}\frac{\mathrm{d}\eta}{(\Theta-\Phi)^2}\right)\,. \end{aligned} \tag{3.54}$$

Changing the integration variable in the last integral from η to Θ, keeping θ fixed, yields $\mathrm{d}\eta = -\mathrm{i}\,\mathrm{d}\Theta/\Theta$. This corresponds to an integration around the unit circle in the complex number plane. The integrand then has two poles at $\Theta = 0$ and $\Theta = \Phi$, with residues of $-\mathrm{i}/\Phi^2$ and i/Φ^2, respectively. If the second pole lies inside the loop, i.e. $\theta > \varphi$, then the integral evaluates to zero since the two residues cancel each other. If $\theta < \varphi$, only the first residue contributes to the integral, yielding a non-zero value. For $\theta = \varphi$ the integration path cuts the second pole, yielding a delta function. Thus,

$$\int \frac{-\mathrm{i}\,\mathrm{d}\Theta}{\Theta(\Theta-\Phi)^2} = \frac{\pi}{\Phi^2}\left[2H(\varphi-\theta) - \varphi\,\delta_{\mathrm{Dirac}}(\varphi-\theta)\right]\,, \tag{3.55}$$

where H is the Heaviside function, combining the cases $\theta > \varphi$ and $\theta < \varphi$. In the following, the last two integrals in (3.54) become

$$\begin{aligned} &\int_0^\infty \mathrm{d}\theta\,\theta\, U(\theta)\,\frac{\pi}{\Phi^2}\left[2H(\varphi-\theta) - \varphi\,\delta_{\mathrm{Dirac}}(\varphi-\theta)\right] = \\ &= \int_0^\varphi \mathrm{d}\theta\,\theta\, U(\theta)\,\frac{2\pi}{\Phi^2} - \varphi^2 U(\varphi)\frac{\pi}{\Phi^2} = \\ &= \frac{\pi\varphi^2}{\Phi^2}\left(\frac{2}{\varphi^2}\int_0^\varphi \mathrm{d}\theta\,\theta\, U(\theta) - U(\varphi)\right)\,. \end{aligned} \tag{3.56}$$

Thus, M_{ap} can be written as

$$\begin{aligned} M_{\mathrm{ap}}(\boldsymbol{\theta}_0) &= \int \mathrm{d}^2\varphi\left[-\varphi^2\,\mathrm{Re}\left(\frac{\gamma(\boldsymbol{\varphi}+\boldsymbol{\theta}_0)}{\Phi^2}\right)\right]\left(\frac{2}{\varphi^2}\int_0^\varphi \mathrm{d}\theta\,\theta\, U(\theta) - U(\varphi)\right) \\ &= \int \mathrm{d}^2\varphi\;\gamma_{\mathrm{t}}(\boldsymbol{\varphi};\boldsymbol{\theta}_0)\;Q(\varphi)\,. \end{aligned} \tag{3.57}$$

Here the *tangential shear* γ_{t} at position $\boldsymbol{\varphi}$ relative to the point $\boldsymbol{\theta}_0$ was defined as

$$\begin{aligned} \gamma_{\mathrm{t}}(\boldsymbol{\varphi};\boldsymbol{\theta}_0) &= -\varphi^2\,\mathrm{Re}\left(\frac{\gamma(\boldsymbol{\varphi}+\boldsymbol{\theta}_0)}{\Phi^2}\right) \\ &= -\mathrm{Re}\left(\gamma\,\mathrm{e}^{-2\mathrm{i}\alpha}\right) \\ &= -\left(\gamma_1\cos 2\alpha + \gamma_2\sin 2\alpha\right)\,, \end{aligned} \tag{3.58}$$

and the new filter function Q is

$$Q(\varphi) = \frac{2}{\varphi^2} \int_0^{\varphi} \mathrm{d}\theta\, \theta\, U(\theta) - U(\varphi)\ . \tag{3.59}$$

Thus $M_{\rm ap}$ can be expressed in terms of the tangential shear with an appropriately chosen filter function. It can be calculated from a finite field if Q becomes zero beyond a certain radius. Note that $\gamma_{\rm t}$ is undefined if $\boldsymbol{\varphi} = 0$, i.e. when the position where $\gamma_{\rm t}$ is to be measured coincides with $\boldsymbol{\theta}_0$.

3.2.2 *S*-statistics and an optimal filter *Q*

***S*-Statistics** It was shown above that by means of the $M_{\rm ap}$-statistics mass concentrations can be found. Apart from the fact that U should be compensated, no further constraints were imposed on U and Q. In the following, various suggestions for the filter functions Q are presented, followed by an analysis of their effectiveness in detecting mass concentrations.

Schneider (1996) showed that the variance of $M_{\rm ap}$ for the unlensed case, respectively the weak lensing regime, is given by

$$\sigma^2_{M_{\rm ap}} = \frac{\pi\sigma_\varepsilon^2}{n} \int_0^{\theta} \mathrm{d}\vartheta\, \vartheta\, Q^2(\vartheta)\,, \tag{3.60}$$

where σ_ε is the ellipticity dispersion and n the number density of background galaxies. The integration is performed over a finite interval since it is assumed that $Q \equiv 0$ for $\vartheta > \theta$. For the application to real data this integral has to be replaced by a sum over individual galaxies. Section 3.2.4 contains the derivation of the corresponding expressions.

With the $\sigma^2_{M_{\rm ap}}$ at hand one defines the *S-statistics*, or the S/N for $M_{\rm ap}$,

$$S(\theta;\boldsymbol{\theta}_0) = \sqrt{\frac{n}{\pi\,\sigma_\varepsilon^2}}\, \frac{\int_0^{\theta} \mathrm{d}^2\vartheta\, \gamma_{\rm t}(\boldsymbol{\vartheta};\boldsymbol{\theta}_0)\, Q(\vartheta)}{\sqrt{\int_0^{\theta} \mathrm{d}\vartheta\, \vartheta\, Q^2(\vartheta)}}\ . \tag{3.61}$$

In the following, $\boldsymbol{\theta}_0$ denotes the position at which $M_{\rm ap}$, respectively the S-statistics, is evaluated. θ gives the size of the aperture, and ϑ measures the distance inside this aperture from its centre at $\boldsymbol{\theta}_0$.

An optimal filter Q The filter function Q that guarantees the highest possible S/N can be derived directly from the S-statistics in (3.61). Assuming a radially symmetric density profile for the dark matter halo, and dropping the constant pre-factor, (3.61) becomes

$$S(\theta) = \frac{\int_0^{\theta} \mathrm{d}\vartheta\, \vartheta\, \gamma_{\rm t}(\vartheta)\, Q(\vartheta)}{\sqrt{\int_0^{\theta} \mathrm{d}\vartheta\, \vartheta\, Q^2(\vartheta)}}\ . \tag{3.62}$$

Using the variational principle, an optimal choice for Q can be derived. Assuming a fixed aperture size ($\delta\theta = 0$), an infinitely small variation δQ leads to a variation δS,

$$\delta S(Q,\theta) = \frac{\partial S}{\partial Q}\,\delta Q + \frac{\partial S}{\partial \theta}\,\delta\theta = \frac{\partial S}{\partial Q}\,\delta Q\ . \tag{3.63}$$

S is extreme if $\delta S = 0$,

$$\begin{aligned}
\delta S &= \frac{\partial}{\partial Q} \frac{\int_0^\theta \mathrm{d}\vartheta\, \vartheta\, \gamma_\mathrm{t}(\vartheta)\, Q(\vartheta)}{\sqrt{\int_0^\theta \mathrm{d}\vartheta\, \vartheta\, Q^2(\vartheta)}}\, \delta Q \\
&= \frac{\sqrt{\int_0^\theta \mathrm{d}\vartheta\, \vartheta\, Q^2(\vartheta)}\ \int_0^\theta \mathrm{d}\vartheta\, \vartheta\, \gamma_\mathrm{t}(\vartheta)\ - \int_0^\theta \mathrm{d}\vartheta\, \vartheta\, \gamma_\mathrm{t}(\vartheta)\, Q(\vartheta)\ \frac{\int_0^\theta \mathrm{d}\vartheta\, \vartheta\, Q(\vartheta)}{\sqrt{\int_0^\theta \mathrm{d}\vartheta\, \vartheta\, Q^2(\vartheta)}}}{\int_0^\theta \mathrm{d}\vartheta\, \vartheta\, Q^2(\vartheta)}\, \delta Q \\
&= 0\,. \qquad (3.64)
\end{aligned}$$

This is satisfied if the numerator in the last equation vanishes,

$$\int_0^\theta \mathrm{d}\vartheta\, \vartheta\, Q^2(\vartheta)\ \int_0^\theta \mathrm{d}\vartheta\, \vartheta\, \gamma_\mathrm{t}(\vartheta) = \int_0^\theta \mathrm{d}\vartheta\, \vartheta\, \gamma_\mathrm{t}(\vartheta)\, Q(\vartheta)\ \int_0^\theta \mathrm{d}\vartheta\, \vartheta\, Q(\vartheta) \qquad (3.65)$$

By comparing the integrands in the last expression, one immediately finds that

$$Q(\vartheta) \propto \gamma_\mathrm{t}(\vartheta) \qquad (3.66)$$

solves the problem, and thus extremises S. This result is intuitively clear, since a signal with a certain shape is best picked up by a similar filter function. The same conclusion was derived by Schneider (1996) in a different way, using the Cauchy-Schwarz inequality.

Still, the exact radial tangential shear profile of a given cluster is not known a priori. This means that a generic filter function will not detect a particular dark matter halo with the highest possible S/N. However, in general it should be as effective as possible. In the following a selection of filter functions Q is discussed.

3.2.3 A sample of filter functions

In the following various filters $U(x)$ and $Q(x)$ are presented, with $x := \vartheta/\theta$. Here ϑ is the projected angular distance on the sky from the aperture centre, normalised by the aperture radius θ. By varying θ, shear patterns respectively dark matter haloes of different extent can be detected.

If M_ap is evaluated close to the border of an image, the aperture covers only part of the data field and thus does no longer give a correct result for M_ap in the sense of its definition in (3.49). Actually, this is the case for virtually all fields and most of the filter scales used in this work. The typical apertures used have diameters of $5'$ - $25'$ and more, compared to an image size of just about $34' \times 34'$. Besides, holes of significant size are spread across the galaxy distribution due to the masking of bright stars which are present in every image (see also Sect. 3.5). Thus, only in a few cases M_ap can be evaluated in its original sense.

Unaffected by this, however, is the capability of M_ap to detect correlated shear patterns in the field, including a S/N-estimate according to (3.62). Hereafter M_ap, respectively the S-statistics, is used in this sense only. This also gives greater freedom in the search of a filter function Q, irrespective of U, which is best suited for the detection of coherent shear patterns.

Polynomial filter function Q In Schneider (1996) it is argued that a filter function that closely follows the tangential shear profile has some disadvantages. First, in the inner part of a cluster the shapes of faint background galaxies can not be measured (reliably) due to the presence of the extended bright cluster galaxies. Besides, these regions of such a cluster may no longer be described by the weak lensing regime. Thus, a better choice for Q follows the tangential shear profile only for larger radii, whereas it drops to zero for small radii, downweighting the troublesome areas. This also takes into account the fact that the tangential shear is undefined for a galaxy at the filter centre. Second, Q has to go to zero (or be very close to zero) at the outer edge of the aperture, so that $M_{\rm ap}$ can be calculated from a finite field. This also ensures that a small shift of $\boldsymbol{\theta}_0$ does not give too much weight to the new galaxies which enter the aperture, leading to high-frequency but low amplitude patterns in the resulting S/N map.

The following filter function U is suggested in Schneider (1996) which satisfies these constraints,

$$U_{\rm S96}(x) = \begin{cases} 1 & \text{for} \quad 0 \le x < \nu_1 \\ \left[\nu_1 \left[(x-\nu_1)^2 + \nu_1^2\right]^{-\frac{1}{2}} - c\right] / (1-c) & \text{for} \quad \nu_1 \le x < \nu_2 \\ b\,(1-x)^2\,(x-\alpha) & \text{for} \quad \nu_2 \le x \le 1 \end{cases} . \tag{3.67}$$

The constants α, b, c are determined requiring smoothness and continuity at $x = \nu_1$ and $x = \nu_2$. They can be evaluated analytically, but are rather cumbersome and not needed for further understanding. The same holds for $Q_{\rm S96}$, which can be constructed piecewise from $U_{\rm S96}$. Instead of writing it down, the graphical representation of $Q_{\rm S96}$ in Fig. 3.2 provides better insight than its analytical expression for a given set of parameters.

In Schneider et al. (1998) these filter functions are replaced by conceptually much simpler polynomials,

$$U_{\rm POLY}(x) = \frac{(l+2)^2}{\pi\,\theta^2}\,(1-x^2)^l\,\left(\frac{1}{l+2} - x^2\right)\,H(1-x)\,, \tag{3.68}$$

$$Q_{\rm POLY}(x) = \frac{(1+l)(2+l)}{\pi\,\theta^2}\,x^2\,(1-x^2)^l\,H(1-x)\,. \tag{3.69}$$

H is the Heaviside step function, so that $U(x) = 0 = Q(x)$ for $x > 1$. It is shown in Fig. 3.6 in the following section that polynomial filters with $l > 1$ do not yield improved results compared to the $l = 1$ case.

An exponential filter function Q A disadvantage of $U_{\rm S96}$ and $U_{\rm POLY}$, and thus the corresponding functions Q, is the strong compensation of U, i.e. the amplitude where U is negative is comparable to the amplitude where U is positive. Thus, if one has a cluster at the centre of U, and a second cluster in the compensated (negative) filter area, the $M_{\rm ap}$ signal of the first cluster gets diluted by the second one. Furthermore, this yields artificially low values of $M_{\rm ap}$, respectively the S-statistics, around a cluster position. A possible solution is to flatten the negative part of U, and extend it to much larger radii to satisfy the compensation criterium, and then calculate Q from it. For example, such a filter function can be constructed from the difference of two Gaussians,

$$U_{\rm EXP}(x) = e^{-16\,x^2} - \frac{1}{4}\,e^{-4x^2}\,, \tag{3.70}$$

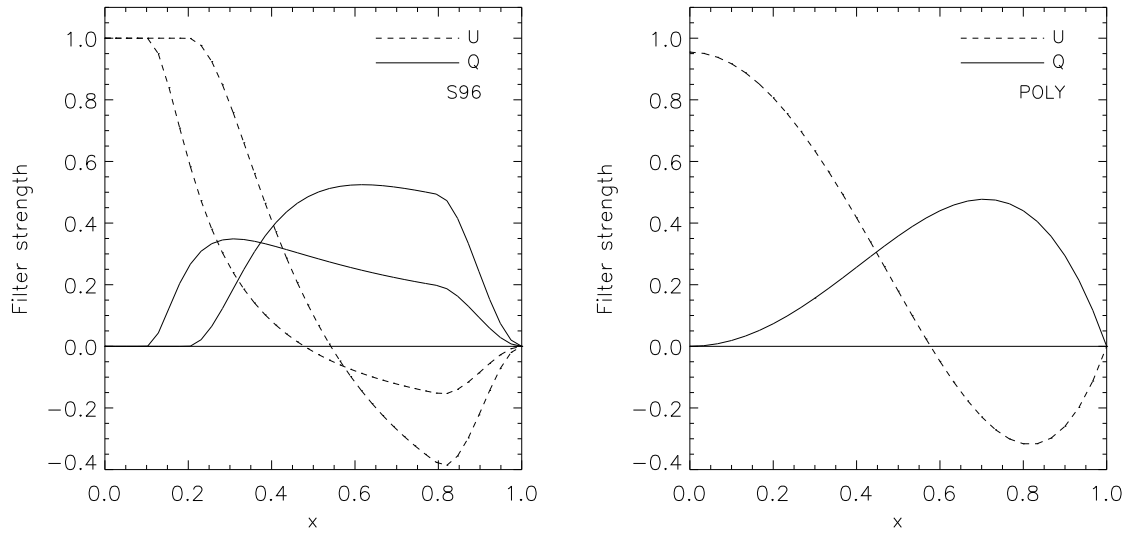

Figure 3.2: Left panel: filters according to Schneider (1996). Two examples with ($\nu_1 = 0.1$, $\nu_2 = 0.8$) and ($\nu_1 = 0.2$, $\nu_2 = 0.8$) are plotted in order to show the variety of curves. Right panel: the polynomial filters ($l = 1$).

$$Q_{\rm EXP}(x) = -\left(1 + \frac{1}{16\,x^2}\right)\, e^{-16\,x^2} + \left(\frac{1}{4} + \frac{1}{16\,x^2}\right)\, e^{-4\,x^2}\,. \tag{3.71}$$

This filter extends formally to infinity, but is limited by the finite size of the data field. The numerical factors are chosen such that $Q(x)$ is close to zero for $x = 1$ (see Fig. 3.3). Q decreases as $\exp(-4x^2)$ for $x > 1$, so that the calculation of the S-statistics can in principle be restricted to a finite field for practical purposes, since galaxies at larger radii virtually do not contribute to the result. Furthermore $Q(0) = 0$, as one can see by expanding the two Gaussians into a Taylor series up to second order around $x = 0$.

Filters following the tangential shear profile As was shown in (3.66), an optimal filter function should resemble the tangential shear profile. In the following such a filter is constructed. Since the expressions involved are relatively complicated and thus slow down the computation process considerably, a simpler analytical formula is given, having a similar functional behaviour and effectiveness.

Navarro et al. (1997) introduced an universal density profile for clusters based on numerical simulations of the structure evolution of the dark matter in the universe. This radial *NFW profile* reads

$$\rho(r) = \frac{\rho_0(z, \Omega_0, \Omega_\Lambda, c)}{y\,(1+y)^2} \qquad \text{with} \quad y = r/r_{\rm s}\,, \tag{3.72}$$

where ρ_0 is a function of cosmology and contains a characteristic cluster density. y is the dimensionless radius, and $r_{\rm s} \approx 200$ kpc is a typical NFW scale radius for a galaxy cluster. Hereafter, ρ_0 is not considered any more since it becomes just a constant factor in Q, and therefore cancels in the S-statistics.

As was shown by Wright & Brainerd (2000) and Bartelmann (1996), the tangential shear

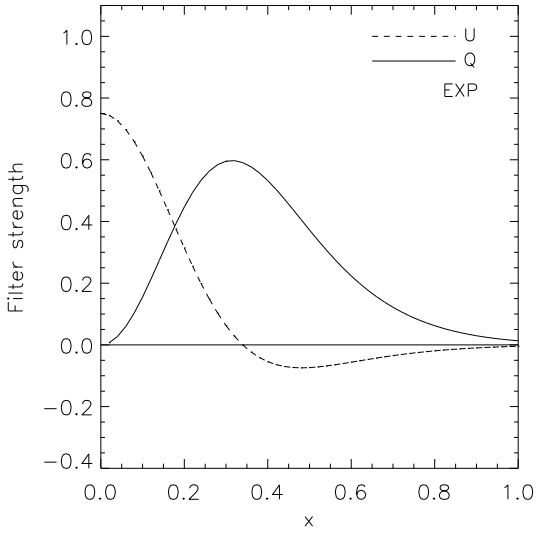

Figure 3.3: $Q_{\rm EXP}$, normalised for better comparison such that it occupies the same area as $Q_{\rm POLY}$ over the $[0,1]$ interval.

$\gamma_{\rm t}$ for the NFW profile can be written as

$$\gamma_{\rm t\,NFW}(y) = \begin{cases} \frac{4(3y^2-2)}{y^2(y^2-1)\sqrt{1-y^2}}\,\mathrm{arctanh}\sqrt{\frac{1-y}{1+y}} + \frac{4}{y^2}\ln\frac{y}{2} + \frac{2}{1-y^2} & \text{for} \quad y<1 \\ \frac{10}{3} - 4\ln 2 & \text{for} \quad y=1 \\ \frac{4(3y^2-2)}{y^2(y^2-1)\sqrt{y^2-1}}\,\arctan\sqrt{\frac{y-1}{1+y}} + \frac{4}{y^2}\ln\frac{y}{2} + \frac{2}{1-y^2} & \text{for} \quad y>1 \end{cases} . \tag{3.73}$$

This expression is smooth and continuous for $y = 1$, and approaches zero as $\ln(y)/y^2$ for $y > 1$. Based on equation (3.66), the optimal filter function is

$$Q_{\rm NFW}(x) \propto \gamma_{\rm t\,NFW}(x)\,, \tag{3.74}$$

where $x = \vartheta/\theta$ as defined at the beginning of this section. Due to the mathematical complexity of (3.73), the calculation of the S-statistics is rather time consuming. An approximating filter function with simpler mathematical form was found, producing similarly good results as $Q_{\rm NFW}$. It is given by

$$Q_{\rm TANH}(x) = \frac{\tanh(x)}{x}, \tag{3.75}$$

having a $1/x$ dependence for larger radii. The hyperbolic function was introduced to compensate the singularity at $x = 0$, yielding $Q_{\rm TANH}(0) = 1$.

Both $Q_{\rm NFW}$ and $Q_{\rm TANH}$ extend as $Q_{\rm EXP}$ formally to infinity, but they approach zero much slowlier than the latter. Furthermore, they give relatively large weight to a few galaxies at the centre of the aperture, which can lead to discontinuous fluctuations in the S-statistics when evaluated on a grid. Therefore, an exponential cut-off is introduced for very small radii, effectively making $Q(0) \approx 0$.

The density profiles of galaxy clusters can be very different from the ideal NFW profile as introduced above. Some greater flexibility in the design of the filter function is useful in this

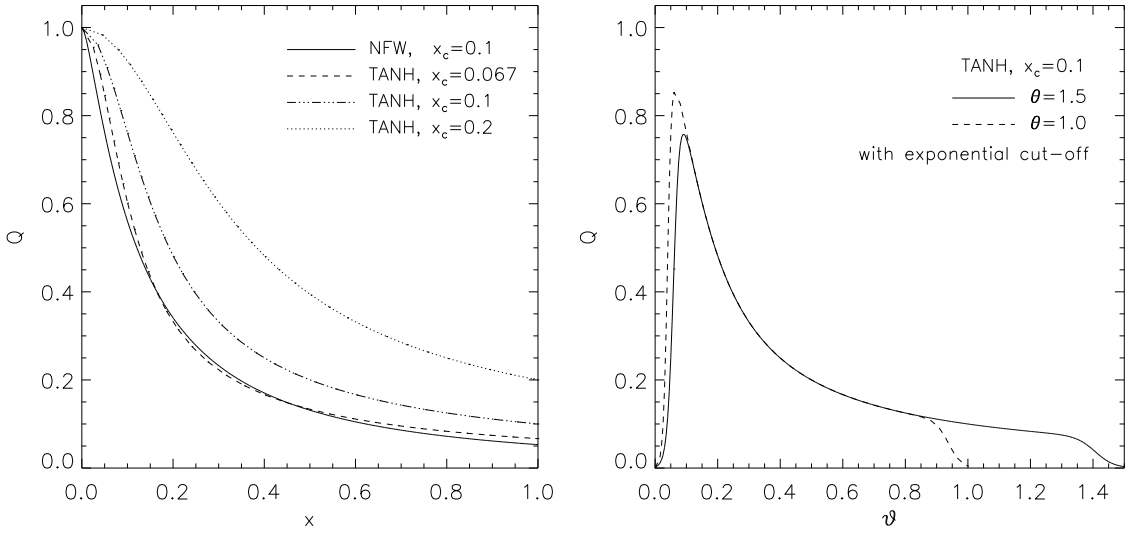

Figure 3.4: Left panel: $Q_{\rm NFW}$ (solid line), together with some of the simpler $Q_{\rm TANH}$. The exponential cut-off for small and large radii is not introduced in this plot in order to show the differences between the two filter types better. As can be seen, the TANH filter is a good approximation for the NFW, giving a bit more weight to smaller radii. Right panel: TANH filter with the cut-off at both ends, plotted against the radial coordinate ϑ. The dashed line ($\theta = 1$) can be compared directly to the dash-dotted line in the left panel. The combination of $x_{\rm c}$ with the aperture size θ yields a larger sample of available filter functions.

respect. For this purpose an exponential cut-off is introduced for larger radii too, together with a scaling parameter $x_{\rm c}$, yielding

$$Q(x) = \frac{1}{1 + {\rm e}^{a-bx} + {\rm e}^{-c+dx}}\, Q_{\rm NFW\,/\,TANH}(x/x_{\rm c})\ . \tag{3.76}$$

Hereafter, these filters are referred to as NFW and TANH, respectively. A choice of e.g. $a = 6$ and $b = 150$ lets Q drop to zero for the innermost part of the aperture. Choosing $c = 47$ and $d = 50$ makes $Q \approx 0$ around $x = 1$ (see right panel of Fig. 3.4). The filter shape remains unchanged for radii in between. The parameter $x_{\rm c}$ changes the width of the filter over the $[0, 1]$ interval, in the sense that more weight is put to smaller radii for smaller values of $x_{\rm c}$.

An example illustrates the greater flexibility. Without $x_{\rm c}$, only the aperture size θ controls the width of the filter. Introducing $x_{\rm c}$ alone has no effect, since twice the aperture size is compensated with a value of $x_{\rm c} = 0.5$. In conjunction with the exponential cut-off for $x \approx 1$ however, different filters can be created (right panel of Fig. 3.4), since this cut-off does not depend on $x_{\rm c}$. Thus, the TANH filter is constructed from the two-dimensional parameter space $(\theta\,, x_{\rm c}$. It turns out that this cut-off does not influence the efficiency of the filter in a negative way if the downweighting takes place on small scales only.

An analysis of the efficiency of the various filters is presented in section 3.2.5.

3.2.4 Tangential ellipticity and *S/N* estimation

Tangential ellipticity For practical purposes, the *tangential ellipticity* $\varepsilon_{\rm t}$ is defined in analogy to the tangential shear in equation (3.58). Geometrically speaking, $\varepsilon_{\rm t}$ is the ellipticity

component perpendicular to the line connecting an image at position $\boldsymbol{\theta} = (\theta_1, \theta_2)$ with a reference position $\boldsymbol{\theta}_0$ (typically the lens position). It is written as

$$\varepsilon_\mathrm{t} = -(\varepsilon_1 \cos 2\alpha + \varepsilon_2 \sin 2\alpha) \qquad \text{with} \qquad \alpha = \arctan \frac{\Delta\theta_2}{\Delta\theta_1}\,, \tag{3.77}$$

where $\Delta\theta_1 = \theta_1 - \theta_{01}$ and $\Delta\theta_2 = \theta_2 - \theta_{02}$. Alternatively,

$$\varepsilon_\mathrm{t} = -\,\frac{\varepsilon_1(\Delta\theta_1^2 - \Delta\theta_2^2) + 2\varepsilon_2\,\Delta\theta_1\,\Delta\theta_2}{\Delta\theta_1^2 + \Delta\theta_2^2}\,. \tag{3.78}$$

Note that ε_t is undefined if the distance between source position and reference position becomes zero. In the weak lensing case, the tangential ellipticity is an unbiased estimator of the tangential shear, $\gamma_\mathrm{t} = \langle\varepsilon_\mathrm{t}\rangle$.

***S/N* estimation** Kruse & Schneider (1999) and Schneider (1996) have shown that an estimate for the noise can be obtained directly from M_ap. In the discrete case, M_ap is given as a sum over the tangential ellipticities of N galaxies, multiplied by the filter function Q,

$$M_\mathrm{ap} = \frac{1}{n}\sum_{i=1}^{N} \varepsilon_{\mathrm{t}\,i}\; Q_i\,. \tag{3.79}$$

Here n is the number density of galaxies per square arcminute. The variance for M_ap is defined as

$$\sigma^2(M_\mathrm{ap}) = \left\langle {M_\mathrm{ap}}^2 \right\rangle - \langle M_\mathrm{ap}\rangle^2\ . \tag{3.80}$$

In the absence of lensing $\langle M_\mathrm{ap}\rangle = 0$, and

$$\sigma^2(M_\mathrm{ap}) = \frac{1}{n^2}\,\sum_{i,j} \langle \varepsilon_{\mathrm{t}\,i}\,\varepsilon_{\mathrm{t}\,j}\rangle\; Q_i\,Q_j = \frac{1}{n^2}\,\sum_i \left\langle {\varepsilon_{\mathrm{t}\,i}}^2\right\rangle\; {Q_i}^2\ . \tag{3.81}$$

This corresponds to a randomisation of the orientations of the galaxies, keeping their positions, and thus the Q_i, fixed (from a large number of such randomisations an estimate for σ^2 can be obtained, too). The $\varepsilon_{\mathrm{t}\,i}$ and $\varepsilon_{\mathrm{t}\,j}$ are mutually independent, and average to zero for $i \neq j$. Thus the summation is taken only over one index. With the definition (3.77) of ε_t,

$$\left\langle {\varepsilon_\mathrm{t}}^2\right\rangle = \left\langle {\varepsilon_1}^2\,\cos^2 2\alpha\right\rangle + \left\langle {\varepsilon_2}^2\,\sin^2 2\alpha\right\rangle + \langle \varepsilon_1\,\varepsilon_2 \sin 2\alpha\,\cos 2\alpha\rangle = \frac{1}{2}\,|\varepsilon|^2\ . \tag{3.82}$$

Hence,

$$\sigma^2(M_\mathrm{ap}) = \frac{1}{2n^2}\,\sum_i |\varepsilon_i|^2\,{Q_i}^2\,. \tag{3.83}$$

Due to the introduction of individual galaxy weighting factors at the end of section 3.1.1, M_ap and the S/N read a bit different,

$$M_\mathrm{ap} = \frac{\sum_i \varepsilon_{\mathrm{t}\,i}\,w_i\,Q_i}{\sum_i\,w_i}\,, \tag{3.84}$$

and

$$\sigma^2(M_\mathrm{ap}) = \frac{\sum_{i,j}\langle\varepsilon_{\mathrm{t}\,i}\,\varepsilon_{\mathrm{t}\,j}\rangle\;w_i\,w_j\,Q_i\,Q_j}{\left(\sum_i\,w_i\right)^2} = \frac{\sum_i |\epsilon_i|^2\,{w_i}^2\,{Q_i}^2}{2\,\left(\sum_i\,w_i\right)^2}\ . \tag{3.85}$$

Since the individual galaxy weights w_i and Q_i are constant for each galaxy, they drop out of the averaging process. The prefactor $1/n$ was omitted, too, since it cancels in the calculation of the final S/N.

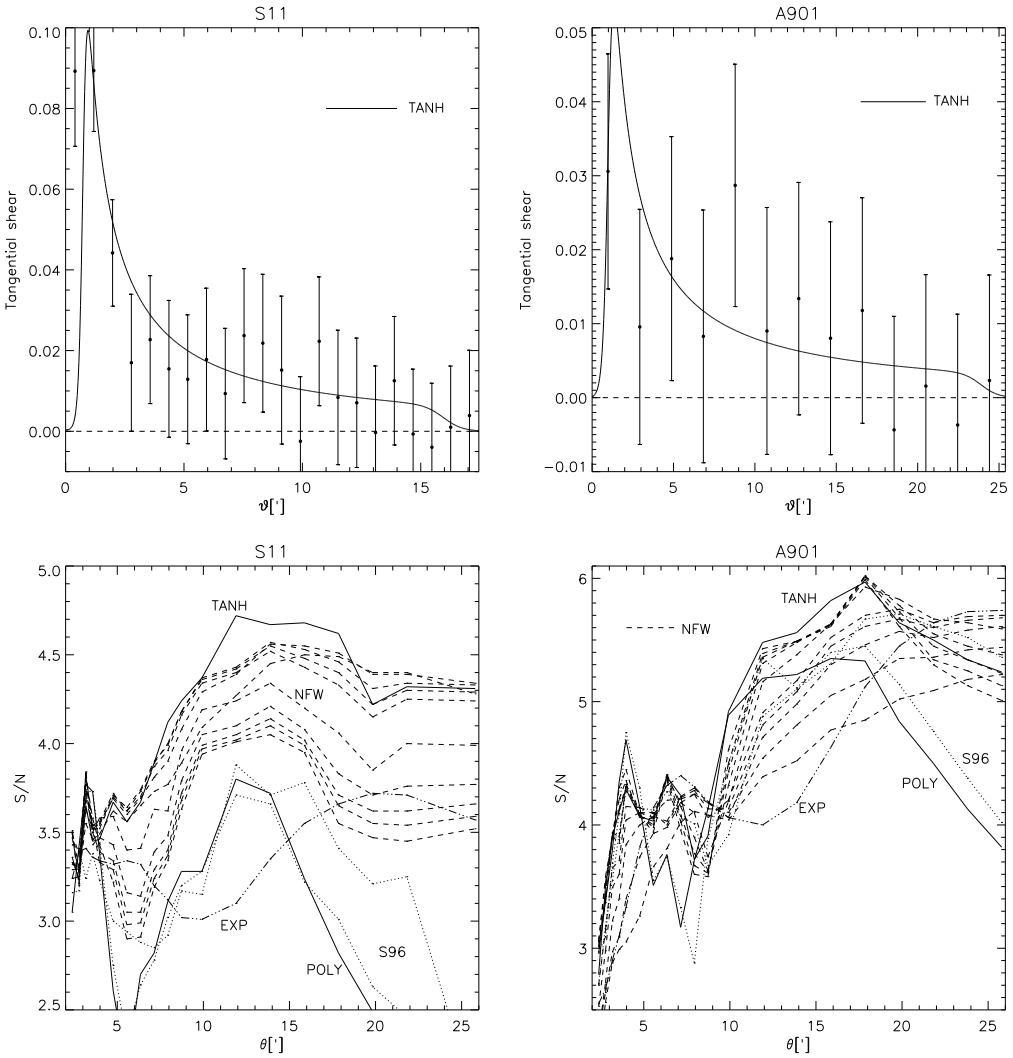

Figure 3.5: Tangential shear and S-profile for the two largest clusters in the survey data. In the upper row the tangential shear is shown, with the Q_{TANH} that yielded the highest S/N overlaid as a solid line. For better comparison the amplitude of Q_{TANH} was scaled so that it best fits the tangential shear. The error bars were decreased by a factor of 4 for better visualisation.
The lower row shows the S-profile of the two clusters for different filters Q. The NFW is plotted for 10 different $x_{\mathrm{c}} \in [0.01, 1.5]$. In case of S11 it is obvious that the NFW and the TANH filters yield much better results than filters EXP, POLY and S96. The detection with the TANH filter is about 50 times more robust than with the POLY filter (i.e. the difference between a 4.7σ and a 3.8σ detection). Both the best fitting NFW and TANH had $x_{rmc} = 0.05$. For A901 the result is similar, however the discrepancy between the filters is not as large, about a factor of 10 in robustness. Here $x_{rmc} = 0.5$ for both filters. Although the tangential shear is smaller for A901 than for S11, the S/N is higher due to the larger number density of galaxies with measured shapes ($n = 15$ arcmin^{-2} for S11, and $n = 24$ arcmin^{-2} for A901).

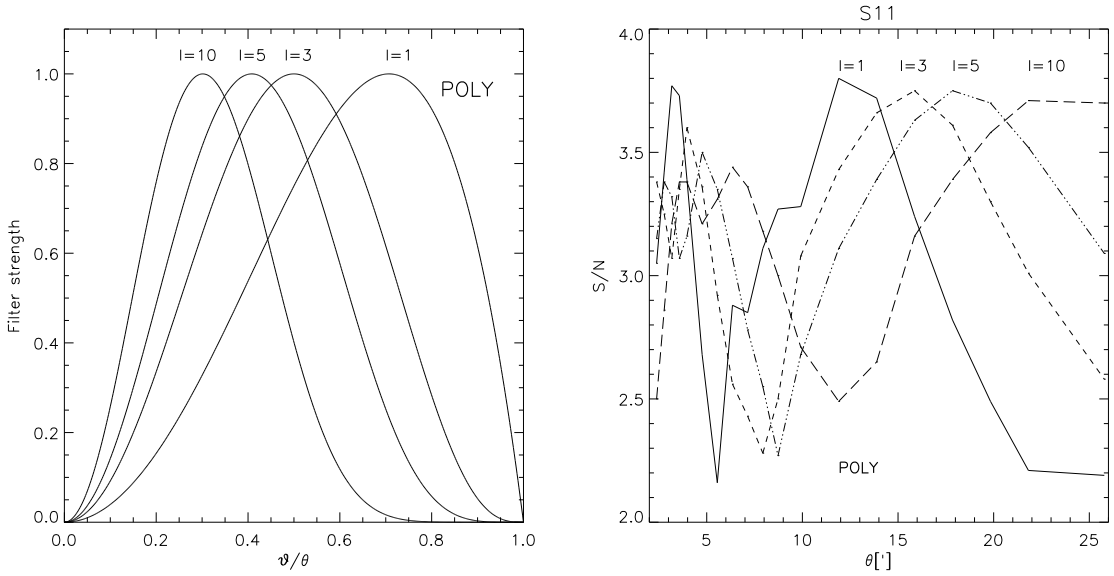

Figure 3.6: Left panel: a sample of POLY filters (3.69) for $l \in [1, 3, 5, 10]$. Their amplitude was normalised in this plot for better comparison. The effect of a growing l is to shift the maximum towards smaller scales while changing the asymmetric shape of the filters a bit. Filters with larger l will therefore produce similar results as the ones with small l, but for correspondingly larger filter scales. This is shown in the right panel, where the S/N for the cluster in the S11 field is shown for various filter scales and l. No improvement is gained in the S/N when moving to larger values for l.

3.2.5 Effect of filter functions on the detection *S/N*

In order to evaluate the performance of the various presented filters, they were tested against each other on two GaBoDS cluster fields (Fig. 3.5) for various filter scales. These plots show that filters which resemble the shear profile yield better results, whereas the others are less effective since they downweight the areas where the lensing signal is strongest.

3.3 Catalogue creation and filtering

The catalogue production can be split into three parts. First, *SExtractor* (Bertin & Arnouts, 1996) is used to create a primary source catalogue. Second, the basic lensing quantities for each of the objects in this catalogue are determined with *KSB* (Kaiser et al., 1995, see Sect. 3.1.2), and are then included in the primary catalogue. Subsequently, several filtering steps ensure that only objects with reliable shear information remain in the final catalogue.

3.3.1 Creation of a source catalogue

Single passband catalogue The basic principle in the detection algorithm of *SExtractor* is that a certain number of connected pixels with a user-defined minimum S/N above the background noise is taken as a single object. The background noise is not determined from the coadded image itself, but from the coadded weight map which is given to *SExtractor* in parallel. This weight map contains the effective exposure time for each individual pixel in the image, and thus an estimate of its noise respectively the reliability of its stored information.

The detection can take place on the image itself, or after it has been convolved with a (e.g. Gaussian) detection kernel. This filtering affects in particular small objects with a very low detection significance of $S/N = 2$ and less. Since reliable lensing information can only be obtained from high-S/N objects, this does not affect the final lensing catalogue. The number of connected pixels used in this work for the primary object detection was 5, and the detection threshold has been set to 2.5 (in units of S/N). These thresholds are rather generous, and many of the detected objects are rejected again in the later filtering process since they were too small and too faint for a realiable shear measurement.

The most relevant parameters in this context provided by *SExtractor* are the magnitude (MAG_AUTO) of the detected object and its *half-light radius* (FLUX_RADIUS), i.e. the radius which contains half of the object's flux. For the present work an absolute calibration of the magnitudes is of little interest, and if required, the adaption of photometric standard zeropoints within an accuracy of $0.1 - 0.2$ mag is sufficient ($\mathrm{ZP_R} = 24.5$ for WFI@2.2).

Multicolour catalogues In case a particular image has been observed in several filters, a colour catalogue can be generated from the individual coadded images. For this purpose the images are rescaled so that their mean background noise is 1, and are then combined into a *detection image*. The weight maps are rescaled and combined accordingly. The detection image, its weight and one of the images taken in a particular filter (*photometry image*) are then given to *SExtractor*, using the same criteria as for the single passband catalogue creation. An object's position and size is then measured in the detection image, and its flux in the photometry image. This guarantees that the magnitude of a particular object in various filters is measured at the same position and within the same aperture, yielding accurate relative colour information for the objects, even when the absolute zeropoints have not been determined precisely. These steps are repeated for all passbands, and the catalogues created are then combined.

Including the lensing information For the extraction of the shapes of lensed galaxies and the PSF corrections the *KSB* method (Kaiser et al., 1995) is used. The details of the involved techniques were already discussed in section 3.1.2. The primary source catalogue obtained with *SExtractor* feeds the initial positions of the detected galaxies into *KSB*, which then performs the actual measurements on the image itself. The galaxy positions are iterated by *KSB* until the first brightness moments vanish. The PSF corrected ellipticities and a number of other parameters (such as the *KSB* detection significance $\nu_{\max}$ and the shear and smear polarisabilities) are then added to the initial catalogue for each object.

3.3.2 Catalogue filtering

Filtering on the *SExtractor* level Adopting a simple detection threshold approach for the creation of the primary source catalogue leads to a large contamination by spurious objects. *SExtractor* offers several ways to avoid such detections. Two of them were already mentioned above, i.e. the minimum number of connected pixels, and the inclusion of weight maps. The latter guarantees that the highly non-uniform effective exposure time in the WFI exposures is taken into account properly, and that no spurious objects are detected at the edges of the image which are typically very noisy.

A common problem in catalogue creation is deblending. Some sources such as spiral galaxies show a lot of substructure or appear clumpy at larger distance, and one wants them

to appear in the catalogue as single objects. Others, such as galaxies in a cluster or objects superimposed onto the bright haloes of stars should be recognised as individual objects. *SExtractor* offers a highly configurable deblending mode which can discern between the two scenarios, and which is very effective already in its default configuration and does not need to be changed for the purpose of this work. In addition, *SExtractor* models the sky background on a user supplied scale (typically a few hundred pixels), taking the model into account when detecting objects and determining their magnitudes. Thus it is guaranteed that objects in the vicinity of brighter stars are still properly detected.

However, stars can have very large diffraction spikes which appear as rather elliptical objects in the source catalogue (mimicking a shear signal), and the shape measurement of faint galaxies is affected the closer they are to the bright stars. Thus, masking stars and their surroundings is a very important step in the creation of a clean catalogue, which is a very cumbersome task when done manually. By switching off the automatic background modelling (BACK_TYPE = MANUAL), and supplying a user defined constant value for the sky background (BACK_VALUE = 0, due to sky subtraction in the pipeline processing), *SExtractor* will not detect any objects in the surrounding area of bright stars that are affected by scattering light, since this area is taken as a single object, then. Figure 3.8 shows an example. The BACK_TYPE and BACK_VALUE keys are not present by default in the *SExtractor* config file, and have to be added by hand if one wants to make use of this feature.

Further filtering on the *SExtractor* level is done by excluding all objects that are flagged with FLAG > 4 and those with half-light radii smaller than 0 (false detections) or larger than 30 pixels (very large unlensed foreground galaxies).

Filtering on the *KSB* level In addition to *SExtractor*, *KSB* also offers a flag parameter (cl), indicating whether problems in the determination of e.g. the shape or the position occurred. Only objects with cl $= 0$ remain in the galaxy catalogue. The stellar catalogue (for PSF correction) is automatically extracted from a diagram showing the half-light radius and magnitudes of the objects. Galaxies with half-light radii smaller than $0.1 - 0.2$ pixels than the left ridge of the stellar branch are rejected from the lensing catalogue, as are those with exceedingly bright magnitudes or a low detection significance ($\nu_{\max} < 10$). See the left panel of Fig. 3.10 for the stellar branch and an illustration of the cuts in the $r_{\rm h}-$mag space.

A significant number of galaxies have sizes comparable to or a bit smaller than the PSF (see Fig. 3.10), which increases the error of their shape measurement as compared to larger objects. The fact that galaxies have measured sizes smaller than the PSF indicates that the exposures are still somewhat undersampled for the detection algorithm. Indeed, image simulations with *SkyMaker* for a seeing of $0\farcs9$ support this assumption. Decreasing the pixel scale from $0\farcs238$ to $0\farcs15$ increased the measured half-light radii of about 70% of the small galaxies to values larger than the characteristic PSF, simplifying the determination of their ellipticities. Yet the number of very small galaxies in the GaBoDS data is large enough so that the shear selection of galaxy clusters can profit significantly when these objects are included in the calculation, even though faint stars will contaminate the sample a bit. For example, in case of S11 the S/N rises from $4.66\,\sigma$ to $4.95\,\sigma$ (18112 respectively 22567 galaxies), and for A901 it rises from $5.97\,\sigma$ to $6.13\,\sigma$ (24137 respectively 28166 galaxies) when these objects are included. Going to even smaller galaxies decreases the S/N again.

Furthermore, all galaxies with a PSF corrected modulus of the ellipticity larger than 1.5 are removed from the catalogue (the ellipticity can become larger than 1 due to the

PSF correction factors), as are those for which the correction factor $(\mathrm{Tr}\, P^{\mathrm{g}})^{-1} > 5$ (see the discussion of (3.47)). The fraction of rejected galaxies due to the cut-off in P^{g} is relatively small, as can be seen from the right panel in Fig. 3.10. However, the smoothness of the two-dimensional visualisation of the S-statistics (hereafter S-map) is significantly improved by rejecting such galaxies (see Fig. 3.11 for an example).

An overall impression of the remaining objects in the final catalogue is given in Fig. 3.9. In total, typically $10 - 20\%$ of the objects are rejected from the catalogue due to the *KSB* filtering steps.

3.4 Sensitivity of the shear-selection method

Kruse & Schneider (1999) outlined how to calculate the expected S/N for a dark matter halo with NFW density profile at redshift z_{d}, taking into account a source redshift distribution $p(z_{\mathrm{s}})$ for the lensed galaxies. In this case M_{ap} becomes

$$M_{\mathrm{ap}} = \int_0^{\theta} \mathrm{d}^2\boldsymbol{\vartheta} \int_{z_{\mathrm{d}}}^{\infty} \mathrm{d}z_{\mathrm{s}}\, p(z_{\mathrm{s}})\, \kappa(\boldsymbol{\vartheta}, z_{\mathrm{d}}, z_{\mathrm{s}})\, U(\vartheta)\ , \tag{3.86}$$

where the normalised redshift distribution is given by Brainerd et al. (1996) as

$$p(z_{\mathrm{s}}) = \frac{3}{2z_0} \left(\frac{z_{\mathrm{s}}}{z_0}\right)^2 \exp\left[-\left(\frac{z_{\mathrm{s}}}{z_0}\right)^{1.5}\right]\ . \tag{3.87}$$

The parameter $z_0 \approx 0.66\,\langle z\rangle$ was fixed for this work based on photometric redshifts, computed from the $UBVRI$ WFI@2.2 data (EIS Deep Public Survey) for the Chandra Deep Field South (see left panel of Fig. 3.7). In this data set, the exposure time in the R filter was 9 ksec. A value of $z_0 \approx 0.5$ is taken for the redshift distribution, even though a fit of the Brainerd model prefers a value of $z_0 \approx 0.4$ due to the lack of galaxies with photometric redshifts around $z = 1$.

The right panel of 3.7 shows some predicted S/N ratios for massive haloes as a function of redshift and for the POLY filter. From this plot it can be seen that medium-sized clusters with masses of $3.2\times10^{14} M_{\odot}$ are detectable up to a redshift of $z = 0.45$, and those with $1.0\times10^{15} M_{\odot}$ can be found up to $z = 0.65$ for a filter size of $3\farcm2$. Structures with $\sim 1.0\times10^{14} M_{\odot}$ can hardly be detected at the $3\farcm2$ scale. Given the very inhomogeneous depth of the GaBoDS data (see Tables 2.1 and 2.2), these values can only serve as a rough reference, as does the filter scale of $3\farcm2$ (compare Fig. 3.5). As was shown above, the NFW and TANH filters yield a better S/N, but on the other hand many of the ASTROVIRTEL fields are shallower in their depth as the obervations of the CDF-S which were used for this estimate.

Hence the shear selection method is not very efficient in detecting clusters of galaxies at larger redshift, since the number density of available galaxies at accordingly high redshift drops rapidly. Yet weak lensing effects for galaxy clusters at redshifts of $z_{\mathrm{d}} \approx 0.8$ were measured from the ground with 8m class telescopes (see Sato et al., 2003, for example). From space it is much easier to reach a remote enough population of galaxies, since the sky brightness is typically a factor of 30-100 smaller, and no atmospheric seeing affects the shape measurements (see Hoekstra et al., 2000, for example). Number densities of $n = 100$ arcmin^{-2} can be reached in comparable exposure times.

Thus, for the selection of higher-redshift clusters, it is much more effective to pick them up by means of their luminosity in the optical or the X-ray part of the electromagnetic spectrum,

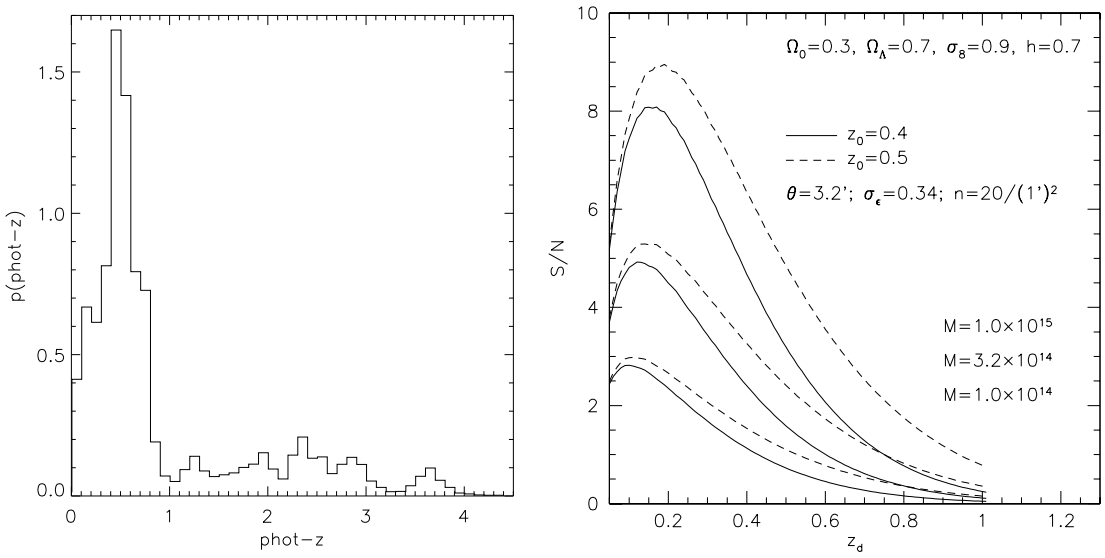

Figure 3.7: Left Panel: Photometric redshift distribution for the Chandra Deep Field South, determined from $UBVRI$ WFI@2.2 photometry (EIS data, only). The redshifts were estimated with *hyperz* (Bolzonella et al., 2000). Only objects that had a good redshift fit of $P(\chi^2) > 0.9$ went into the distribution shown.
Right panel: The expected S/N ratios for NFW dark matter haloes with 1.0×10^{15}, 3.2×10^{15} and 1.0×10^{15} solar masses, measured with the POLY filter. The assumed number density of the background galaxies is $n = 20$ arcmin^{-2}, which corresponds to an exposure time of $10 - 20$ ksec, depending of various filtering thresholds. Two galaxy populations with different redshift distributions (3.87) were used for the calculation. The higher redshifted population leads to a somewhat larger sensitivity (dashed line).

and not by means of their mass. For example, the red cluster sequence method (Gladders & Yee, 2000) has been used with great success in recent years to detect clusters even at higher redshifts $z_\mathrm{d} \approx 1$ (see Barrientos et al., 2003, for example), and combined narrow and broad band imaging techniques can reveal structures out to $z = 4$ (Venemans et al., 2002). However, with these methods only luminous clusters are detected, objects with very high M/L ratios can go unnoticed even at low redshifts.

3.5 Exclusion of side-effects

Unit width of the unlensed S-distribution Figure 3.12 shows the typical appearance of the S-maps for various filters. The bright patch above the centre is the detection of the galaxy cluster Abell 901. Even though these maps appear rather different, the distribution of the S-statistics (hereafter *S-distribution*) would be by definition a Gaussian of unit width if no lensing by A901 took place. In fact, the distribution is slightly wider than one with unit width.

Figure 3.13 exemplarily shows the S-distribution for a POLY and a TANH filter of $3'$ and $12'$ scale, respectively. For each plot in the left column, the galaxy orientations in an arbitrarily selected, empty field were randomised 300 times, thus removing any lensing signal. A mean, unlensed S-distribution and its error were then calculated from these 300 realisations.

The S-distribution can be approximated by a Gaussian with a width of 1.006 ± 0.002 (for the $3'$ scale). This is shown in the right column of the figure, where once a unit Gaussian and then a best-fit Gaussian was subtracted from the mean distribution. The widening is caused by the application of equation (3.85) to a data set with a finite number of galaxies, so that the result approaches a normal distribution, but does not resemble it exactly. Therefore, the analysis in the next Chapter uses only randomised data sets as an *unlensed* reference instead of a unit or a best-fit Gaussian.

Effect of holes in the data field The number density of background galaxies inside a $M_{\rm ap}$ aperture is not a constant over the field due to the masking of brighter stars. The lower right panel of Fig. 3.14 shows a typical projected distribution of the galaxies in the final object catalogue. As long as the holes in this distribution are small compared to the $M_{\rm ap}$ filter size, and as long as their number density is small enough so that no significant overlapping of holes takes place, the effects onto the S-statistics are small. The S/N of the peaks in such areas is then simply lowered by the smaller effective number density of galaxies inside the aperture.

However, if the size of the holes becomes comparable to the aperture, spurious peaks appear in the S-map at the position of the holes since the underlying galaxy population changes significantly when the aperture is moved to a neighbouring grid point. The affected areas are excluded from the statistics and masked in the S-map, even though these spurious peaks are typically not very significant ($\sim 2\sigma$). The S-statistics is not evaluated at a given grid point if the effective number density of the galaxies in the aperture is reduced by more than 50% due to the holes. Spurious peaks become very noticeable if the holes cover about 80% of the aperture, which is rarely the case for the GaBoDS fields unless the aperture size is rather small ($2'$ - $3'$), or a particular star is very bright.

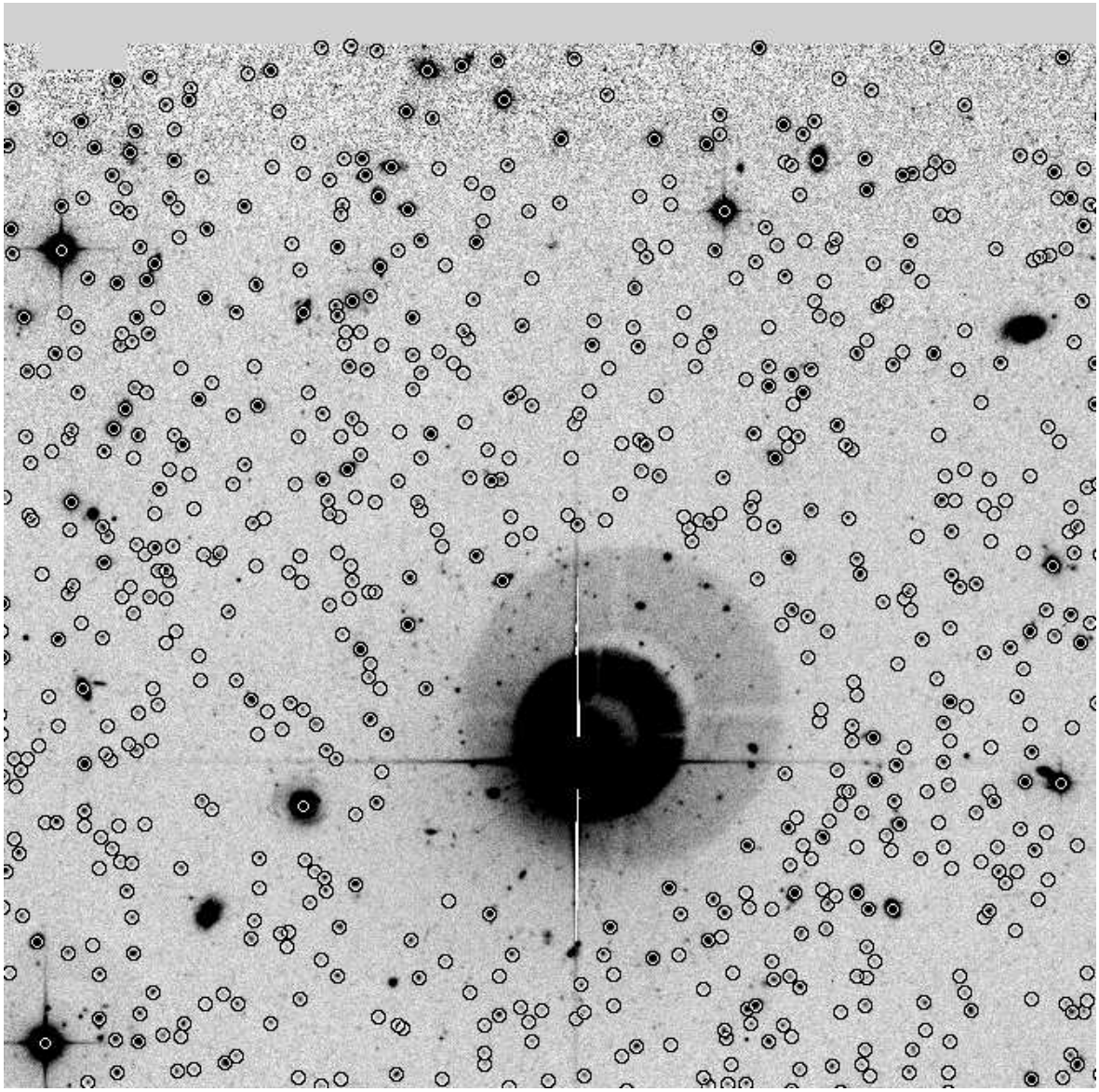

Figure 3.8: Automatic masking of bright stars, achieved by forcing *SExtractor* to use a constant, user-supplied value for the sky background. Note that at the upper image border no spurious objects are detected, although this region is very noisy because of little effective exposure time. This is due to the use of a proper weight map. No *KSB* filtering has taken place for this plot.

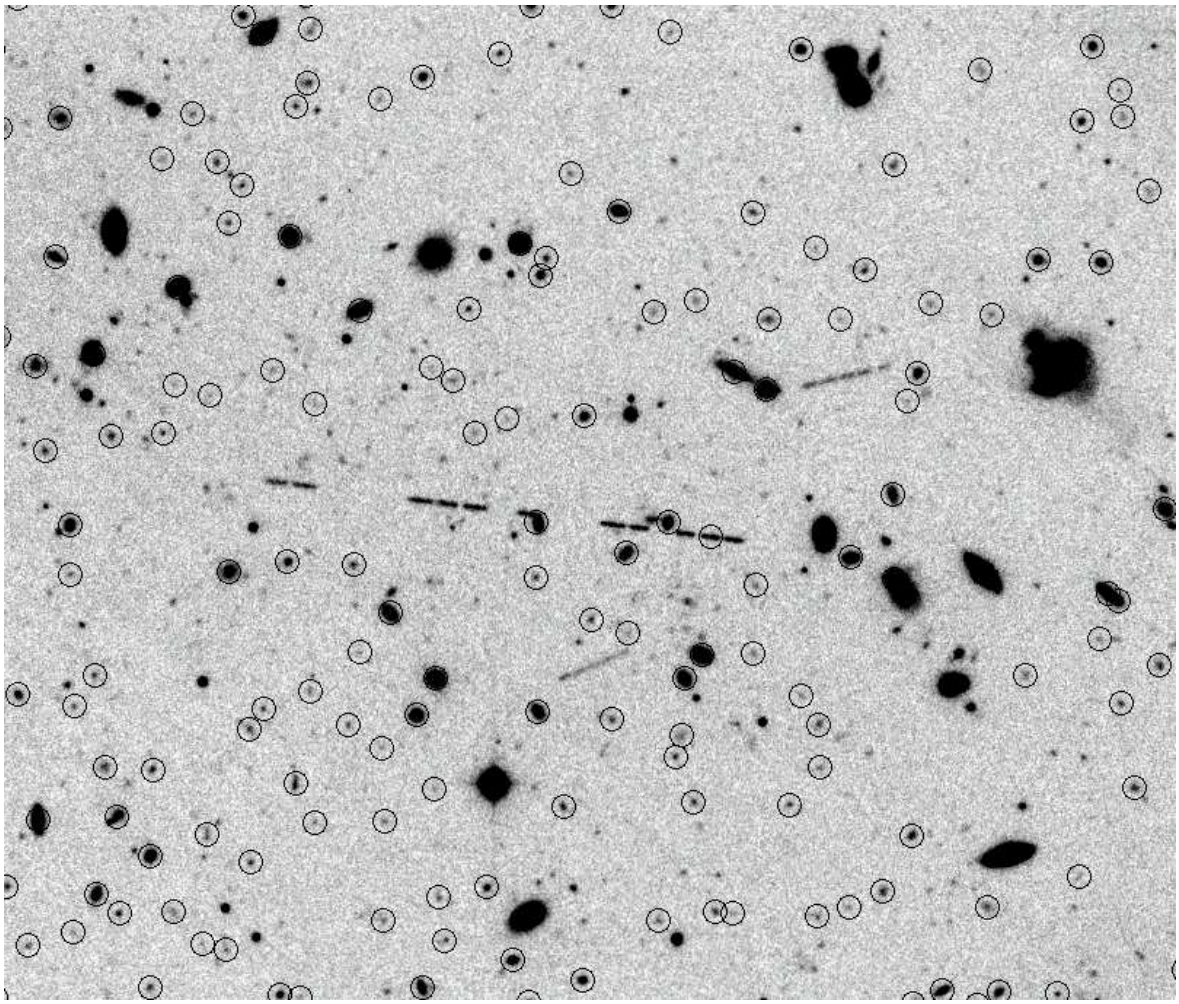

Figure 3.9: Lensing catalogue after all typical filtering steps. Only fainter background galaxies are kept. Brighter sources, spurious detections, stars and highly elliptical objects such as asteroid tracks are largely absent from the catalogue.

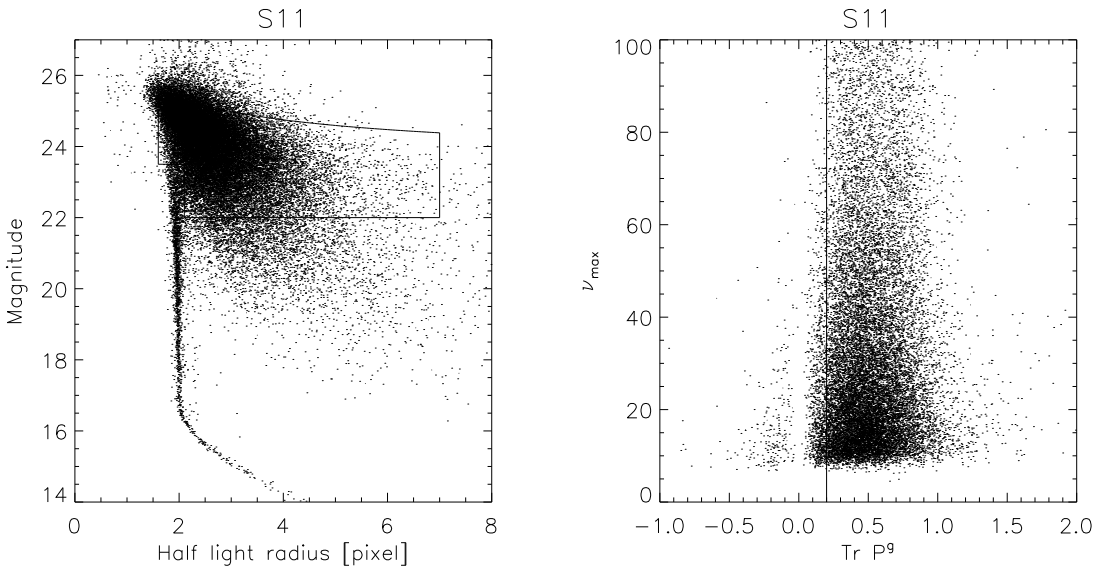

Figure 3.10: Left panel: Stars appear as a vertical branch in a r_h-mag plot. Those brighter than $R = 16.5$ saturate the detector and thus increase in size. The solid line encircles the galaxies which are used for the lensing analysis. The upper curved line indicates a cut in detection significance ($\nu_{max} > 10$), which has proven to work better than a constant cut on the faint end of the magnitudes. Right panel: ν_{max} against P^g. Objects left of the indicated threshold are rejected from the lensing catalogue. Typically 1% of the galaxies are removed during this step. The effect of this cut onto the S-statistics is shown in Fig. 3.11.

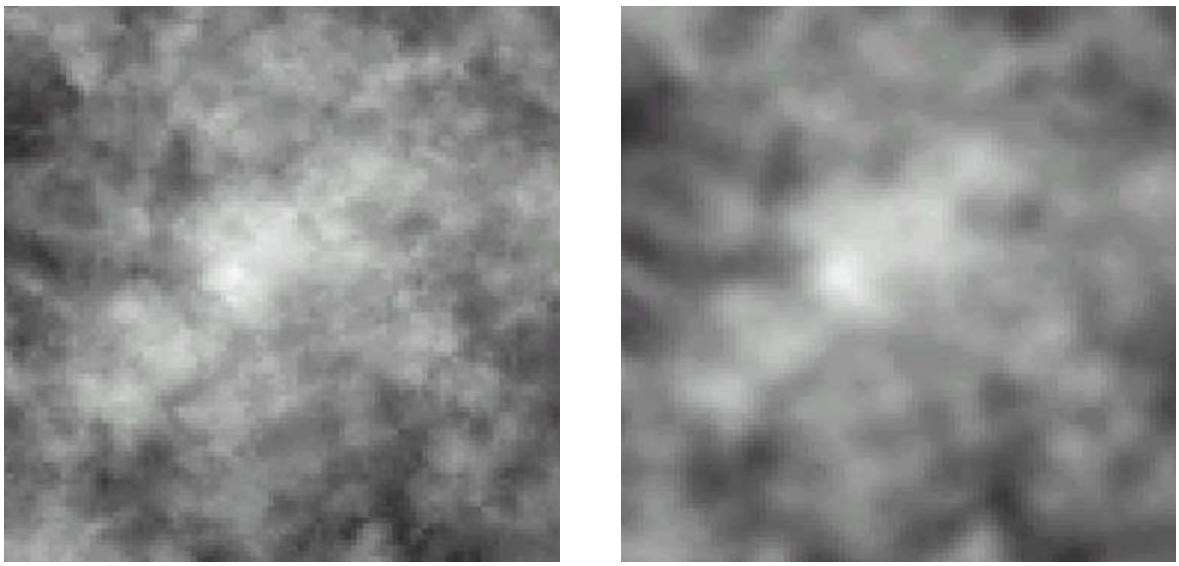

Figure 3.11: Effect of the cut-off in P^g. Shown is the S-statistics calculated with TANH for a 15′ wide field centered on the cluster in the S11 field. The left panel is without, the right panel with the cut-off. The aperture size is 14′ . The peak significance in the right panel decreases marginally from $4.72\,\sigma$ to $4.66\,\sigma$.

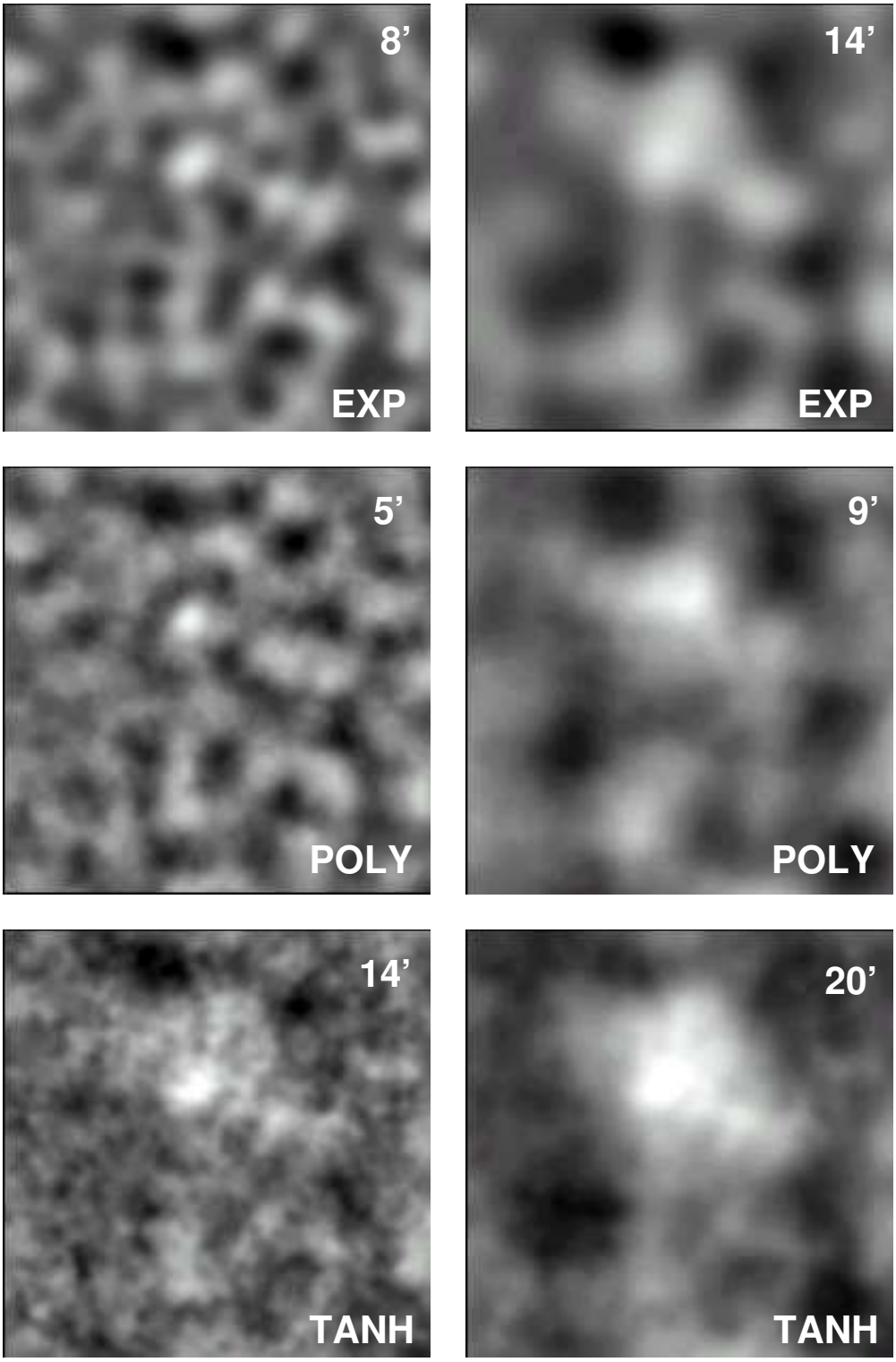

Figure 3.12: Appearance of the S-map for various filter types and scales. The data shown corresponds to the full $34' \times 34'$ A901 field. Smaller filter scales were chosen for the left column, and larger ones for the right one. The scales were adapted such that the size of the structures in the maps within a column are comparable. The EXP filter yields the smoothest results. The intensity levels of this grey-scale representation correspond to $[-4\,\sigma, 5\,\sigma]$ for the left column, and to $[-4\,\sigma, 6\,\sigma]$ for the right one.

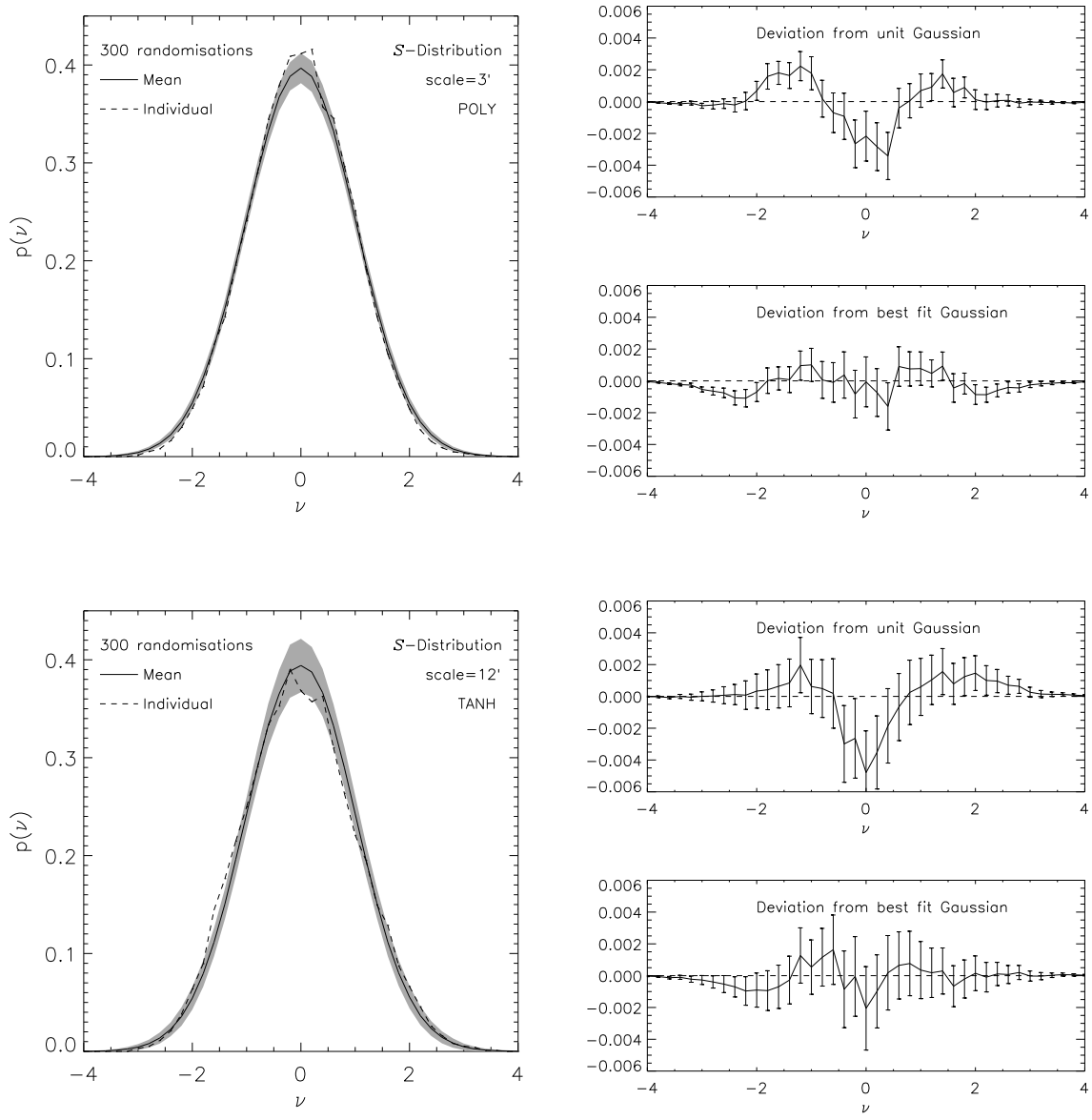

Figure 3.13: Width of the unlensed S-distribution for two filters. In the left column the normalised mean S-distribution is shown for 300 randomisations of the galaxy orientations. The shaded region depicts the 1σ scattering amongst the randomisations, and the dashed line shows one of them for comparison. The right panels depict the difference between the mean distribution and a unit Gaussian, and between the mean distribution and a best-fit Gaussian. The error bars there were obtained by bootstrapping, i.e. 300 randomly chosen realisations were selected from the sample, and their mean was calculated. A particular realisation can be drawn several times. This was repeated 300 times, which yielded an error estimate for the mean. As can be seen, the S-distribution is slightly wider than the unit Gaussian.

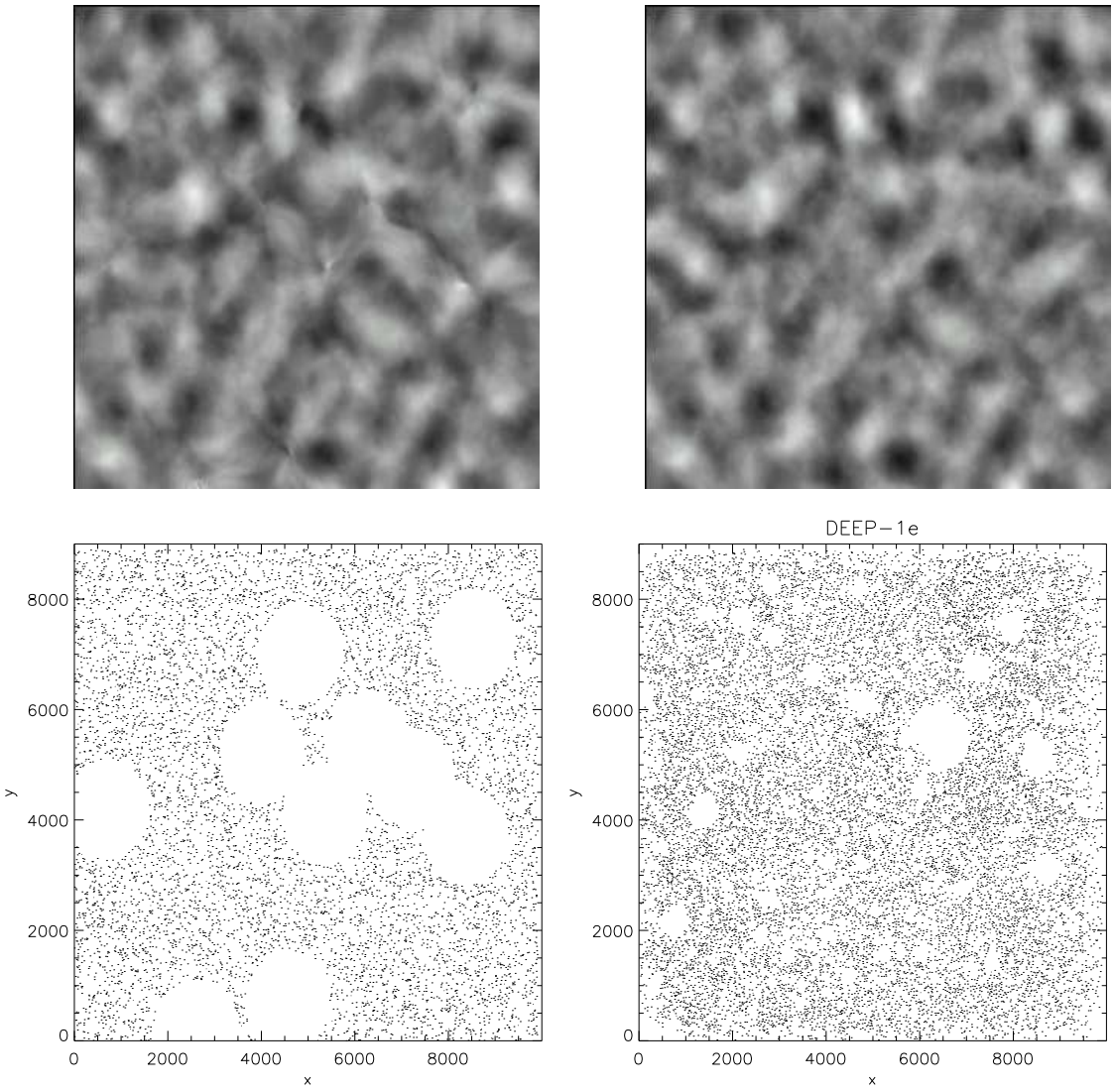

Figure 3.14: Upper right: S-map (POLY, $4'$) for randomised galaxy orientations and positions. Upper left: The same S-map, evaluated after 10 randomly positioned holes with a radius of 90% of the filter scale were cut into the data field (lower left). Artificial features show up in the S-map at the positions of the holes, which are exaggerated in number and size for better visualisation. Lower right: True galaxy distribution in this field. The largest hole corresponds to an 8th magnitude star.

Chapter 4

Shear-selection in the GaBoDS

Whereas rather massive clusters can be clearly detected by weak gravitational lensing, less massive haloes merge with the surrounding noise in the S-map, which is mostly due to the intrinsic ellipticities of the galaxies. Nevertheless, evidence for the presence of gravitational lensing in such fields can be obtained by comparing the S-statistics of the total survey area to an "unlensed" data set with randomised galaxy orientations. Gravitational lensing by clusters and the lensing effect of the large scale structure in the universe (*Cosmic Shear*) broaden the S-distribution, but these two effects are difficult to disentangle. In Sect. 4.1 the combined S-distribution for GaBoDS is presented. It is shown that very significant deviations from the unlensed profile are present for all filters at all scales, even for the sub-sample of GaBoDS in which no significant mass concentrations were found. The contribution by Cosmic Shear is considerable.

In Sect. 4.2 a list of individual, highly significant shear-selected mass concentrations is presented. A simple classification scheme for these peaks is introduced ("bright" and "dark", i.e. with and without optical counterparts), and analysed with respect to differences between the two classes. It is shown that with multi-colour data at hand clusters of galaxies can be easily identified as possible counterparts, thus verifying the weak lensing detection (Sect. 4.3). Finally, remaining "open issues" that could not be addressed in this work, and a number of smaller and larger follow-up projects are given in Sect. 4.4.

4.1 Combined S-distribution

Unlensed reference S-distribution In order to show the actual presence of weak gravitational lensing in the survey fields, the combined S-distribution is compared against an unlensed reference distribution. For the latter, the positions, shapes and weights of the catalogued galaxies from all 62 fields were combined into a master catalogue, irrespective of the inhomogeneous exposure times and thus redshift distributions of the fields (see right panel of Fig. 2.3). However, the large majority of the fields was taken with relatively short exposure times, so that the contribution of the deep fields to this master catalogue is only about 10%. Furthermore, the ellipticity distribution of the galaxies is only marginally changed by weak lensing, and the seeing in the images is comparable ($0\farcs85$ to $1\farcs0$). Therefore, the master catalogue provides a representative sample of galaxy shapes for the creation of an unlensed reference S-distribution.

From this catalogue 15000 galaxies were randomly extracted, which corresponds to the

average number density of $n = 13$ arcmin^{-2} of the survey fields. The orientations of the galaxies in this mock catalogue were randomised and the S-distribution for a particular filter and scale was calculated. This was repeated for 400 different mock catalogues, resulting in 400 S-distributions that were then averaged yielding the reference S-distribution. Thereafter, the actual distributions for the 62 survey fields were calculated and averaged, yielding the sheared S-distribution. Since the differences between the two distributions are rather small, the reference distribution was subtracted from the sheared distribution for better visualisation in Figs. 4.1 and 4.2. The rrror estimates were obtained by bootstrapping (see caption of Fig. 3.13).

Contribution of Cosmic Shear and Clustering For the determination of the effect the Cosmic Shear has on the S-distribution, 50 independent galaxy fields with similar properties as the actual observations were simulated. These fields are $29' \times 29'$ in size, with random ellipticities but an imprinted Cosmic Shear signal (P. Simon, private communication). The assumed cosmological parameters were $\Omega_0 = 0.3$, $\Omega_\Lambda = 0.7$, $\sigma_8 = 0.9$, $H_0 = 70\,\mathrm{km\,s^{-1}\,Mpc^{-1}}$, and the galaxy population was chosen to match a typical GaBoDS field ($\langle z \rangle = 0.8$, $\sigma_\varepsilon = 0.35$, $n = 15$ galaxies arcmin^{-2}). The Cosmic Shear contribution was calculated based on a power spectrum for a Gaussian density field. The spectrum was corrected for non-linear effects on smaller angular scales according to the Peacock & Dodds (1996) prescription (see 1.3.2 for details).

For the creation of an unlensed reference S-distribution a similar approach as for the survey data was chosen. The galaxies from all 50 fields were combined into a master catalogue, from which 300 mock catalogues with 12600 galaxies each (as many as in one simulated field) were randomly selected. Again, the orientations of the galaxies were randomised and the S-distributions calculated.

For all filter scales and types significant deviations from the unlensed reference distribution are found for the GaBoDS data. Cosmic Shear is seen in all but the smallest filter scales of $2'$ and partly $3'$, for which a significant deviation from the reference distribution is found. The simulation is consistent with the observations in the $[-3\sigma, 3\sigma]$ interval, apart from the largest and broadest filters ($12'$ TANH with $x_\mathrm{c} = 0.2$, and POLY with $8'$ and $5'$). The tails of the distribution ($|\nu| > 3\sigma$) are negative for the smallest scales, meaning that in the randomised data more mass peaks and voids (underdense regions) are found than in the actual observations. With increasing filter scale the signs of the tails change, thus more peaks and voids than in the reference data are observed. The differences between the simulation and the observation are attributed to the non-linear clustering in the density field which is not accounted for in the simulation.

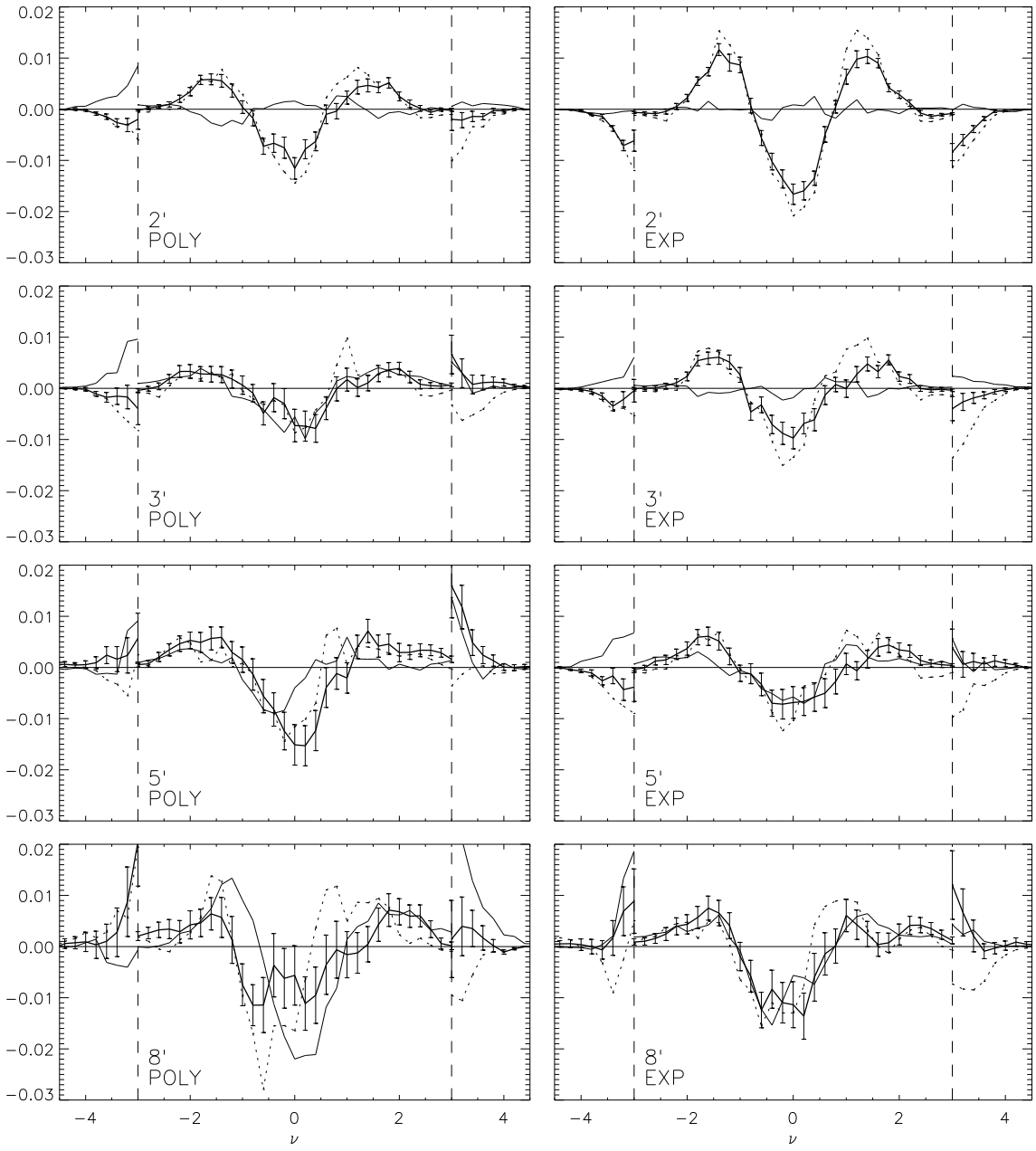

Figure 4.1: Differences between the sheared and the reference S-distribution. The error bars resemble the combined rms of both the reference and the sheared distribution. The thick lines were calculated from all fields ($n = 62$) in GaBoDS, and the dotted lines show only those fields ($n = 21$) that do not contain any weak lensing signal higher than 4σ in any filter at any scale. The thin line is obtained from simulations. The error bars for this line are comparable with the ones for the actual data, and are omitted to avoid cluttering. The tails ($|\nu| > 3\sigma$) of the distributions were magnified in amplitude by a factor of 10.

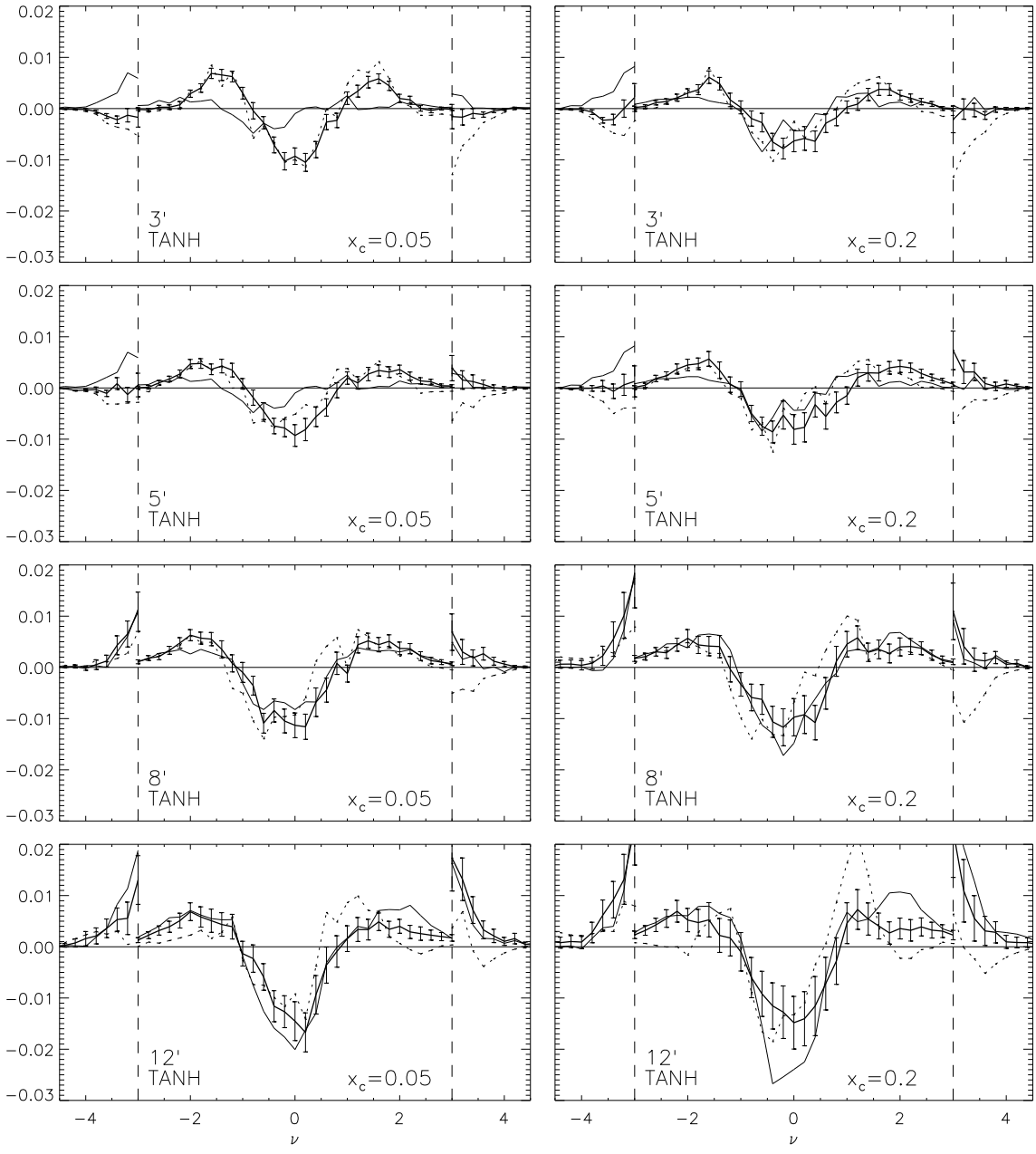

Figure 4.2: Same as Fig. 4.1, but for other filter types.

4.2 Shear-selected mass concentrations

4.2.1 The sample

Tables A.1 to A.3 in the appendix list all shear-selected mass concentrations with a $S/N \geq 4.0$ in at least one filter, sorted in right ascension. The S/N-threshold keeps the contamination of the sample with spurious noise detections small. Columns 1, 2 and 3 contain a preliminary name for the mass concentration, and its coordinates. The maximum detection significance and a classification are given in columns 4 and 5. The latter is either the redshift[1] of the optical counterpart, the statement "bright" if no redshift could be found, or "dark" if no obvious optical counterpart is present. The term "unclear" is explained below. Thereafter, columns 6, 7 and 8 list the filter, its core radius (if applicable) and its scale for the individual detection. Finally, column 9 has the name of the corresponding GaBoDS field. The tables are followed by the images showing these peaks.

Redshifts, positional accuracy and projection effects If at least two galaxies of an optical counterpart of a mass concentration have similar redshifts, then this value is given in the table. The only exceptions are SSMC-004 and SSMC-005, whose redshifts were deduced from the colours of their elliptical galaxies instead of spectroscopy, and SSMC-017, for which only a single redshift is known. The redshift measurements themselves were taken from Colless et al. (2001), Gonzalez et al. (2001), Goto et al. (2002), Olsen et al. (1999) and Vettolani et al. (1998).

From those mass concentrations with spectroscopically confirmed counterparts and from a few others associated with bright galaxies (SSMC-026, 033, 062, 076), it is found that the lensing position can be offset with respect to the counterpart by up to $2'$. The position itself rarely shifts more than about $0'.5$ when switching to different filter scales and types. For the largest clusters in the sample, Abell 901 (SSMC-024) and Abell 1364 (SSMC-053), the positions of the weak lensing detections are usually well in agreement with the brightest cluster galaxies for small filter scales. Offsets occur only for larger filter scales in the sense that the detection appears to be shifted towards the centre of mass, i.e. away from the brightest galaxies into the direction of sub-clumps present in these clusters. This does not come unexpectedly, since the filter becomes insensitive to the structures in the central mass distribution of a cluster when probing the shear field on large scales.

A similar effect is observed for lensing detections next towards a projection of clusters at different redshifts. For example, SSMC-032 sits close to the centre of the triangle formed by the clusters LCDCS-0188, -0189 and -0190 at redshifts 0.52, 0.41 and 0.60, respectively (partially visible in the corresponding figure). It is detected at the 4σ-level only for larger filter scales that encompass the shear fields of all three clusters. The components alone are not found by means of the shear-selection method. A similar situation is probably given for SSMC-083, which is located between a rather distant overdensity of galaxies to the North-West, and another one with lower (also unknown) redshift to the South-East. The angular distances to the centres of both of these concentrations are about $2'$ each, and the lensing contours are extended parallel to the line connecting the two clusters. Besides, like in the case of SSMC-032, the best-matched filter is rather large.

[1] Redshifts were taken from the NASA Extragalactic Database (NED) and the references to the literature therein.

The observed tangential shear in these cases is a result of the projection of the surface mass densities of the individual clusters along the line of sight (*multiple lens plane*). In this manner, the combined shear of smaller clusters of galaxies that would not be detected individually can be found.

4.2.2 Underluminous clusters

The above mentioned projection effects could be a possible explanation for the "dark" mass concentrations, lacking obvious optical counterparts. Instead of a single, underluminous galaxy cluster, possibly with very red galaxies that emit their light predominantly at longer passbands than the R-band filter used ($z \approx 0.9$ and larger), a projection of small galaxy groups along the line of sight could trigger a similar detection. Since it is known from the bright mass concentrations that the offsets can be as large as $2'$, two or three smaller groups with low central concentrations can easily submerge in the surrounding galaxy field at opposite sides of the lensing position. Thus, a dark and extended cluster would be mimicked (e.g. SSMC-008, 012, 054).

Besides, there is a non-negligible number ($\sim 10\%$ of the sample) of very compact detections that are found with filter scales of less than $2'$ (e.g. SSMC-011, 037, 042, 046, 074). All of them are dark apart from one which has been classified as unclear. Normal galaxy clusters can not explain these detections, independent of their redshift. If they were rather close they would be seen in the images and the lensing signal would be more extended. In the R-band and with 2-3 hours of exposure time, such clusters can be seen out to redshifts of 0.8 or 0.9. But then their masses must be much larger than $10^{15} M_{\odot}$ (see also Fig. 3.7) in order for the clusters to be detected by weak lensing with a $S/N \geq 4$ in the GaBoDS data. Such masses, in turn, are extremely rare according to current theories of structure formation. Since the peaks found occur mainly in the smallest filter and disappear for larger scales, they could simply be noise peaks as is argued further below.

Proving the actual existence of dark clumps in the universe, and clearifying their exact nature is obviously an extraordinary difficult task. In the case of the first dark cluster found (Erben et al., 2000), a large number of checks have been made with the data and the methods used for the weak lensing analysis. This dark clump ($\sim 5\sigma$) has been verified independently by various groups, using different techniques and telescopes. Extensive follow-up observations were made in the infrared from the ground (Gray et al., 2001, H-band), searching for a population of red galaxies that has not been found. Space-based observations confirm the lensing results, albeit with a lower significance. Furthermore, they do not reveal a luminous counterpart either, leaving open the possibility for the existence of truly dark cluster-sized objects.

Finally, a few of the mass concentrations detected could not be classified and are thus marked as "unclear". Either they are further away than $2'$ from a neighbouring galaxy cluster (SSMC-019, 021, for example), or the underlying concentration of galaxies is too distant to be safely identified as a probable cluster based on the single-passband data alone (e.g. SSMC-031, 034, 061). Or, as is the case for SSMC-099, the detection is located in the middle of a very extended ($\sim 10'$) projection of four galaxy groups at different redshifts (0.126, 0.135, 0.143, 0.240), showing no concentration of galaxies to their centres. SSMC-099 itself, however, appears only for smaller filter scales, which makes it less likely that it is associated with these foreground sheets of matter. Therefore it was marked as "unclear".

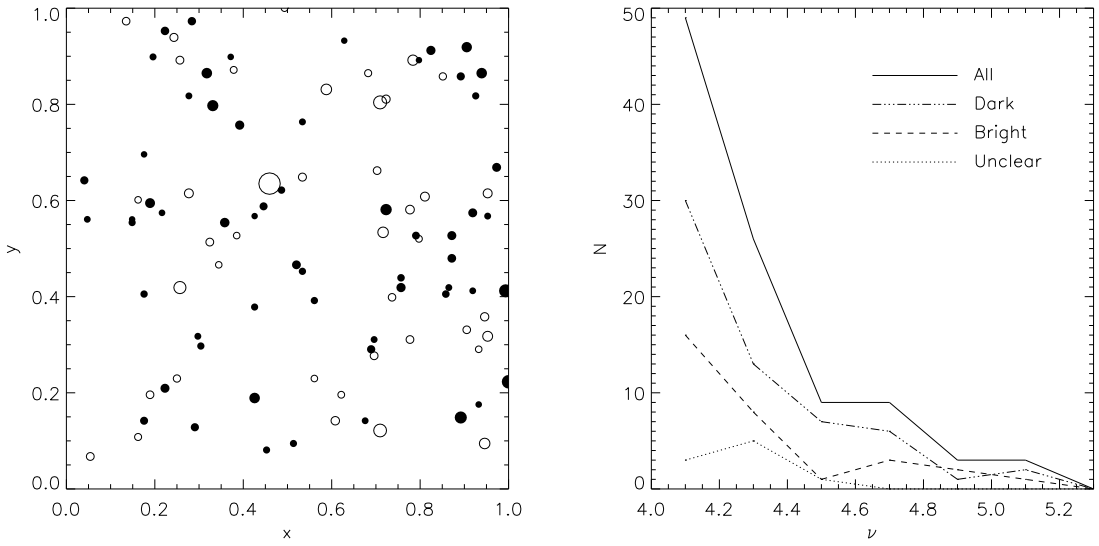

Figure 4.3: Left panel: combined spatial peak distribution for all WFI mosaics. Filled symbols indicate dark peaks, open symbols bright and unclear peaks. The size of the dots indicates the S/N. Right panel: peak distribution in bins of 0.2σ.

4.2.3 Some statistics

All these examples show that the variety of mass concentrations found with the shear-selection method is quite big. The 100 detections made allow some basic statistics of the sample, shedding more light on the population of bright and dark peaks. 59 of the 100 detections presented are dark, with SSMC-082 being the most significant one (5.1σ). 15 of the 31 optical counterparts have measured redshifts, and 10 detections remain unclassified. Thus, about twice as many mass concentrations are dark rather than bright. This fraction is larger than for the individual shear-selected mass concentrations that were published in the literature so far (Erben et al., 2000; Umetsu & Futamase, 2000; Maoli et al., 2001; Wittman et al., 2001, 2002; Miralles et al., 2002; Miyazaki et al., 2002; Dahle et al., 2003; Schirmer et al., 2003). About 50% of these candidate mass concentrations are dark. However, the two figures are difficult to compare since the sample presented in this work is a factor of 10 larger than what has been published to date, and the authors from the cited papers used different methods for their cluster detection. Larger surveys (such as the Red Cluster Sequence Survey or the CFHT Legacy Survey) that are or will be systematically analysed with respect to weak lensing will provide a much better comparison in the near future.

Figures 4.3 and 4.4 provide more insight into the population of bright and dark peaks. The left panel of the former shows that the peaks from Tables A.1 to A.3 appear to be randomly distributed in the WFI mosaics. As expected, the S-statistics does not select peaks above average near the image borders. The right panel shows the absolute frequencies of occurrence the dark, bright and unclassified peaks (the filters used are not the same). Apart from the amplitudes no differences between the three distributions are apparent. The S/N of the peaks as a function of filter scale is shown in the left panel of Fig. 4.4, where the vertical line patterns are due to a discrete set of filter scales used for the analysis (1.6, 2.0, 2.4, 2.8, 3.2, 3.6, 4.0, 4.8, 5.6, 6.3, 7.1, 7.9, 8.7, 9.9, 11.9, 13.9, 15.9, 17.9, 19.8 arcminutes). The number of

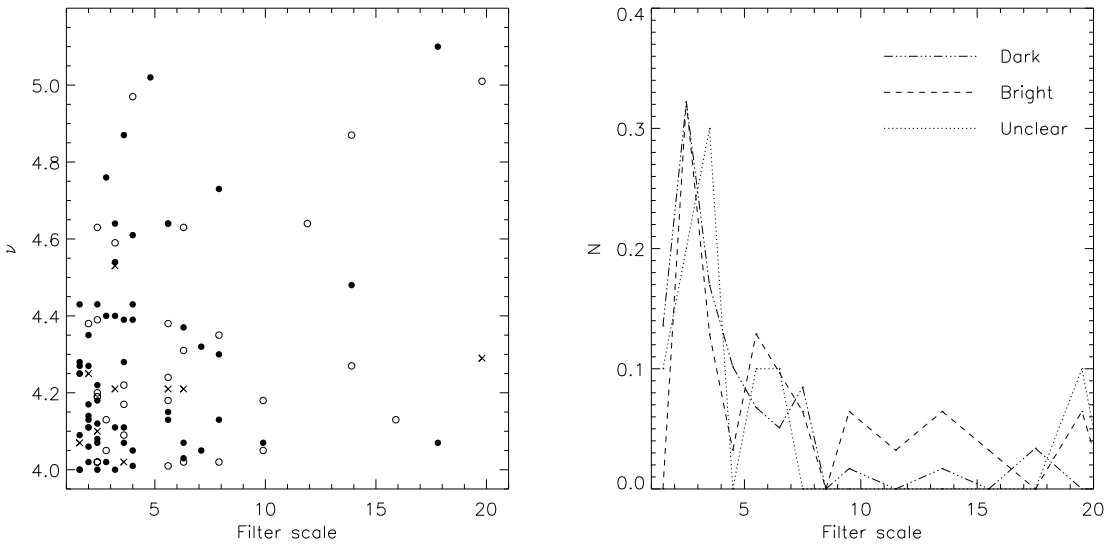

Figure 4.4: Left panel: S/N of the peaks as a function of the filter scale for which they appeared most significantly. Filled, open and cross symbols denote dark, bright and unclear peaks, respectively. Right panel: number of peaks per filter scale, normalised to unit area for better comparison.

data points per filter scale in this plot is shown in the right panel. There are disproportionate more bright than dark peaks between $10'$ and $15'$, and considerably more dark than bright peaks for the smallest filter scale of $1'.6$, as was already mentioned above. Apart from these two regions the distributions are quite similar.

Comparison with randomised data sets In order to evaluate the contamination of the sample with spurious noise peaks, the galaxy orientations in the 62 GaBoDS fields were randomised once. The number of galaxies in the individual fields was not changed. Thereafter, the S-statistics was calculated for the same filter types and scales as for the real data, and the peaks were selected in the same manner, i.e. they must have $S/N > 4$ in at least one filter. A total of 869 peaks were found, almost 9 times as many as in the actual survey data. The significance of the highest noise peak was 5.58 (7 peaks had a $S/N > 5$). Thus, from a single S-map alone one can not tell whether a peak is a real or a spurious detection, but a look at the S-profile helps in clearing the situation.

Figures A.18 to A.22 show the S-profiles for the actual data. The filter type for a given panel corresponds to the type for which the peak under consideration was detected most significantly. Figure A.24 depicts some of the profiles for the data with randomised orientations. The latter ones are much more erratic than the survey data, even for the POLY and EXP filters that distribute their weight more evenly onto the galaxies than some of the sharper TANH filters. Highly significant peaks disappear when switching to the next larger or smaller filter scale, so that no coherence in the S-maps as a function of filter scale is observed. Only for 21 (3) out of the 869 noise peaks was the S-profile higher than 3σ for 2 (3) neighbouring filter scales. Most of the shear-selected mass concentrations in GaBoDS, however, show much broader profiles. Thus, as a good discriminator between true peaks and spurious peaks serves the width of the profile above the 3σ-level. Based on this criterium, SSMC-010, 029, 046,

047, 051, 074, 075 and 077 would then be noise-peaks, since they have $S/N > 3$ only for two or three neighbouring filter scales. Interestingly, all of the latter peaks have very small filter scales and were classified as dark or unclear. Based on this, an estimate for the contamination of the mass-selected cluster sample by spurious detections of $\sim 10\%$ is derived. For further comparison, Fig. A.23 shows some S-profiles of the GaBoDS fields (without randomisation of orientations), but for randomly selected positions in the field. The patterns are considerably smoother than for the data set with randomised galaxies, indicating a non-zero shear alignment in these fields.

It is surprising that in the fields with randomised orientations so many more (9 times) significant peaks are found than in the true data. This clearly shows that in the observed fields the galaxy orientations are very different from being randomly distributed, which obviously suppresses the number of noise peaks or their significance very efficiently. This, in turn, is not intuitively clear and needs to be investigated further, for example by adding increasingly larger amounts of randomness to the orientations of the galaxies in the field. Two different tests show that at least less significant peaks react rather sensitively on minor changes of the galaxy orientations. The S-maps for the same data set, for example, once coadded with *drizzle* and once with *SWarp*, look very different below the 3 to 3.5σ level, even though the ellipticities are correlated tightly (see Fig. 2.7). The same is true if two coadditions are created for the same data set, the first one with exposures with better PSFs, and the second one with the remaining exposures.

4.3 A case study: NGC 300

4.3.1 Field characteristics

One of the fields identified during the ASTROVIRTEL programme (see Sect. 2.1.2) was centred on NGC 300, a face-on spiral galaxy in the Sculptor group at a distance of about 2.1 Mpc (Freedman et al., 2001). Its angular size is $25' \times 18'$, occupying about 40% of the WFI@2.2 field of view. The field did thus not meet all requirements for GaBoDS, but the image seeing of a significant fraction of the R-band data (15 ksec) was around $1\farcs0$, so that a lensing analysis became feasible. Deep V-band observations ($\sim$ 37 ksec, $1\farcs1$ image seeing) were available too. The WFI@2.2 data for NGC 300 was taken in 34 nights between July 1999 and January 2000 for an identification of the Cepheid population in this galaxy (Pietrzynski et al., 2002a).

Upon visual inspection in the Digitized Sky Survey (DSS) before the data retrieval request, two concentrations of fainter galaxies were recognised North-East and South-East of NGC 300, at the edge of the WFI@2.2 field. 21 spectra were taken for the first concentration by Cappi et al. (1998), confirming a galaxy cluster at $z = 0.165$. The second, less prominent concentration is known as EDCC-499 at $z = 0.117$ (Collins et al., 1995). Hereafter, these two clusters are refered to as CL0056.03 and CL0056.02, respectively, using their epoch 2000.0 right ascensions.

Data reduction and catalogue creation The data was reduced essentially in the same way as described in Chapter 2. Due to the large extent of this galaxy, however, a superflat could only be calculated for the field outside NGC 300. Pixels lying inside the galaxy were only corrected for the gain differences, which were determined from the unaffected outer area. The same held for the sky subtraction of individual images before the coaddition process.

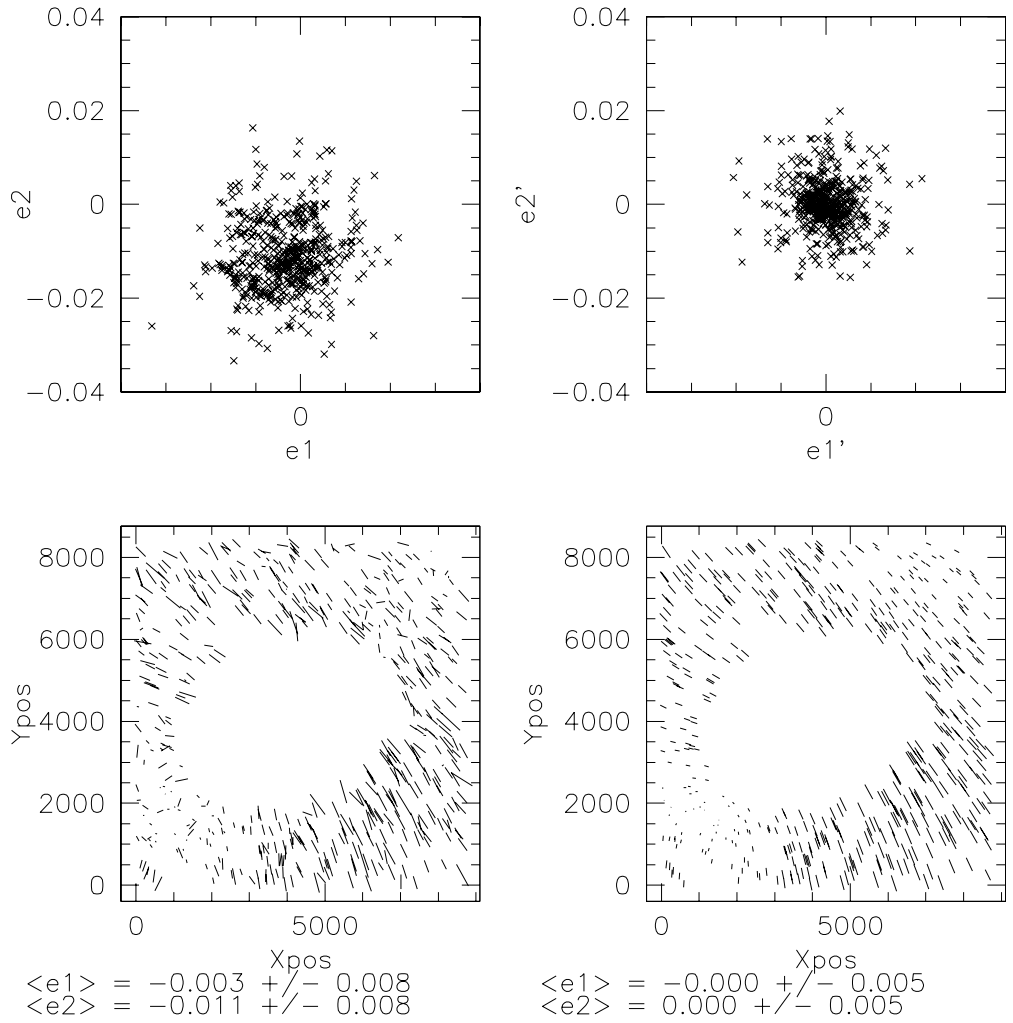

Figure 4.5: PSF anisotropies in the NGC 300 R-band image. Upper left: before correction. Upper right: after correction. Lower left: anisotropies as measured in the image. Lower right: a two-dimensional polynomial fit to the PSF anisotropies.

The sky was modeled outside NGC 300 and assumed to be constant inside, so that no discrete jumps appeared between the inner and outer part. This image was then smoothed with a large kernel and subtracted. A substantial part of the images suffered from secondary scattering light, and from occasional vignetting caused by the filter holder. Most affected was the south-eastern corner of the field, where CL0056.02 is located. This cluster was therefore excluded from the subsequent analysis.

The photometric zeropoint of the coadded V-band image was determined by matching stellar magnitudes to the secondary standard stars established by Pietrzynski et al. (2002b) in the Johnson-Cousins system. No calibration was available for the R-band, for which a zeropoint was determined based on the expected $V - R$ colours for the elliptical galaxies in CL0056.03. This zeropoint is estimated to be accurate within $0\overset{\mathrm{m}}{.}1$, which is sufficient for the analysis presented here since a highly accurate absolute photometry is not required.

For the catalogue creation NGC 300 was masked and replaced by the mean sky background in order to avoid any biasing of the source detection algorithm. Thus, most of the flux present in the image was removed. With *SExtractor* all objects with at least 6 connected pixels $\geq 2\sigma$ above the sky background noise were detected. This catalogue contained 44146 objects, for which shear estimates were obtained with KSB after PSF correction (Fig. 4.5). After filtering ($\nu_{\max} > 12$, $R > 23.0$), the catalogue of the background galaxies contained 12694 objects with reliable shapes, corresponding to a number density of ~ 20 galaxies arcmin^{-2}.

4.3.2 *S*-statistics for the NGC 300 field

Fig. 4.7 shows the S-statistics for the POLY filter on the $4'$ scale. As can be seen, CL0056.03 is recovered at the 3σ level within 50–100″ south of the cluster centre. It is seen on a similar level also for filter scales up to $6'$. CL0056.02 at the very lower left is not or only marginally detected, since useful shear information could only be obtained from about 30% of the area which would be available if the cluster did not lie next to the field corner in a region with bad image quality. The argument of field truncation also holds for CL0056.03, but to a much lesser extent. There the useable field was limited by the edge of the image, $2'.5$ east of the cluster centre, and NGC 300 $5'.5$ to the South-West. From Fig. 3.7 and the cluster redshift of $z = 0.165$ it is concluded that a mass of $\sim 1.4 \times 10^{14} M_{\odot}$ would produce a comparably significant lensing detection. This is a lower limit, since the number of galaxies with a measured shear signal was reduced by the field geometry, thus decreasing the detection S/N.

The S-statistics furthermore picks up a number of other peaks at various filter scales (clumps A and C). The latter one rises to the 3σ level on the $3'$ scale. Besides, a stable peak is found inside the mask of NGC 300 at the $3.0 - 3.5\sigma$ level for filter scales of $3'$ to $6'$. Such a detection is not surprising, since $M_{\rm ap}$ is a highly non-local measure. It can pick up those parts of the shear field of a possible cluster hidden behind NGC 300 that extend beyond NGC 300 itself, provided that this putative cluster is massive enough. The detection in question is at the very outer edge of the galaxy disk, but the confusion limit of foreground stars in NGC 300 is already reached. Yet the optical thickness of the disk is still small enough close to the edge, so that larger and brighter galaxies can be seen through the galaxy. Thus, if there was a massive lower redshift cluster such as CL0056.03 at this position, it could be directly identified. More distant clusters, however, could no longer be seen as such, since their smaller and fainter images are drowned in the foreground confusion. At the position of this hidden peak no optical counterpart could be identified, but clumps A and C lie within 20–70″ and 50″ of two concentrations of red galaxies, as is shown in the next section.

4.3.3 Peak verification

The red cluster sequence technique Apart from a spectroscopic confirmation of optical counterparts, multi-colour data can be used do exclude a chance projection of galaxies at various redshifts, mimicking a larger galaxy cluster. This method makes use of the fact that due to the consumption of gas during cluster formation no new stars can be formed any more, and thus the stellar populations of the cluster galaxies have similar ages and colours. Clusters can therefore be identified by searching for overdensities of galaxies with similar properties in multi-colour space (see Postman et al., 1996, for a description). Furthermore, richer clusters form a tight sequence in a colour-magnitude diagramme of the total galaxy population, a feature which is then easily picked up (Gladders & Yee, 2000).

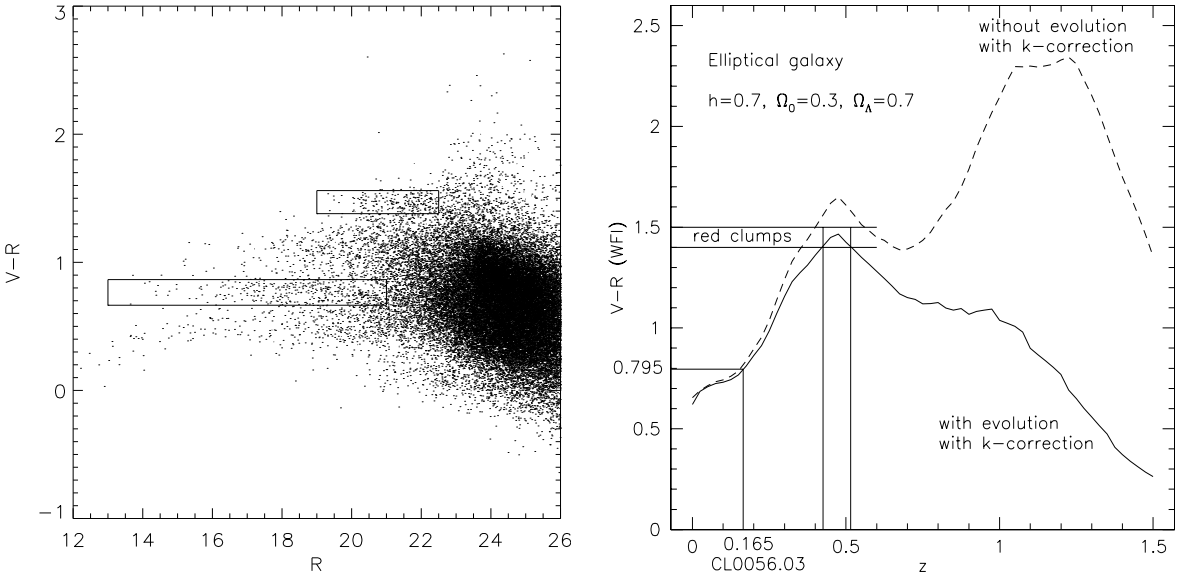

Figure 4.6: Left: colour-magnitude diagramme for all galaxies in the field. The large box marks the cluster sequence for CL0056.03. The small box outlines the only galaxies besides the members of CL0056.03 for which spatial clumping has been observed (see Fig. 4.9). Right: Shown are the predictions for WFI $V-R$ colours of elliptical galaxies as a function of redshift (Bolzonella et al., 2000; Bruzual & Charlot, 1993). Based on the track that includes evolutionary effects the redshifts of the cluster candidates are estimated.

In a ($V-R$, R)-colour-magnitude diagramme (Fig. 4.6), the red cluster sequence of CL0056.03 is indicated by the large box. The distribution of these galaxies on the sky is displayed in Fig. 4.8, where CL0056.03 as well as CL0056.02 stand out significantly over the rest of the field. By moving a smaller window over the galaxies in this colour-magnitude space, another population of redder galaxies ($V-R \approx 1.45$) was found that forms four very significant overdensities in the field (see Fig. 4.9). Two of them coincide with the shear-selected mass concentrations A and C. From the colours of the galaxies in these cluster candidates, redshift estimates of $z \approx 0.45-0.5$ were deduced (right panel of Fig. 4.6), which translates to mass estimates of $M_{\rm A}(4\farcm0) \approx (4\pm3)\times10^{14}\,M_\odot$ and $M_{\rm C}(3\farcm2) \approx (6\pm3)\times10^{14}\,M_\odot$ for the filter scales in which they are detected most significantly. These clusters are not yet spectroscopically confirmed.

X-ray observations In order to obtain further evidence for the physical existence of the presented mass concentrations, a 100 ksec X-ray exposure of NGC 300 taken with XMM-*Newton* by M. Turner (2002, unpublished) was overlaid over the optical data set in Fig. 4.10. However, the field of view of XMM is a bit smaller than the one for WFI@2.2, thus clump C is missed. Diffuse X-ray emission from the hot intra-cluster gas is detected at the fringes of CL0056.03, but not for clump A, which sits at the very edge of the field where the total throughput of XMM drops to 28% due to vignetting. Thus, a X-ray confirmation of the latter was not possible. From the detection that was made behind the disk of NGC 300 no X-ray flux is received, either.

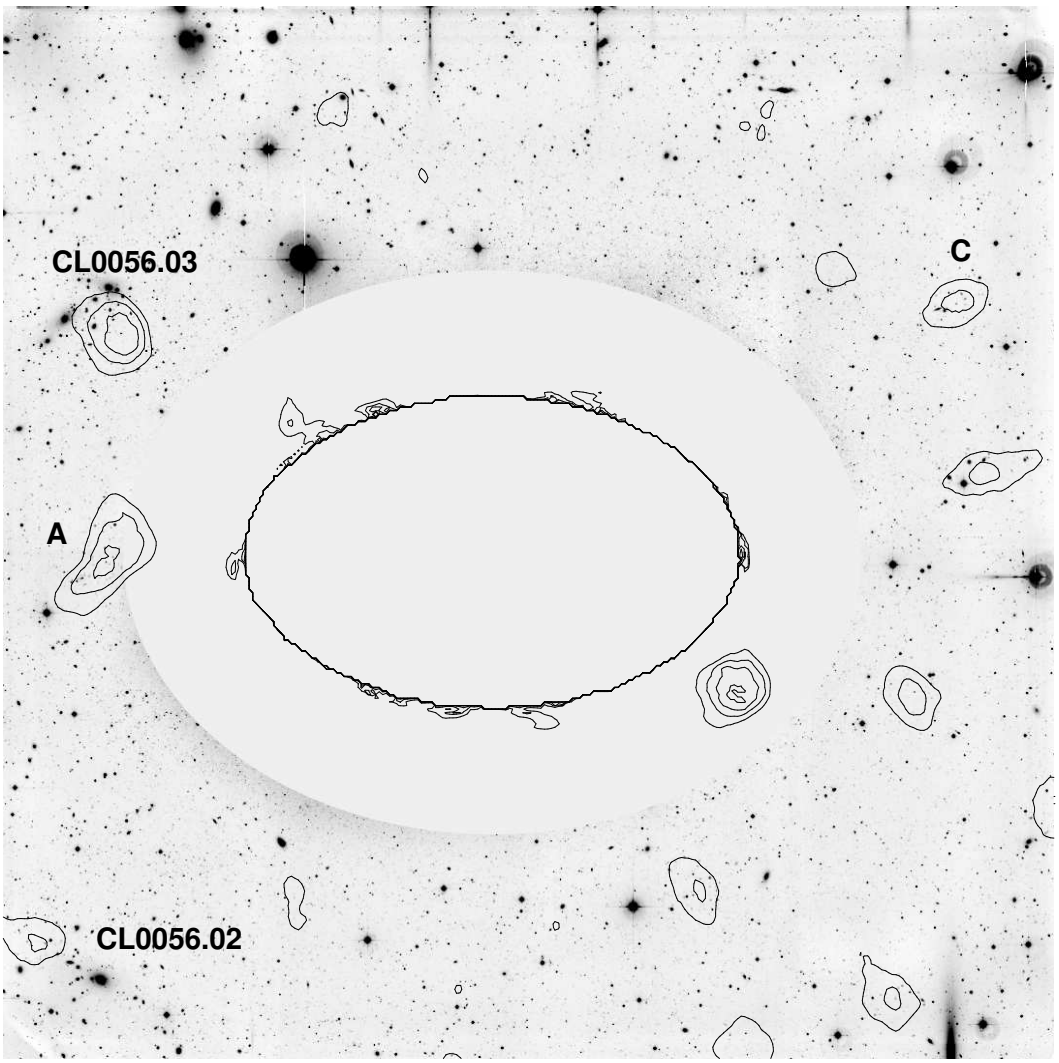

Figure 4.7: S-statistics for the NGC 300 field (POLY, $4'$). The contours depict the 2.0, 2.5, 3.0, 3.5σ levels. The large elliptical contour arises from the fact that $M_{\rm ap}$ can not be determined at the positions inside due to the absence of galaxies.

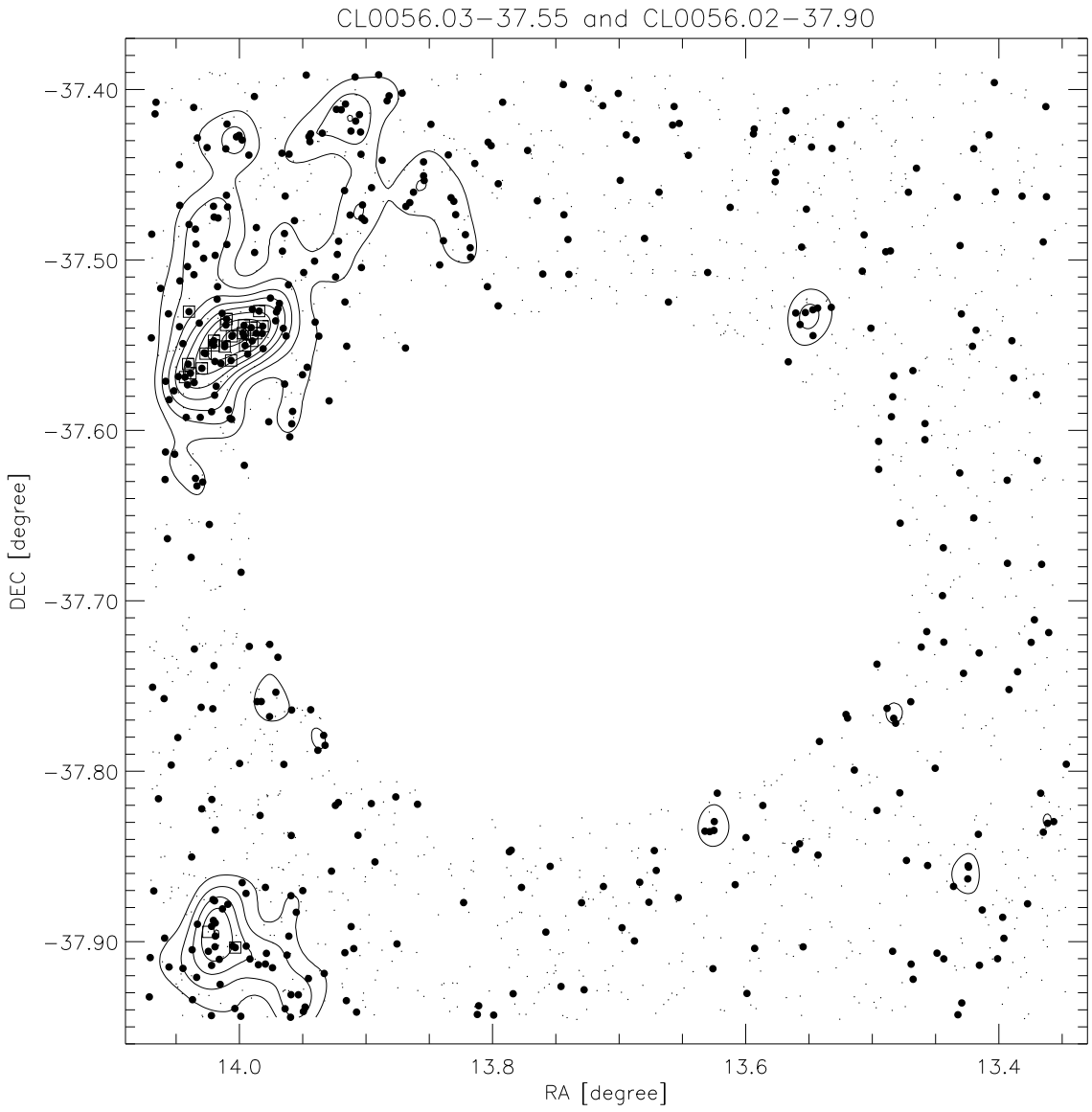

Figure 4.8: Positions of the galaxies that were selected in the colour-magnitude diagramme of Fig. 4.6 by the large box (big dots). The small dots indicate galaxies brighter than $R = 21$ which do not fall inside the red sequence window. The overlaid contours are isodensity contours for the red sequence members, smoothed at a 3.′6 scale, and starting with the 1σ-overdensity contour in steps of 1σ. CL0056.03 and CL0056.02 are detected at the 8σ and 5σ level, respectively. CL0056.03 appears strongly elongated, with an intersecting $12'$ long filament extending north-south at its eastern side. Part of the filament could belong to Abell S0102 at $(\alpha, \delta) = (13.91, -37.41)$, a poor cluster at $z = 0.05$. Galaxies with measured spectra are highlighted with small squares around them.

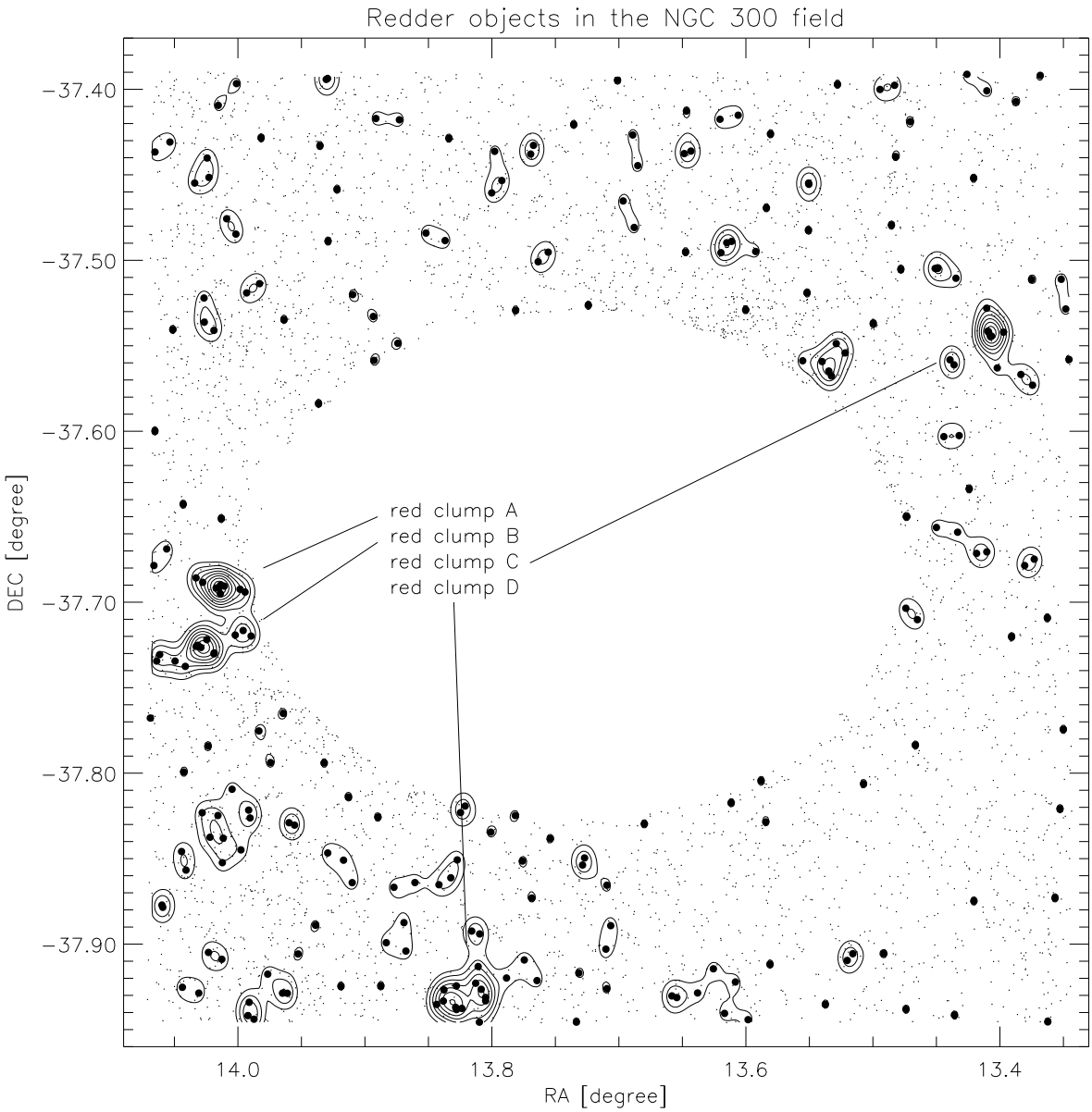

Figure 4.9: Positions of the galaxies that were selected in the colour-magnitude diagramme of Fig. 4.6 by the small box (big dots). These galaxies are shown as big dots, whereas all other galaxies brighter than $R = 22.5$ are resembled by the small dots. Overlaid are isodensity contours for the big dots, smoothed on the 1.′5 scale, and starting with the 1σ overdensity contour in steps of 1σ. The overdensities for clumps A to D are found at the 10, 7, 7, and 5σ levels, respectively.

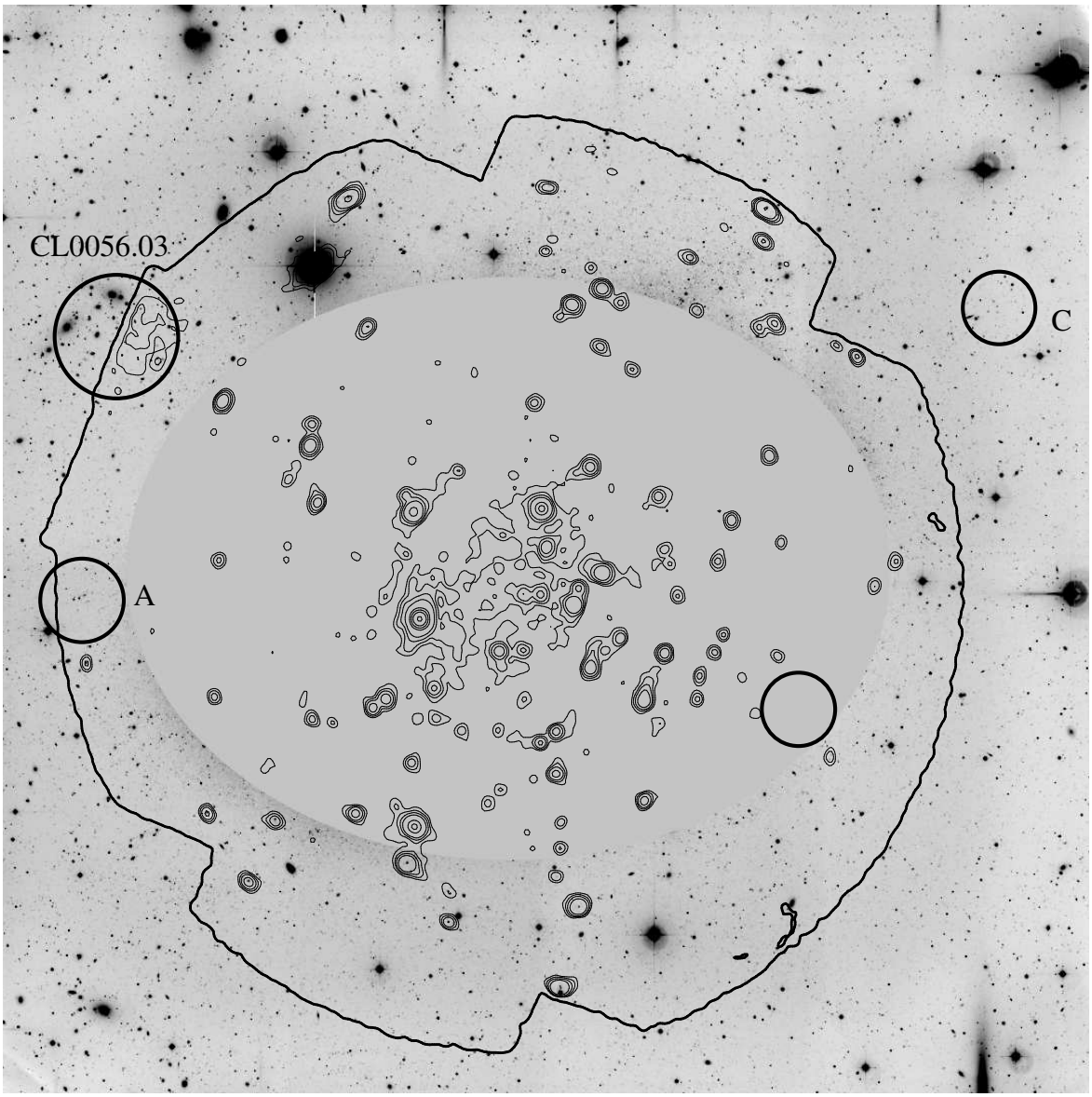

Figure 4.10: A 100 ksec XMM-*Newton* observation of the NGC 300 area. Shown are X-ray (0.3-6.0 keV) contours and the XMM field of view, superimposed on the optical WFI data. The most significant shear detections are indicated by the circles.

4.4 Future work

Increasing the sample In a first step, one can change the various thresholds in the catalogue creation process in a way that, e.g., only galaxies within the faintest 2 magnitudes instead of the faintest 3.5 magnitudes are used. Thus the sensitivity of the shear-selection method would be increased for more distant clusters of galaxies. Furthermore, the lower S/N-threshold of 4σ could be decreased to 3.5σ, which will increase the number of objects in the shear-selected sample by several hundred, but also the contamination by spurious noise detections. One might also try less conservative object detection thresholds for the *SExtractor* catalogue creation.

Spurious detections, real detections, dark detections A larger effort has yet to be undertaken in the analysis of the so-called noise peaks. It was demonstrated that highly significant noise peaks can appear, and that these can be distinguished from real peaks by means of the width of the S-profile above the 3σ-threshold. Noise peaks disappear again for filter scales not much larger or smaller than the one in which the peak was detected. This is because the galaxies mimicking the shear signal leave the aperture again, or get downweighted by the filter and by the large number of new galaxies with random orientations that enter the aperture. For these reasons the disproportionate occurrence of compact dark peaks that are seen in the smallest, $1\farcm6$ wide filter, could be due to noise (see Fig. 4.4). A real mass concentration, on the other hand, imprints its shear signal in principle at arbitrarily large radii, and it is only up to the depth of the exposure and the seeing to measure it to such distances. Therefore, a true peak is seen at a wider range of filter scales, i.e. its S-profile is wider than the one of a noise peak. A proper mathematical combination of the S-statistics for various filter scales could lead to a new definition of the S/N for the peaks under consideration, resulting in more efficient detection criteria. This has to take into acount a proper measure for the overlap of filters with similar scales.

An effect that has to be further investigated is the disproportionately large number of noise peaks in data sets with randomised ellipticities, as compared to the observed data. Adding increasingly larger random angles to the true galaxy orientations will significantly contribute to the understanding of the nature of the peaks observed. This, in turn, will yield constraints on the minimum accuracy of the astrometric solution and the coaddition procedure used. The effects of these data reduction steps onto the weak lensing statistics presented must be investigated in more detail.

***M/L* ratios** Of great interest is a comparison of the mass-to-light ratios of the bright peaks in this sample with the peaks from flux-selected samples from similar surveys. Significant differences can be expected, as is indicated by the presence of dark peaks (which can not have a M/L ratio assigned). For this purpose, the corresponding fields have to be observed in bluer bands (B or V) for the identification of further cluster members and for an estimate of the cluster redshift (see Sect. 4.3).

A question which will probably remain unanswered for the next years is whether the dark peaks, if they are not a statistical fluke, are truly dark, or whether they consist of extremely red and relatively dark galaxies. First constraints on this were already obtained by Gray et al. (2001), but a lot more observations of these targets with the largest telescopes have to be made before one can come to a robust conclusion. If these dark clumps indeed turn out to

be dark, possibly consisting of dark matter only, then the question has to be answered why they did not attract any baryons contrary to their luminous cousins.

Cross-correlation with other surveys Even though this work has shown that there is good evidence for the existence of dark and bright mass concentrations in the universe that can be selected by weak gravitational lensing, one would like to gain even more faith in those detections. Spectroscopic follow-up observations of the bright peaks can confirm the existence of a cluster into a particular direction, and from the derived velocity dispersion a mass estimate can be obtained. However, the optical counterparts of a typical bright peak in the sample presented do not appear very rich. Therefore the velocity dispersion in conjunction with the virial theorem will yield unreliable results if only an insufficient number of spectra can be obtained, leaving open the question whether the mass peak is physically related to the galaxies seen, or whether it is a spurious detection that just happened to coincide with the light. The amount of the latter cases is cut down by the requirement of a $\geq 4\sigma$ detection, and further constraints can be obtained from the S-profile. Yet a statistical analysis that evaluates the probability of a noise peak to fall on top of a galaxy group would be very useful in this respect.

Closely related to this is the calculation of the correlation function between the S-map and the light map obtained for the particular line of sight. In addition, a correlation with the X-ray maps from the ROSAT All Sky Survey (Voges et al., 1999) should be performed, since at least some of the bright peaks (and maybe the dark peaks, too) could be filled with hot gas. Another analysis worth being done is a correlation of the mass peaks with the known quasars in the field. It is known that for the brightest quasars a positive correlation exists with flux-selected mass concentrations, since the latter ones magnify the quasars by their gravitational lensing effect (*magnification bias*). If such a correlation is found for the shear-selected mass concentrations too, then this would be a direct and independent verification for the existence of these objects. Furthermore, the correlation could be done with the dark peaks only. However, such a correlation measurement requires a homogeneously selected, flux-limited sample of quasars for the investigated area, which does not exist for the GaBoDS data. The recently started CFHT legacy survey can provide such a data set, since it goes deep enough for lensing studies, and allows for quasar classification based on a five-band multi-colour photometry.

Another possibility for proving the reality of dark peaks is the statistical combination of the number density of background galaxies behind the mass concentrations. In such a sample one can search for changes of the number density as a function of angular distance to the lens, since gravitational lensing leads to a magnification of the space behind the lens, thus diluting the galaxies in the corresponding volume projected on the sky. At the same time, however, the fluxes of the lensed background galaxies are enlarged, thus fainter objects can be detected which go unnoticed, otherwise (see Broadhurst et al., 1995, for further discussion). Whether the one or the other of these two effects dominates, depends on the slope of the luminosity function of the galaxies in the observed wavelength range. In the blue bands the two effects cancel each other, whereas in the red bands a diluting of the galaxies can be seen. For this purpose, carefully determined absolute photometric zeropoints must be determined for the GaBoDS fields.

Appendix A

Table A.1: Shear-selected mass concentrations

ID	α(2000.0)	δ(2000.0)	ν	z/class	Filter	x_c	Scale	Field
SSMC-001	00 44 52	-29 34 12	4.40	dark	TANH	2.0	2′.8	SGP
SSMC-002	00 44 55	-29 38 43	4.18	dark	POLY		2′.4	SGP
SSMC-003	00 45 15	-29 38 58	4.17	bright	TANH	2.0	3′.6	SGP
SSMC-004	00 45 20	-29 23 54	5.01	0.2	TANH	0.025	19′.8	SGP
SSMC-005	00 45 37	-29 48 31	4.31	0.5	TANH	0.05	6′.3	SGP
SSMC-006	00 45 50	-29 36 58	4.13	dark	TANH	0.025	5′.6	SGP
SSMC-007	00 45 58	-29 30 41	4.15	dark	TANH	0.025	5′.6	SGP
SSMC-008	00 46 25	-29 24 09	4.73	dark	POLY		7′.9	SGP
SSMC-009	00 46 37	-29 20 38	4.22	bright	TANH	0.1	3′.6	SGP
SSMC-010	01 05 03	-25 53 10	4.17	dark	TANH	2.0	2′.0	FDF
SSMC-011	01 06 33	-25 36 40	4.09	dark	TANH	1.0	1′.6	FDF
SSMC-012	03 31 11	-27 34 03	4.64	dark	TANH	0.5	5′.6	CDF-S
SSMC-013	03 31 40	-27 55 35	4.20	0.095	POLY		2′.4	CDF-S
SSMC-014	03 32 18	-27 58 44	4.02	0.125	TANH	0.2	2′.4	CDF-S
SSMC-015	03 32 30	-27 28 48	4.02	0.146	POLY		2′.4	CDF-S
SSMC-016	03 53 26	-49 42 27	5.02	dark	TANH	0.2	4′.8	AM1
SSMC-017	03 54 08	-49 38 45	4.05	0.22 (unclear)	TANH	2.0	9′.9	AM1
SSMC-018	03 56 16	-49 36 12	4.54	dark	TANH	0.2	3′.2	AM1
SSMC-019	04 20 31	-36 02 11	4.10	unclear	TANH	2.0	2′.4	Comparison
SSMC-020	05 03 58	-28 41 35	4.39	dark	TANH	0.1	4′.0	SHARC2
SSMC-021	05 06 01	-28 31 34	4.25	unclear	POLY		2′.0	SHARC2
SSMC-022	09 55 47	-10 00 07	4.63	0.160	TANH	2.0	6′.3	A901
SSMC-023	09 55 59	-09 45 59	4.00	dark	EXP		1′.6	A901
SSMC-024	09 56 24	-09 56 31	6.30	0.160	TANH	0.1	19′.8	A901
SSMC-025	10 06 15	-00 08 32	4.13	0.185	TANH	2.0	2′.8	Pal3
SSMC-026	10 40 03	-11 51 28	4.19	bright	TANH	0.5	2′.4	CL1040-1155
SSMC-027	10 41 01	-12 03 35	4.07	dark	TANH	1.0	9′.9	CL1040-1155
SSMC-028	10 53 35	-12 53 05	4.18	$0.07 - 0.122$	TANH	0.1	5′.6	CL1054-1245
SSMC-029	10 54 54	-11 53 54	4.13	dark	POLY		2′.0	CL1054-1146
SSMC-030	10 54 58	-11 33 38	4.07	dark	TANH	0.05	3′.6	CL1054-1146
SSMC-031	10 58 32	-13 02 25	4.21	unclear	TANH	0.1	5′.6	CL1059-1253
SSMC-032	10 59 17	-12 53 37	4.02	$0.4 - 0.6$	TANH	2.0	6′.3	CL1059-1253
SSMC-033	10 59 45	-13 05 16	4.19	bright	POLY		2′.4	CL1059-1253
SSMC-034	11 16 26	-21 46 57	4.53	unclear	TANH	2.0	3′.2	DEEP3d
SSMC-035	11 17 36	-21 34 08	4.24	bright	TANH	0.1	5′.6	DEEP3d
SSMC-036	11 18 22	-11 27 06	4.38	bright	TANH	0.5	5′.6	CL1119-1129
SSMC-037	11 18 36	-21 53 46	4.25	dark	TANH	0.1	1′.6	DEEP3d
SSMC-038	11 19 00	-21 43 09	4.07	dark	POLY		17′.8	DEEP3c
SSMC-039	11 25 24	-21 35 25	4.38	bright	POLY		2′.0	DEEP3a
SSMC-040	11 26 10	-21 56 44	4.21	unclear	TANH	0.2	3′.2	DEEP3a

Table A.2: Shear-selected mass concentrations (continued)

ID	α(2000.0)	δ(2000.0)	ν	z/class	Filter	x_c	Scale	Field
SSMC-041	11 39 51	-25 36 26	4.02	bright	TANH	0.05	7′.9	A1347_P1
SSMC-042	11 41 08	-25 26 59	4.00	dark	TANH	0.1	1′.6	A1347_P1
SSMC-043	11 41 25	-24 59 23	4.21	unclear	TANH	0.025	6′.3	A1347_P3
SSMC-044	11 41 41	-24 43 36	4.32	dark	TANH	0.05	7′.1	A1347_P3
SSMC-045	11 41 53	-01 38 18	4.39	bright	POLY		2′.4	S11
SSMC-046	11 42 02	-01 29 35	4.27	dark	TANH	0.5	1′.6	S11
SSMC-047	11 42 21	-01 45 19	4.43	dark	TANH	0.5	1′.6	S11
SSMC-048	11 42 26	-01 39 30	4.76	dark	TANH	2.0	2′.8	S11
SSMC-049	11 42 26	-01 31 17	4.27	bright	TANH	0.05	13′.9	S11
SSMC-050	11 42 40	-01 53 18	4.05	0.119	POLY		2′.8	S11
SSMC-051	11 43 15	-01 29 06	4.07	unclear	POLY		1′.6	S11
SSMC-052	11 43 30	-24 45 48	4.02	dark	TANH	0.1	2′.8	A1347_P4
SSMC-053	11 43 33	-01 45 19	4.87	0.106	TANH	0.025	13′.9	S11
SSMC-054	12 05 46	-07 36 25	4.48	dark	POLY		13′.9	NDF
SSMC-055	12 05 57	-07 20 45	4.30	dark	TANH	0.1	7′.9	NDF
SSMC-056	12 15 33	-12 16 41	4.63	bright	TANH	0.5	2′.4	CL1216-1201
SSMC-057	12 17 01	-11 50 48	4.43	dark	TANH	0.5	4′.0	CL1216-1201
SSMC-058	12 17 09	-12 02 09	4.01	bright	TANH	2.0	5′.6	CL1216-1201
SSMC-059	12 17 13	-11 46 34	4.64	dark	TANH	0.2	3′.2	CL1216-1201
SSMC-060	13 02 23	-11 50 19	4.40	dark	POLY		3′.2	CL1301-1139
SSMC-061	13 02 37	-11 20 26	4.18	bright	TANH	2.0	9′.9	CL1301-1139
SSMC-062	13 52 45	-11 24 54	4.64	bright	TANH	0.025	11′.9	CL1353-1137
SSMC-063	14 16 23	-12 11 40	4.39	dark	TANH	2.0	3′.6	C0400
SSMC-064	14 16 54	-12 21 06	4.28	dark	POLY		5′.6	C0400
SSMC-065	14 19 00	-11 24 29	4.64	dark	TANH	2.0	5′.6	C04p2
SSMC-066	14 19 04	-14 13 13	4.22	dark	TANH	2.0	2′.4	C04m4
SSMC-067	14 20 06	-12 28 50	4.08	dark	TANH	2.0	2′.4	CL1420-1236
SSMC-068	14 20 08	-12 39 15	4.37	dark	POLY		6′.3	CL1420-1236
SSMC-069	14 20 25	-13 30 24	4.43	dark	TANH	1.0	2′.4	C04m3
SSMC-070	14 20 52	-12 35 28	4.03	dark	TANH	0.2	6′.3	CL1420-1236
SSMC-071	14 21 16	-12 35 56	4.05	dark	TANH	0.1	4′.0	CL1420-1236
SSMC-072	14 21 53	-13 37 35	4.01	dark	TANH	0.05	4′.0	C04m3
SSMC-073	14 24 20	-34 38 34	4.07	dark	TANH	0.5	2′.4	F17_P1
SSMC-074	14 27 00	-34 35 53	4.28	dark	TANH	2.0	1′.6	F17_P1
SSMC-075	21 26 37	-40 31 51	4.11	dark	TANH	0.5	2′.0	F4_P1
SSMC-076	21 27 44	-40 31 21	4.09	bright	TANH	0.2	3′.6	F4_P1
SSMC-077	21 27 56	-40 25 09	4.02	dark	TANH	0.2	2′.0	F4_P3
SSMC-078	21 28 21	-39 59 14	4.00	dark	TANH	1.0	2′.4	F4_P3
SSMC-079	21 28 44	-40 26 23	4.06	dark	EXP		2′.0	F4_P3
SSMC-080	21 29 06	-39 47 25	4.13	dark	TANH	0.025	7′.9	F4_P4

Table A.3: Shear-selected mass concentrations (continued)

ID	α(2000.0)	δ(2000.0)	ν	z/class	Filter	x_c	Scale	Field
SSMC-081	21 30 23	-39 41 20	4.00	dark	TANH	0.1	3.′2	F4_P4
SSMC-082	22 40 12	-09 44 03	5.10	dark	TANH	0.05	17.′8	B8p0
SSMC-083	22 40 19	-10 09 34	4.29	unclear	TANH	0.05	19.′8	B8m1
SSMC-084	22 40 21	-10 24 22	4.12	dark	TANH	1.0	2.′4	B8m2
SSMC-085	22 40 23	-09 37 48	4.05	dark	POLY		7.′1	B8p0
SSMC-086	22 40 25	-09 21 02	4.61	dark	EXP		4.′0	B8p0
SSMC-087	22 40 26	-09 46 30	4.87	dark	POLY		3.′6	B8p0
SSMC-088	22 40 29	-09 35 33	4.35	dark	TANH	0.2	2.′0	B8p0
SSMC-089	22 40 32	-08 23 01	4.13	bright	TANH	0.05	15.′9	B8p2
SSMC-090	22 40 41	-09 21 56	4.59	bright	TANH	0.5	3.′2	B8p0
SSMC-091	22 40 51	-09 17 24	4.97	bright	POLY		4.′0	B8p1
SSMC-092	22 40 52	-08 11 08	4.07	dark	TANH	0.1	6.′3	B8p3
SSMC-093	22 41 25	-11 18 44	4.11	dark	POLY		2.′0	B8m3
SSMC-094	22 41 26	-10 01 58	4.25	dark	TANH	0.1	1.′6	B8m1
SSMC-095	22 41 29	-09 08 54	4.11	dark	TANH	2.0	3.′6	B8p1
SSMC-096	22 41 47	-10 17 11	4.27	dark	TANH	0.5	2.′0	B8m1
SSMC-097	22 42 03	-09 38 01	4.14	dark	TANH	1.0	2.′0	B8p0
SSMC-098	22 42 06	-09 03 05	4.11	dark	POLY		3.′2	B8p1
SSMC-099	22 50 21	-40 06 04	4.02	unclear	TANH	0.5	3.′6	DEEP1c
SSMC-100	22 54 20	-40 06 51	4.35	0.151	TANH	0.05	7.′9	DEEP1a

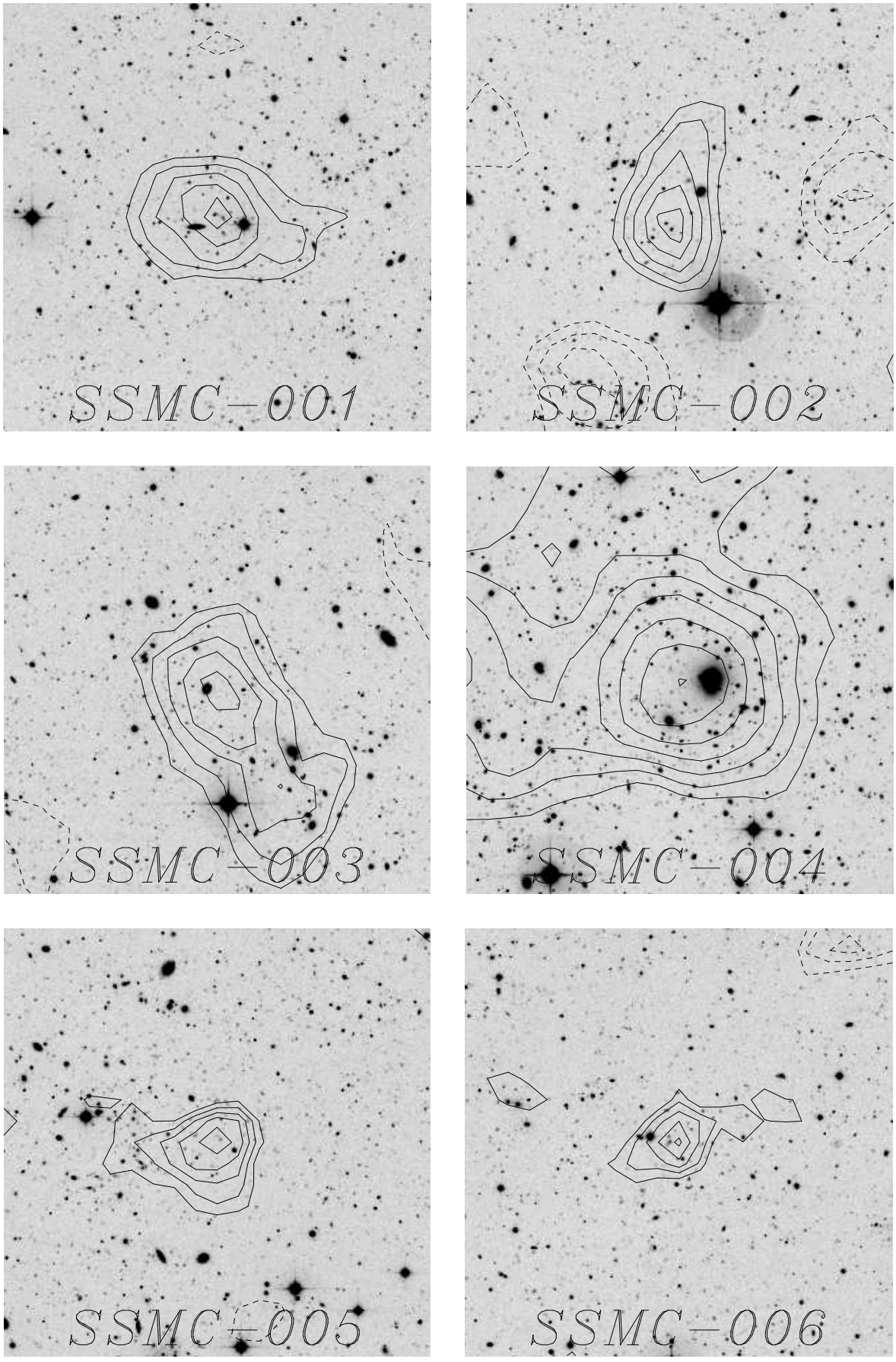

Figure A.1: Shear selected mass concentrations (a)The field of view in all these plots is 4′.3.

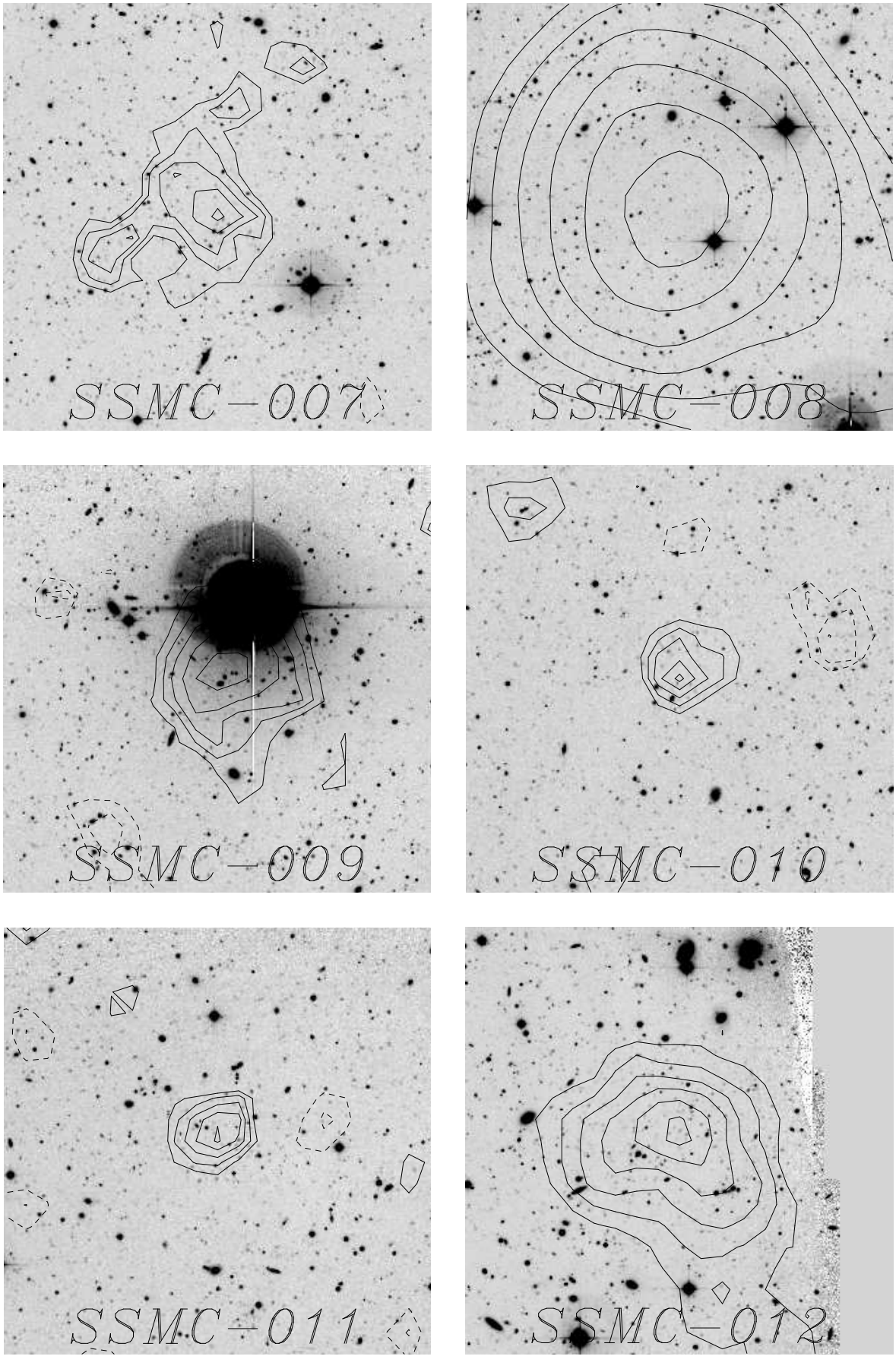

Figure A.2: Shear selected mass concentrations (b)

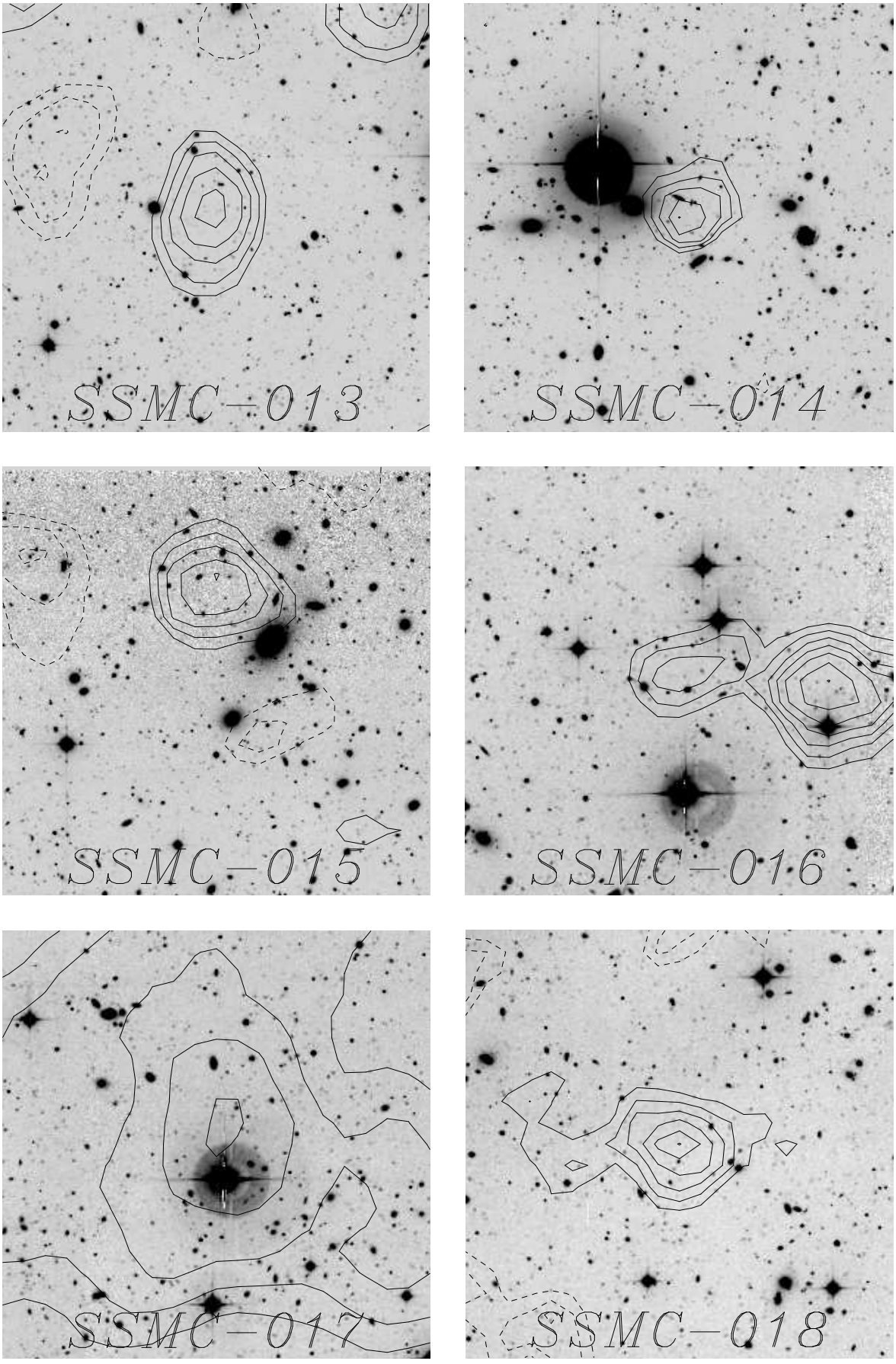

Figure A.3: Shear selected mass concentrations (c)

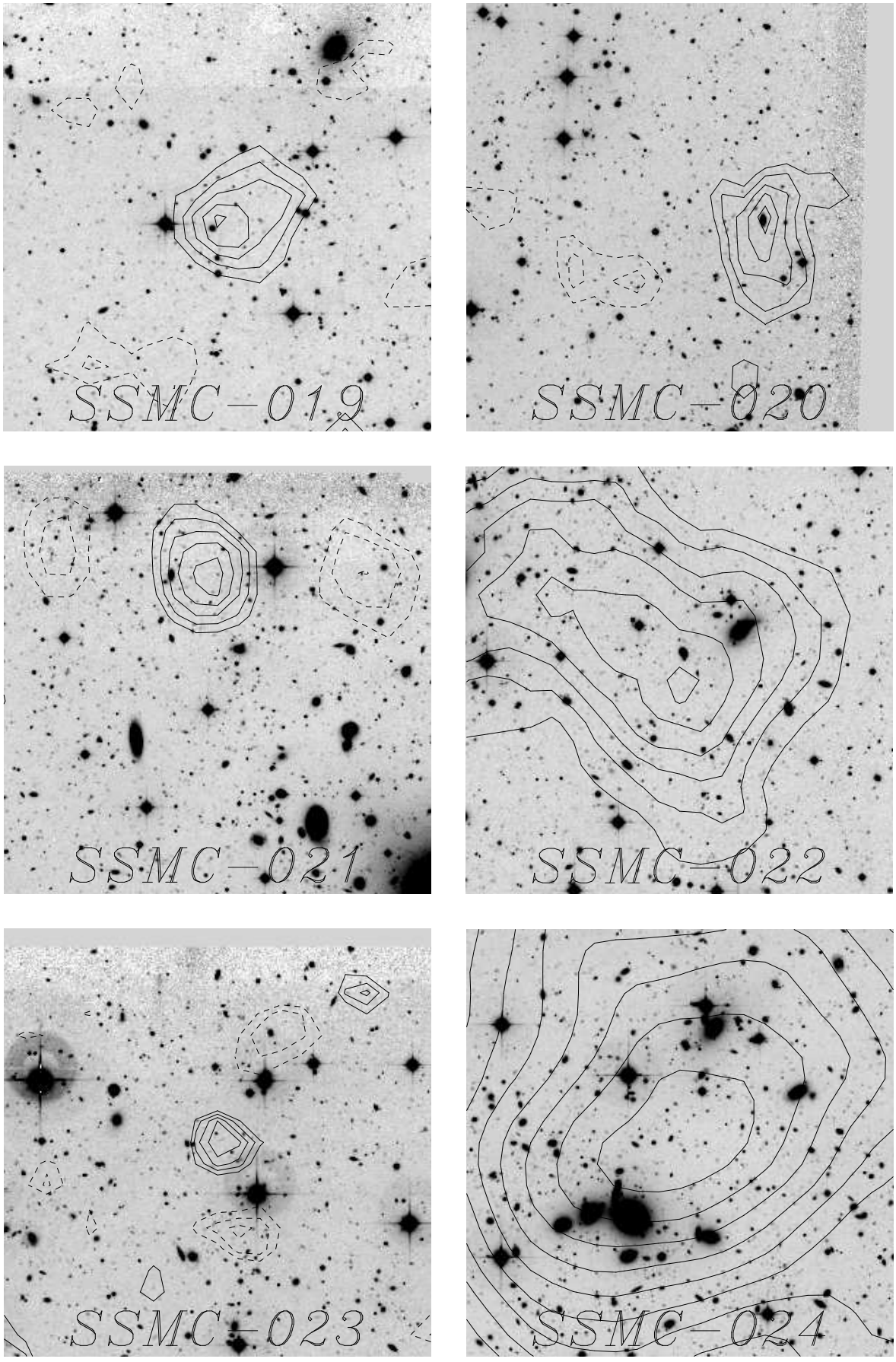

Figure A.4: Shear selected mass concentrations (d)

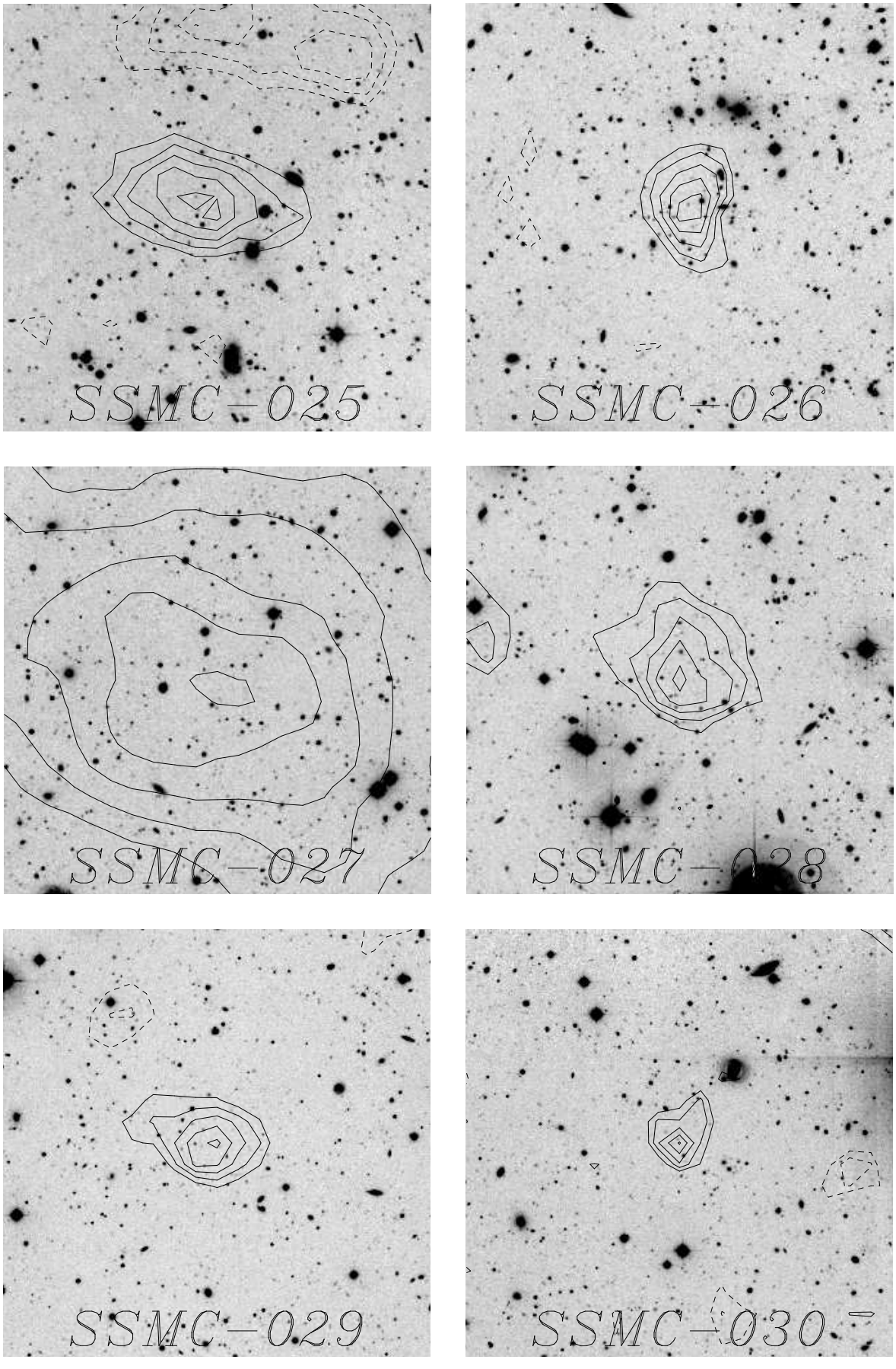

Figure A.5: Shear selected mass concentrations (e)

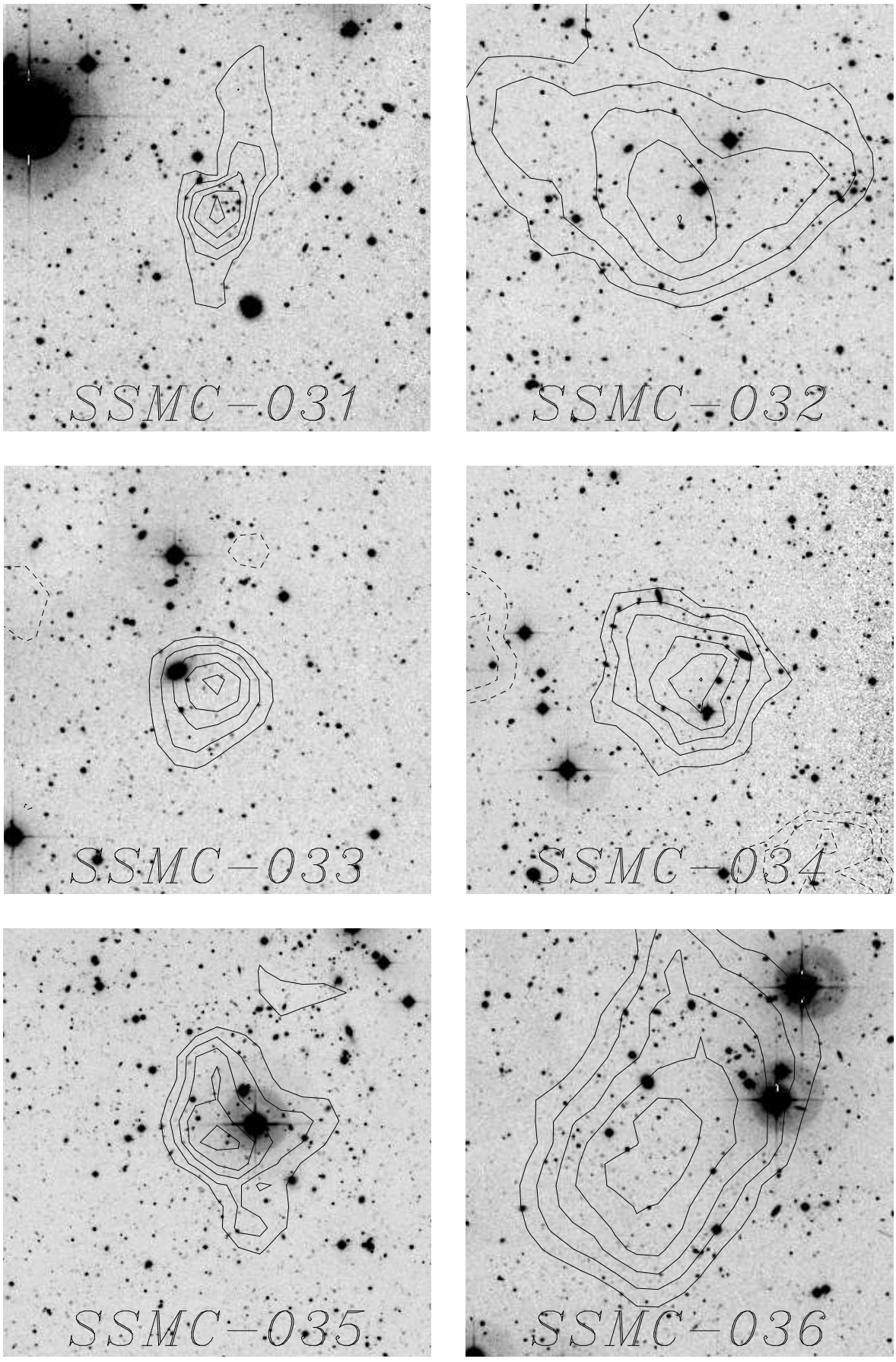

Figure A.6: Shear selected mass concentrations (f)

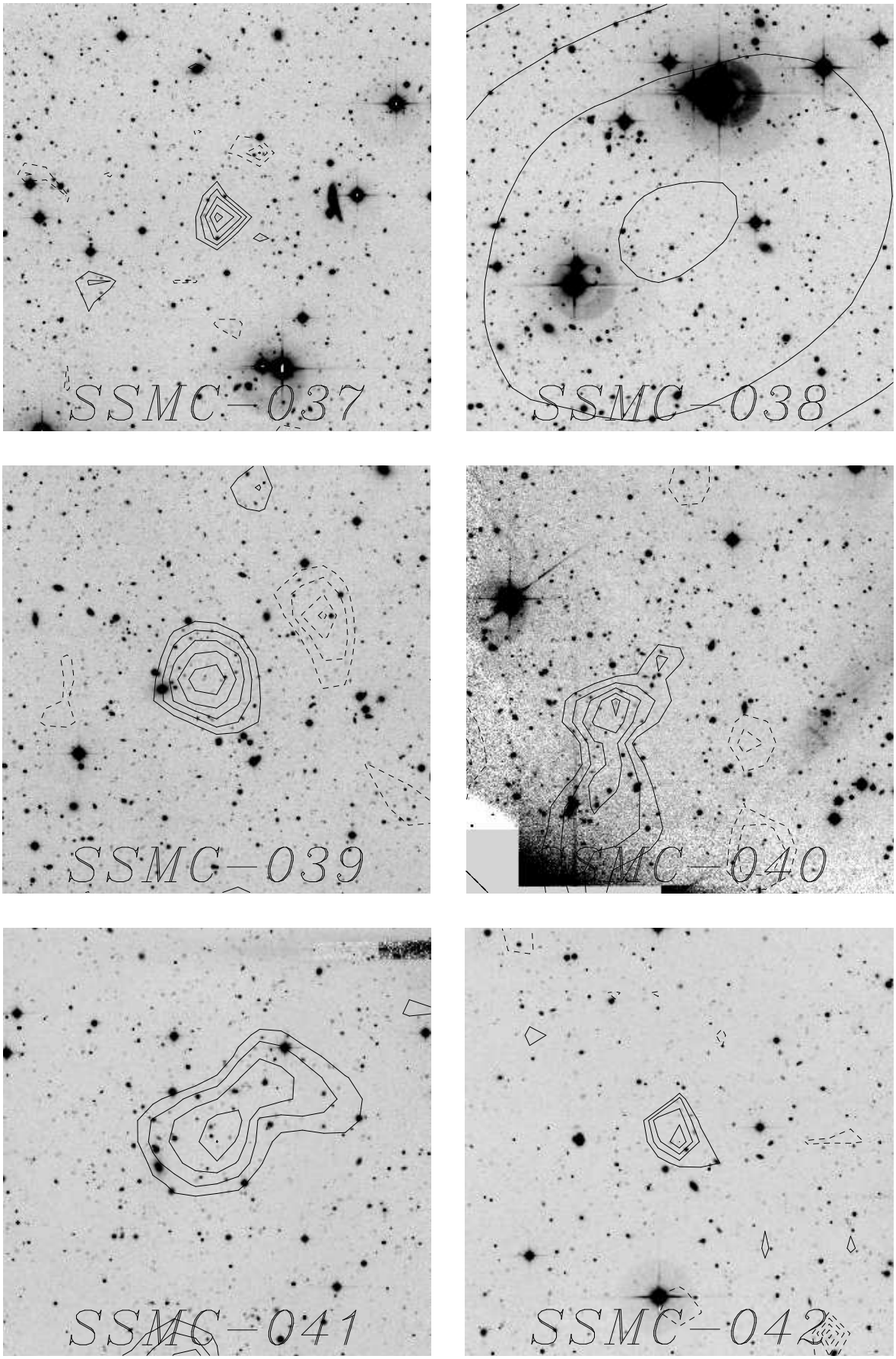

Figure A.7: Shear selected mass concentrations (g)

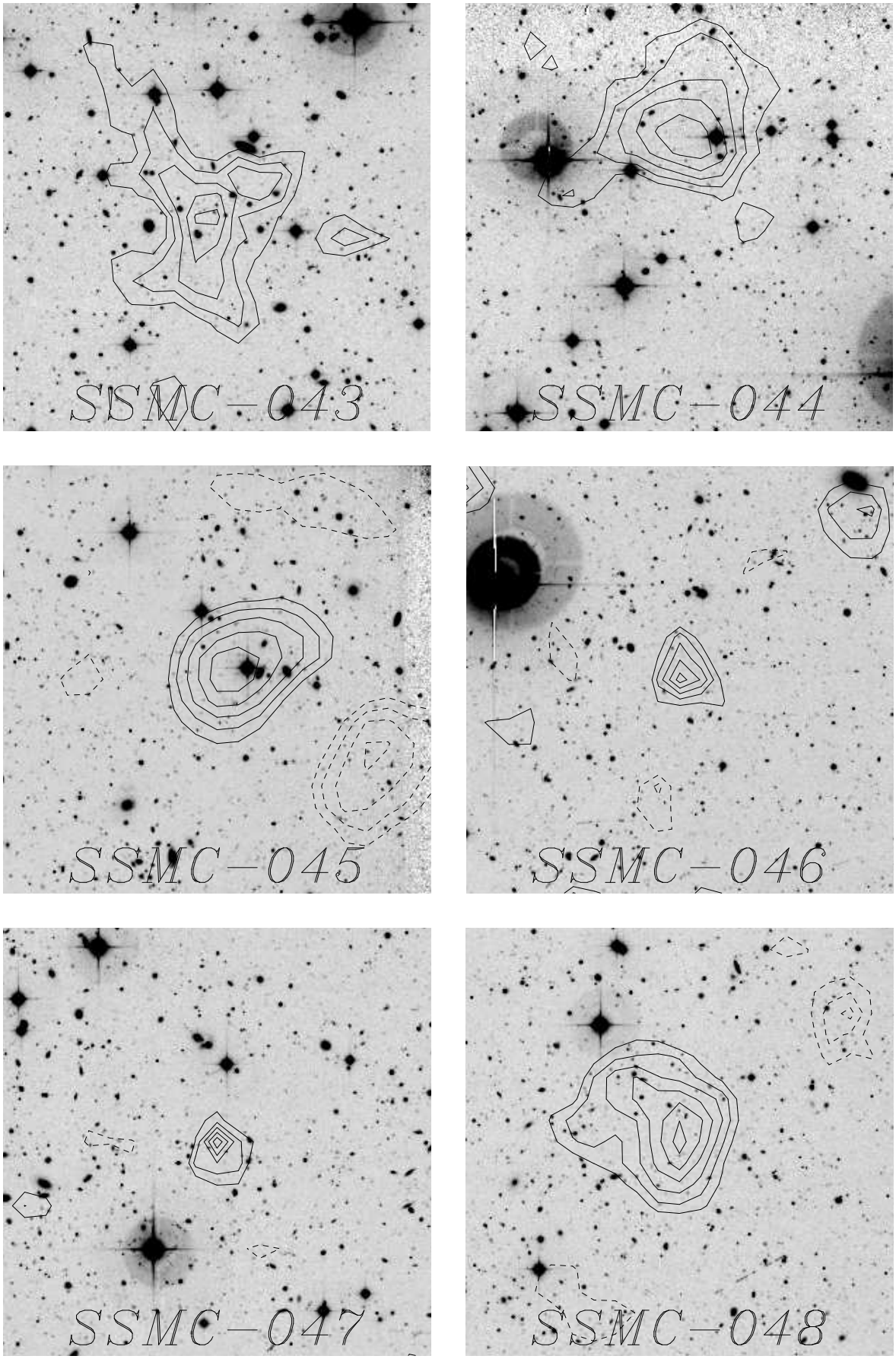

Figure A.8: Shear selected mass concentrations (h)

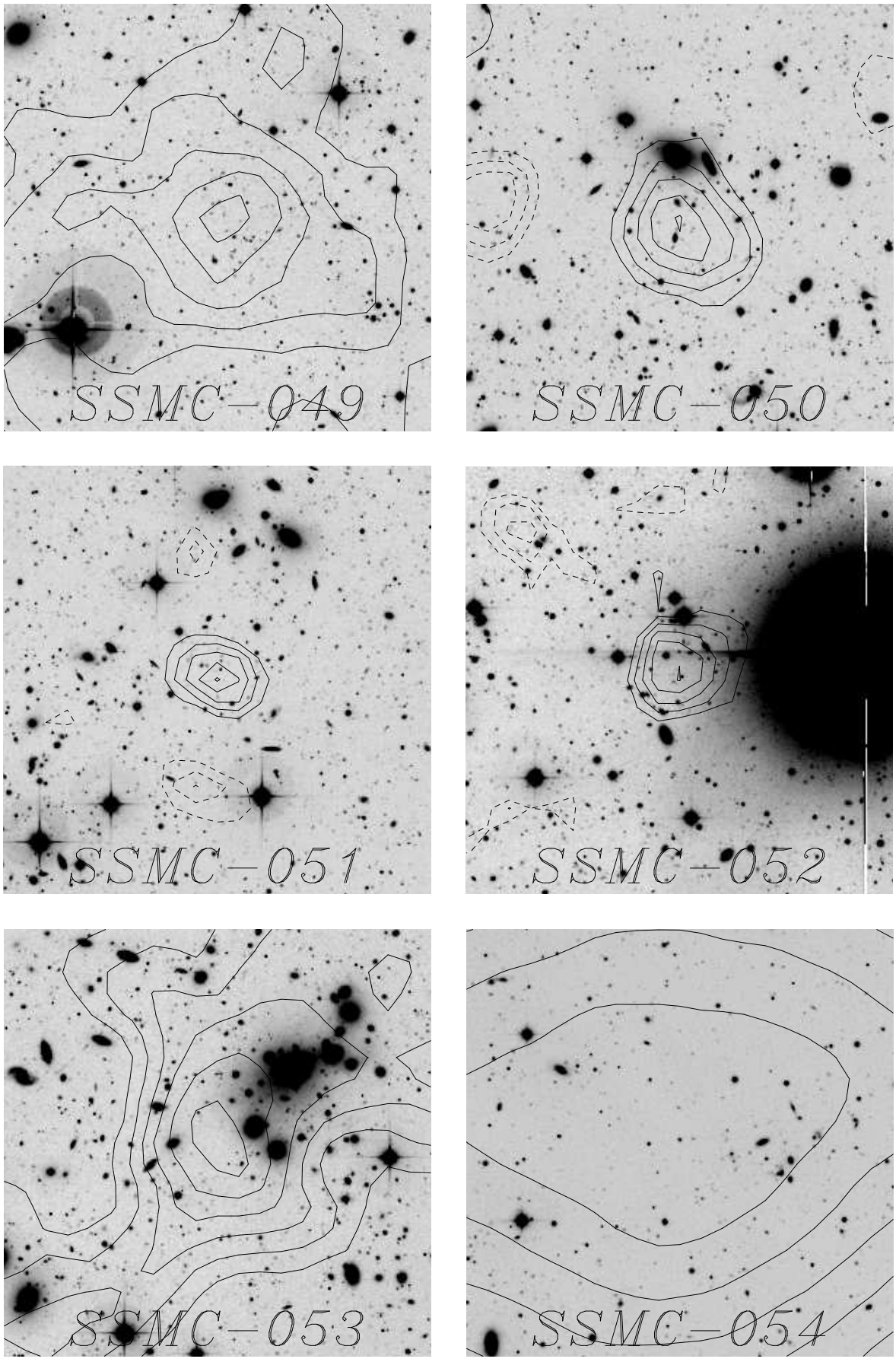

Figure A.9: Shear selected mass concentrations (i)

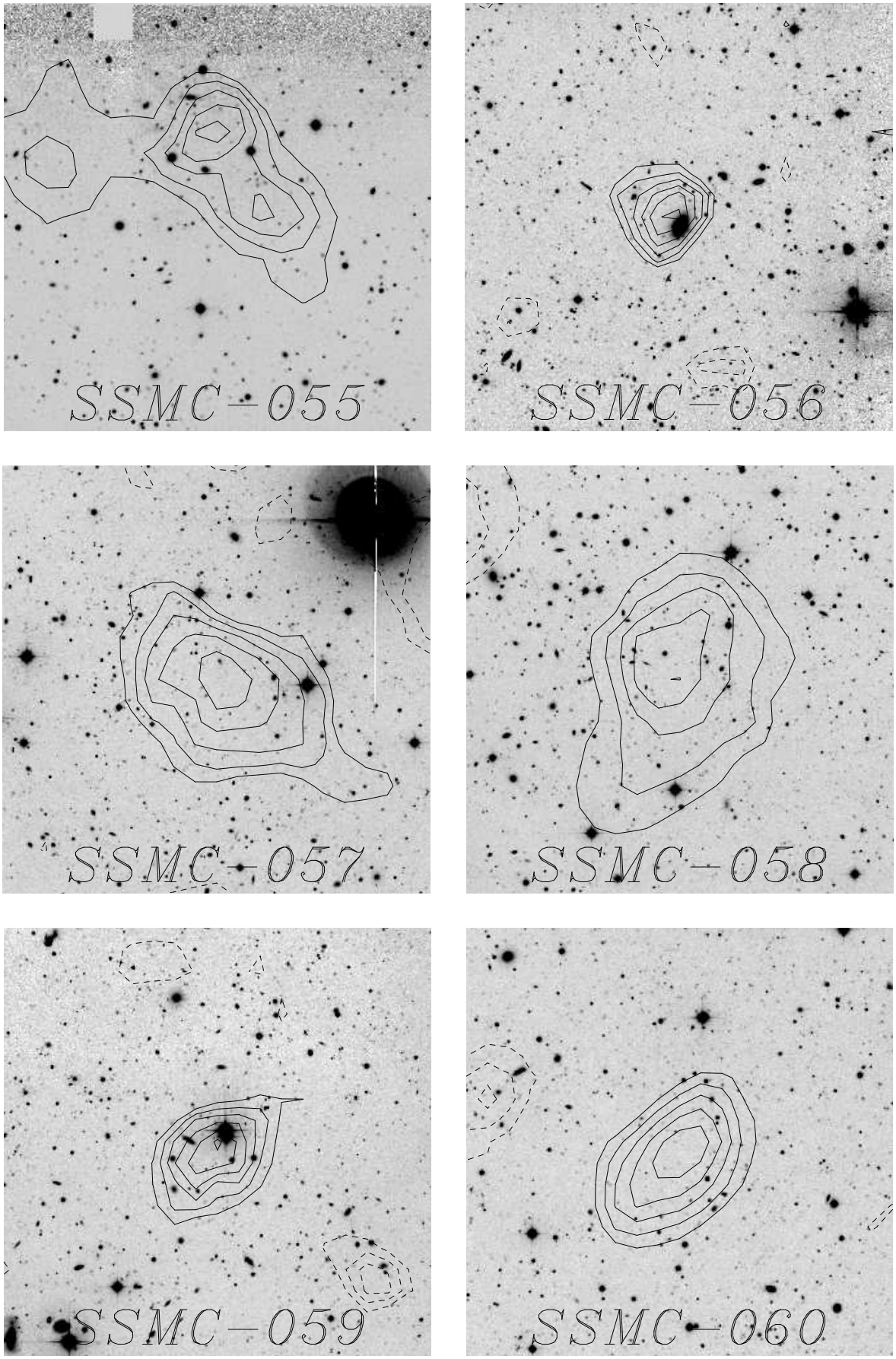

Figure A.10: Shear selected mass concentrations (j)

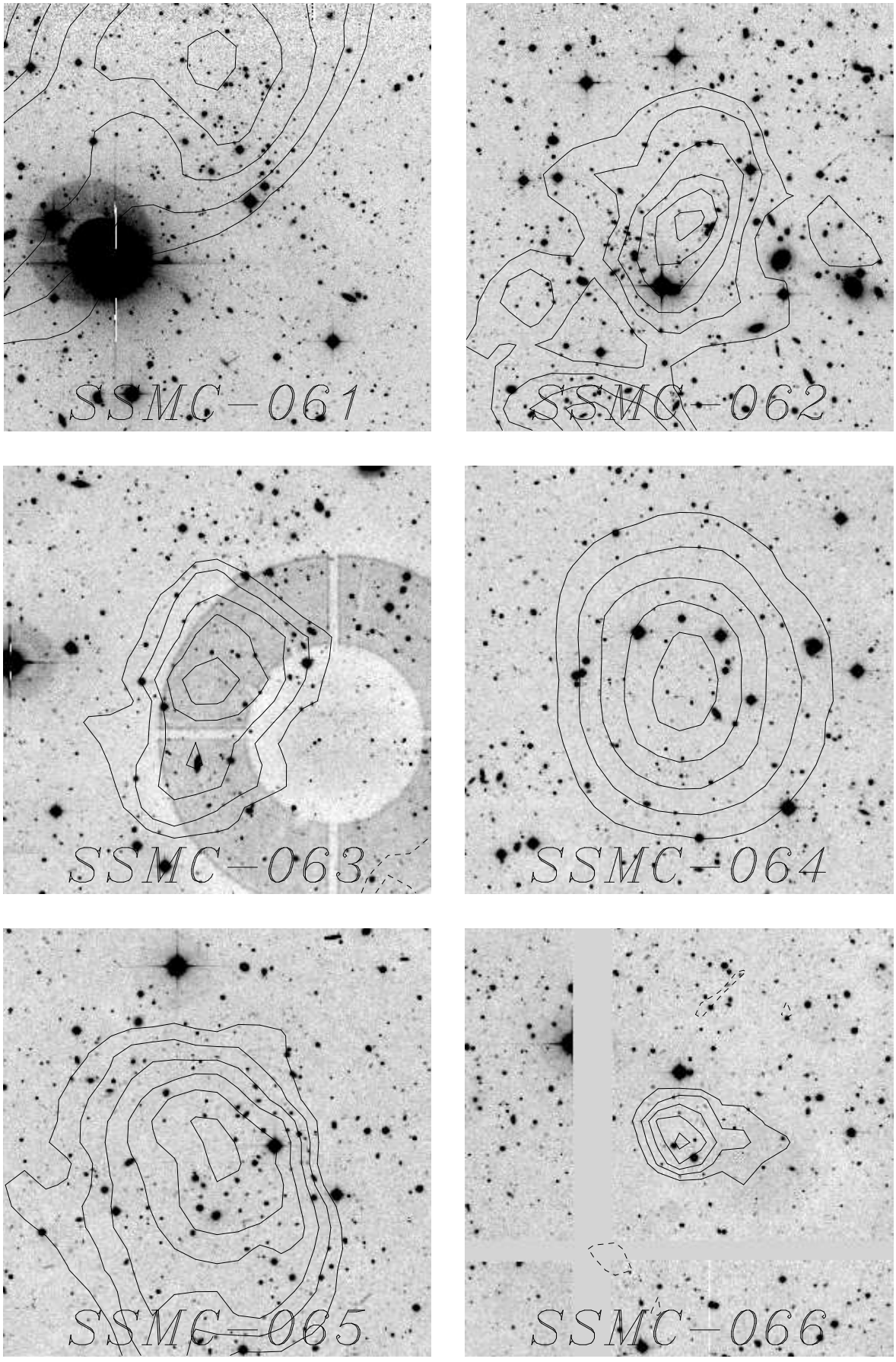

Figure A.11: Shear selected mass concentrations (k)

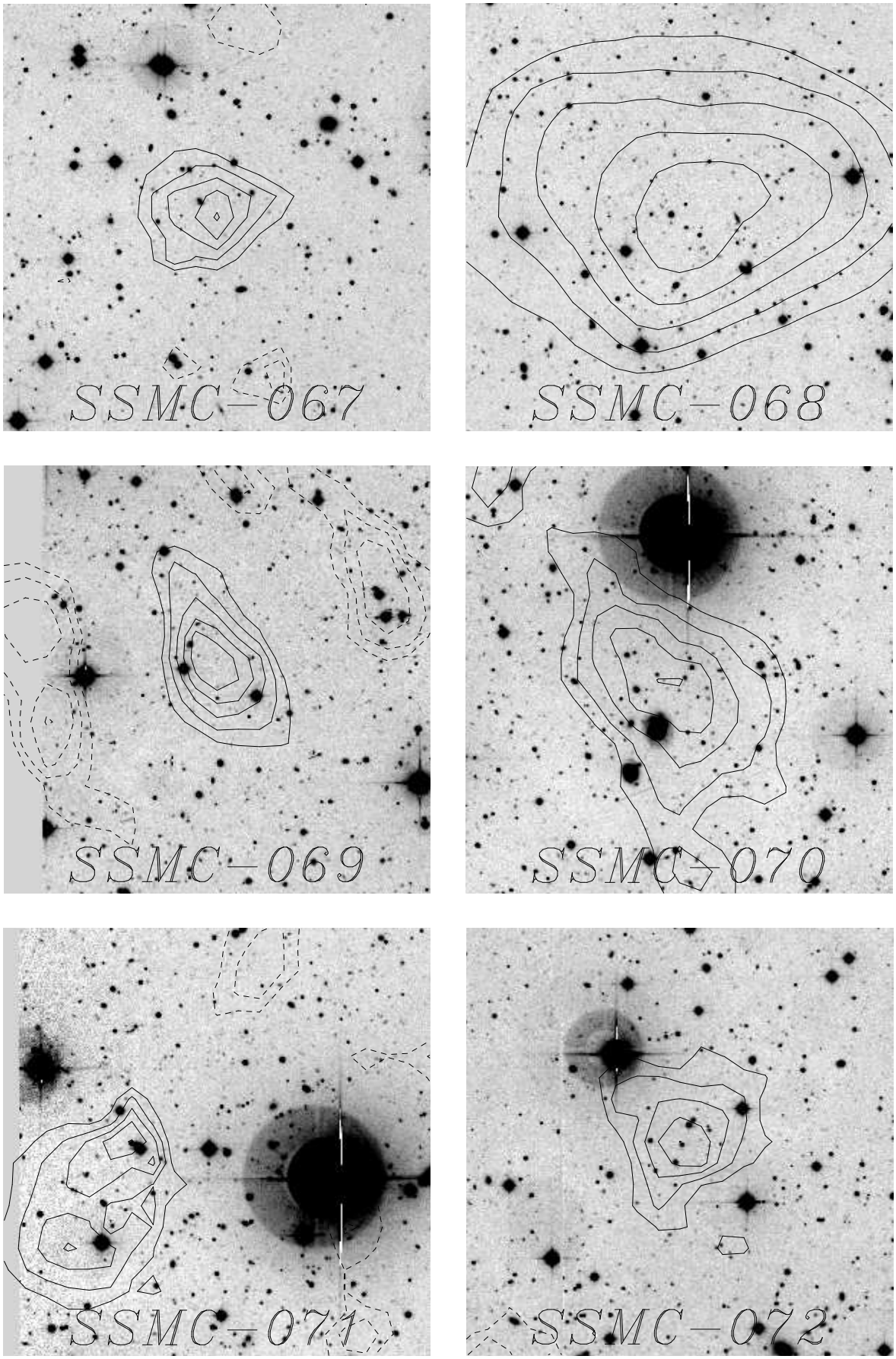

Figure A.12: Shear selected mass concentrations (l)

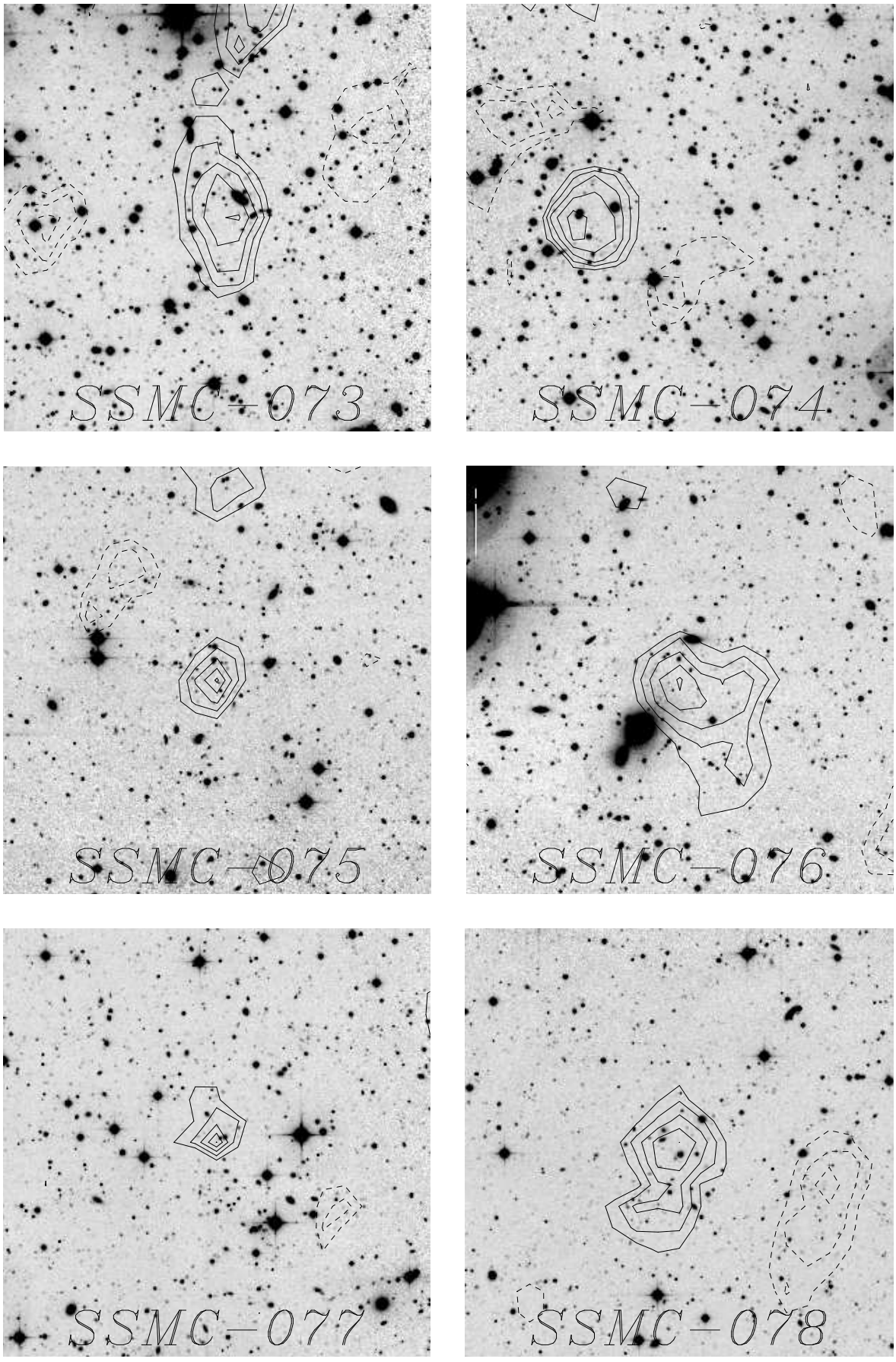

Figure A.13: Shear selected mass concentrations (m)

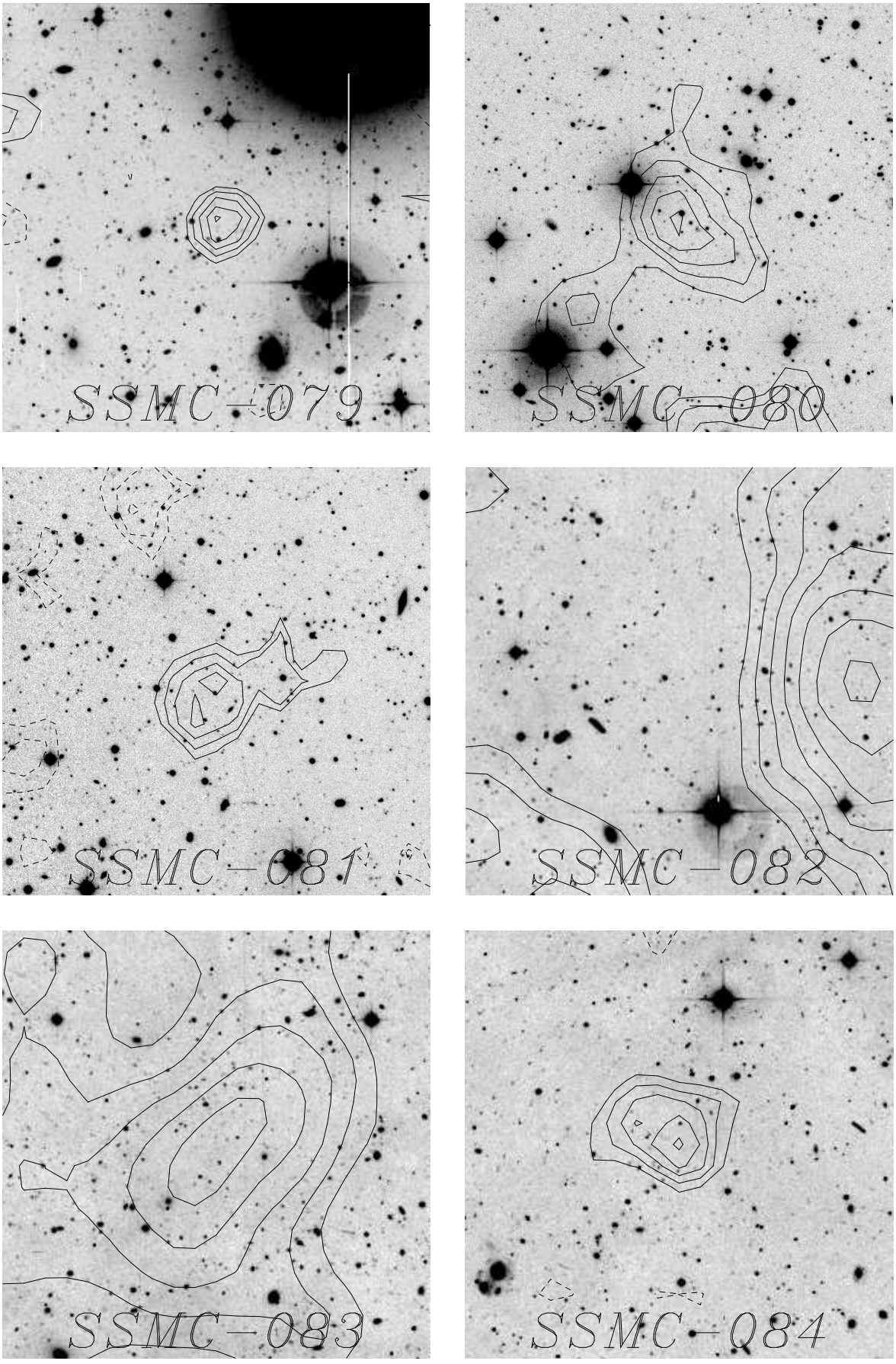

Figure A.14: Shear selected mass concentrations (n)

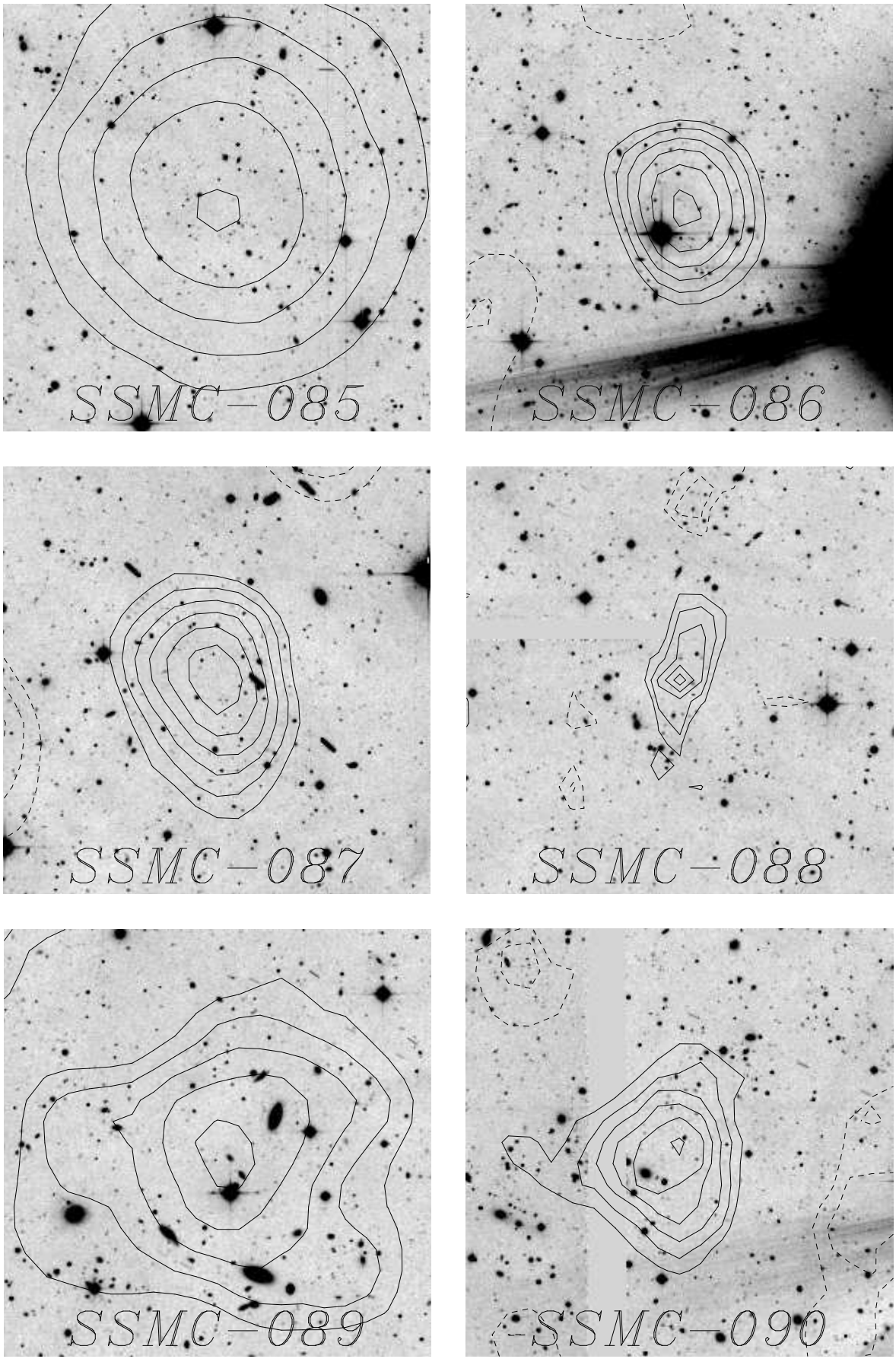

Figure A.15: Shear selected mass concentrations (o)

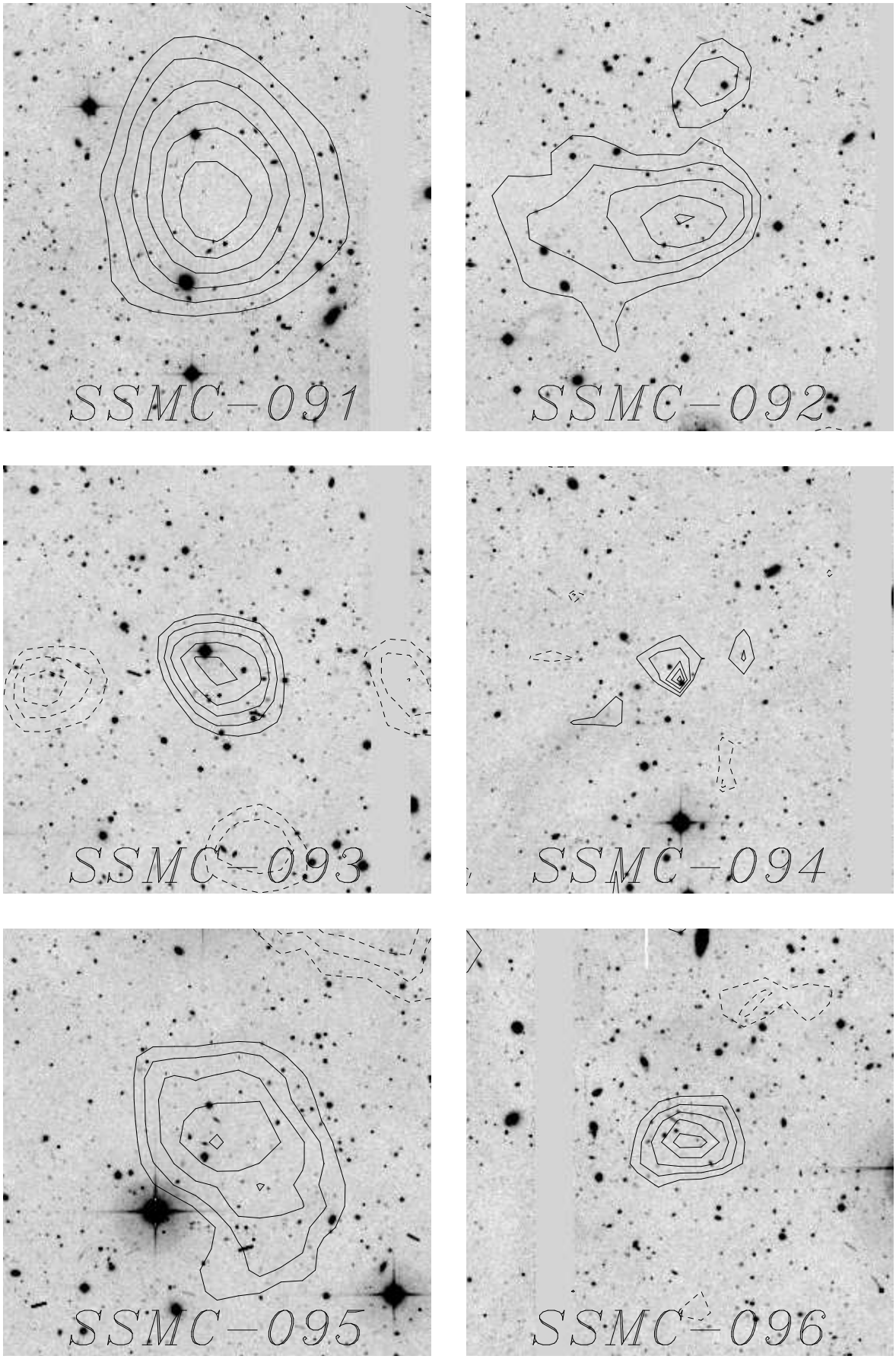

Figure A.16: Shear selected mass concentrations (p)

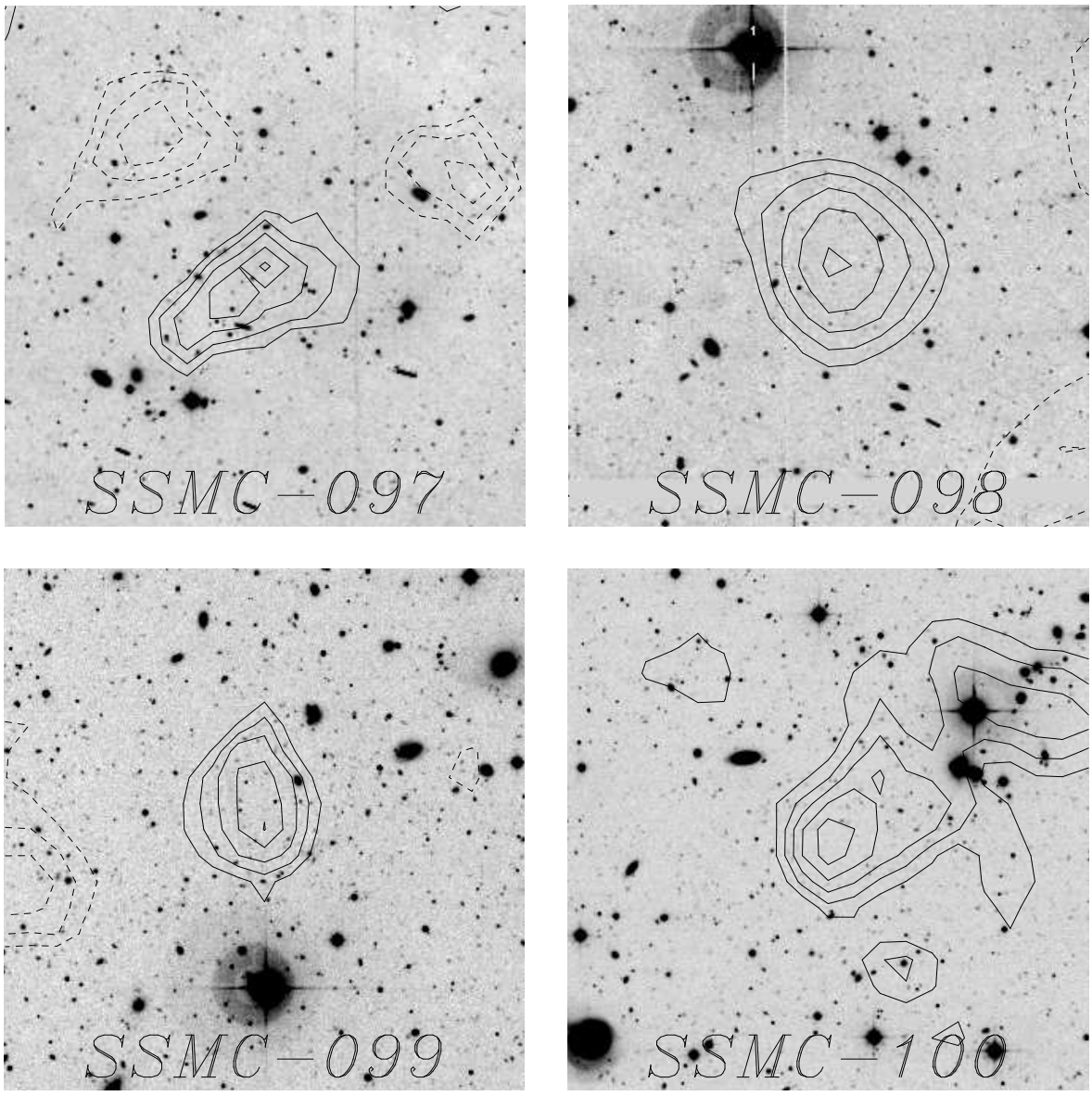

Figure A.17: Shear selected mass concentrations (q)

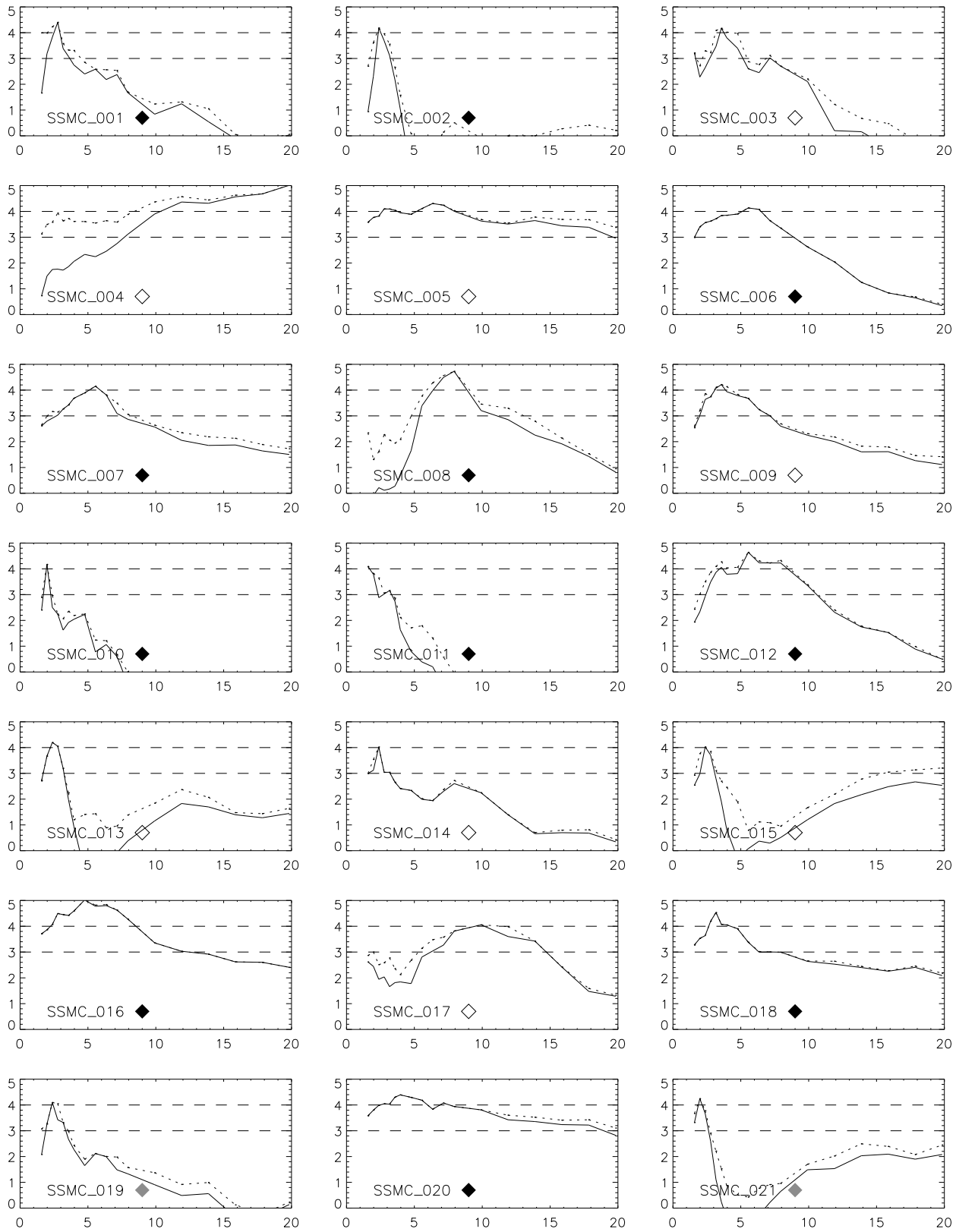

Figure A.18: S-profiles for the shear-selected mass concentrations from GaBoDS. The x-axis shows the filter scale in arcmin, the y-axis the detection significance. The dashed line takes into account that the peak position can vary slightly for different scales, whereas the solid line shows the S/N for the one position in the S-map at which the peak was detected most significantly. Dark, grey and white diamonds indicate the classifications *dark*, *unclear* and *bright*, respectively.

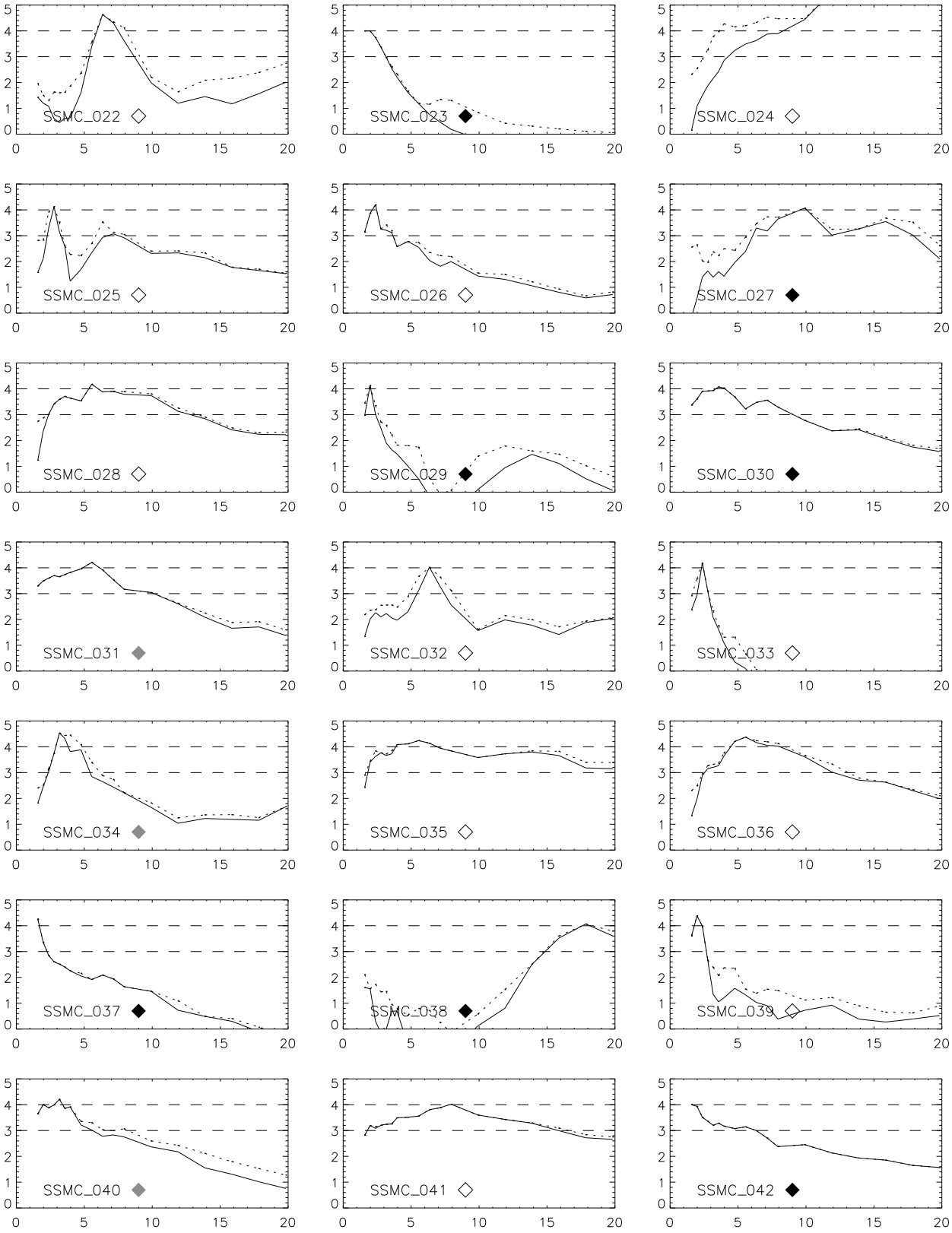

Figure A.19: *S*-profiles for GaBoDS

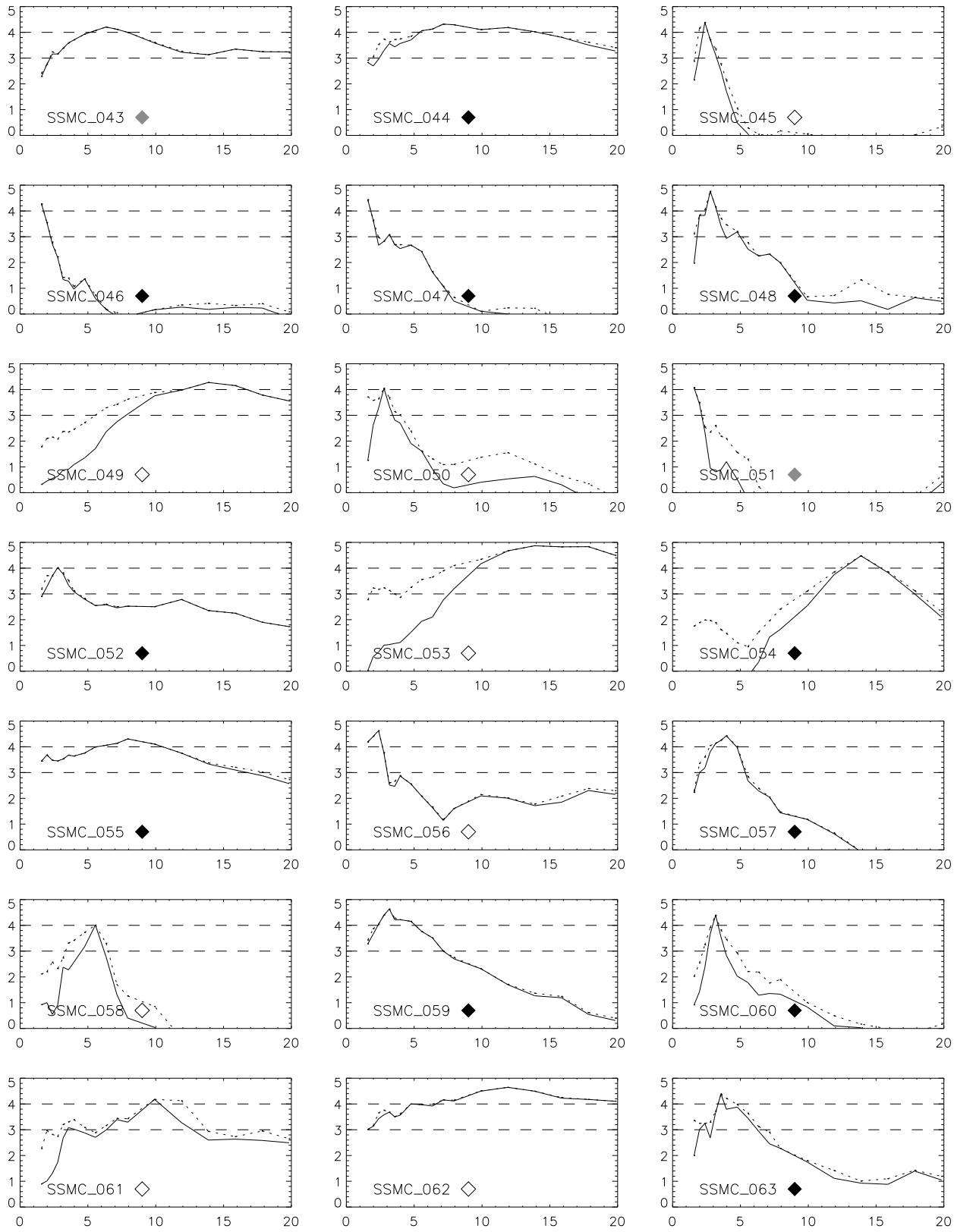

Figure A.20: *S*-profiles for GaBoDS

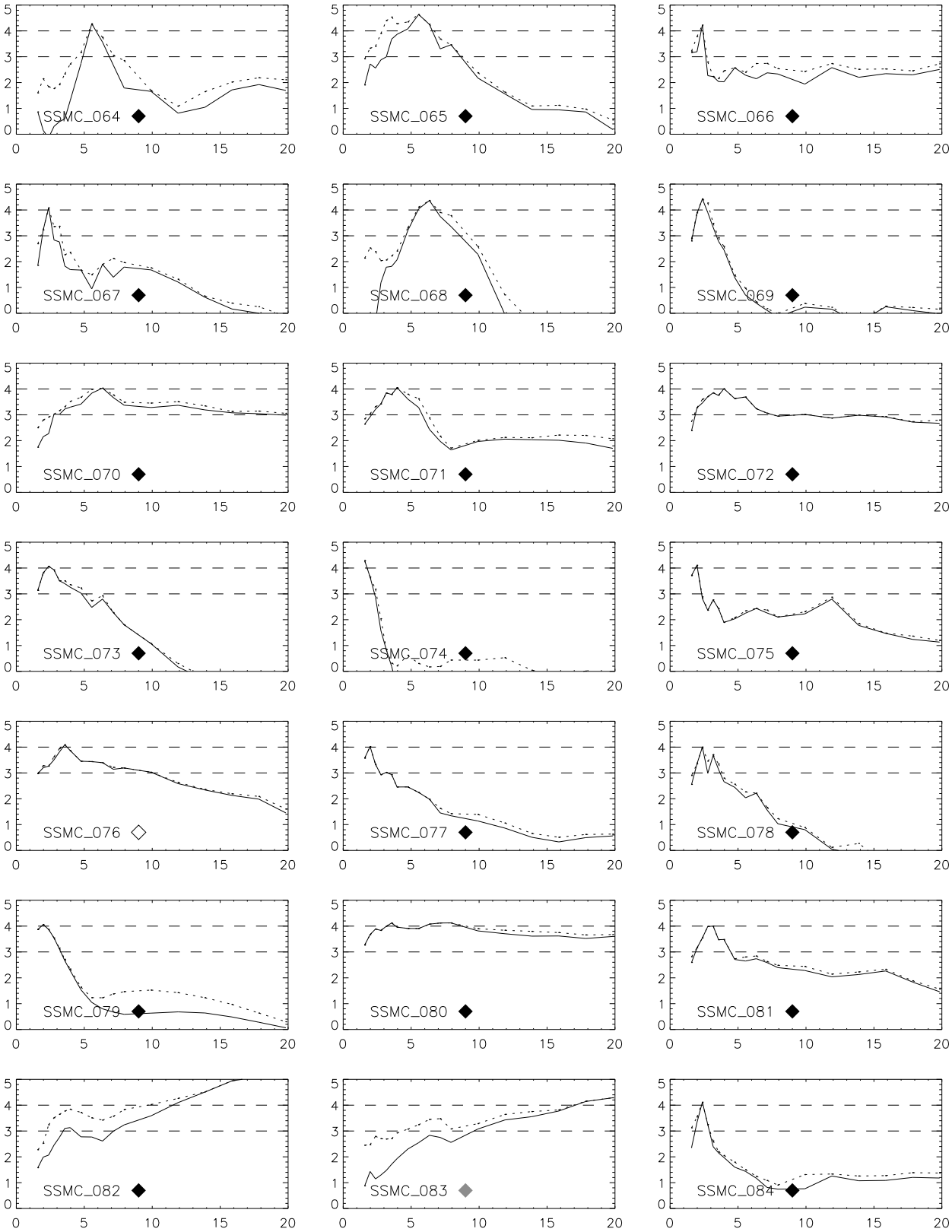

Figure A.21: *S*-profiles for GaBoDS

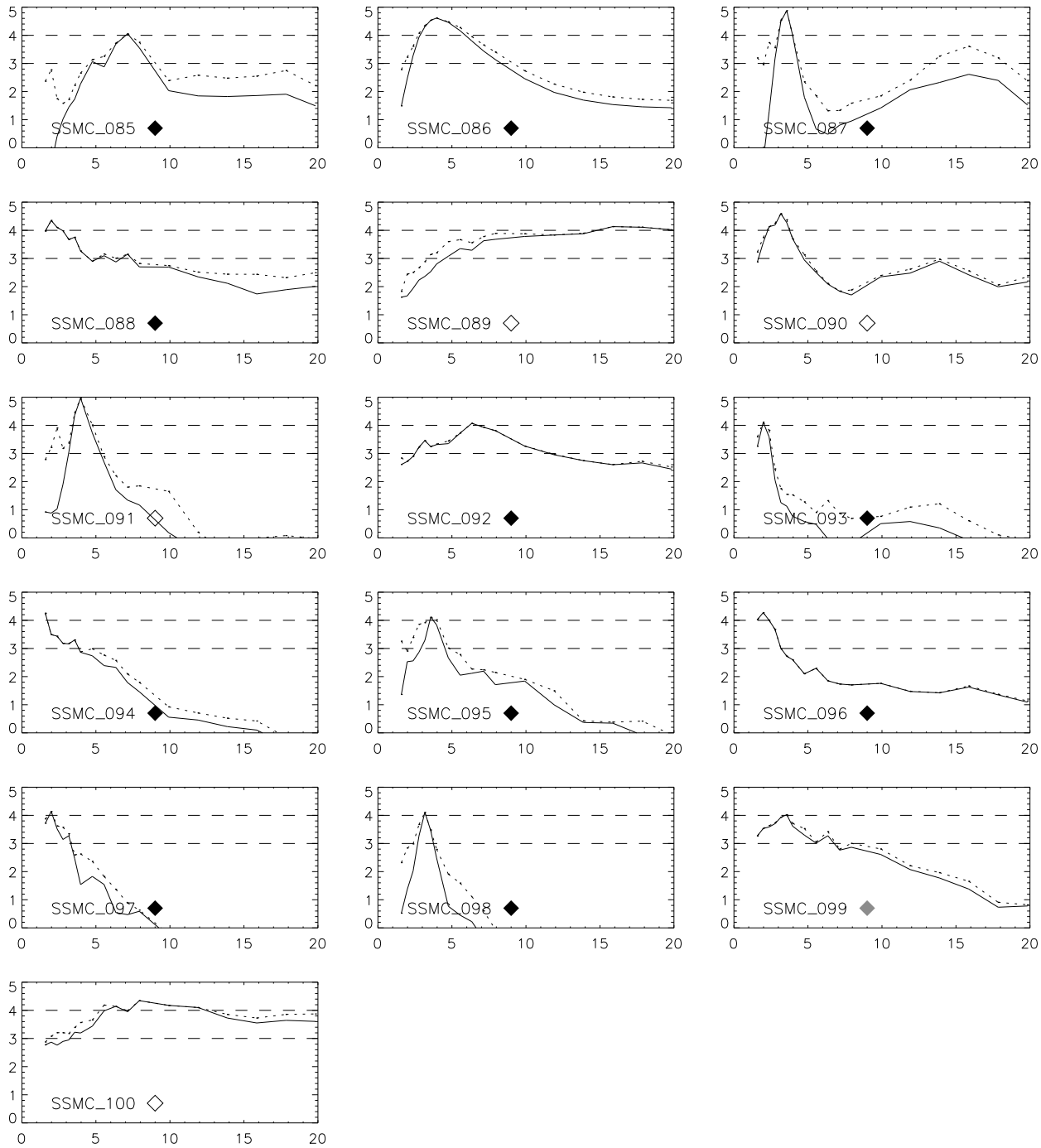

Figure A.22: *S*-profiles for GaBoDS

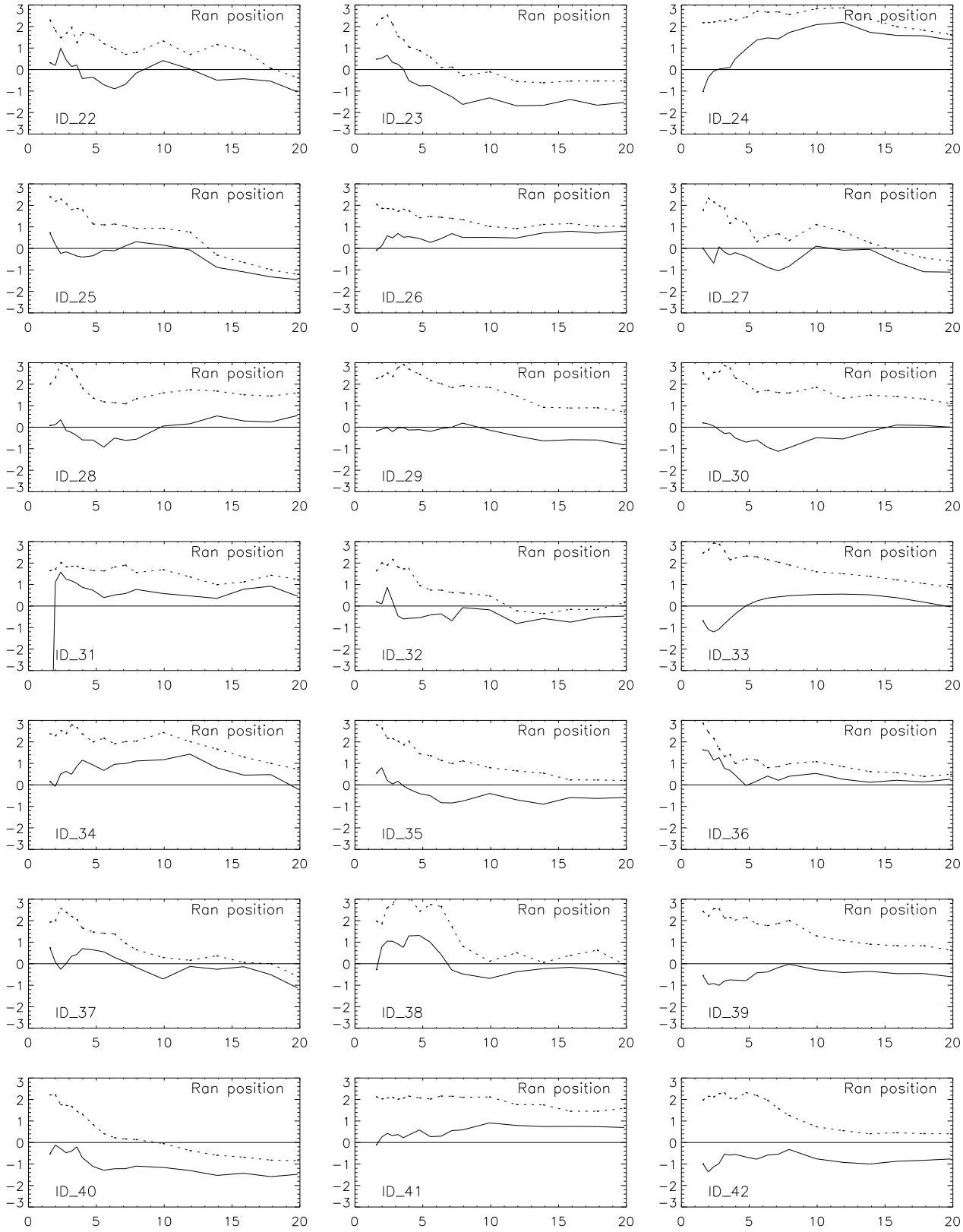

Figure A.23: S-profiles for GaBoDS calculated for randomly selected positions and filter types in the fields without randomisation of the galaxy orientations. The dashed line is explained in the caption of Fig. A.18.

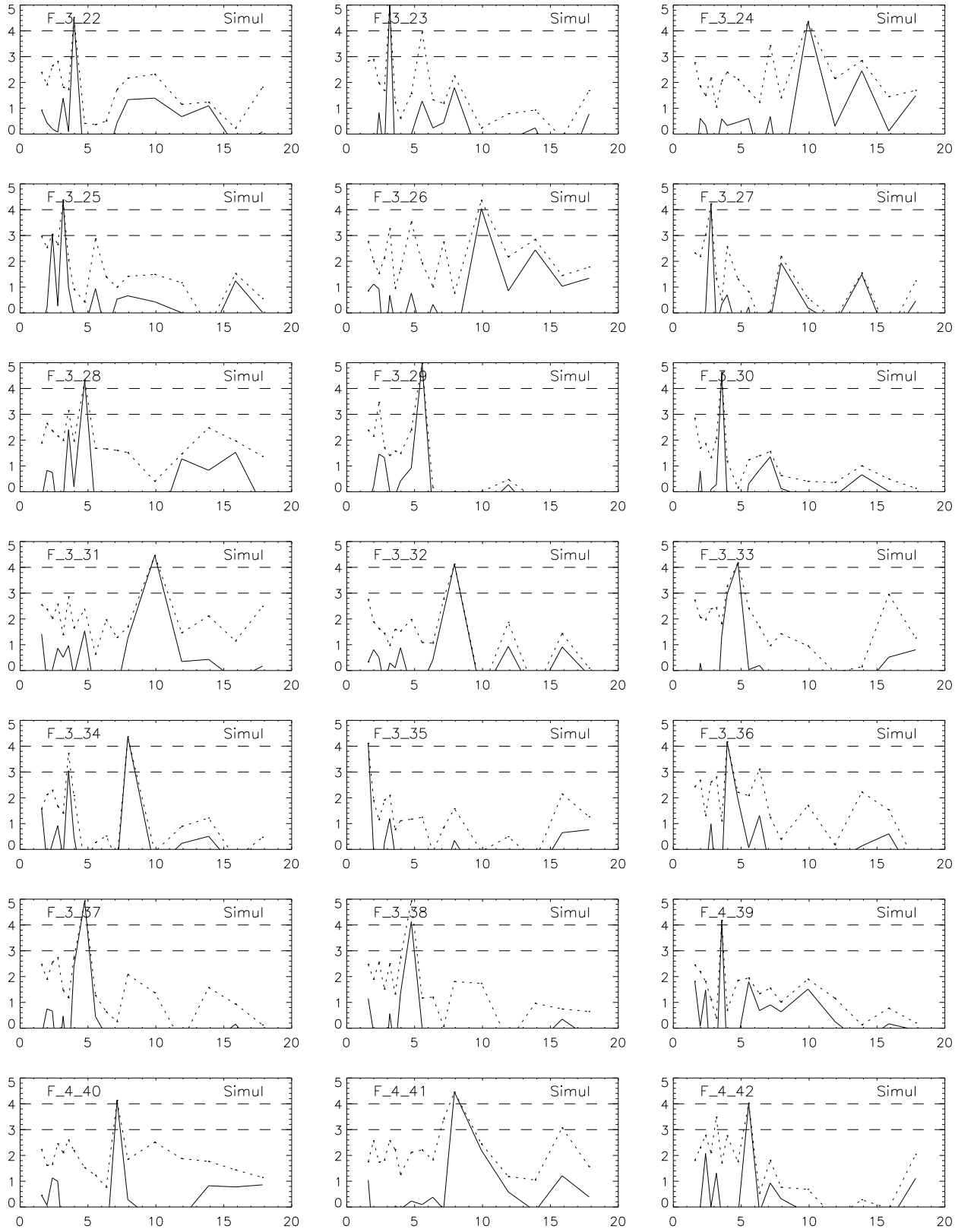

Figure A.24: Noise S-profiles calculated from data sets with randomised galaxy orientations. These are much more erratic than the S-profiles determined from real data, independent of the filter type. The plots labeled F_3_26, F_3_31 and F_3_34 were calculated for the POLY filter, and F_3_42 for the EXP filter. All others are TANH with varying widths x_c. The dashed line is explained in the caption of Fig. A.18.

Bibliography

Baade, D. 2000, ESO, *Wide Field Imager (WFI) User Manual*

Bacon, D.J., Refregier, A.R. & Ellis, R.S. 2000, MNRAS, 318, 625

Barrientos, F., Gladders, M., Yee, H. et al. 2003, The Messenger, 112, 40

Bartelmann, M. 1996, A&A, 313, 697

Bartelmann, M., Narayan, R. 1996, Jerusalem Winter School, *Lectures on Gravitational Lensing*

Bartelmann, M. & Schneider, P. 2001, Phys. Rep. 340, 291

Bertin, E. 2002, *SWarp user's guide*

Bertin, E. & Arnouts, S. 1996, A&AS, 117, 393

Bolzonella, M., Miralles, J.M. & Pelló, R. 2000, A&A, 363, 476

Bonnet, H. & Mellier, Y. 1995, A&A, 303, 331

Brainerd, T., Blandford, R. D. & Smail, I. 1996, ApJ, 466, 623

Broadhurst, T. J., Taylor, A. N., & Peacock, J. A. 1995, ApJ, 438, 49

Bruzual, A.G., Charlot, S. 1993, ApJ, 405, 538

Buchert, T. 1992, MNRAS, 254, 729B

Cappi, A., Held, E. V., & Marano, B. 1998, A&AS, 129, 31

Carroll, S.M., Press, W.H., Turner, E.L. 1992, Ann. Rev. Astr. Astrophys., 30, 499

Colless, M., Dalton, G., Maddox, S., Sutherland, W., Norberg, P., Cole, S. et al. 2001, MNRAS, 328, 1039

Collins, C. A., Guzzo, L., Nichol, R. C., & Lumsden, S. L. 1995, MNRAS, 274, 1071

Dahle, H., Pedersen, K., Lilje, P. B., Maddox, S. J., & Kaiser, N. 2003, ApJ, 591, 662

Erben, T., van Waerbeke, L., Mellier, Y., Schneider, P., Cuillandre, J.-C.; Castander, F. J.; Dantel-Fort, M. 2000, A&A, 355, 23

Erben, T., van Waerbeke, L., Bertin, E., Mellier, Y., Schneider, P. 2001, A&A, 336, 717

Freedman, W.L., Madore, B.F., & Gibson, B.K. et al. 2001, ApJ, 553, 47

Friedmann, A. 1922, Zeitschrift für Physik 10, 377-386

Gladders, M.D. & Yee, H.K.C. 2000, AJ, 120, 2148

Gonzaga, S., Biretta, J., Wiggs, M.S. et al. 1998, STScI Internal Publications, ISR 98-04, *The Drizzling Cookbook*

Gonzalez, A. H., Zaritsky, D., Dalcanton, J. J., Nelson, A. 2001, ApJS, 137, 117

Goto, T., Sekiguchi, M., Nichol, R. C. et al. 2002, AJ, 123, 1807

Gray, M. E., Ellis, R. S., Lewis, J. R., McMahon, R. G. & Firth, A. E. 2001, MNRAS, 325, 111

Greisen, E. W. & Calabretta, M. R. 2002, A&A, 395, 1061

Heymans, C. & Heavens, A. 2003, MNRAS, 339,711

Hoekstra, H., Franx, M., Kuijken, K. & Squires, G. 1998, ApJ, 504, 636

Hoekstra, H., Franx, M. & Kuijken, K. 2000, ApJ, 532, 88

Jain, B. & van Waerbeke, L. 2000, ApJ, 530, L1

Jing, Y. P. 2002, MNRAS, 335, L89

Kaiser, N. & Squires, G. 1993, ApJ, 404, 441

Kaiser, N. 1995, ApJ, 439, L1

Kaiser, N., Squires, G., Broadhurst, T. 1995, ApJ, 449, 460

Kaiser, N., Wilson, G., Luppino, G.A. 2000, astro-ph/0003338

Kruse, G. & Schneider, P. 1999, MNRAS, 302, 821

Kruse, G. & Schneider, P. 2000, MNRAS, 318, 321

Lynds, R. & Petrosian, V. 1986, BAAS, 18, 1014

Maoli, R., van Waerbeke, L., Mellier, Y. et al. 2001, A&A, 368, 766

Miralles, J.M., Erben, T., Hämmerle, H. et al. 2002, A&A, 388, 68

Misner, C. W., Thorne, K. S. & Wheeler, J. A. 1973: *Gravitation*, W. H. Freeman and Company

Miyazaki, S., Hamana, T., Shimasaku, K. et al. 2002, ApJ, 580, L97

Navarro, F., Frenk, C. S., White, S. D. M 1996, ApJ, 462, 563

Navarro, F., Frenk, C. S., White, S. D. M 1997, ApJ, 490, 493

Olsen, L. F., Scodeggio, M., da Costa, L. et al. 1999, A&A, 345, 363

Peacock, J. A. 2001, *Cosmological Physics*, Cambridge University Press

Peacock, J. A., & Dodds, S. J. 1996, MNRAS, 280, 19

Pierfederici, F. 2001, Proc. SPIE Vol. 4477, p. 246

Pietrzynski, G., Gieren, W., Fouqué, P., & Pont, F. 2002a, AJ, 123, 789

Pietrzynski, G., Gieren, W., & Udalski, A. 2002b, PASP, 114, 298

Postman, M., Lubin, L. M., Gunn, J. E. et al. 1996, AJ, 111, 615

Robertson, H. P. 1935, ApJ, 82, 284

Sato, J., Umetsu, K., Futamase, T. & Yamada, T. 2003, ApJ, 582, 67

Schirmer, M., Erben, T., Schneider, P. et al. 2003, A&A, 407, 869

Schneider, P., Ehlers, J. & Falco, E. E. 1992, *Gravitational lenses*, Springer Verlag, Heidelberg

Schneider, P. & Seitz, C. 1995, A&A, 294, 411

Schneider, P. 1996, MNRAS, 283, 837

Schneider, P., van Waerbeke, L., Jain, B. & Kruse, G. 1998, MNRAS, 296, 873

Schneider, P., King, L.J. & Erben, T. 2000, A&A, 353, 41

Seitz, C. & Schneider, P. 1997, A&A, 318, 687

Soucail, G., Fort, B., Mellier, Y., & Picat, J. P. 1987, A&A, 172, 14

Soucail, G., Mellier, Y., Fort, B., Hammer, B., & Mathez, G. 1987, A&A, 184, 7

Umetsu, K. & Futamase, T. 2000, ApJ Lett., 539, L5

van Waerbeke, L., Mellier, Y., Erben, T. et al. 2000, A&A, 358, 30

Venemans, B. P., Kurk, J. D., Miley, G. H. et al. 2002, ApJ, 569, 11

Vettolani, G., Zucca, E., Merighi, R. et al. 1998, A&AS, 130, 323

Voges, W., Aschenbach, B., Boller, T. et al. 1999, A&A, 349, 389

Walker, A. G. 1936, Proc. Lond. Math. Soc (2) 42, 90

Walsh, D., Carswell, R. F., & Weymann, R. J. 1979, Nature, 279, 381

Wilson, G., Cole S., Frenk, C. S. 1996, MNRAS, 280, 199

Wittman, D., Tyson, J.A., Kirkman, D., Dell'Antonio, I. & Bernstein, G. 2000, Nature, 405, 143

Wittman, D., Tyson, J.A., Margoniner, V.E. et al. 2001, ApJ, 557, 89

Wittman, D., Margoniner, V. E., Tyson, J. A., Cohen, J. G., Becker, A. C., & Dell'Antonio, I. P. 2003, ApJ, 597, 218W

Wright, C. O. & Brainerd, T. G. 2000, ApJ, 534, 34